MODELLING TRANSIENT INCLUSION BEHAVIOUR DURING REFINING OF SI-MN KILLED STEEL

MODELLING TRANSIENT INCLUSION BEHAVIOUR DURING REFINING OF SI-MN KILLED STEEL

BY
ANGSHUMAN PODDER, M.Tech.

A THESIS
SUBMITTED TO THE SCHOOL OF GRADUATE STUDIES
IN PARTIAL FULFILMENT OF THE REQUIREMENTS
FOR THE DEGREE OF
DOCTOR OF PHILOSOPHY

Doctor of Philosophy (2023) McMaster University
(Materials Science and Engineering) Hamilton, Ontario, Canada

TITLE:	Modelling transient inclusion behaviour during refining of Si-Mn killed steel
AUTHOR:	Angshuman Podder M.Tech. (Process Engineering), Indian Institute of Technology (IIT), Bombay, India
SUPERVISOR:	Dr. Kenneth S. Coley and Dr. André Phillion
NUMBER OF PAGES:	xxiii, 187

Abstract

Certain non-metallic inclusions are known to cause deleterious effects in steel products and affect the production efficiency of steelmaking if not controlled. Most of these are oxide inclusions formed during deoxidation in refining processes, especially in the ladle metallurgy furnace (LMF), an understanding of which is essential for process control. The composition of these inclusions changes subsequently while interacting with other phases like slag, alloy additions, and refractories. The efficient removal and composition control of inclusions are important variables to consider for any steelmaker. Moreover, desulphurisation of steel is another aspect that needs attention since excess sulphur can precipitate sulfide inclusions while cooling. Hence, tracking the composition evolution of different phases in a ladle furnace is beneficial for the steelmaking industry.

Previous researchers in the authors' laboratory developed a model that could be used to predict the kinetics of steel-slag-inclusion reactions in aluminium (Al) killed steel. The current work focusses on developing a kinetic model that can be used to describe the inclusion evolution during ladle treatment of silicon-manganese (Si-Mn) killed steel. For this, firstly, the formation of complex oxides in Si-Mn-killed steel was analyzed using a mathematical model of nucleation and growth of particles in melts. The results revealed that spontaneous nucleation of complex oxides occur during alloy additions, resulting in different compositions of oxide nuclei, based on the local supersaturation conditions. Sensitivity analysis with different parameters was carried out to understand the influence of physicochemical variables on the model. Following this, two kinetic models were built: 1) average inclusion composition tracking method; and 2) multi oxide inclusion (MOI) composition tracking method. The latter approach included the thermodynamics and kinetics of different inclusion formation and could further incorporate the total inclusion number density variation in steel. The MOI model can be used to predict the changes in not only the average inclusion composition but also the type of inclusions precipitating in steel. Following this, laboratory deoxidation

experiments were carried out using FeSi and FeMn to understand the inclusion behaviour post alloy additions. The MOI model showed good potential in simulating these laboratory deoxidation experiments and was then coupled with a previously developed steel-slag model to simulate actual ladle refining reactions. The calculated results were compared with different industrial data and showed good agreement with what is observed in reality, showing the success of this new approach. Similar to previous investigations, the rate-determining step could be attributed to the availability of solutes in steel (from slag or alloys) along with their transport to the steel-inclusion interface. The overall model was also able to simulate the desulphurization behaviour in steel. The effects of different processing conditions such as [Al], [O] content, reoxidation, and stirring conditions, were also examined and discussed through a parametric analysis.

तमसोमा ज्योतिर् गमया

Tamsoma Jyotirgamaya
May the light of knowledge remove the darkness of ignorance

Dedicated to my family
&
In loving memory of my
late grandmother

Acknowledgements

I express my sincere gratitude to Dr. Kenneth Coley and Dr. André Phillion for giving me the opportunity to conduct Ph.D. studies with them. Their guidance and support have proven to be invaluable and significant in finishing this work on time amidst a global pandemic. Moreover, their patience and willingness to allow me to explore different ideas have helped me develop sharp and critical research skills that I wish to carry with in the future. Also, I would like to thank Dr. Christopher Swartz for being a member of my supervisory committee, whose useful suggestions and encouragement have kept me on the right track. I convey my sincere acknowledgment to the other faculty members of our research group, Dr. Neslihan Dogan and Dr. Leili Tafaghodi, for adding their valuable insights.

I would like to thank staff members of the Materials Science and Engineering Department, especially Mary Anne Bechamp, technicians, Ed McCaffery, Dr. Xiaogang Li, and Doug Culley, for their help at different stages of my graduate study and for providing resources pertaining to experimental and administrative work. I also acknowledge the members of CCEM, Jhoynner Martinez and Chris Butcher, who helped me to understand the different dimensions of SEM microscopy. I consider myself extremely fortunate to have worked with Dr. Yves Brechét for a brief time, whose command on modeling and mathematical techniques mesmerized me and inspired me to emulate his caliber. I am also grateful to McMaster Steel Research Center, Natural Science Engineering Research Council, and McMaster University for the financial support.

In my four years, needless to say, my PhD journey would have been incomplete without beautiful friendships (Jonas, Ale, Nizia, Bita, Alessandra, Rohit, Dipankar, Sai, Kaustubh, Elnaz, Cal, Satyam, Shrikant, Debanjan). I would also like to thank members of the McMaster Process Metallurgy Group (Jayasree, Aliyeh, Mukesh, Michelia, Ali, Suwam, Guang, Bhavya) and SIM3P group (Pardis, Yi, Pravakar, Coleton, Neil, Abhishek, Stefan) for the wonderful social interactions, along with everyone who directly or indirectly have contributed to a work-life balance. My friends (Roy, Maddy,

Ankit, Anuja, Sanjoy) and cousins back at home (Kaustav, Arindam) also deserve equal acknowledgment for having given me moral support and time, which helped me overcome the mental fatigue of my Ph.D. On the academic front, I am grateful to Yousef for explaining the framework of the model initially. Special thanks to the best postdocs I could have wished for, Kezhuan and Nabeel, who have tolerated me, helped me with my project and experiments, and, most importantly, carried out extremely helpful discussions on my ever-evolving ideas.

It would be unfair not to acknowledge the contribution of two professors in my life, Prof. N. B. Ballal and Prof. P. K. Dutta whose teachings and life wisdom in various topics during undergrad and Masters study inculcated in me, a deep desire to pursue metallurgy as a career. Ultimately, I would like to thank my parents, Babli Podder and Ashoke Kumar Podder, and brother, Anupam Podder, for letting me pursue my dreams in a different country and providing much-needed support and encouragement during good and bad times. Lastly, I would like to express my deepest appreciation and gratitude to my grandparents, especially my late grandmother (*dida*), Parul Rani Saha, for her endless, unconditional love and care during my formative years, who will be surely proud to see me where I am today. I will be forever indebted to my family for their sacrifices throughout my life and dedicate this thesis to them.

Last but not least, this PhD would not have been possible without *Google*, helping countless souls like me traverse the vast depths of the wide ocean of literature.

Contents

List of Figures

List of Tables

List of Abbreviations

AOD	Argon Oxygen Decarburization
ANN	Artificial Neural Network
BOF	Basic Oxygen Furnace
BO	Bridging Oxygen
CAT	Cell Average Technique
CNT	Classical Nucleation Theory
CFD	Computational Fluid Dynamics
DPM	Discrete Particle Model
EAF	Electric Arc Furnace
EPMA	Electron Probe Micro-Analysis
ECD	Equivalent Circle Diameter
FVM	Finite Volume Method
FPT	Fixed Point Technique
GEM	Gibbs Energy Minimization
IGFIA	Inert Gas Fusion Infrared Absorptiometry
KWN	Kampmann Wagner Numerical
LES	Large Eddy Simulation
LIMCA	Liquid Metal Cleanliness Analyzer
MIDAS	Mannesmann Inclusion Detection by Analyzing Surfboards
mtc	Mass transfer coefficient
MTM	Mixing Tank Model
NMI	Non metallic Inclusions
NBO	Non-Bridging Oxygen
NMR	Nuclear Magnetic Resonance Spectroscopy
OES-PDA	Optical Emission Spectroscopy - Pulse Distribution Analysis
PSD	Particle Size Distribution
PSG	Particle Size Grouping
PBE	Population Balance Equations
PDF	Probability Density Function
PMA	Pseudomolecule Approach
QMOM	Quadrature Method of Moments
SEM-EDS	Scanning Electron Microscope-Energy Dispersive Spectroscopy

SM	Sectional Method
SCM	Shrinking Core Model
SRSM	Sub Regular Solution Model
TO	Total Oxygen
UIPF	Unified Interaction Parameter Formalism
VD	Vacuum Degassing
VOF	Volume of Fluid
WDS	Wave Dispersive Spectroscopy
XRD	X-Ray Diffraction

List of Symbols

$(\%S)$	Sulphur concentration in slag ($wt\%$)
$[\%S]$	Sulphur concentration in steel ($wt\%$)
β_i	Collision rates of inclusions (m^3/s)
$\dot{N}_i$	Mass transfer rate (mol/s)
γ	Angle between buyouant plume and vertical
$\mathrm{C}^{\mathrm{m}}_{\mathrm{i,b}}$	Concentration of i in the bulk on the metal side (mol/m^3)
$\mathrm{C}^{\mathrm{s}}_{\mathrm{i,b}}$	Concentration of i in the bulk on the slag side (mol/m^3)
$\mathrm{k_m}$	Metal mass transfer coefficient (m/s)
$\mathrm{k_o}$	Overall mass transfer coefficient (m/s)
$\mathrm{k_s}$	Slag mass transfer coefficient (m/s)
L	Species partition coefficient
$\mathrm{t_c}$	Contact time (s)
μ	Liquid viscosity (kg/m/s)
μ_t	Turbulent viscosity (kg/m/s)
ρ^*	Density ratio
ρ_m	Density of metal (kg/m^3)
ρ_s	Density of slag (kg/m^3)
σ	Surface tension of metal (N/m)
σ_{IM}	Interfacial tension of inclusion/metal (N/m)
σ_{IS}	Interfacial tension of inclusion/slag (N/m)
σ_{MS}	Interfacial tension of metal/slag (N/m)
θ_{IMS}	Overall wettability factor
ε	Energy dissipation rate (m^2/s^3)
A^*_{e}	Non dimensional slag eye area
a_{i}	Species activity
C_O	Total oxygen concentration (ppm)
C_S	Sulphide capacity
$C_{v,m}$	Molar density of species in steel (mol/m^3)
d_D	Droplet diameter (m)
D_i	Diffusivity of i in steel (m^2/s)
$D_{\mathrm{i,m}}$	Molecular diffusivity (m^2/s)
f_S	Henrian activity of sulphur in steel

g	Acceleration due to gravity (m/s^2)
h^*	Non dimensional liquid height
K_O	Deoxidation constant (/s)
P	Total pressure (N/m^2)
p_i	Partial pressure of i in gas (atm)
Q^*	Non dimensional flow rate
r_{ox}	Radius of oxide inclusion (m)
Re_{p}	Particle Reynolds number
Sc	Schmidt number
$t/0/e$	Subscripts indicate (at time t), (at time 0), (at equilibrium)
u_i	Steel velocity at interface (m/s)
v	Kinematic diffusivity (m^2/s)

Chapter 1

Introduction

1.1 Research Background

Molten steel undergoes different refining treatments based on the grade being manufactured, which are broadly referred to as 'secondary steelmaking'. Nonmetallic inclusions (NMIs) produced during refining are well-known to have a detrimental effect both on the steel performance [1] and also, on processability. To ensure uniform and uninterrupted casting schedules, control over inclusions and their compositions has thus become necessary. Constant efforts are being made to increase the effectiveness of refining processes to produce steel with the desired 'cleanliness'. This has necessitated the use of dynamic models that can simulate real industrial conditions in a computer environment and help steelmakers towards better process control.

During the ladle refining process, several chemical reactions can take place between different phases in the liquid steel. It is essential to understand the close coupling between these phases in order to predict the effect of different process variables on their compositional changes. One of the important objectives of ladle refining is to obtain inclusions that are favourable for processing during the continuous casting of steel, i.e., inclusions that remain in the liquid state to temperatures well below the casting temperature. Complex deoxidation by Si and Mn is beneficial for certain long steel products since it leads to the formation of low-temperature melting manganese silicates [2]. These inclusions are liquid at casting temperatures (around 1500 °C), thus reducing clogging and allowing longer casting sequences. Moreover, inclusions that remain liquid or deformable at lower temperatures do not impair the mechanical properties of steel products. However, unwanted

reactions and poor process control in high-temperature reactors lead to deviations from what is sought. In this regard, understanding the effect of process variables on the evolution dynamics of inclusions is crucial, backed up by experimental and modelling studies.

Over the past ten years or so, researchers at McMaster University [3, 4] have worked towards the development of a process model for predicting the evolution of spinel and calcium aluminate inclusions during the refining of Al-killed steels in a ladle metallurgical furnace (LMF). The model consists of a calcium dissolution model and a shrinking core model for inclusion transformation, which is further coupled to a slag-steel reaction model [5]. This model is able to track changes in the composition of steel, slag, and the evolution of inclusions with time-based on actual industrial conditions. The model results have shown promising results with heat data from a single North American steel plant. However, in its current version, the model is limited to a narrow range of alumina and aluminate inclusions and thus is not applicable to a generic steel plant. Si-Mn killed steel forms the necessary precursor for long-product steels; a better understanding of the mechanisms for inclusion formation in such steels needs a thorough investigation. Furthermore, it would be beneficial for the steelmaking industry to have the capacity to predict the conditions facilitating the formation of harmful inclusions for any killing practice employed. For this, critical analysis of industrial data, along with an understanding of the underlying principles of the process, is required.

In summary, a structured approach for identifying and modelling the predominant inclusions in Si-Mn killed steels is required for developing a reliable process model. Subsequently, this model should be validated against experimental data. From an industrial point of view, the change in total oxygen as well as the composition of the steel and the inclusions in relation to process variables is of prime importance. This study is expected to address the following steelmaker needs:

- How to obtain liquid inclusions and avoid harmful inclusions in Si-Mn killed steel?
- How to optimize the top slag chemistry for better deoxidation, desulphurization, and inclusion control?
- How to use a fundamental-based model in actual steelmaking conditions?

1.2 Objectives of the study

The goal of the research is to develop a multicomponent, multiphase kinetic model that is capable of tracking the steel, slag, and inclusion composition over time in Si-Mn killed steel, taking into consideration the different interactions between the slag, inclusions, and molten steel. Specifically, the following objectives have been identified:

1. To develop a fundamental kinetic model which can be used to simulate steel-slag-inclusion reactions in Si-Mn killed steel to study the effect of top slag characteristics on inclusion composition;
2. To compare the model results with experimental data and plant data to show applicability to actual steelmaking conditions.
3. To perform sensitivity analysis on the model to understand the influence of the important parameters governing the process.

1.3 Outline of thesis

This thesis is comprised of eight chapters.

Chapter 1 provides a general background to the motivation for the current study, along with an outline of the objectives of the current research as well as an overall thesis outline.

Chapter 2 reviews the pertinent up-to-date literature related to thermodynamics and kinetics of important refining reactions, inclusions in Si-Mn killed steels, and models related to secondary steelmaking.

Chapter 3 develops two sub-models of complex oxide formation during Si-Mn deoxidation considering spontaneous nucleation and modification of existing simple oxides. A detailed parametric analysis with composition variables and physical properties is carried out to explore their effects on inclusion composition.

Chapter 4 presents an overall multi-component steel-slag reaction interface model and a kinetic model for steel-inclusion reactions to model average inclusion chemistry changes in Si-Mn killed steels. Data from laboratory experiments are presented to validate the model. Subsequently, the model is used to examine the effect of alumina in slag on steel and inclusion chemistry, including Al pick-up rate in steel and deoxidation behavior.

Chapter 5 describes a new modeling approach that tracks the competition between multiple oxide inclusions arising after deoxidation in molten steel. The model includes six different types of inclusions and shows a significant improvement over the model described in Chapter 4. The results are applied to previous literature data pertaining to the refining of Si-Mn killed steels.

Chapter 6 presents an application of the coupled steel-slag reaction model [5] and the model developed in Chapter 5 to the industrial refining process of Si-Mn killed steels to predict inclusion composition, sulfur and oxygen in steels. A detailed parametric analysis as a function of steel chemistry, slag chemistry, and process variables is presented to demonstrate the benefits of the model.

Chapter 7 presents a summary of the laboratory experiments carried out to study the sequential deoxidation of iron by ferroalloys (FeSi and FeMn), where the effect of oxygen and alloying practice on inclusion chemistry and size distribution have been studied. Total oxygen, chemical composition and extensive inclusion analysis were performed to characterize the transient nature of inclusion composition evolution with time.

Finally, Chapter 8 draws together the important findings from each of the previous chapters illustrating how each contributes to meeting the objectives. General conclusions are also offered, and the scope of future work is presented.

At this time, the contents of Chapter 3 were presented at the STEELSIM2021 conference and were later selected to be published in Steel Research International (DOI 1). Chapter 4 was published in Metallurgical and Materials Transactions B (DOI 2). Chapter 5 was published in Metallurgical and Materials Transactions B (DOI 3). Finally, Chapters 6 and 7 will be submitted to peer-reviewed international journals in the near future.

References

[1] A. Ghosh: Secondary Steelmaking: Principles and Applications, CRC Press, 2001.
[2] R.J. Fruehan: Ladle Metallurgy Principles and Practices, Iron and steel society, AIME, 1985.
[3] A. Galindo: Kinetic modelling for the formation of Magnesium Aluminate Inclusions in the Ladle Metallurgy Furnace. MA.Sc thesis, McMaster University, 2015.
[4] Y. Tabatabaei: Modeling of inclusion evolution in Ladle Metallurgy Furnace. Ph.D. thesis, McMaster University, 2018.
[5] K. J. Graham: Integrated Ladle Metallurgy Control. PhD thesis, McMaster University, 2008.

Chapter 2

Literature review

2.1 Secondary steelmaking

Ironmaking and steelmaking have evolved over the last 150 years (maybe multi-centuries!) with different operating practices and various updates in technology. After the onset of continuous casting, steelmaking has seen many improvements with a greater focus on cleanliness and tighter control on properties. Modern steelmaking processes can be classified into primary and secondary steelmaking processes which are shown in Figure 2.1. Broadly, the final steel products can be termed as flat products or long products based on their length-to-width dimensions (Figure 2.1).

Primary steelmaking involves the production of crude steel from the molten metal made in blast furnaces or by directly melting scrap or direct reduced iron (DRI). It is often very difficult to carry out certain aspects of refining in primary steelmaking conditions. Therefore, steel undergoes further processing and refining in other reactors that constitute 'secondary steelmaking'. Different reactors like ladle furnace (LF), AOD (Argon Oxygen Decarburization), VOD (Vaccum Oxygen Decarburization) and RH (Ruhrstahl Heraeus) degassing, VD (Vaccum degassing) furnaces (shown in Figure 2.2) are used by steelmakers to refine and 'adjust' the steel based on the specifications of the final product. The thermodynamic and kinetic aspects of these processes have been well summarised by Lange [2]. Due to the strict grade requirements by customers, there has been a growing impetus for improving the process control of these secondary steelmaking processes to make steels of better quality.

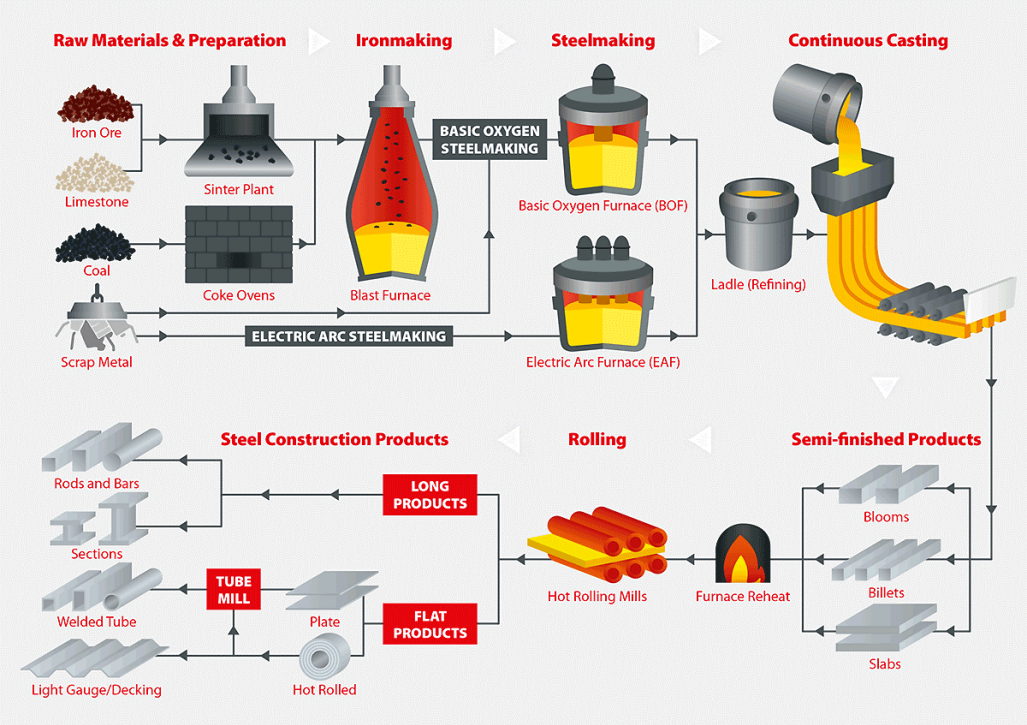

Figure 2.1: *Typical steelmaking routes [1].*

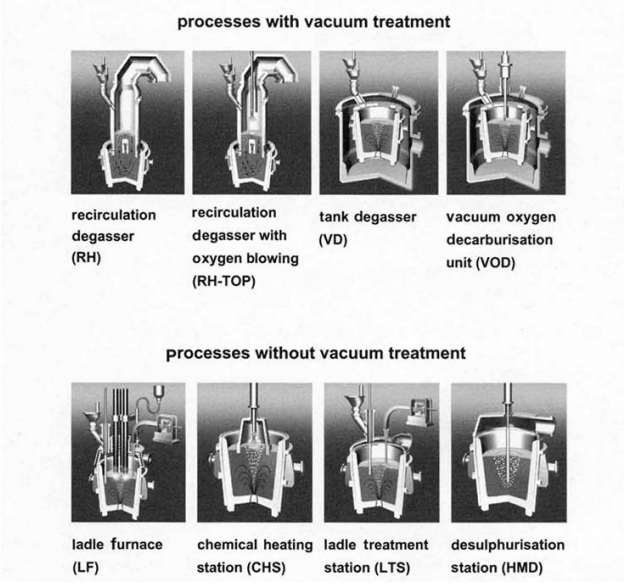

Figure 2.2: *Different secondary steelmaking reactors with and without vacuum treatment [4].*

The ladle metallurgy furnace (LMF/LF) serves as an important reactor where the steelmaker can have better control of the steel quality. A schematic of

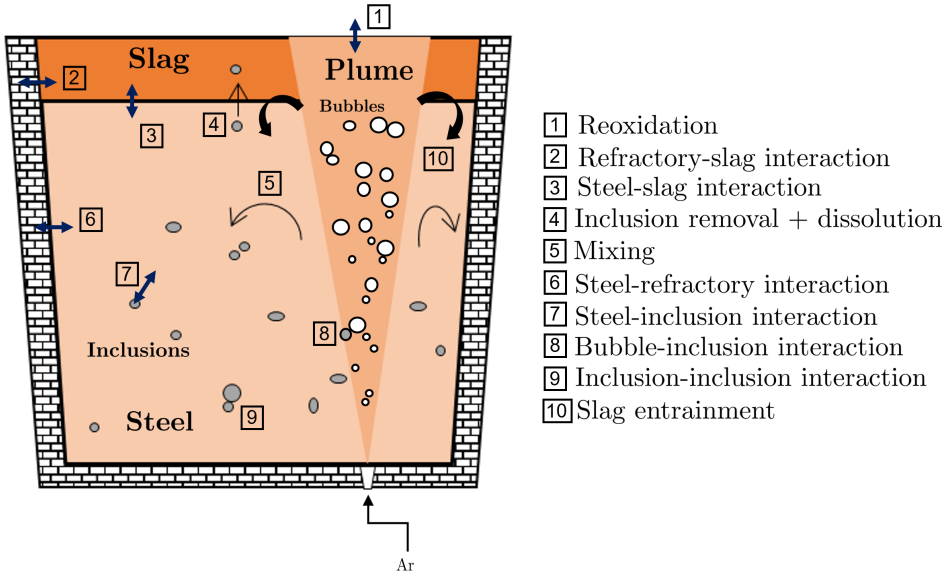

Figure 2.3: *Schematic of ladle furnace showing the most important interactions.*

the conventional LF is shown in Figure 2.3. The main objectives of ladle furnace consists of [3]:

1. Homogenization of ladle steel,
2. Composition control by alloying additions,
3. Sulphur removal,
4. Oxygen control,
5. Inclusion control,
6. Temperature control, and

The two important additions that are done during ladle refining of steel are: 1) Deoxidizers and 2) Synthetic slag formers. Deoxidation is a crucial step for lowering dissolved oxygen levels from 500-600 ppm which are generated during primary steelmaking furnaces like the Basic Oxygen Furnace (BOF) or Electric Arc Furnace (EAF) [26], since this would otherwise cause 'blow-holes' or casting problems. After deoxidation, stirring by Ar, addition of ferroalloys, modification of slag, arc heating constitute the major operations in LF. Strong stirring is preferred for agglomeration of micro-inclusions while soft stirring is done for floatation and homogenization [3]. The ladle system essentially consists of six distinct phase types: steel, slag, inclusions, gas bubbles, refractory, ferroalloys, interactions between which result in the gradual refining of the steel.

2.2 Non-metallic inclusions in liquid steel

Non-metallic inclusions are essentially chemical products that arise as the product of chemical reactions, physical effects, and contamination that occurs during the melting and pouring process [3, 26]. The 'cleanliness' of steel is determined by the content and type of non-metallic inclusions [3]. The level of steel cleanliness is dictated by the customer requirements and accordingly, appropriate steelmaking practices are adopted [6].

Inclusions can be classified based on their origin: 1) endogenous inclusions which are the by-products of chemical reactions in the reactor, and 2) exogenous inclusions, which arise from the chemical reoxidation or the physical entrainment of slag or interactions with ladle glaze, refractory, mold flux etc. [5]. Inclusion can be further referred to as macro-inclusions and micro-inclusions, based on their size. The former arise mainly from slag emulsification, while the latter are remnants of deoxidation and are ($<$10 μm) usually suspended in molten steel [8]. Typically, the major source of inclusions is deoxidation, via which different oxides precipitate. However, there are different types of other inclusions that can also be found in the final steel, such as nitrides, oxysulfides, and sulfides, which are mostly encountered during solidification or cooling. Kaushik et al. [9] have recently summarized the different problems caused by inclusions experienced in plants together with the characterization techniques frequently employed to study them. Pretorius et al. [6] have also reviewed the inclusion requirements for the steel industry where they emphasized some of the key reasons of clogging in the tundish and strategies to mitigate them. It can be agreed that the most frequently encountered oxide inclusions in industry [6, 9, 10] are :

1. Al killed - Ca treated : Alumina (Al_2O_3), Mg-spinels ($MgAl_2O_4$) and Ca-bearing inclusions.
2. Si killed : silica, Al silicates, Ca silicates, Ca-aluminosilicates.
3. Si-Mn killed : Mn- silicates, Mn-aluminosilicates
4. Al-Ti killed : Alumina, titania (TiO_2), alumino-titanates ($AlTiO_x$).

2.2.1 Thermodynamics of deoxidation

The reaction of the deoxidizer, (M = [Si], [Mn], [Al] etc.) with the dissolved oxygen, [O] leads to the formation of corresponding oxides, according to:

$$x[M] + y[O] = (M_xO_y) \tag{2.2.1}$$

for which the equilibrium constant can be written as:

$$K_{M_xO_y} = \frac{(a_{M_xO_y})}{[a_M]^x \cdot [a_O]^y} \tag{2.2.2}$$

The denominator in Eq. 2.2.2 is sometimes referred to as the solubility product/deoxidation constant (K'). Table 2.2.1 lists some of the important solubility products for [M]-[O] reactions. It can be seen that l ower the solubility product, stronger is the deoxidation capability of the element. For e.g. Al_2O_3 has a K' of 2.5×10^{-14} while MnO has a K' of 5.3×10^{-2}. The equilibrium between oxygen and various deoxidizer elements at 1600°C is presented in Figure 2.4.

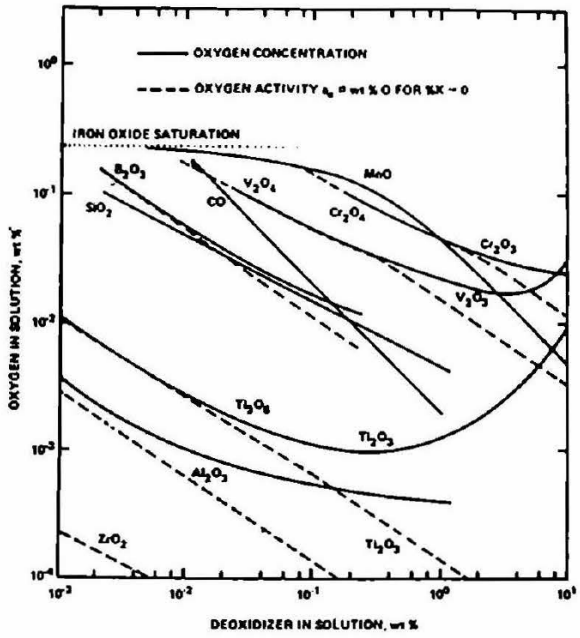

Figure 2.4: *Equilibrium between oxygen and various deoxidizer elements at 1873 K [5].*

Table 2.2.1: *Equilibrium constants for important reactions [12].*

Reaction	$\log K_{eq}$	K' (1873 K)
2[Al] +3[O] = Al_2O_3 (s)	64000/T - 20.57	2.5×10^{-14}
[Si] + 2[O] = SiO_2 (s)	30410/T - 11.59	2.3×10^{-5}
[Mn] + [O] = MnO (s)	14880/T - 6.67	5.3×10^{-2}
[Ca] + [O] = CaO (s)	25653/T - 7.64	8.7×10^{-7}

Deoxidation of iron by Si results in either solid silica or liquid iron silicates

depending on the silicon/oxygen ratio in iron based on the FeO-SiO_2 phase diagram [12]. Simple deoxidation systems are hardly encountered in actual industrial practices, and hence, equilibria relations for complex deoxidation processes are established. For complex deoxidation by Si, Mn, the following can be written:

$$2(MnO) + [Si] = 2[Mn] + (SiO_2) \tag{2.2.3}$$

The equilibrium for the above is given by:

$$K_{Mn/Si} = \frac{(a_{SiO_2})[a_{Mn}]^2}{[a_{Si}](a_{MnO})^2} \tag{2.2.4}$$

The oxygen levels achieved with Si-Mn complex deoxidation are lower than with just Si since the activity of SiO_2 is lower. According to Turkdogan [11], the inclusions would be either Mn-silicates or solid silica (Refer Figure 2.5) based on the temperature and the amount of Si/Mn ratio in steel. Rao

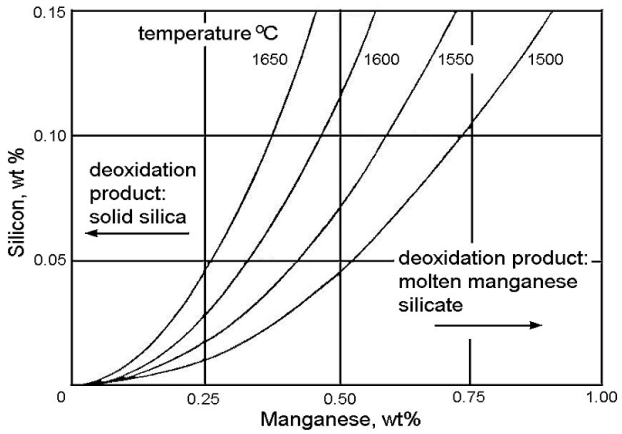

Figure 2.5: *Stabilities of deoxidation product in Fe-Si-Mn-O system for various [Si] and [Mn] contents at various temperatures [11].*

and Gaskell [13] have further investigated the thermodynamic properties of $MnO{-}SiO_2$ systems at different temperatures of steelmaking interest and computed the activities of relevant oxide species. Another system that has been a topic of a lot of investigations [14, 15, 16] is the $MnO{-}SiO_2{-}Al_2O_3$ system since deoxidation practice with a combination of Mn, Si, and Al is common, and Al is frequently encountered in steel. Similar studies [18, 19] have also been conducted to investigate the thermodynamic properties relevant to CaO–MnO–Al_2O_3–SiO_2 system.

2.2.2 Kinetics of inclusion evolution in liquid steel

After deoxidizers are added to the melt, dissolution, and mixing lead to a state of supersaturation from an unsaturated state. As a result, stable nuclei form as a result of homogenous nucleation which then grows via different mechanisms like diffusional growth, Ostwald ripening, and other collision events. Presence of additional oxide impurities present in the added ferroalloys serve as ideal heterogeneous nucleation sites for inclusion particles. It has been shown that the nucleation rates of inclusion following deoxidation are considerably fast leading to a quick lowering of dissolved oxygen while the rate of overall deoxidation is mainly determined by the removal of inclusions [7] as shown in Figure 2.6.

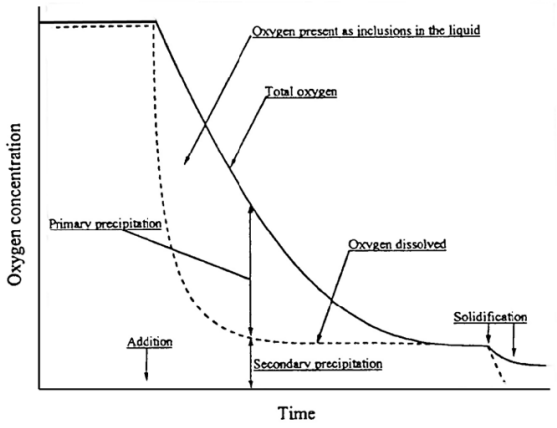

Figure 2.6: *Dissolved and total oxygen content during ladle processing [7].*

Growth kinetics

The primary growth of particles can be considered to be through mass transfer in the melt. For particles suspended in a fluid medium, the mass transfer coefficient is given by [20]:

$$Sh = 2 + 0.552 Re_{\mathrm{p}}^{0.50} Sc^{0.33} \tag{2.2.5}$$

However since most particles i.e. inclusions are smaller than few microns, the effect of fluid flow can be neglected and diffusion can solely dictate the growth of inclusions. As a result, Sherwood number (Sh) reaches the limiting value of 2 [12] and the mass transfer rate ($\dot{N}_i$) can thus be calculated using:

$$\dot{N}_i = 4\pi r_{\mathrm{ox}} D_i C_{v,m} \left(X_i^b - X_i^* \right) \tag{2.2.6}$$

Other than primary growth by diffusion, collision growth is another mechanism by which the size of inclusions changes in an industrial-scale ladle changes (Refer to Figure 2.7), resulting in an evolving inclusion size distribution with time (Figure 7.10). Agglomeration and coagulation of inclusions

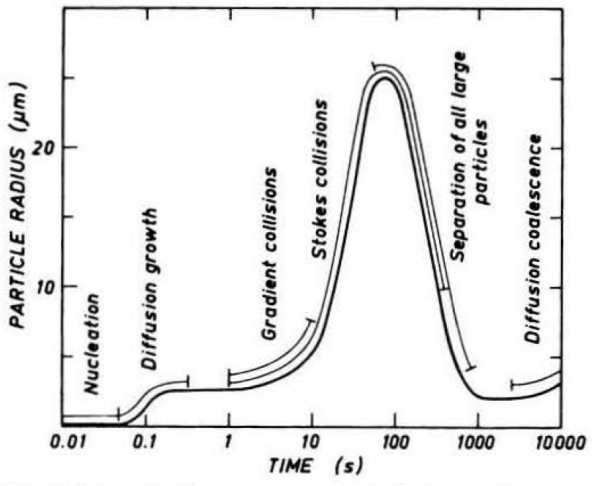

Figure 2.7: *Dominant growth mechanisms for particle size in steel melts post deoxidation [21].*

decide to a large extent how fast inclusions will be removed from molten steel. Based on research on particle-fluid dynamics, different physical aggregation mechanisms are postulated as dominant and relevant to steelmaking conditions:

- Brownian: random collisions of particles.
- Stokes: collisions resulting from differences in ascending velocities of particles.
- Turbulent: collisions resulting from the action of turbulent fluid flow on particles.

However, a steady state is reached after most large-size inclusions are removed from the steel which is evident from particle size distribution (PSD) plots (Refer to Figure 2.8).

In spite of the improvement in characterization methodologies, it becomes difficult to 'accurately' quantify the variation in inclusion quantity at different locations in the ladle over time. In this regard, many model studies have been carried out to simulate inclusion behavior in an effort to correlate the process parameters with inclusion nucleation, growth and removal rates from a fundamental standpoint. Zhang and Pluschkell [23] were among

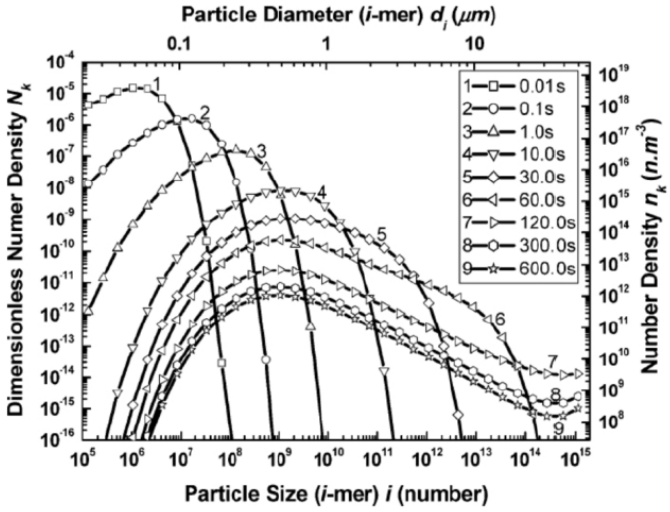

Figure 2.8: *Schematic of inclusion PSD changes with time [22].*

the first to develop a comprehensive mathematical model encompassing the nucleation and various growth mechanisms based on classical nucleation theory (CNT) [24] and pseudomolecule diffusion theory [25]. In this context, psuedomolecules ('embryos') are units of a cluster of inclusions in the size range 1 - 100 μm. From their simulations, they concluded that the growth of inclusions $<$ 1 microns is mainly controlled by diffusion of pseudomolecules and Brownian collision while inclusions $>$ 2 μm in size are mainly controlled by turbulent collisions, with inclusions in 1-2 μm show a change in growth mechanism.

The aggregation process of solid inclusions after collision depends upon the interfacial energy and wetting angle between inclusions and the liquid steel [26] . Yin et al. [27] found from Confocal Scanning Laser Microscopy (CSLM) studies that solid inclusions aggregate more easily than liquid inclusions which agrees with the cavity bridge agglomeration mechanism. On the other hand, Ferreira et al. [28] showed that liquid calcium aluminates agglomerated quite efficiently when they observed the inclusion characteristics after adding Ca to Al-killed steel in a laboratory setting. However, the collision tendency of such inclusions was not properly discussed by these authors. To further clarify and understand the coagulation behavior of liquid inclusions, more studies are warranted in this field using in-situ CSLM high-temperature microscopy and fundamental models.

Removal kinetics

In an agitated melt, inclusions can be removed to different sites such as steel-slag interface and refractory walls based on their trajectories imposed by the melt hydrodynamics [7]. The removal rate to the steel-slag interface is influenced by floatation (via Stokes' law) as well as bubble-assisted transport [30]. Different flow rates in a gas-stirred ladles influence the bubble characteristics which in turn affect the inclusion removal rates as shown by Lou and Zhou [29]. However, the attachment probability of inclusion to a bubble is governed by the contact angle in a particle-liquid-gas system where it has been shown that higher contact angles (>90°) lead to a higher attachment probability [30]. In order to quantify the inclusion removal rates, the variation of total oxygen (T.O.), which after deoxidation is almost entirely present as inclusions, is often described with a first order kinetic equation shown as follows:

$$\frac{dC_O}{dt} = -K_O C_O \tag{2.2.7}$$

Figure 2.9 shows the relationship between K_o and stirring energy (ϵ) for different operating furnaces.

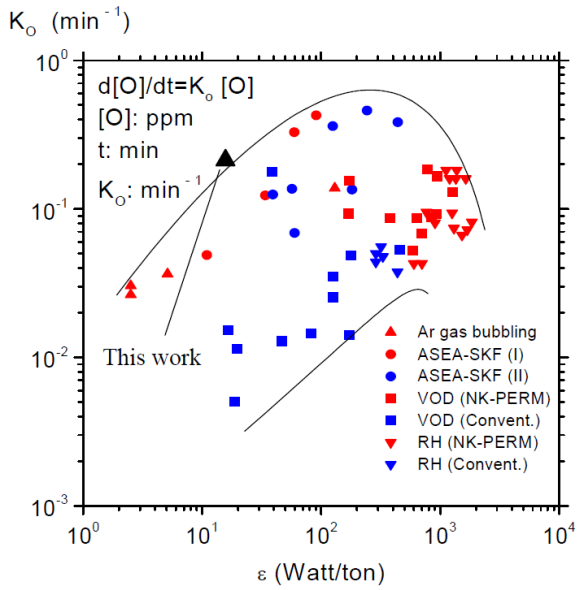

Figure 2.9: *Relationship between K_O and stirring energy for different operating furnaces [32].*

It is also important to consider that the process of inclusion removal to the slag depends on slag-inclusion interaction. Once an inclusion reaches the steel-slag interface, the separation of inclusions to the slag and the dissolution

process (solid inclusions) depends on the morphology, size, and type of the inclusions. The successful crossover of inclusion to the slag phase is also dictated by the fluid flow, slag viscosity, and overall wettability [31] which is given by:

$$\cos\theta_{\mathrm{IMS}} = \frac{\sigma_{\mathrm{IM}} - \sigma_{\mathrm{IS}}}{\sigma_{\mathrm{MS}}} \tag{2.2.8}$$

Kinetics of inclusion chemistry change

While a major fraction of inclusions gets removed from the steel, a certain proportion of the inclusion population remains suspended and keeps recirculating in the steel bath, with a slower rate of aggregation. These inclusions that remain within the steel get transformed by chemical reactions. Additionally, inclusions generated from reoxidation also interact with existing inclusions and solutes in the melt. The composition evolution of inclusions has received a great deal of attention from researchers since the inclusion type decides the final quality of steel as well as the processability which has been broadly referred to as 'inclusion engineering'. Recently, Webler and Pistorius [33] presented a review of processing conditions that affect concentration changes in inclusions where they described slow inclusion changes to occur from steel-slag and steel-refractory reactions. Although inclusions have an overall large surface area, indicating the potential for rapid steel-inclusion reactions, measurements indicate a wide variation in inclusion chemistry within a particular sample. As a result, there exists some uncertainity about whether true equilibrium exists between steel and inclusions. The author believes the driving force for mass transfer to inclusions is transient, unequal, and competitive and depends on the degree of solute concentration differences (Mn, Si versus Al, Ca) between the bulk steel and steel/inclusion interface. This, together with concentration and temperature inhomogeneities, can be surmised to cause variance in inclusion chemistry. In other words, while inclusions of apparently significantly different compositions may have formed at different points in the process, the difference in thermodynamic stability between them is not sufficient to drive homogenization. This will be discussed in detail in Chapter 3.

2.2.3 Inclusion analysis methods

Inclusion characterization is important to ensure good process control and consists of understanding the size, morphology, distribution, and chemical composition of inclusions. There are several methods: direct and indirect which depend on whether direct observation of inclusions is carried out. Zhang and Thomas [34] have reviewed various methods that have been widely

used to detect and understand inclusions encountered in steelmaking and continuous casting. A comparison of the frequently used techniques has been shown in Figure 2.10.

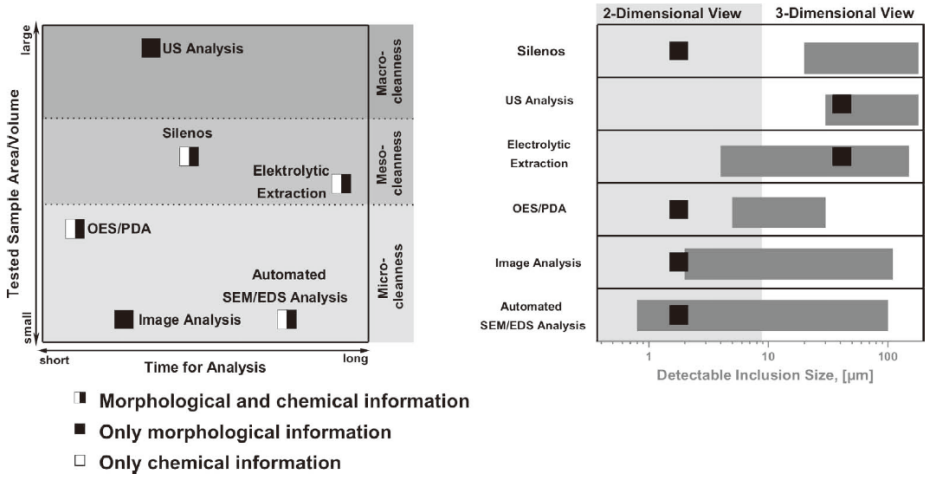

Figure 2.10: *Comparison of the frequently used techniques for inclusion analysis [35]*

Volumetric methods such as MIDAS (Mannesmann Inclusion Detection by Analysing Surfboards) allows one to characterize the macroscopic cleanliness of the steel where the steel product is cross-rolled transverse to the casting direction. The MIDAS system uses an ultrasonic transducer (SEB lOK4) on a coarse but fast scanning grid of x = y =1 mm , allowing it to detect oxide inclusions with a minimum particle size of 50 microns [36]. However, in order to assess the characteristics of inclusions on a 'finer' scale, other characterization tools need to be used in conjunction with MIDAS.

With regard to surface methods, the use of image analysis tools with optical microscopy gives an overall picture of cleanliness of the steel but finds limitation in providing information about chemical composition and high resolution images. In order to perform a detailed compositional analysis over a polished sample (using conventional metallographic techniques), the most widely used way is Energy-dispersive X-ray spectroscopy (EDS) under the scanning electron microscope (SEM). Manual EDS allows one to investigate the chemistry of individual inclusions at specific sites while automated inclusion/feature analysis (AIA/AFA) enhances the capability of analyzing large areas with a single run [37]. Many considerations still need to be made with regard to area of analysis [35], electron voltage [38] and other operational parameters to ensure a reliable and fast assessment of the inclusion landscape.

However, a vast wealth of information can be obtained from automated SEM-EDS analysis which is why it is frequently used for quality inspection and process control in industries. In order to map out the distribution of inclusions in 3D space, the measured 2D particles are extrapolated to 3D size distribution plots using statistical methods like the Schwartz-Saltykov method [39]. However, the resolution limit of SEM-EDS is about 1 microns since the analysis of sub-micron particle is not reliable owing to considerable matrix interaction. Analysis of inclusions after isolating from the steel matrix gives a more accurate description of not only 3D inclusion morphology but the chemical composition and size distribution of sub-micron particles. This can be achieved by different chemical and electrolytic dissolution methods, an extensive review of which has been recently done by Babu and Michelic [40]. From their study, it was concluded that 10% AA (10% acetyl acetone–1% tetra methyl ammonium chloride–methanol) to be the most widely used reagent for electrolytic extraction methods for a lot of different steel grades.

Another common route employed to study the inclusion amount in steel is to use the optical emission spectroscopy method with pulse distribution analysis (OES-PDA) which often is referred to as 'spark' analysis. Useful information from OES-PDA can be obtained like total oxygen, inclusion composition, amount of CaS, MnS inclusions etc. [6, 9]. Although this method can be applied to limited steel grades and has less interpretability of inclusion chemistry data, it is popular in industries owing to its convenience of use.

On the other hand, total oxygen content analysis using Inert Gas Fusion Infrared Absorptiometry (IGFIA) finds routine use in industries to characterize steel cleanliness in multiple heats [6, 9]. The variation of total oxygen, which is the sum of soluble oxygen in liquid steel and oxygen bound in oxide inclusions offers a quick and easy method to roughly determine the inclusion amount changes in steel. Recently, Hong and Kang [42] devised a novel method of calculating the soluble and insoluble oxygen contents in steel simultaneously using IGFIA. However, no information regarding the chemical composition and morphology of the oxide inclusions or other inclusion types can be obtained from such a method.

For measurement of inclusion in molten metals directly, different methods like ultrasonic techniques [43] and Liquid Metal Cleanliness Analyzer (LIMCA) [44] have proven useful for light metals but not yet seen successful use in steels. Recently, Confocal Scanning Laser Microscopy has allowed an in-situ method to observe the inclusion behavior at steel-gas interfaces, such as their nucleation [45], collision and agglomeration [27], as well as their dissolution

behaviour in slags [46].

2.2.4 Inclusions in Si-Mn killed steels at LMF

In products such as tire cord steels, thin strip castings, cold drawn wires, stainless steel long products, the presence of solid and non-deformable phases such as alumina (Al_2O_3), spinels ($MgAl_2O_4$) and Ca-bearing inclusions must be mitigated [47]. The deformation characteristics of oxide inclusion particles is shown in Figure 2.11. To reduce product failures and increase fatigue

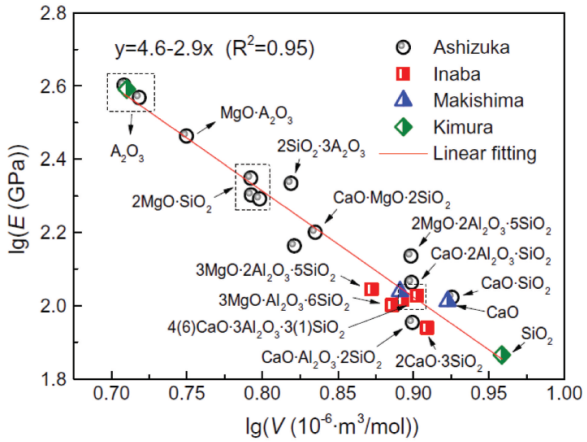

Figure 2.11: *Relationship between Young's modulus and oxide mean atomic volume in the $MgO-Al_2O_3-SiO_2-CaO$ system [49].*

performance, deoxidation practice with Si and Mn is preferred since they generate primary Mn silicate inclusions which are soft and deformable at casting temperatures (Figure 2.12).

Zhang [47] and Chen et al. [49] have provided a comprehensive review of the inclusions encountered in tire-cord and saw wire steel where they have reported the common industrial practices for 'inclusion engineering' in such Si-Mn killed steels. These authors emphasized that the type of treatments and final product chemistry largely influence the types of inclusion composition. Most inclusions reported in Si-Mn killed steels belong to the $CaO-MnO-SiO_2-Al_2O_3$ system where the major oxide phases/compounds are listed below.

- Silica (SiO_2): Quartz , Cristobalite, Tridymite
- Alumina (Al_2O_3) : Corundum
- Mn silicates : Rhodonite ($MnO{\cdot}SiO_2$), Tephroite ($2MnO \cdot SiO_2$)
- Mn aluminates: Galaxite ($MnO \cdot Al_2O_3$)

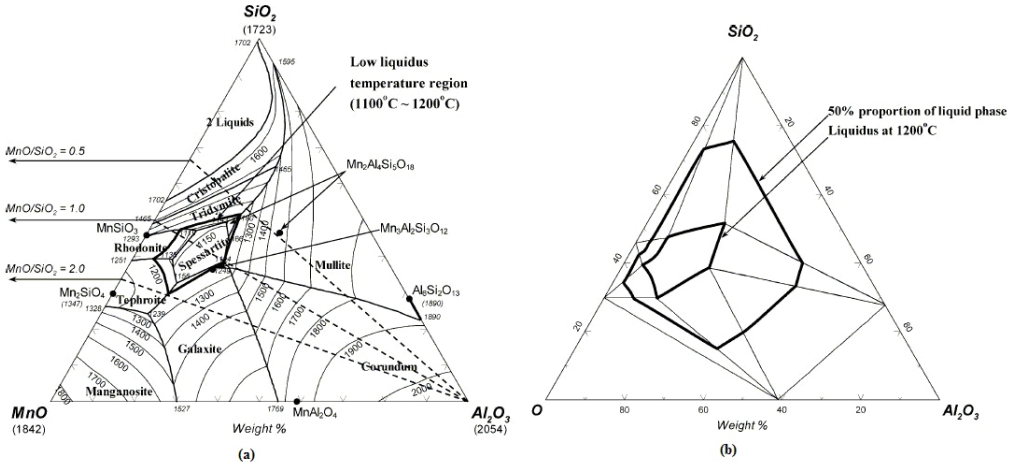

Figure 2.12: *a) Calculated liquidus regions and b) liquid mass proportion of 50 % in a $MnO-SiO_2-Al_2O_3$ system at 1200 ℃ [48].*

- Mn aluminosilicate: Spessartite ($3MnO{\cdot}Al_2O_3{\cdot}3SiO_2$), Mn coerdite ($2MnO{\cdot}2Al_2O_3{\cdot}5SiO_2$), Mn-Anorthite ($MnO{\cdot}Al_2O_3{\cdot}2SiO_2$)
- Aluminosilicates : Mullite ($3Al_2O_3{\cdot}2SiO_2$)
- Ca silicates : ($CaO{\cdot}SiO_2$)
- Ca aluminosilicates : ($CaO{\cdot}Al_2O_3{\cdot}SiO_2$)

Al_2O_3 in inclusions

Although Mn silicates form as a result of the complex deoxidation by Si and Mn, the situation can be aggravated by the presence of Al. Since Al has a stronger affinity for oxygen, it readily leads to alumina-rich inclusions by reacting with dissolved oxygen or by reducing less stable oxides like FeO, MnO, SiO_2. Excess amounts of dissolved Al leads to a change in the inclusion population where galaxite and corundum might form instead of liquid products (Refer to Figure 2.12). The presence of these phases is detrimental to casting operations and final steel quality. Thus, controlling the semikilled condition with Al is a sensitive task. From an industrial perspective, spessartite ($3MnO.3SiO_2.Al_2O_3.$) type inclusions is preferred due to its viscosity, low wettability, and good deformability [47]. However, Malley et al. [7] indicated that having solid inclusions during initial stages of refining leads to better floatation while at later stages, these inclusions should transform to compositions around the liquidus region at 1200 °C (Refer to Figure 6.13). Zhang [47] suggested that inclusions with high SiO_2 content and low Al_2O_3 content have a suitable deformability index under rolling conditions. An increase of Al_2O_3 of more than 10 wt% in the inclusions is believed to cause castability issues. Garlick et al. [50] found a direct relationship between the Al_2O_3 in

the inclusions and the [Al] in steel which caused a change in the inclusion compositions as shown in Figure 2.13. Maeda et al. [51] also showed that Al_2O_3 content along with higher slag basicity in slag leads to more Al_2O_3 in the inclusions (Figure 2.14).

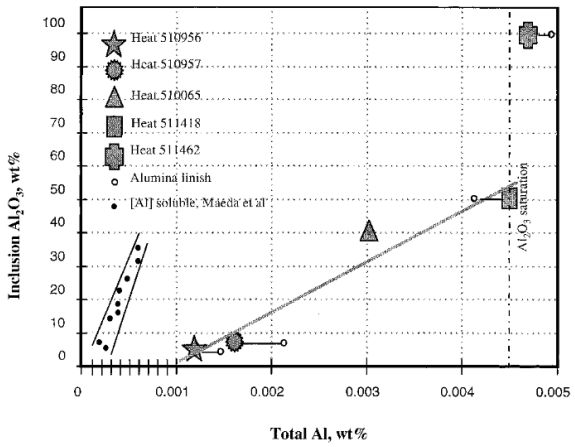

Figure 2.13: *Relationship between average Al_2O_3 content of inclusions and total Al content of steel [50].*

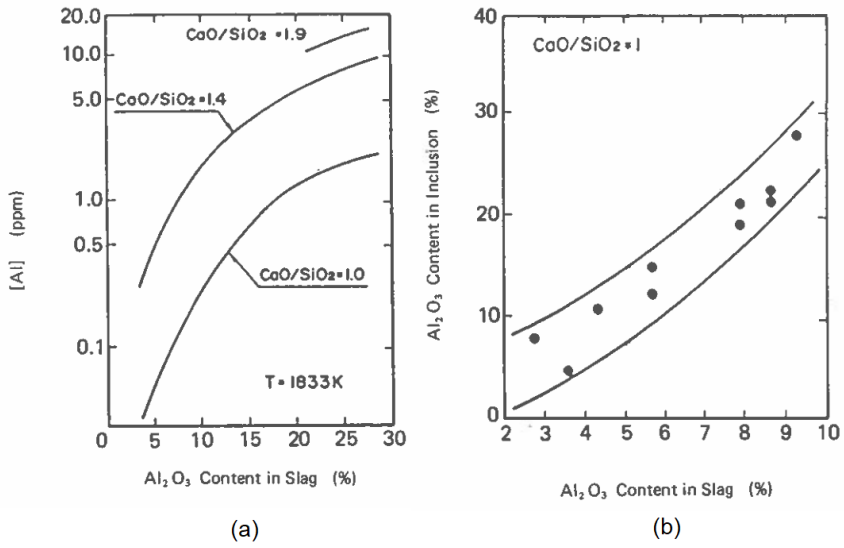

Figure 2.14: *(a) Relationship between [Al] content of steel and the Al_2O_3 in the slag; (b) relationship between the average Al_2O_3 content of inclusions with Al_2O_3 in the slag [51].*

Al pick up can occur with steel/slag reactions where Al_2O_3 in the slag can be reduced by Si owing to lower Al activity in the steel. Park and Park [52] showed that the effect of increasing the basicity R (= CaO/SiO_2) in slag from 0.7 - 2.1 led to an increase in the Al_2O_3 content of inclusions from

10 to 40 mol%. However, the study did not report any alumina inclusions which is surprising as high alumina slags (30.7 - 52.4 wt%) were utilized. Furthermore, the study utilized Al_2O_3 crucibles in the experiments, which also did not cause severe Al pick-up in the steel. On the other hand, Piva et al. [53] conducted steel-slag experiments in an MgO crucible and found that alumina rich slag led to a change in the inclusion population from $MnO-SiO_2$ $\rightarrow MnO-SiO_2-Al_2O_3$ $\rightarrow Al_2O_3$ inclusions. This was further supported by kinetic model results using FactSage calculations.

Another possible source of Al can be attributed to ferroalloys. In the absence of deliberate addition of Al, impurities found in ferroalloys can lead to Al pick up in the inclusions. Wijk and Brabie [54] carried out deoxidation experiments to study the effect of impurities such as Al and Ca on the inclusion formation process where they found Al $>$ 1 wt% led to the formation of alumina, silica and mullite inclusions while highly pure FeSi gave SiO_2-rich silicates. Lyu et al. [55] performed inclusion analysis of industrial samples of spring steels (Mn/Si $<$ 1) and also indicated that $Al_2O_3-SiO_2$ inclusions form when high Al containing FeSi is used. A similar conclusion was reached by Park and Kang [56] who conducted Si deoxidation experiments in the presence of slag. Additionally, they found that inclusions changed from Mn silicates to Mg silicates when the Si content in the steel increase from 0.7 to 3 wt%. This was attributed to reduction of MgO from the slag by the FeSi. Li et al. [57] even found pure Al_2O_3 inclusions during their deoxidation experiments with high Al FeSi ($\approx$1.6 %). Mizuno et al. [58] also found Al_2O_3 and $MgO-Al_2O_3$ inclusions during the deoxidation of 304 stainless steel with FeSi containing 2.91% Al. Based on these studies it can be concluded that Al impurity level should be strictly controlled to less than 1 wt% to achieve plastic inclusions.

CaO in inclusions

In addition to $MnO-SiO_2-Al_2O_3$ inclusions, $CaO-SiO_2-Al_2O_3$ type inclusions also are commonly found in Si-Mn killed steels. However, the formation of $CaO-SiO_2-Al_2O_3$ type inclusions has been largely debated. There are arguments about whether they form via transfer of Calcium by reduction at the slag/metal interface of by interactions between inclusions and entrapped slag particles. Nurmi et al. [59] and Chen et al. [60] have indicated that equilibration with slag could result in CaO pickup in inclusions. Wang et al. [61] also concluded that the inclusions in FeSi-killed stainless steel with an [Al] $<$ 40 ppm could be modified by the top slag. On the other hand, many studies [51, 62, 63, 64] have indicated that the origin of $CaO-SiO_2-Al_2O_3$ based inclusions is emulsified slag droplets. Further coalescence of slag droplets with

deoxidation products along with the reaction of these exogenous inclusions by [Al] can lead to varying inclusion chemistry within Ca aluminosilicates. This seems to be more plausible since the solubility of Ca is less than 0.0001 wt% [65]. Investigations have revealed that the inclusion compositions seem to be close to the top slag composition as shown in Figure 2.15. However, reduction of CaO by Si can also lead to $CaO-SiO_2$ inclusions at the steel-slag interface. Since these inclusions often tend to show up in spring steels having high Si/Mn ratios, more studies are required using steel with higher ratios (2-3) to probe the reaction kinetics of CaO in slag and Si.

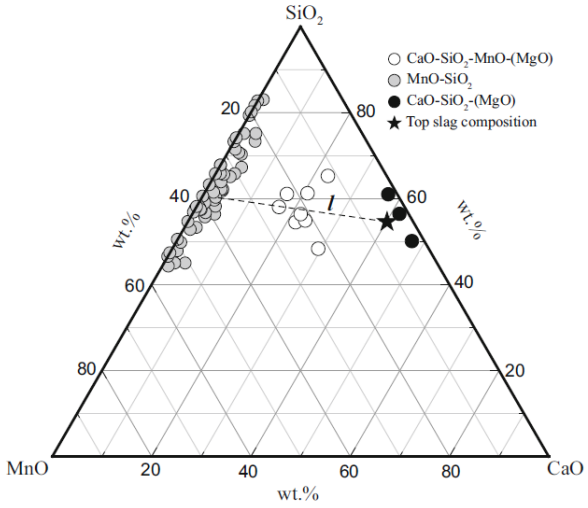

Figure 2.15: *Comparison of Ca-silicate inclusions with top slag composition [63].*

Another source of CaO in inclusions could be Ca impurities in FeSi. Wang et al. [63] concluded from their deoxidation experiments that Ca pickup from their ferroalloys was negligible since the Ca content was very less (FeSi = 0.038; FeMn = 0.055 wt %). However, Piva and Pistorious [66] showed that the Ca yield is higher through FeSi-based addition with 2 wt% Ca which led to a new population of CaO inclusions rather than a modification of existing inclusions. A similar observation was made by Li et al. [57] where they used FeSi with 1.3 wt% Ca. They found existing $MnO-SiO_2$ inclusions to change to large $CaO-SiO_2-Al_2O_3$ inclusions.

Since too much Al pickup in inclusions is detrimental to the casting of steel

as discussed above, the external addition of Ca can be a potential solution, which can be an additional source of Ca in inclusions. Thermodynamic calculations reveal that Ca helps in decreasing the liquidus temperature of the $MnO-SiO_2-Al_2O_3$ inclusions. These calculations were confirmed by industrial measurements . Thus, Ca in ppm levels might help alleviate problems related to casting through proper inclusion engineering of $CaO-SiO_2-MnO-Al_2O_3$ inclusions. This was demonstrated by Wang et al. [61] where they showed the benefit of Ca treatment on inclusions in steels with [Al] more than 40 ppm. Tiekink et al. [67] also reported similar observations where Ca injection helped reduce irregular flow during casting. Many industries have practiced Ca injection for the inclusion modification of existing inclusions [68, 69, 70]. However, the 'precise' conditions where Ca treatment is needed are still unclear.

FeO in inclusions

In a few reports, while analyzing the inclusion compositions through electron probe micro-analyzer (EPMA) and SEM-EDS, FeO content has been reported as a primary component. Turpin and Elliot [71] found hercynite and iron aluminates in samples having less than 0.01 wt% Al. Kawashita et al. [72] had a similar finding when the Al was around 0.0006 wt%. FeO based inclusions were also observed by Hilty et al. [73] in molten steel containing 0.015 wt% Si. Thapliyal et al. [74] recently found that after Si-Mn deoxidation of steel containing 0.1% oxygen, inclusions comprised of mainly FeO rich $FeO-MnO-SiO_2$ (Figure 2.16). Such observations indicate that if

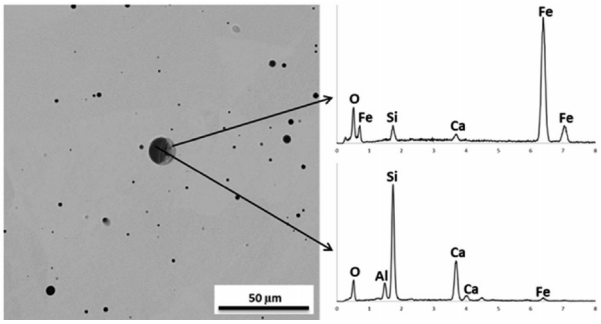

Figure 2.16: *FeO rich inclusions in Si killed steels [74].*

the deoxidant-to-oxygen ratio is low, FeO could be present in the inclusions. However, it needs to be noted that there could be a significant contribution of the steel matrix in overpredicting the Fe content in inclusions. In principle, the interaction volume of the SEM electron beam should be comparable to the inclusion sizes being observed in order for the data to be 'reliable'. Doostmohammadi et al. [75] and Gram et al. [76] proposed that Fe peaks

should not be considered while analyzing the EDS spectra of micron-sized inclusions. Recently, this problem was further investigated by Mayerhofer et al. [77, 78] where SEM-EDS investigations (15 kV) were verified with electrolytic extraction methods. They concluded that the measured FeO content of particles with ECD > 2 microns was representative of the actual composition and should be considered in the analysis. Lyu et al. [55] came to a similar conclusion when they used Monte Carlo simulations to confirm the penetration depth in the inclusions by WDS electron trajectories. Their calculation showed that FeO can be believed to be an inherent constituent of an inclusion detected by WDS below 5 keV. However, general practice during inclusion analysis is to ignore Fe during post-compositional analysis. Since SEM-EDS is the most common technique employed to observe inclusions in steel samples, proper care should be taken in analyzing and interpreting the results, considering the size-composition relationships.

2.2.5 Inclusions in Si-Mn killed steels during cooling

Primary inclusions which mostly consist of deoxidation inclusions, determine the processability of steel, while the secondary inclusions occurring as a result of cooling and solidification decide the mechanical properties of steel. Inclusion phases like nitrides (TiN, AlN, VN etc.) and sulfides (MnS) are encountered frequently since their solubility product becomes significant at solidification temperatures. The formation of MnS inclusions have certain beneficial effects, like helping the formation of acicular ferrite [79], thereby requiring comprehensive understanding and control of their precipitation behaviour during solidification. Furthermore, secondary oxide inclusions also precipitate owing to the lowering solubility of oxygen in Fe with temperature like silica, alumina, and manganese silicates [80]. A phenomenon that is important to consider for solidification analysis is microsegregation, which results from uneven partition of solutes in the solid and liquid steel at the dendritic scale. The solute rejection can lead to concentration buildup at solid/liquid interface, which affects the pre-existing inclusion compositions or result in additional nucleation of inclusions.

In Fe-Si-O systems, Forward et al. [81] found that oxygen rejection in the inter-dendritic spaces caused the nucleation of new iron silicates and silica over time. In Si-Mn killed steels, internal precipitation of silica within Mn-silicates can occur during cooling [82, 83] which can be described using the saturation limit of the MnO–SiO_2 oxide system (Refer to Figure 2.17). The role of inclusion coalescence on the formation of a MnO–SiO_2 inclusion with a SiO_2-rich precipitate during solidification was also suggested in the work by Gamutan et al. [84]. Consideration of these inclusions is important since

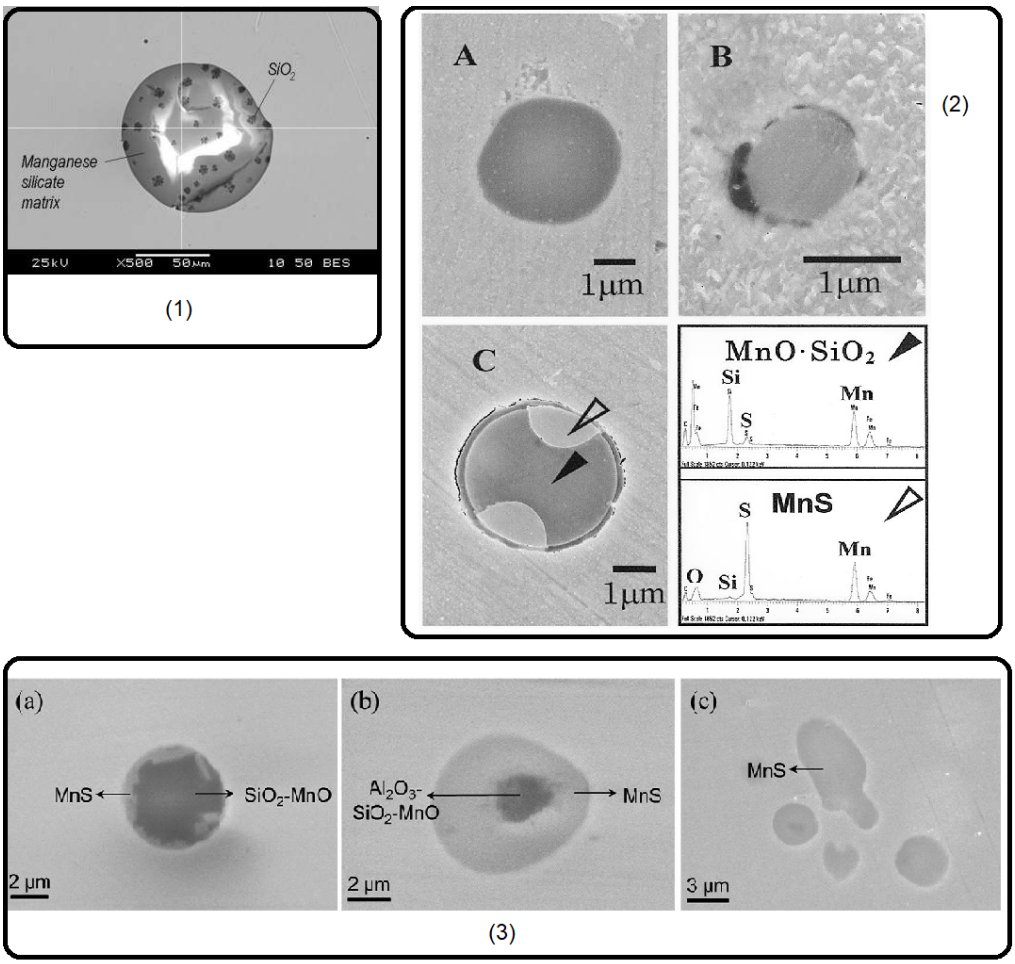

Figure 2.17: *Composite inclusions containing oxide and MnS phases that are obtained on cooling in Si-Mn killed steels [82, 86, 87].*

their effect can be significant under rolling conditions. Additionally, MnS inclusions are also typically found to precipitate on pre-existing manganese silicates, leading to a Mn-depleted zone (Refer to Figure 2.17(2)) that aids in acicular ferrite formation [79]. Kim et al. [85] investigated the precipitation behavior during cooling in Si–Mn and Si–Mn–Ti deoxidized steels where they found that cooling rates and primary oxide seed composition affected the secondary MnS inclusion formation. Furthermore, they concluded based on the sulfide capacity of oxide inclusions and holding time at elevated temperatures, the amount of Mn depleted zone can vary. Ren and Zhang [87] conducted laboratory experiments with Si–Mn-killed 304 stainless steels where they found that increase in Al gives rise to more Al-rich inclusions, which provide for more misfit for MnS to precipitate. However, their analysis

assumed 'pure' thermodynamic equiblirium conditions and lacked the effect of diffusion or reaction kinetics. In the last few decades, different models have been proposed by researchers to address the issue of microsegregation and its effect of inclusion formation kinetics during cooling and solidification. A review of such models is out of scope of the current work and can be found elsewhere [88, 89].

2.3 Other ladle refining reactions

2.3.1 Steel-slag reactions

Since high-temperature reactions in steelmaking are assumed to occur fast, steel-slag reactions are essentially believed to be controlled by either steel/slag mass transport or both. In order to predict the mass transfer between two immiscible, fluid phases where both phases can be considered to offer resistance to mass transfer [91], an expression needs to be constructed. This forms the 'heart' of the coupled reaction model proposed by Robertson et al. [90]. For reactions of interest, the following can be written:

$$\mathrm{N_i} = \frac{\mathrm{k_m k_s}}{\mathrm{k_s} + \mathrm{k_m}/L}\left(\mathrm{C}^{m}_{\mathrm{i,b}} - \frac{\mathrm{C}^{\mathrm{s}}_{\mathrm{i,b}}}{L}\right) = \mathrm{k_o}\left(\mathrm{C}^{m}_{\mathrm{i,b}} - \frac{\mathrm{C}^{\mathrm{s}}_{\mathrm{i,b}}}{L}\right) \tag{2.3.1}$$

$$\mathrm{k_o} = \frac{1}{\frac{1}{\mathrm{k_m}} + \frac{1}{\mathrm{k_s}L}} \tag{2.3.2}$$

Although steel mass transport control seems to be the prominent finding for steel/slag reactions during ladle refining [93], Deo and Boom [94] suggested that slag mass transport control should be considered for viscous slags, low partition coefficient (L) and partial mixing of slag. However, none of the conditions or species considered in the current work are likely to lead to such a scenario. Hence, determining the steel mass transfer coefficient proves sufficient.

Now, to assess the steel *mtc* ($\mathrm{k_m}$) for the transfer of species across the steel-slag interface, two popular theories can be used. They are:

1. Two-Film theory: This theory is based on essentially the boundary layer theory which states that the resistance to mass transfer acts via a stagnant layer of thickness δ in a somewhat idealized manner as:

$$\mathrm{k_m} = \frac{\mathrm{D_i}}{\delta}. \tag{2.3.3}$$

Based on the boundary layer theory, the *mtc* can be found to be proportional to the diffusivity (D_i). This is the most used theory for steel-slag reactions where two films are presumed to exist in both phases at the interface which decides the rate of liquid-liquid mass transfer.

2. Penetration theory: This theory, also known as Higbie's model [95] assumes that liquid packets come in contact with the interface for a certain time before they are replaced by new fresh fluid packets. The *mtc* in this case is given by :

$$k_m = \sqrt{\frac{4D_{i,m}}{\pi t_c}} \tag{2.3.4}$$

Here, the residence time or time of contact (t_c) is the important parameter and depends on the phenomena being investigated. It does not remain fixed with time and follows the local fluctuation velocity, bubble characteristics or turbulence theories [96]. This gives rise to different surface renewal theories [93]. A common expression to evaluate the mass transfer coefficient based on the small eddy model [97] is given by :

$$k_m = 0.4\sqrt{D_{i,m}}\left(\frac{\varepsilon}{\upsilon}\right)^{0.25}. \tag{2.3.5}$$

Since the diffusivities of slag species ($D_{i,s}$) is about two orders of magnitude of that of metal, slag mass transfer coefficient is evaluated as:

$$k_s = \frac{k_m}{10} \tag{2.3.6}$$

The determination of *mtc* is important for developing reliable kinetic models and is somewhat difficult to estimate from the foregoing theories directly for industrial conditions. Moreover, since interfacial area (A) quantification is difficult, a more widely used approach to model *mtc* is to calculate kA. Thus, the *mtc* is primarily calculated from experiments and correlations.

The effect of stirring energy, ϵ (or, gas flow rate, Q) influences the overall mass transfer constant or mass transfer capacity coefficient, K that combines the mass transfer coefficient, slag-metal interfacial area, and steel volume as:

$$K = \frac{k_m \cdot A}{V_m} \tag{2.3.7}$$

For ladles stirred by bottom blowing which is why many correlations are

proposed in the form of:

$$K = B\epsilon^{C} \quad \text{or,} \quad K = B'Q^{C'} \tag{2.3.8}$$

Here, the values of B, C, B', C' differ with the reactor characteristics. It also needs to be pointed out that the calculation of stirring energy from flow rate also vary from study to study [98]. Recently, Conejo [93] extensively reviewed the topic of physical and mathematical modelling of liquid-liquid mass transfer due to bottom gas injection where he has compiled such correlations from various studies. He also concluded that slag emulsification occurs when stirring energy is more than 4-6 W/t in which case the exponent C is greater than 1. However, Asai et al. [99] indicated that such emulsification occurs above the limiting value of 60 W/t. In practice, the value of the *mtc* depends on other different process variables such as, nozzle's radial position, bubble diameter, nozzle diameter, slag viscosity and volume, liquid depth, and ladle dimensions [100]. The influence of these variables can be investigated numerically using computational fluid dynamics (CFD) or cold models. However, not many studies have been conducted in unifying the above-mentioned theories through a consistent formulation of *mtc*.

Slag-aided deoxidation

The lowering of the thermodynamic activities of certain slag constituents, increases the oxygen partition coefficient (L_O), thus increasing the extent of deoxidation of the steel, which is referred to as 'slag-aided deoxidation'. While deoxidation by Al is very efficient owing to its high oxygen affinity, the role of slag is important for oxygen control since deoxidation by Si/Mn alone does not allow low [O] values. Nurmi et al. [59] showed that the presence of low silica activity and intense stirring can help bring down [O] levels in steel down to thermodynamic limits imposed by the slag. Bhansali et al. [69] recently demonstrated that a basic top slag exerts its control over the steel oxygen levels, more than the deoxidation inclusions generated from Si, Mn, which can go up to 10 ppm levels. Interestingly, the residence time of certain chemically unstable oxide inclusions is long even at such low oxygen potentials, suggesting a nonequilibrium state of the inclusions or a partial mixed state of the ladle.

Desulphurisation

Sulfur control in steel is very important since it causes undesirable reactions such as sulfide precipitation (Section 2.2.5) which can lead to cracks during solidification [3]. Different grades of steel have tolerances set for sulphur, for e.g. pipeline steel specifies 0.0010 wt%, some AHS steel specifies 0.0050 wt%.

Hence, desulphurisation of steel constitues as a key operation in steelmaking, especially during ladle refining as conditions are better suited than oxygen steelmaking [94]. Typically, solubility of sulphur is measured using gas-slag equilibrium studies which can be summarised as follows:

$$\frac{1}{2}S_2(g) + \left(O^{2-}\right)_{\text{slag}} = \left(S^{2-}\right)_{\text{slag}} + \frac{1}{2}O_2(g) \tag{2.3.9}$$

The equilibrium constant for Reaction 2.3.9 can be given as:

$$K_{2.3.7} = \frac{a_{(S^{2-})} \cdot p^{1/2}_{O_{2(g)}}}{a_{(O^{2-})} \cdot p^{1/2}_{S_{2(g)}}} = \frac{f_{(S^{2-})} \cdot (\%S)}{a_{(O^{2-})}} \cdot \sqrt{\frac{p_{O_{2(g)}}}{p_{S_{2(g)}}}} \tag{2.3.10}$$

On the other hand, the ionic transfer of sulfur in metal/slag reactions can be described as:

$$[S]_{\text{metal}} + \left(O^{2-}\right)_{\text{slag}} = \left(S^{2-}\right)_{\text{slag}} + [O]_{\text{metal}} \tag{2.3.11}$$

According to Fincham and Richardson [103], the capacity of a slag to hold sulphur is described using the concept of sulfide capacity, which is defined as:

$$C_S = \frac{K_S a_{O^{2-}}}{f_{S^{2-}}} = (\%S)\sqrt{\frac{p_{O_2}}{p_{S_2}}} \tag{2.3.12}$$

The sulfide capacity is related with the partition coefficient of sulphur (L_S) as:

$$\begin{aligned} \log L_{\text{S}} = \log \frac{(\%\text{S})^*}{[\%S]^*} = -\frac{935}{T} + 1.375 + \log\left(C_S\right) \\ + \log f_{\text{S}} - \log a^*_{\text{O}}, \end{aligned} \tag{2.3.13}$$

It can be well agreed from the above mentioned equations that desulphurisation capability of the slag increases with high slag basicity and low oxygen potential at the slag metal interface along with good slag fluidity, sufficient contact and high temperatures [3].

Different researchers have derived empirical models to compute the sulfide capacity (C_S) like that by Sommerville and Sosinsky [104], Young et al. [105], Taniguchi et al. [106] and Zhang et al. [107]. There also exist short range order (SRO) models that are used to predict the sulfide capacity considering the physico-chemical nature of the slag like that develped by Reddy and Blander [108], KTH [109]. Ma et al. [110] used Artificial Neural network (ANN) models to predict the sulfide capacity and showed it is applicable and accurate for wide range of calcium aluminosilicate slag compositions. However,

the data centric models like ANN seem to fail when sufficient data for certain slag systems are not available. Recently, Jung and Moosavi-Khoonsari [111] discussed that the concept of sulfide capacity fails at high concentrations of (S) in slag. Alternatively, the IRSID slag model by Gaye et al. [112] offers a different approach to calculate sulfide capacity indirectly by using a thermodynamic description of sulphur solubility in oxide slags and performing free energy minimization. This was also followed by Kang and Pelton [113]. Recently, an overview of different thermodynamic desulphurisation models, both employing and not employing sulfide capacity has been provided by Kang [114].

In order to compute the kinetics of desulphurisation, kinetic models are frequently employed, which are described in detail in Section 2.4.1. Essentially, the mass transfer coefficient (k_o) needs to calculated in :

$$\frac{dn_s}{dt} = k_{\mathrm{o}}\, A \left(C_{v,m} X^b_{[S]} - C_{v,s} \frac{X^b_{(S)}}{L_S} \right) \tag{2.3.14}$$

where,

$$\frac{1}{k_{\mathrm{o}}} = \frac{1}{k_m} + \frac{1}{k_s L_S} \tag{2.3.15}$$

For gas-stirred ladles, k_m or $k_m A$ is calculated from stirring energy correlations [93]. Alternatively, CFD models coupling sulphur reactions were developed by Jonsson et al. [116] which considered a metal-slag mixing zone where such reactions proceed, disregarding the need for an interface.

The contribution of slag droplets to desulphurisation was investigated by Lachmund et al. [117] and validated with plant data where they showed that about 90 % of the desulphurisation achieved through slag droplets (Refer to Figure 2.18). Liao et al. [118] showed that the role of slag viscosity and slag FeO are crucial to determining the extent of desulphurisation in gas stirred ladles. The behaviour of oxygen activity at the steel-slag interface is also influenced by the different elements such as Si, Al. Freuhan [101] found that $CaSi_2O_4$ forms at higher Si concentrations and the effect of Al accelerates the desulphurisation rate more than Si. Roy et al. [102] concluded that having high Si helps lower the consumption of Al that helps in the desulphurisation. However, no studies in the author's knowledge have investigated the role of (Al/Si) ratio on desulphurisation since it is a better parameter to help ascertain the mechanism. Also, such studies should help to investigate the effect of low (Al/Si) ratios that are typically encountered in Si-Mn killed steels.

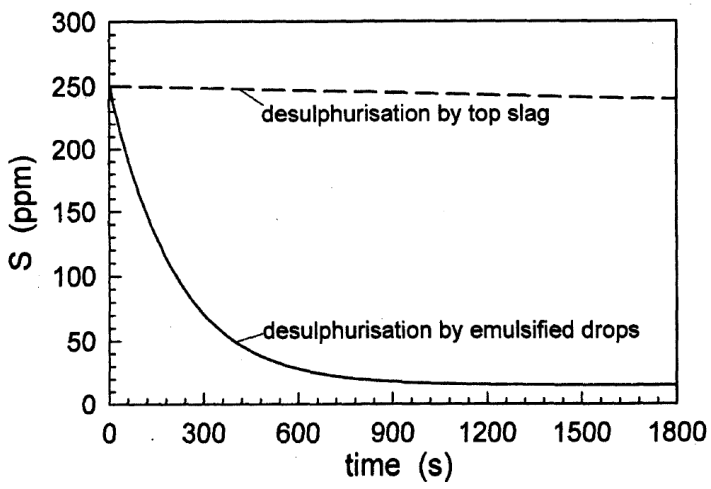

Figure 2.18: *Desulphurisation of steel by top slag and emulsified drops from bottom stirring [117].*

Emulsification

In gas-stirred ladles, the slag layer can be easily displaced and dispersed in the presence of high-intensity stirring. This phenomenon is commonly referred to as 'slag emulsification' and generates an increase in steel-slag interfacial area, thereby enhancing the reaction rates between the steel and slag [100, 117]. In principle, the detachment process can be believed to be a balance between the surface tension forces and buoyancy forces against inertial forces. Based on the formulation proposed by Oeters [12], a number of factors decide the equilibrium size of these droplets such as the flow rate (u_i), take-off angle ($\cos\gamma$), and thermo-physical properties of the slag such as surface tension (σ) and density difference between slag and steel ($\rho_m - \rho_S$):

$$d_D = \frac{3}{8}\frac{\rho_S u_i^2}{g\left(\rho_m - \rho_S\right)\cos\gamma}\left\{1 - \left[1 - \frac{128\sigma g\left(\rho_m - \rho_S\right)\cos\gamma}{3\rho_S^2 u_i^4}\right]^{\frac{1}{2}}\right\} \tag{2.3.16}$$

Such quantification along with the droplet generation rate can aid in developing accurate desulphurisation models since the overall rate is considered to be influenced by both the slag metal interfacial reaction as well as droplet-steel interaction as shown by Lachmund et al. [117]. Slag emulsification is not only found in gas-stirred systems but stirred tanks in general. Inomoto et al. [119] investigated the slag emulsification by stirring with a stationary AC electromagnetic field and found the slag-metal interfacial reaction rates correlate with the intensity of the electromagnetic power supply (Refer to Figure 2.19).

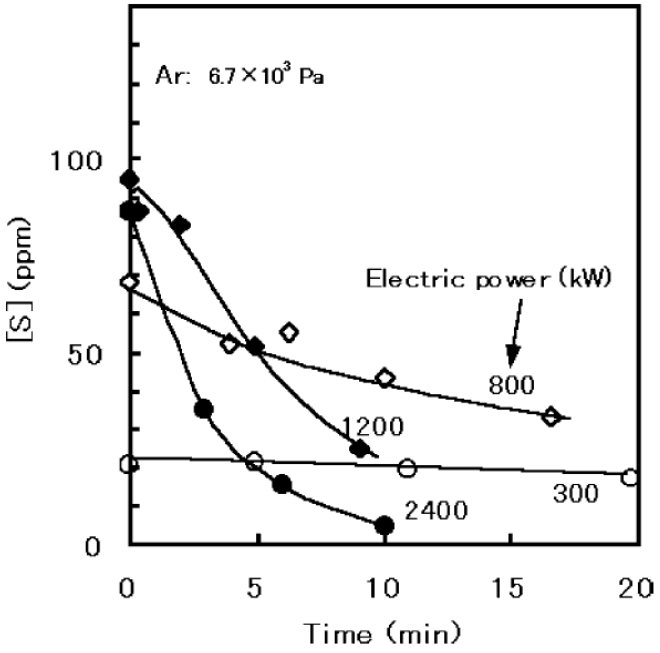

Figure 2.19: *Increase in desulphurisation rates with increase in electric power in non-gas stirred systems [119].*

With the slag entrainment process, a new population of inclusions can be generated in the vicinity of the gas plume if the droplet size distribution show a log normal distribution (higher number of microinclusions). These particles can later enter into the bulk because of recirculation currents if the buoyancy forces do not push them to the slag. Inclusions with $CaO{-}SiO_2$ composition are typically found in Si/Si-Mn killed steels whose origin is still debated. Valentin et al. [64] found many Ca silicate inclusions in Si killed steel stirred by flowrates ranging from 30 – 40 STP m^3/h. These inclusions exhibited a similar composition to the top slag, indicating at slag entrapped particles. The effects of slag emulsification is hard to trace with ladle experiments owing to many simultaneous reactions, making the use of tracers beneficial in that regard. This was shown by Fuhr et al. [120] where they found the presence of the tracer in one-third of the large inclusions in heats where BaO tracer added to the ladle slag, suggesting the role of slag emulsification.

Reoxidation

Reoxidation is said to occur when elements in molten metal are oxidized in the presence of oxidizing agents such as air FeO and MnO. When steel is tapped open air into a teeming ladle or tundish, there could be reoxidation at the surface of the stream as well as the turbulent surface at the top of

the melt [132]. Moreover, during the gas stirring of ladles, there could be exposed steel in the region of the slag 'eye' where we could expect reoxidation [121]. Lou and Zhou [122] developed a model to calculate the effect of slag eye open area on the reoxidation and desulphurisation kinetics of Al-killed steel. They found its influence to be significant at later stages of refining owing to increase in oxygen activity.

Apart from these, during transfer of steel from primary steelmaking furnaces, carryover slag is commonly encountered which can contain significant amount of FeO and MnO. These oxides tend to react with [Al], [Si], [Mn] in the steel provided by the alloying additions, resulting in less recovery rates [123] (70-85% for Mn, 60-70% for Si, and 35-50% for Al). In Figure 2.21, it can be

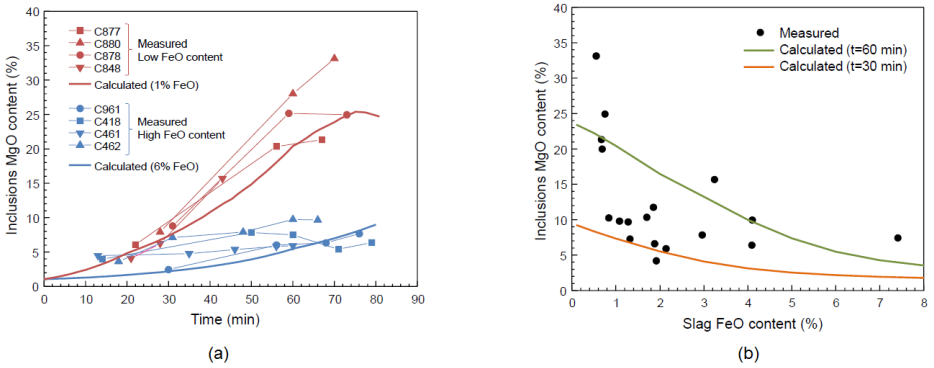

Figure 2.20: *(a) Variation of inclusions MgO content in heats with low and high slag FeO content; (b) Relationship between inclusion MgO contents at the end of the process with different FeO contents [124].*

clearly seen that (FeO + MnO) reduces the desulphurization rate, which is mainly due to the influence on interfacial oxygen activity.

Reoxidation inevitably impacts the overall efficiency of the refining process and impairs the 'cleanliness' of steel by generating unwanted inclusions, especially towards the end of the refining stage, which left untreated cause casting problems. The impact of late reoxidation on additional inclusion formation depends on the grade and the melt supersaturation ([M]:[O] ratio). In Al killed steels, alumina inclusion formation takes place while Mn-silicates with certain Al, Ca can form in Si-Mn killed steel [125]. Cicutti et al. [124] found that in Al killed steels, there was a clear relationship between the MgO in the inclusions and the FeO + MnO in the slag as can be seen in Figure 2.20. Additionally, Tan [126] conducted experiments with reoxidation and observed that Ca treatment will cause alumina and Mg spinels to return

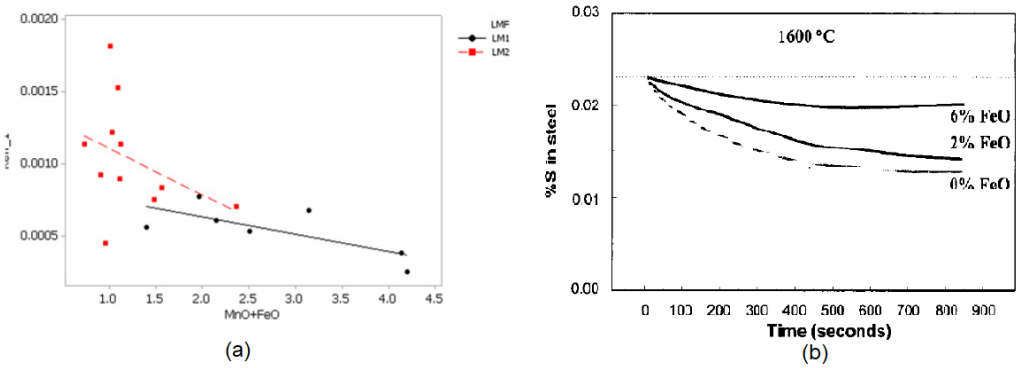

Figure 2.21: *Effect of FeO+MnO on sulphur mass transfer coefficient; (b) Influence of different initial FeO contents in top slag on desulphurisation of steel (100 ton; 1600°C; 130 NL/min; S_0=0·023%) [118, 131].*

some Al, Mg to return to the melt which upon reoxidation would form alumina and secondary spinels respectively. For steels containing Al-Ti, Deng et al. [127] concluded that supersaturated oxygen in steel gives rise to unstable Al_2O_3−TiO_x, which later decompose and disappear, forming stable Al_2O_3 and TiO_2 inclusions. Thermodynamic models have often been used to investigate the effect of FeO on oxidation behaviour on inclusion composition [129, 130]. On the other hand, an integrated kinetic model has been developed by Carlson and Beckermann [132] for predicting inclusion formation during the filling of steel castings. Recently, the use of inclusion analysis with the help of Probability Density Function (PDF) plots [126, 133, 134, 135] have helped steelmakers identify reoxidation events as shown in Figure 2.22.

2.3.2 Alloy dissolution

Ferroalloys like FeSi, FeMn, FeTi, FeCr etc. are added to steel during ladle refining to carry out deoxidation and to adjust the composition of the steel. Ferroalloy dissolution rates should lead to different supersaturation, which affects the nucleation and growth of inclusions. This inevitably causes variation in inclusion composition and morphology owing to variations in species concentration profiles. Thus, it is important to understand the fundamental factors responsible for dissolution of alloys.

Argyropoulos and Guthrie [136] reviewed alloy dissolution characteristics of different Class I (melting point less than steel freezing point such as FeAl, FeSi, FeMn, SiMn) and Class II (melting point more than steel freezing point such as FeMo, FeW, FeTi). For ferroalloys used for deoxidation like FeAl, FeSi, FeMn, and SiMn, a solid steel shell forms at the surface which dissolves

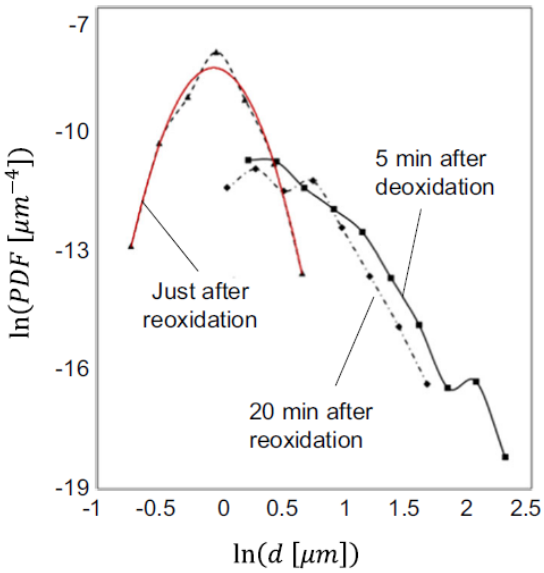

Figure 2.22: *Difference in PDF plots of inclusions just after, 5 min, and 20 min post reoxidation [126].*

after which the alloy is exposed to the melt. All of these steps can constitute rate-determining steps for bath homogenization. Additionally, it has been found that ferroalloy dissolution is a function of the alloy melting point, density, heat capacity, and enthalpy of mixing, along with the particle size distribution of the added alloy. Different correlations have been proposed [12, 93, 137] to quantify the times needed for the dissolution of ferroalloys. Together with this and CFD models, it has been possible to study the effect of flow patterns during the teeming of steel on ladle mixing times [138, 139, 140].

Impurities in ferroalloys (such as FeSi) can also affect the inclusion composition by causing Al or Ca to pick up as shown by Wijk and Brabie [54], and Li et al. [57]. Pretorius [141] also showed that Ca-containing ferrosilicon is quite effective in modifying existing Al_2O_3 inclusions to Ca-aluminates in Al-killed steel. Furthermore, inclusions in ferroalloys can affect the inclusion population in steels by providing additional heterogeneous nucleation sites. Recently, Wang et al. [142] have provided an exhaustive review of how inclusions in ferroalloys affected the final steel quality. They found inclusions present in FeMn, SiMn (e.g., MnO, $MnO-SiO_2$) had little influence on final steel cleanliness while macrosized SiO_2 inclusions in FeSi and FeMo alloys and Al_2O_3 inclusions in FeV, FeTi, and FeNb alloys were more dominant. They also suggested that the efficiency of the production process for ferroalloys has a bigger role to play in the overall control of inclusions.

2.3.3 Steel-refractory reactions

Typically, steel industries employ MgO or Al_2O_3-based refractories based on the operation being carried out in the reactor. In Al-killed steels, the reactions between high Al in steel and the refractory lining can be significant in the presence of low oxygen activity in steel. Hence, studies have been carried out to investigate the kinetics of Mg spinel formation in Al-killed steel systems, which can affect nozzle clogging [143, 144, 145, 146, 147, 148]. However, in Si-Mn-killed steel, Piva et al. [66] showed that Mg pick-up in inclusions from the MgO refractories is negligible. Deng et al. [149] showed that MgO could influence the inclusion composition if there are Al_2O_3 (0.3 %) impurities in the refractories. They also indicated that $MgO.Al_2O_3$ inclusions could be stable that are found within MgO-based refractories even in Si-Mn-killed grades.

2.4 Mathematical models

The modelling of secondary steelmaking systems have continuously improved over time, utilizing the existing physico-chemical principles and new theoretical, statistical and computational tools. The most important modelling aspects have been briefly described below.

2.4.1 Multicomponent-multiphase reaction models

Thermodynamic models

These models are 'static' in nature in the sense that there is no role of time. They predict the system behaviour under equilibrium conditions and are generally used for understanding the relationships between different composition variables. Essentially, these models are based on CALPHAD principles and extensive thermodynamic databases. However, since they assume global equilibrium between phases, which is not often the case in industries, their direct application to predicting reactions can be somewhat 'questionable'. Nonetheless, they offer directions for process metallurgists in providing guidelines for better process control and designing optimum conditions for producing 'desirable' steel quality.

Thermodynamic models greatly rely on the accurate description of activities for different phases based on consistent thermodynamic principles. The activities of elements in liquid steel have been modeled typically using the:

1. Wagner's interaction parameter model [150]

2. Darken formalism [151]
3. Unified Interaction Parameter Formalism (UIPF) [152]
4. Associate Model [153]

Most studies employ Model 1 which under dilute conditions, works well. However, Model 3 which is a modification of Models 1 and 2 seems to work at higher ranges of concentrations. On the other hand, Model 4 introduced the concept of associates like Al*O, Ca*O, etc. to improve the model accuracy for strong deoxidation reactions.

The activities of oxides/sulfides/fluorides in liquid slags have been studied extensively in the last 50 years. The popular models are:

1. Cell model [112]
2. Central atom model (Modified Cell model) [152]
3. Reciprocal Ionic Liquid model [155]
4. Modified Quasichemical model [156]
5. Regular solution model [157]
6. Sub regular solution model [158]
7. Ionic Molecular Coexistence model [159]

Models 1, 2, and 4 are quasichemical models that incorporate the structure of silicate slags. They have been optimized against experimental measurements and have shown great accuracy, making them the basis of computational thermodynamic packages such as Factsage [160] and Thermocalc [161]. Models 5, 6 and 7 are semi-empirical in nature and are easy to interpret despite their less robustness in complex systems. Different applications of computational thermodynamics to inclusion engineering have been presented by Jung et al. [162], Kang et al. [163] and Costa e Silva [164].

Kinetic models

These models allow one to track the change of parameters with time taking into consideration the kinetics of the reaction/process. In this regard, two kinetic modelling approaches have been used widely to explain experimental findings and to simulate industrial conditions:

Reaction zone modelling This approach assumes that the chemical reactions reach equilibrium in effective reaction volumes/'zones' near each reaction interface. The volume of these different 'zones' needs to be determined *apriori*. However, most researchers have chosen to characterize these zones using the definition of mass transfer coefficient. It utilizes thermodynamic

databases with a 'macros'-based tool which consists of performing internal Gibbs energy Minimization (GEM) calculations. This allows one to consider the composition changes of the different phases in multiple reaction zones over time in a metallurgical reactor like the ladle furnace. This has been a choice of many researchers [66, 176, 177, 178, 181, 183] since it allows the use of existing commercial thermodynamic software like FactSage [160] along with process simulation software such as METSIM [165]. The concept of local equilibrium in the steel phase is used to model the evolution of different inclusion phases, with the assumption being that of fast reaction kinetics between the steel and the inclusions [66]. However, these models cannot tackle problems such as interface reaction controlled reactions or non-equilibrium inclusions.

Reaction interface modelling This approach was initially proposed by Robertson et al. [90], which considers the calculation of compositions at the interface between reacting phases by utilizing equilibria and flux density equations. Mass transfer coefficients for different species are used to characterize the kinetics of phase interaction. By solving a series of differential equations, dynamic change of composition of multiple components in a multiphase system can be calculated simultaneously. For steel-inclusion reactions, the compositional trajectory is modeled with consideration of mass transfer through a boundary layer, and product layer of an inclusion [166, 167, 168]. However, it needs to be noted that such an approach requires somewhat *apriori* knowledge of the predominant inclusion system to be modelled.

It has been demonstrated within the study (Refer to Appendix B) that the equations for the reaction interface model and reaction zone model are similar with the latter exploiting the nature of the commercial thermodynamic packages for the construction of interfacial zones. Some of the important models utilizing these approaches are tabulated in Table 2.4.1.

2.4.2 Mixing and transport models

Understanding different phenomena including hydrodynamics, mass and heat transfer, and particle dynamics are of important consequence in improving the efficiency of secondary steelmaking reactors. In the past four decades, there has been considerable progress in describing the interaction of multiple phases such as bubbles, particles, steel and slag through computational fluid dynamic (CFD) modelling approaches. These methods have been explored by a number of workers and are discussed in detail elsewhere [100, 186, 187]. Despite the comprehensiveness, CFD models are still computationally expensive, which is why they do not attract use as process models in industries.

Table 2.4.1: *Different kinetic models of ladle refining process*

Authors	**Year**	**Deoxidant**	**Scale**	**Approach**	**Interactions**	**Ref.**
Peter et al.	2005	Al ; Si-Mn	Ind.	RZM (MetSim) + MTM	Steel-Slag	[68]
Conejo et al.	2007	Al	Ind.	RIM	Steel-Slag	[98]
Visser and Boom	2008	Al-Ca	Ind.	RIM +MTM	Steel-Slag-Ca plume-inclusion	[169]
Graham and Irons	2009	Al	Ind.	RIM	Steel-Slag	[115]
Kargul and Falkus	2010	Al	Ind.	RZM + MTM	Steel-Slag-Alloy	[170]
Harada et al.	2013	Al	Ind. + Exp.	RIM	Steel-slag-inclusions-refractory	[171]
Scheller et al.	2014	Al-Ca	Ind.	RZM + MTM	Steel-slag-inclusions-refractory	[172]
Lou and Zhou	2014	Al	Ind.	RIM + CFD	Steel-Slag-Air	[173]
Rimbert et al.	2014	Al-Ti	Ind.	CFD + RIM + PBE	Steel-inclusions	[174]
Cicutti et al.	2015	Al	Ind.	RIM + GEM (inc.)	Steel-slag-inclusions-refractory-Air	[124]
Galindo et al.	2015	Al	Ind.	RIM	Steel-slag-inclusions	[166]
Ende and Jung	2017	Al	Ind.	RZM	Steel-slag-inclusions-refractory	[175]
Shin et al.	2017	Al	Exp.	RZM	Steel-slag-inclusions-refractory	[176]
Ren et al.	2017	Al	Ind. + Exp.	RZM + MTM	Steel-Ca plume-inclusions	[177]
Zhang et al.	2017	Si-Mn	Ind.	RZM + MTM	Steel-inclusion	[178]
Zhang et al.	2018	Al	Ind.	RIM	Steel-slag-inclusions-refractory-Air	[179]
Piva et al.	2018	Si-Mn	Exp.	RZM	Steel-slag-inclusions-refractory	[66]
Ren et al.	2018	Al-Ti	Ind.	RZM + MTM	Steel-inclusion	[180]
Kumar et al.	2019	Al	Ind. + Exp.	RZM	Steel-slag-inclusions-refractory	[181]
Tabatabaei et al.	2019	Al-Ca	Ind.	RIM	Steel-slag-Ca plume-inclusions	[182]
You et al.	2020	Al	Ind.	RZM + MTM	Steel-slag-inclusions-refractory-Air	[183]
Cao and Nastac	2020	Al	Ind.	RIM	Steel-slag	[184]
Podder et al.	2022	Si-Mn	Exp.	RIM	Steel-slag-inclusions	[185]

RZM: Reaction Zone Model; RIM: Reaction Interface Model; MTM: Mixing Tank Model; CFD: Computational Fluid dynamics; GEM: Gibbs Energy Minimization; PBE: Population Balance Equation

However, they are used to aid in process design like the choice of alloy addition location and time, bottom gas plug configuration, etc. Furthermore, some lumped parameter models utilizing the knowledge of CFD results have been proposed to predict important variables like mixing time and mass transfer coefficients, among others. A detailed review of such macro models can be found in the article by Mazumder and Evans [137]. Another class of models have aimed to capture the mixing behavior in the ladle through the use of so-called reactors or 'tanks'. This approach seems to circumvent the problem of computational challenges posed by CFD models while retaining information about the effect of stirring on melt flow. These models were popularized by Oeters and co-workers [188, 189, 190, 191] in ladle metallurgy, and their principles find use in sophisticated process simulation software like METSIM, SIMUSAGE. Moreover, it is straightforward to link its model parameters to CFD models, as shown by Lekhakh and Robertson [192]. A recent approach has been to combine the chemical reaction models (steel-slag-inclusion) with such tank models in order to remove the assumption of uniform bath compositions [68, 170, 178, 180, 183].

2.5 Summary

A comprehensive review of the predominant interactions encountered during the ladle refining process has been provided in this Chapter, and essentially how they relate to different sources of inclusions. For Si-Mn killed steels, most inclusions are Mn-silicates, but undesirable reactions from ferroalloy reactions, slag entrapment, or steel-slag reactions contribute to Ca and Al-rich inclusions. These inclusions can be harmful to the castability and properties of the steel.

Since equilibrium between steel, slag, and inclusions is not fully established in industrial steelmaking conditions, a local equilibrium approach for modeling inclusions is not always adequate. In this regard, the kinetics of inclusion formation and modification should be considered in developing process models that can be used for online control. Ladle refining reactions can be considered to be multiphase in nature and reactions happen at different phase interfaces, making modeling a complicated task. However, based on existing knowledge from experiments and industrial trials, simplifications can be made, and a structured approach to modelling can be followed.

From a scientific angle, there also seem to be some gaps in the literature that need to be filled. For example, the rate-determining steps concerning nucleation and growth of complex oxides, like Mn silicates following Si-Mn

deoxidation, have not been addressed adequately. Questions like when does the critical mechanism of deoxidation switch from one primarily involving inclusions to one primarily involving slag? and how do changes to the top slag affect inclusion evolution? are not clearly answered. While most experimental results have been substantiated with thermodynamic models, few kinetic models are available in the literature that have been validated with industrial data for Si-Mn killed steels.

All of the above forms the incentive for this study. In this regard, a modelling approach based on the mass transfer kinetics of critical chemical species in steel, slag, and inclusion phases is likely to be fruitful. This model should take into account the simultaneous competition of different inclusion types in Si-Mn killed steel, such as Mn-silicates, alumina, Mn-aluminosilicates, etc. Overall, it should be able to track the composition trajectory of slag, steel, and inclusions during ladle processing. Subsequent chapters will present the author's approach to this type of model.

References

[1] https://www.vepica.com/blog/steel-production-from-iron-ore-to-functional-industrial-products [accessed December 15, 2022]
[2] K.W. Lange: Int. Mater. Rev., 1988, vol. 33, pp. 53–89.
[3] A. Ghosh: Secondary SteelmakingPrinciples and Applications, CRC Press, 2001.
[4] G. Stolte: Secondary Metallurgy. Fundamentals. Processes, Applications, 2002, pp. 14
[5] R.J. Fruehan: Ladle Metallurgy Principles and Practices, Iron and steel society,AIME, 1985.
[6] E.B. Pretorius, H.G. Oltmann, and B.T. Schart: Iron Steel Technol., 2015, vol. 12, pp. 333–45.
[7] R.J. O'Malley: AISTech - Iron Steel Technol. Conf. Proc., 2017, vol. 2, pp. 1567–85.
[8] H.J. Visser, R. Boom, and M. Biglari: Rev. Metall. Cah. D'Informations Tech., 2008, vol. 105, pp. 172–80.
[9] P. Kaushik, J. Lehmann, and M. Nadif: Metall. Mater. Trans. B Process Metall. Mater. Process. Sci., 2012, vol. 43, pp. 710–25.
[10] S.K. Michelic and C. Bernhard: Steel Res. Int., DOI:10.1002/srin.202200086.
[11] E.T. Turkdogan: J. Iron Steel Inst., 1966, pp. 914–9.
[12] F. Oeters: Metallurgy of Steelmaking, Verlag Stahleisen, 1994.
[13] B.K.D.P. Rao and D.D.R. Gaskell: Metall. Trans. B, 1981, vol. 12, pp. 311–7.
[14] Y.J. Kim, D.H. Woo, H. Gaye, H.G. Lee, and Y.B. Kang: Metall. Mater. Trans. B Process Metall. Mater. Process. Sci., 2011, vol. 42, pp. 535–45.
[15] H. Ohta and H. Suito: Metall. Mater. Trans. B Process Metall. Mater. Process. Sci., 1996, vol. 27, pp. 943–53.
[16] I.H. Jung, Y.B. Kang, S.A. Decterov, and A.D. Pelton: Metall. Mater. Trans. B Process Metall. Mater. Process. Sci., 2004, vol. 35, pp. 259–68.
[17] X. Zhang, H. Roelofs, S. Lemgen, U. Urlau, and S. V. Subramanian: Steel Res. Int., 2004, vol. 75, pp. 314–21.

[18] Y.B. Kang, I.H. Jung, S.A. Decterov, A.D. Pelton, and H.G. Lee: ISIJ Int., 2004, vol. 44, pp. 975–83.
[19] X.K. Di Zhang Xiao Bing, Jiang Guo Chang: in Molten Slags, Fluxes And Salts '97 Conference, vol. 0, 1997, pp. 259–62.
[20] N. Frossling, Gerlands Beitr, Geophys., 52, 170 (1938).
[21] U. Lindborg and K. Torselh Trans. TMS-AIME, 1968, vol. 242, p. 94.
[22] J. Zhang and H.G. Lee: ISIJ Int., 2004, vol. 44, pp. 1629–38.
[23] L. Zhang and W. Pluschkell: Ironmak. Steelmak., 2003, vol. 30, pp. 106–10.
[24] J. H. Hollomon and D. Turnbull: in 'Progress in metal physics 4', 1961, pp. 333–403.
[25] L. Kampmann and M. Kahlweit: Ber. Bunsenges. Phys. Chem., 1970, vol. 74, pp. 456–62.
[26] K. Nakajima, W. Mu, and P.G. Jönsson: Metall. Mater. Trans. B Process Metall. Mater. Process. Sci., 2019, vol. 50, pp. 2229–37.
[27] H. Yin, H. Shibata, T. Emi, and M. Suzuki: ISIJ Int., 1997, vol. 37, pp. 946–55.
[28] M.E. Ferreira, P.C. Pistorius, and R.J. Fruehan: Front. Mater., 2021, vol. 8, pp. 1–10.
[29] W. Lou and M. Zhu: Metall. Mater. Trans. B Process Metall. Mater. Process. Sci., 2013, vol. 44, pp. 762–82.
[30] L. Zhang and S. Taniguchi: Int. Mater. Rev., 2000, vol. 45, pp. 59–82.
[31] D. Bouris and G. Bergeles: Metall. Mater. Trans. B Process Metall. Mater. Process. Sci., 1998, vol. 29, pp. 641–9.
[32] J. Aoki, L. Zhang, and B.G. Thomas: ICS 2005 - Proc. 3rd Int. Congr. Sci. Technol. Steelmak., 2005, pp. 319–31.
[33] B.A. Webler and P.C. Pistorius: Metall. Mater. Trans. B Process Metall. Mater. Process. Sci., DOI:10.1007/s11663-020-01949-y.
[34] L. Zhang and B.G. Thomas: XXIV Natl. Steelmak. Symp., 2003, pp. 138–83.
[35] S.K. Michelic, G. Wieser, and C. Bernhard: ISIJ Int., 2011, vol. 51, pp. 769–75.
[36] H.F. Jacobi: Steel Res. Int., 2005, vol. 76, pp. 595–602.
[37] M. Nuspl, W. Wegscheider, J. Angeli, W. Posch, and M. Mayr: Anal. Bioanal. Chem., 2004, vol. 379, pp. 640–5.
[38] D. Tang, M.E. Ferreira, and P.C. Pistorius: Microsc. Microanal., 2017, vol. 23, pp. 1082–90.
[39] T. Li, S.I. Shimasaki, S. Taniguchi, and S. Narita: ISIJ Int., 2016, vol. 56, pp. 1625–33.
[40] S. Ramesh Babu and S.K. Michelic: Materials (Basel)., DOI:10.3390/ma15093367.
[41] D. Janis, P.G. Jönsson, A. Appell, and J. Janis: Ironmak. Steelmak., 2016, vol. 43, pp. 121–9.
[42] H.M. Hong and Y.B. Kang: ISIJ Int., 2021, vol. 61, pp. 2464–73.
[43] A.J. Currie, S. Millman, and S. Johnstone: AIP Conf. Proc., 2009, vol. 1096, pp. 1735–42.
[44] P. Le Bran and F. Taina: Light Met. 2015, 2015, pp. 991–6.
[45] W. Mu, P. Hedström, H. Shibata, P.G. Jönsson, and K. Nakajima: Jom, 2018, vol. 70, pp. 2283–95.
[46] M. Sharma, W. Mu, and N. Dogan: Jom, 2018, vol. 70, pp. 1220–4.
[47] L. Zhang: steel Res. Int., 2006, vol. 77, pp. 158–69.
[48] Y.B. Kang and H.G. Lee: ISIJ Int., 2004, vol. 44, pp. 1006–15.
[49] C. Chen, Z. Jiang, Y. Li, L. Zheng, X. Huang, G. Yang, M. Sun, K. Chen, H. Yang, H. Hu, and H. Li: Steel Res. Int., 2019, vol. 90, pp. 1–13.
[50] C. Garlick, M. Griffiths, P. Whitehouse, and C. Gore: Ironmak. Steelmak., 2002, vol. 29, pp. 140–6.
[51] S. Maeda, T. Soejima, T. Saito, H. Matsumoto, H. Fujimoto, and T. Mimura: in 1989 Steelmaking Conference Proceedings, 1989, pp. 379–85.
[52] J.S. Park and J.H. Park: Metall. Mater. Trans. B Process Metall. Mater. Process.

Sci., 2014, vol. 45, pp. 953–60.
[53] S.P.T. Piva, D. Kumar, and P.C. Pistorius: Metall. Mater. Trans. B Process Metall. Mater. Process. Sci., 2017, vol. 48, pp. 37–45.
[54] O. Wijk and V. Brabie: ISIJ Int., 1996, vol. 36, pp. S132–5.
[55] S. Lyu, X. Ma, Z. Huang, Z. Yao, H.G. Lee, Z. Jiang, G. Wang, J. Zou, and B. Zhao: Metall. Mater. Trans. B Process Metall. Mater. Process. Sci., 2019, vol. 50, pp. 732–47.
[56] J.H. Park and Y.B. Kang: Metall. Mater. Trans. B Process Metall. Mater. Process. Sci., 2006, vol. 37, pp. 791–7.
[57] W. Li, Y. Ren, and L. Zhang: Ironmak. Steelmak., 2019, vol. 9233, pp. 1–7.
[58] K. Mizuno, H. Todoroki, M. Noda, and T. Tohge: Iron Steelmak., 2001, vol. 28, pp. 93–101.
[59] S. Nurmi, S. Louhenkilpi, and L. Holappa: Steel Res. Int., 2013, vol. 84, pp. 323–7.
[60] J. Chen, Q. Zhu, D. Huang, S. Zheng, J. Zhang, and H. Li: in IOP Conference Series: Materials Science and Engineering, vol. 230, 2017.
[61] Q. Wang, L. Wang, J. Zhai, J. Li, and K. Chou: Metall. Mater. Trans. B Process Metall. Mater. Process. Sci., 2018, vol. 49, pp. 325–33.
[62] K. Karihara: Kobelco Technol. Rev., 2011, vol. 30, pp. 62–65.
[63] K.P. Wang, M. Jiang, X.H. Wang, Y. Wang, H.Q. Zhao, and Z.M. Cao: Metall. Mater. Trans. B Process Metall. Mater. Process. Sci., 2017, vol. 48, pp. 2961–9.
[64] P. Valentin, C. Bruch, and J. Gaule: Steel Res. Int., 2009, vol. 80, pp. 746–52.
[65] C.B. Guo, H.T. Ling, L.F. Zhang, C. Liu, G.S. Wang, and Y.B.Gao: 6th Int. Congress Sci. Technol. Steelmaking, Beijing. 2015. pp. 817–20.
[66] S.P.T. Piva, D. Kumar, and P.C. Pistorius: Metall. Mater. Trans. B Process Metall. Mater. Process. Sci., 2017, vol. 48, pp. 37–45.
[67] W. Tiekink, R. Van Den Bogert, T. Breedijk, and A. Ferguson: Ironmak. Steelmak., 2003, vol. 30, pp. 146–50.
[68] J. Peter, K.D. Peaslee, D.G.C. Robertson, and B.G. Thomas: AISTech - Iron Steel Technol. Conf. Proc., 2005, vol. 1, pp. 959–73.
[69] A. Bhansali, H. Oltmann, and E. Pretorius: in AIST proceedings: AISTech 2021, 2021, pp. 1–13.
[70] Y. Dai, J. Li, C. Shi, and W. Yan: Metall. Res. Technol., DOI:10.1051/metal/2018130.
[71] M.L. Turpin and J.F. Elliott: Jisi, 1966, vol. 204, pp. 217–24.
[72] Y. Kawashita and H. Suito: ISIJ Int., 1995, vol. 35, pp. 1459–67.
[73] D.C. Hilty and W. Crafts: J. Met., 1950, vol. 2, pp. 414–24.
[74] V. Thapliyal, A. Kumar, D.G.C. Robertson, and J.D. Smith: Ironmak. Steelmak., 2015, vol. 42, pp. 382–94.
[75] H. Doostmohammadi, A. Karasev, and P. Jo¨nsson: Steel Res. Int., 2010, vol. 81, pp. 398–406.
[76] T. Gram: PhD thesis. KTH Royal Institute of Technology, Sweden, 2015.
[77] A. Mayerhofer, D. You, P. Presoly, C. Bernhard, and S.K. Michelic: Metals (Basel)., 2020, vol. 10, pp. 1–16.
[78] A. Mayerhofer, P. Presoly, C. Bernhard, and S.K. Michelic: AISTech - Iron Steel Technol. Conf. Proc., 2020, vol. 2, pp. 1526–34.
[79] M. Wakoh, T. Sawai, and S. Mizoguchi: Tetsu-to-Hagane´, 1992, vol. 78 (11), pp. 73-80.
[80] D. You, S.K. Michelic, and C. Bernhard: Metals (Basel)., DOI:10.3390/met8060452.
[81] G. Forward, J.F. Elliott, J.F. Elliott, and T. Kuwabara: Metall. Trans., 1970, vol. 1, pp. 2889–98.
[82] A.A. Alexeenko and D.A. Ponomarenko: Russ. Metall., 2009, vol. 2009, pp. 697–704.

[83] K. Wang, M. Jiang, X. Wang, Y. Wang, H. Zhao, and Z. Cao: Metall. Mater. Trans. B Process Metall. Mater. Process. Sci., 2015, vol. 46, pp. 2198–207.
[84] J. Gamutan, T. Miki, and T. Nagasaka: Tetsu-To-Hagane/Journal Iron Steel Inst. Japan, 2022, vol. 108, pp. 509–16.
[85] H.S. Kim, H.G. Lee, and K.S. Oh: ISIJ Int., 2002, vol. 42, pp. 1404–11.
[86] H.S. Kim, H.G. Lee, and K.S. Oh: Metall. Mater. Trans. A Phys. Metall. Mater. Sci., 2001, vol. 32, pp. 1519–25.
[87] Y. Ren and L. Zhang: Ironmak. Steelmak., 2019, vol. 46, pp. 558–63.
[88] T. Matsumiya: Mater. Trans., JIM, 1992, 33, vol. 33.
[89] D. You, S.K. Michelic, P. Presoly, J. Liu, and C. Bernhard: Metals (Basel)., 2017, vol. 7, pp. 1770–8.
[90] D.G.C. Robertson, B. Deo, and S. Ohguchi: Ironmak. Steelmak., 1984, vol. 11, pp. 41–55.
[91] N.J. Themelis: Transport and Chemical Rate Phenomena, Routledge (Taylor and Francis), 2004.
[92] F.D. Richardson: Physical Chemistry of Melts in Metallurgy, Academic Press (Elsevier), 1974.
[93] A.N. Conejo: Processes, DOI:10.3390/PR8070750.
[94] B. Deo and R. Boom: Fundamentals of Steelmaking Metallurgy, 1993.
[95] R. Higbie: Trans. AIChE, 1935, vol. 31, pp. 365–89.
[96] P.V. Danckwerts: Eng. Process Dev. 1951, vol. 43, pp. 1460–1467.
[97] J.C. Lamont and D.S. Scott: AIChE J., 1970, vol. 16, pp. 513–19.
[98] A.N. Conejo, F.R. Lara, M. Macias-Hernández, and R.D. Morales: steel Res. Int., 2007, vol. 78, pp. 141–50.
[99] S. Asai, M. Kawachi, and I. Muchi: *SCANINJECT III, Refin. Iron Steel by Powder Inject.*, 1983, p. 12.
[100] D. Mazumdar and R.I.L. Guthrie: ISIJ Int., 1995, vol. 35, pp. 1–20.
[101] R.J. Fruehan: Metall. Trans. B, 1978, vol. 9, pp. 287–92.
[102] D. Roy, P.C. Pistorius, and R.J. Fruehan: Metall. Mater. Trans. B Process Metall. Mater. Process. Sci., 2013, vol. 44, pp. 1095–104.
[103] C.J.B. Fincham and F.D. Richardson: Proc. R. Soc. London. Ser. A. Math. Phys. Sci., 1954, vol. 223, pp. 40–62.
[104] D.J. Sosinsky and I.D. Sommerville: Metall. Trans. B, 1986, vol. 17, pp. 331–37.
[105] R.W. Young, J.A. Duffy, G.J. Hassall, and Z. Xu: Ironmak. Steelmak., 1992, vol. 29, p. 201.
[106] Y. Taniguchi, N. Sano, and S. Seetharaman: ISIJ Int., 2009, vol. 49, pp. 156–63.
[107] G. H. Zhang, K. C. Chou, and U. Pal: ISIJ Int., 2013, vol. 53, pp. 761–67.
[108] RG. Reddy and M. Blander: Metall. Trans. B, 1987, vol. 18, pp. 591–96
[109] M.M. Nzotta, D. Sichen, and S. Seetharaman: ISIJ Int., 1998, vol. 38, pp. 1170–79.
[110] A. Ma, S. Mostaghel, and K. Chattopadhyay: ISIJ Int., 2017, vol. 57, pp. 114–22.
[111] I.H. Jung and E. Moosavi-Khoonsari: Metall. Mater. Trans. B Process Metall. Mater. Process. Sci., 2016, vol. 47, pp. 819–23.
[112] H. Gaye, J. Lehmann, T. Matsumiya, and W. Yamada, in Proceedings of 4th Molten Slags, S. Ban-ya, ed., Fluxes and Salts, ISIJ, 1992, pp. 103–08.
[113] Y.B. Kang and A.D. Pelton: Metall. Mater. Trans. B, 2009, vol. 40B, pp. 979–94.
[114] Y.B. Kang: Metall. Mater. Trans. B Process Metall. Mater. Process. Sci., 2021, vol. 52, pp. 2859–82.
[115] K.J. Graham and G.A. Irons: Iron Steel Technol., 2009, vol. 6, pp. 164–73.
[116] L. Jonsson, D. Sichen, and P. Jönsson: ISIJ Int., 1998, vol. 38, pp. 260–7.
[117] H. Lachmund, Y. Xie, T. Buhles, and W. Pluschkell: Steel Res., 2003, vol. 74, pp. 77–85.

[118] D. Liao, S. Holko, A.S. Moreno, and K. Boylan: Proc. 8th Int. Conf. Model. Simul. Metall. Process. Steelmak. STEELSIM 2019, 2019, pp. 1–12.
[119] T. Inomoto, Y. Ogawa, and T. Toh: ISIJ Int., 2003, vol. 43, pp. 828–35
[120] F. Fuhr, G. Torga, F. Medina, and C. Cicutti: Ironmak. Steelmak., 2007, vol. 34, pp. 463–70.
[121] K. Krishnapisharody and G.A. Irons: ISIJ Int., 2008, vol. 48, pp. 1807–9.
[122] W. Lou and M. Zhu: Metall. Mater. Trans. B Process Metall. Mater. Process. Sci., 2013, vol. 44, pp. 762–82.
[123] E.T.Turkdogan: Ironmak. Steelmak., 1988, vol. 15, pp. 311–7.
[124] C. Cicutti, C. Capurro, and C. Cerrutti: in 9th International Conference and Exhibition on Clean Steel, 2015.
[125] K. Miyazawa and H. Goto: ISIJ Int., 1998, vol. 38, pp. 256–9.
[126] J. Tan: Carnegie Mellon University Pittsburgh, PA, 2017.
[127] A. Deng, Y. Xia, H. Dong, H. Wang, and D. Fan: Sci. Rep., 2020, vol. 10, pp. 1–10.
[128] K. Miyazawa and H. Goto: ISIJ Int., 1998, vol. 38, pp. 256–9.
[129] S.H. Kim and B. Song: Metall. Mater. Trans. A Phys. Metall. Mater. Sci., 1999, vol. 30, pp. 435–42.
[130] W.W. Huh and W.G. Jung: ISIJ Int., 1996, vol. 36, pp. 36–9.
[131] A.M.T. Andersson, L.T.I. Jonsson, and P.G. Jösson: Scand. J. Metall., 2003, vol. 32, pp. 123–36.
[132] K.D. Carlson and C. Beckermann: Mater. Sci. Technol., 2005, vol. 1, pp. 35–46.
[133] M.A. Van Ende, M. Guo, E. Zinngrebe, B. Blanpain, and I.H. Jung: ISIJ Int., 2013, vol. 53, pp. 1974–82.
[134] E. Zinngrebe, C. Van Hoek, H. Visser, A. Westendorp, and I.H. Jung: ISIJ Int., 2012, vol. 52, pp. 52–61.
[135] S. Li, L. Zhang, Y. Ren, W. Fang, W. Yang, S. Shao, J. Yang, and W. Mao: ISIJ Int., 2016, vol. 56, pp. 584–93.
[136] S.A. Argyropoulos and R.I.L. Guthrie: in Steelmaking Conference proceedings, ISS Warrendale, 1982, pp. 156–67.
[137] D. Mazumdar and J.W. Evans: ISIJ Int., 2004, vol. 44, pp. 447–61.
[138] H. Berg, H. Laux, S.T. Johansen, and O.S. Klevan: Ironmak. Steelmak., 1999, vol. 26, pp. 127–39.
[139] D. Mazumdar and R.I.L. Guthrie: Metall. Trans. B, 1993, vol. 24, pp. 649–55.
[140] H. Duan, L. Zhang, and B.G. Thomas: Steel Res. Int., 2019, vol. 90, pp. 1–8.
[141] E. B. Pretorius, US 7,785,393 B2 (2010).
[142] Y. Wang, A. Karasev, J.H. Park, and P.G. Jönsson: Metall. Mater. Trans. B Process Metall. Mater. Process. Sci., 2021, vol. 52, pp. 2892–925.
[143] F. Huang, L. Zhang, Y. Zhang, and Y. Ren: Metall. Mater. Trans. B Process Metall. Mater. Process. Sci., 2017, vol. 48, pp. 2195–206.
[144] C. Liu, F. Huang, J. Suo, and X. Wang: Metall. Mater. Trans. B Process Metall. Mater. Process. Sci., 2016, vol. 47, pp. 989–98.
[145] T.M. Richards, R.J. O'Malley, J.D. Smith, and T.P. Sander: AISTech - Iron Steel Technol. Conf. Proc., 2021, vol. 2021-June, pp. 1279–88.
[146] Z. Deng, Z. Liu, M. Zhu, and L. Huo: ISIJ Int., 2021, vol. 61, pp. 1–15.
[147] S. Yang, Q. Wang, L. Zhang, J. Li, and K. Peaslee: Metall. Mater. Trans. B Process Metall. Mater. Process. Sci., 2012, vol. 43, pp. 731–50.
[148] J.H. Park and H. Todoroki: ISIJ Int., 2010, 50, vol. 50.
[149] Z. Deng, L. Cheng, L. Chen, and M. Zhu: Steel Res. Int., 2019, vol. 90, pp. 1–12.
[150] C. Wagner: Thermodynamics of Alloys, Addison-Wesley, Reading, MA, 1962, p. 51.
[151] L.S. Darken: Trans. TMS-AIME, 1967, vol. 239, pp. 90-96.
[152] C.W. Bale and A.D. Pelton: Metall. Trans. A, 1990, vol. 21, pp. 1997–2002.

[153] I.H. Jung, S.A. Decterov, and A.D. Pelton: Metall. Mater. Trans. B Process Metall. Mater. Process. Sci., 2004, 35, vol. 35.
[154] J. Lehmann and L. Zhang: Steel Res. Int., 2010, vol. 81, pp. 875–9.
[155] M. Hillert, B. Jansson, and B. Sundman: Metall. Trans. B, 1990, vol. 21, pp. 404–6.
[156] A.D. Pelton, S.A. Degterov, G. Eriksson, C. Robelin, and Y. Dessureault: Metall. Mater. Trans. B Process Metall. Mater. Process. Sci., 2000, vol. 31, pp. 651–9.
[157] S. Ban-ya: in 4th International Conference on Molten Slags and Fluxes, 1992, Sendai, ISIJ, 1992, pp. 8–13.
[158] K. Xu, G. Jiang, X. Zhang, K. Tang, J. Xu, and W. Ding: Jinshu Xuebao/Acta Metall. Sin., 1998, 34, vol. 34.
[159] Z. Jian: in 4th International Conference on Molten Slags and Fluxes, 1992, Sendai , ISIJ, 1992, pp. 244–9.
[160] https://www.factsage.com [accessed December 15, 2022]
[161] https:/thermocalc.com [accessed December 15, 2022]
[162] I.H. Jung, S.A. Decterov, and A.D. Pelton: ISIJ Int., 2004, vol. 44, pp. 527–36.
[163] Y.B. Kang, H.S. Kim, J. Zhang, and H.G. Lee: J. Phys. Chem. Solids, 2005, vol. 66, pp. 219–25.
[164] A. Costa e Silva: Rare Met., 2006, vol. 25, pp. 412–9.
[165] https://metsim.com [accessed December 15, 2022]
[166] A. Galindo, G.A. Irons, S. Sun, and K.S. Coley: Proc. Challenges and Transformative Solutions to Sustainable Steelmaking and Casting for Environment-Friendly Metallurgical Innovation, Iron and Steel Institute of Japan, Tokyo, 2015, pp. 22–31.
[167] Y. Tabatabaei, K.S. Coley, G.A. Irons, and S. Sun: Metall. Mater. Trans. B, 2018, vol. 49B, pp. 375–87.
[168] G. Okuyama, K. Yamaguchi, S. Takeuchi, and K. Sorimachi: ISIJ Int., 2000, vol. 40, pp. 121–28.
[169] H.J. Visser, R. Boom, and M. Biglari: Rev. Metall. Cah. D'Informations Tech., 2008, vol. 105, pp. 172–80.
[170] T. Kargul and J. Falkus: Steel Res. Int., 2010, vol. 81, pp. 953–8.
[171] A. Harada, N. Maruoka, H. Shibata, and S.Y. Kitamura: ISIJ Int., 2013, vol. 53, pp. 2118–25.
[172] P.R. Scheller and Q. Shu: Steel Res. Int., 2014, vol. 85, pp. 1310–6.
[173] W. Lou and M. Zhu: Metall. Mater. Trans. B Process Metall. Mater. Process. Sci., 2014, vol. 45, pp. 1706–22.
[174] N. Rimbert, L. Claudotte, P. Gardin, and J. Lehmann: Ind. Eng. Chem. Res., 2014, vol. 53, pp. 8630–9.
[175] M.A. Van Ende and I.H. Jung: Metall. Mater. Trans. B Process Metall. Mater. Process. Sci., 2017, vol. 48, pp. 28–36.
[176] J.H. Shin, Y. Chung, and J.H. Park: Metall. Mater. Trans. B Process Metall. Mater. Process. Sci., 2017, vol. 48, pp. 46–59.
[177] Y. Ren and L. Zhang: ISIJ Int., 2017, vol. 57, pp. 68–75.
[178] Y. Zhang, Y. Ren, and L. Zhang: Metall. Res. Technol., 2017, vol. 114, pp. 1–8.
[179] Y. Zhang, Y. Ren, and L. Zhang: Metall. Res. Technol., DOI:10.1051/metal/2018059.
[180] Y. Ren and L. Zhang: Ironmak. Steelmak., 2018, vol. 45, pp. 585–91.
[181] D. Kumar, K.C. Ahlborg, and P.C. Pistorius: Metall. Mater. Trans. B Process Metall. Mater. Process. Sci., 2019, vol. 50, pp. 2163–74.
[182] Y. Tabatabaei, K.S. Coley, G.A. Irons, and S. Sun: Metall. Mater. Trans. B Process Metall. Mater. Process. Sci., 2018, vol. 49, pp. 2744–56.
[183] D. You, S.K. Michelic, and C. Bernhard: Steel Res. Int., 2020, vol. 91, pp. 1–9.
[184] Q. Cao and L. Nastac: Ironmak. Steelmak., 2020, vol. 47, pp. 873–81.

[185] A. Podder, K.S. Coley, and A.B. Phillion: Steel Res. Int., 2022, vol. 2100831, p. 2100831.
[186] R.D. Morales, F.A. Calderón-Hurtado, K. Chattopadhyay, and S.J.G. Guarneros: Metall. Mater. Trans. B Process Metall. Mater. Process. Sci., 2020, vol. 51, pp. 628–48.
[187] Y. Liu, M. Ersson, H. Liu, P.G. Jönsson, and Y. Gan: Metall. Mater. Trans. B Process Metall. Mater. Process. Sci., 2019, vol. 50, pp. 555–77.
[188] J. Mietz and M. Bruehl: Steel Res., 1990, vol. 61, pp. 105–12.
[189] F. Oeters, W. Pluschkell, E. Steinmetz, and H. Wilhelmi: Steel Res., 1988, vol. 59, pp. 192–201.
[190] J. Mietz and F. Oeters: Steel Res., 1989, vol. 60, pp. 387–94.
[191] J. Mietz and F. Oeters: Can. Metall. Q., 1989, vol. 28, pp. 19–27.
[192] S.N. Lekakh and D.G.C. Robertson: ISIJ Int., 2013, vol. 53, pp. 622–8.
[193] G.G. Krishnamurthy: ISIJ Int., 1989, vol. 29, pp. 49–57.
[194] W. Lou and M. Zhu: Metall. Mater. Trans. B Process Metall. Mater. Process. Sci., 2013, vol. 44, pp. 762–82.

Chapter 3

Mathematical study of the formation mechanisms of complex oxide inclusions in Si-Mn killed steel

In Chapter 3, the original concept of nucleation and growth analysis of complex oxides was conceived by me. The model development and the analysis were entirely carried out by me. Useful discussions on the results were provided by Dr. Kenneth S. Coley and Dr. André B. Philion.

The manuscript was initially drafted by me and edited to the final version by Dr. Kenneth S. Coley and Dr. André B Philion. This chapter has been published in Metallurgical and Materials Transactions B, 2022, DOI: https://doi.org/10.1007/s11663-022-02630-2. The following Chapter is the pre-publication version of the article.

Mathematical study of the formation mechanisms of complex oxide inclusions in Si-Mn killed steel

Angshuman Podder[1], **Kenneth Coley**[1,2], **André Phillion**[1]

[1] *McMaster Steel Research Center*
Department of Materials Science and Engineering,
McMaster University, Hamilton, Ontario, Canada, ON L8S 4L7
[2] *Department of Mechanical and Materials Engineering,*
Western University, London, Ontario, Canada, ON N6A 3K7

Abstract

Deoxidation and inclusion control are important aspects of secondary steelmaking. Due to various reactions taking place between the solutes in the molten steel reactor, it sometimes becomes difficult to understand the formation mechanisms of complex oxide inclusions. In this study, a mathematical model including nucleation and mass transfer is proposed for the prediction of composition evolution of primary oxide inclusions generated after steel deoxidation by addition of Si and Mn. Complex inclusions resulting from homogeneous nucleation and transformation of existing simple oxides like silica are also taken into consideration. The results show that the spontaneous nucleation of complex oxides is favourable and has almost three times higher driving force relative to simple oxides during deoxidation of steel. Also, the transformation of simple to complex oxides is essentially very fast (< 1 s) owing to the high driving forces for mass transfer. These results demonstrate the model's ability to predict the chemical composition of the complex oxide nuclei growing in the steel melt along with the final inclusion composition.

3.1 Introduction

Deoxidation of steel is required in secondary steelmaking to reduce the oxygen content of the steel, which is accompanied by the production of numerous oxide inclusions as a by-product. Complex oxide inclusions i.e., inclusions containing more than one cationic species, are more commonly observed in practice relative to simple oxides inclusions. Understanding the formation mechanisms of these inclusions occurring in molten steel will help in achieving better overall inclusion control in the final steel product.

Si-Mn deoxidation is preferred for the production of steel long-products since using Al gives rise to harmful alumina inclusions that are sometimes detrimental to the final steel quality and limit the overall ease of processing [1, 2].

During the deoxidation process, various interactions take place between oxygen and the added deoxidizers. This results in the formation of different complex oxide inclusions, mostly liquid manganese silicates in Si-Mn killed steel, which can form via several routes as described below and shown schematically in Figure 3.1:

1. Spontaneous nucleation due to the presence of sufficient supersaturation for oxide precipitation in the steel melt or at heterogeneous sites.
2. Chemical modification of simple oxides through reaction with solutes in molten steel.
3. Physical interactions such as agglomeration and coagulation of existing simple oxide inclusions.

In the last few decades, there has been considerable progress in the research into different oxide inclusions, especially the occurrence and dynamics of various complex inclusions in molten steel [3, 4, 5, 6]. Elliot and co-workers have conducted extensive research on the topic of deoxidation, more notably in Fe-Si-O where they employed different techniques like rapid cooling of the saturated melt [7], solidification experiments [8], and electrochemical measurements [9] to study the nucleation kinetics of inclusion formation. From these studies, it was shown that the homogeneous nucleation of silica can occur even at low supersaturation ratios, of about 80. In comparison, supersaturation ratios of about 3×10^6 are needed for homogeneous nucleation of alumina. Furthermore, they showed that the rate of mixing of deoxidizers has an effect on the number of particles forming in the steel melt. Frederiksson and Hammer [10] investigated the deoxidation of Fe-50 % Ni alloys with Mn, Si and Al and concluded that FeO quickly transforms to different iron silicates or aluminates. Turkodogan [11] and Turpin and Elliot [7] used Classical Nucleation Theory (CNT) to model liquid manganese silicate inclusions. However, they did not consider the composition of the nucleation product that might form spontaneously in the melt nor did they include the transformation of existing silica particles in their calculations. Due to the abundance of chemical driving force in a liquid melt at high temperature, complex oxides may nucleate in the melt along with simple oxides. Thus, additional considerations seem necessary for modelling the origins of complex oxide inclusions that form during the refining process. While the exact analytical or numerical solutions to the kinetics of inclusion evolution may be difficult to obtain, the use of approximations enables important conclusions to be made for situations of practical interest.

In the past, multiple researchers have developed models to predict the occurrence of inclusions predominant in Al-killed steel including Ca aluminates

[12] and Mg spinels [13, 14], based on the shrinking core model (SCM) [15]. However, modelling of inclusions in the Si-Mn killed steel has not been as thoroughly studied. A frequently used approach to model the occurrence of inclusions has been to implement a local thermodynamic equilibrium approximation to compute the compositions of the inclusions [17, 18, 19, 20]. By considering a mathematical analysis of the formation mechanisms, it is possible to determine the range of physical parameters over which such an approach is useful. Furthermore, the variance in inclusion composition within a steel sample at the same location cannot be explained with a thermodynamic approach alone, necessitating also the consideration of additional kinetic factors.

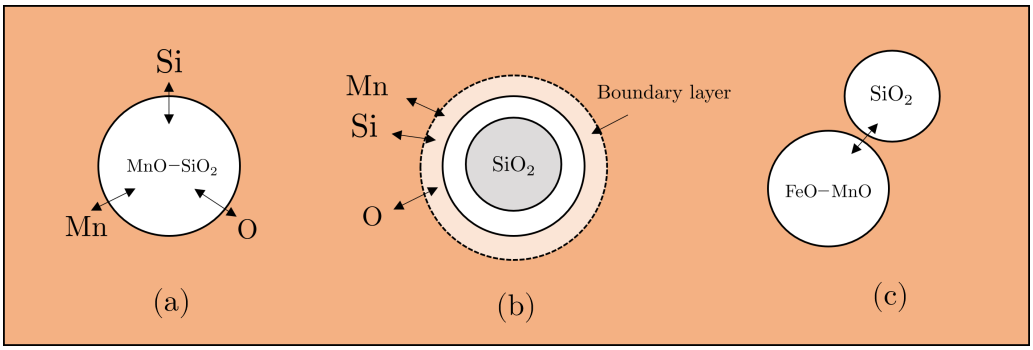

Figure 3.1: *Formation mechanism of manganese silicates in liquid steel (a) by direct nucleation (Route 1), (b) by transformation of a silica inclusion to a complex manganese silicate (Route 2), and (c) by coagulation of simple or complex oxide inclusions (Route 3).*

In this study, a mathematical model is developed to predict the formation of complex oxide inclusions in a Si-Mn killed steel prior to solidification and thus to evaluate the kinetics of the chemical reactions occurring in the steel melt. While this paper is entirely computational or theoretical in nature, specific cases have been highlighted at appropriate points in the text to support the qualitative aspects of these nucleation calculations. The model is justified by well-established knowledge of the $MnO-SiO_2$ system and considers the practical conditions of deoxidation. Furthermore, without a nucleation model, those attempting to model population balances or even average inclusion compositions, are limited to guessing the initial inclusion population. To date, only a small number of authors have applied some form of nucleation models as a precursor to inclusion population balance models [21, 22] but restricted to simple oxide systems like alumina, magnesia etc. The current work is part of a larger program to develop a model describing inclusion evolution during ladle treatment of Si-Mn killed steel which includes the effects of steel-slag reaction on the compositional changes of the inclusions.

In the text below, first, the model formulation is described for inclusions

that evolve through Routes 1 and 2. Second, the nucleation calculations are compared for silica and Mn-silicate inclusions to assess the competition between the two phases. Third, the results of the mass transfer model are presented, after which the discussions about the effect of different process and model parameters are made. Finally, the applicability of the current model to the development of a process model for ladle refining is discussed.

3.2 Model

In order to analyze the formation mechanism of Mn-silicate type inclusions during Si-Mn deoxidation, two models representing both direct nucleation (Route 1) and transformation of simple oxide inclusions (Route 2) have been developed. From both these models, the objective is to assess the evolution of these inclusions under different parameters. In the first model, the stability of silica and Mn-silicate type inclusions has been evaluated. Particularly, the chemical driving force, critical radii and nucleation rates have been calculated using CNT. In the second model, the modification of SiO_2 particles and the overall attainment of steel-inclusion equilibrium has been evaluated through a mass transfer model. This model predicts the transformation time, compositional changes and size changes of an average inclusion belonging to the $MnO{-}SiO_2$ system considering a mean-field approach.

3.2.1 Route 1

Theory

The change in total free energy of the liquid steel melt following a nucleation event can be calculated using

$$\Delta G = \frac{4\pi r^3}{3}\frac{\Delta G_{\mathrm{v}}}{\Omega} + 4\pi r^2\sigma, \tag{3.2.1}$$

where ΔG_v is the volumetric Gibbs free energy change, Ω is the molar volume of the oxide, r is the nucleus radius, σ is the interfacial tension between the nucleus and parent phase (in this case the oxide and steel). From Eq. 3.2.1, by considering the competition between volumetric Gibbs free energy change and surface energy, one can obtain expressions for both the minimum total Gibbs free energy change, ΔG^* (Eq. 3.2.2) as well as the critical nucleus radius (Eq. 3.2.3),

$$\Delta G^* = \frac{16\pi\sigma^3}{3\Delta G_v^2}, \text{ and} \tag{3.2.2}$$

$$r_c = \frac{-2\sigma}{\Delta G_v}. \tag{3.2.3}$$

Finally, from CNT the homogeneous nucleation rate, J, can be calculated via

$$J = A \exp\left(\frac{-\Delta G^*}{k_B T}\right), \tag{3.2.4}$$

where k_B is the Boltzmann constant, T is the temperature, and A refers to the pre-exponential factor and is dependent on the available nucleation sites, frequency factor and Zeldovich constant [23]. For the system under study, a constant value of 10^{32} [7] is used for simplicity. It is noted that although this value in reality changes based on the inclusion type, the nature of the expression in Eq. 3.2.4 shows more dependence on the exponential term.

In order to obtain the rate of nucleation, it is essential to calculate the ΔG_v for complex oxides. In principle, the composition of the oxide nuclei will be such to minimize the chemical driving force for precipitate nucleation, ΔG_v. A detailed description of this calculation is provided in Section 3.2.1. This is done to find the minimum nucleation barrier or total Gibbs free energy change during the nucleation process, ΔG needed for oxide nucleation. Consequently, it should produce an oxide nucleus of minimum radius (Eq. 3.2.3). The underlying assumptions of the model are as follows:

1. Inclusion particles are spherical.
2. Nucleation occurs homogeneously in the liquid steel melt.
3. The system is taken to be isothermal. Thus, any heat change associated with the reaction under consideration is neglected.

Thermodynamics of nucleation

In this study, $(MnO)_y$−$(SiO_2)_{1-y}$ (alternatively $Mn_ySi_{1-y}O_{2-y}$) is taken as the inclusion system that precipitates out of the steel by considering the equilibrium reactions in the Fe-Si-Mn-O system. Here the value of y, where $0 \leq y \leq 1$, must be determined that minimizes ΔG_v and r_c. The total free energy associated with the solute elements in the liquid Fe-Mn-Si-O system can be written in terms of their activities, a_i,

$$\sum x_i \mu_i = RT[y \ln a_{\mathrm{Mn}} + (1-y) \ln a_{\mathrm{Si}} + (2-y) \ln a_{\mathrm{O}}], \tag{3.2.5}$$

where x_i, and μ_i are the mole fraction and partial Gibbs free energy associated with i^{th} species (i = Si, Mn, O), respectively and R is the gas constant.

Concurrently, the free energy of the $Mn_ySi_{1-y}O_{2-y}$ phase can be calculated as

$$\Delta G^{\circ}_{Mn_ySi_{1-y}O_{2-y}} = y\Delta G^{\circ}_{MnO} + (1-y)\Delta G^{\circ}_{SiO_2} + \Delta G^{mix,id} + \Delta G^{XS}, \quad (3.2.6)$$

where ΔG°_j refers to the Gibbs free energy of formation of the oxide j, $\Delta G^{mix,id}$ is the free energy of ideal mixing, and ΔG^{XS} is the excess free energy change during the formation of a complex oxide. The expressions to compute these variables are given by:

$$\Delta G^{\circ}_j = -RT \log K_j, \quad (3.2.7)$$

$$\Delta G^{mix,id} = -T\Delta S^{mix} = RT[y \ln y + (1-y)\ln(1-y)], \text{and} \quad (3.2.8)$$

$$\Delta G^{XS} = RT[y \ln \gamma_{MnO} + (1-y)\ln \gamma_{SiO_2}], \quad (3.2.9)$$

where K_j is the equilibrium constant of the reaction associated with the formation of oxide j, ΔS^{mix} is the ideal entropy of mixing and γ_i refers to the activity coefficients,.

Now, the Gibbs free energy change, ΔG_v associated with the formation of $Mn_ySi_{1-y}O_{2-y}$ can be calculated using the difference between Eqns. 3.2.5 and 3.2.6 and written as

$$\Omega\Delta G_v = \Delta G^{\circ}_{Mn_ySi_{1-y}O_{2-y}}(y) - RT(y \ln a_{Mn} + (1-y)\ln a_{Si} + (2-y)\ln a_O) \quad (3.2.10)$$

$$\text{or, } \Delta G_v = -\frac{RT}{\Omega} \cdot \Bigg[y \ln a^i_{Mn} + (1-y)\ln a^i_{Si} + (2-y)\ln a^i_O - y\frac{\Delta G^{\circ}_{MnO}}{RT} - (1-y)\frac{\Delta G^{\circ}_{SiO_2}}{RT} - \frac{\Delta G^{mix,id}}{RT} - \frac{\Delta G^{XS}}{RT} \Bigg], \quad (3.2.11)$$

where the activities, a^i_i correspond to that of the initial melt. Now, one needs to obtain minimum the oxide composition, i.e. the minimum value of y, denoted y_{min}, at which the ΔG_v will be minimum. This also corresponds to the minimum in the critical nucleus radius, r_c. As will be described below, the solution was first obtained analytically to approximate y_{min}, and then numerically for a more accurate estimation.

Analytical solution

The analytical solution for y_{min} can be obtained by differentiating the expression on the right-hand side of Eq. 3.2.11 with respect to the compositional parameter, y and then setting it to zero. Excluding the ΔG^{XS} term from

Eq. 3.2.11 for simplicity during differentiation yields

$$\ln a^i_{\mathrm{Mn}} - \ln a^i_{\mathrm{Si}} - \ln a^i_{\mathrm{O}} - \frac{\Delta G^{\circ}_{\mathrm{MnO}}}{RT} + \frac{\Delta G^{\circ}_{\mathrm{SiO_2}}}{RT} - \ln\left(\frac{y_{min}}{1-y_{min}}\right) = 0. \quad (3.2.12)$$

Now, by rearranging the terms of Eq. 3.2.12, the expression for y_{min} can be obtained as

$$y_{min} = \left(\frac{a^i_{\mathrm{Si}} \cdot a^i_{\mathrm{O}}}{a^i_{\mathrm{Mn}}} \cdot \exp\left(\frac{\Delta G^{\circ}_{\mathrm{MnO}} - \Delta G^{\circ}_{\mathrm{SiO_2}}}{RT}\right) + 1\right)^{-1}. \quad (3.2.13)$$

Finally, by substituting the value of y_{min} in Eq. 3.2.11, the expression for the chemical driving force for nucleation, ΔG_v (Eq. 3.2.14) is obtained,

$$\begin{aligned}\Delta G_v = -\frac{RT}{\Omega} \cdot \Bigg[& y_{min} \ln a^i_{\mathrm{Mn}} + (1-y_{min}) \ln a^i_{\mathrm{Si}} + (2-y_{min}) \ln a^i_{\mathrm{O}} \\ & - y_{min} \frac{\Delta G^{\circ}_{\mathrm{MnO}}}{RT} - (1-y_{min}) \frac{\Delta G^{\circ}_{\mathrm{SiO_2}}}{RT} - \frac{\Delta G^{mix,id}}{RT} - \frac{\Delta G^{XS}}{RT} \Bigg].\end{aligned} \quad (3.2.14)$$

Additionally, from Eqs. 3.2.3 and 3.2.14, one can compute the critical radius r_c using

$$\begin{aligned}r_c = \frac{2\sigma\Omega}{RT} \cdot \Bigg[& y_{min} \ln a^i_{\mathrm{Mn}} + (1-y_{min}) \ln a^i_{\mathrm{Si}} + (2-y_{min}) \ln a^i_{\mathrm{O}} \\ & - y_{min} \frac{\Delta G^{\circ}_{\mathrm{MnO}}}{RT} - (1-y_{min}) \frac{\Delta G^{\circ}_{\mathrm{SiO_2}}}{RT} - \frac{\Delta G^{mix,id}}{RT} - \frac{\Delta G^{XS}}{RT} \Bigg]^{-1}.\end{aligned} \quad (3.2.15)$$

Thus, from the model described above, one now has expressions for y_{min}, ΔG_v, and r_c which can be together used to compute the homogeneous nucleation rate, J using Eq. 3.2.4. Note that although the assumption of excluding the ΔG^{XS} terms is a significant one, this (a) allows for validation of the numerical approach and (b) enables determination of the importance of the ΔG^{XS} term on the values of y_{min} and r_c as will be discussed in Sec. 3.4.1.

Numerical methodology

In order to include the term ΔG^{XS}, a numerical solution to Eq. 3.2.11 is used. For ease of implementation, Eq. 3.2.11 is rearranged as

$$\Delta G_v = -\frac{RT}{\Omega} \cdot \left[(1-y) \log\left(\frac{K_{\mathrm{SiO_2}} a^i_{\mathrm{Si}} a^{i2}_{\mathrm{O}}}{a_{\mathrm{SiO_2}}}\right) + y \log\left(\frac{K_{\mathrm{MnO}} a^i_{\mathrm{Mn}} a^i_{\mathrm{O}}}{a_{\mathrm{MnO}}}\right)\right], \quad (3.2.16)$$

where the K_j are obtained by replacing the ΔG_j° terms using Eq. 3.2.7, and a_{MnO}, $a_{\mathrm{SiO_2}}$ are the activities of the oxides in the $\mathrm{MnO{-}SiO_2}$ system. The above equation is rendered non-linear by the activity terms which are a function of y, and obtained by combining Eq. 3.2.8 and 3.2.9. In order to compute the value of y_{min}, the minimum value of ΔG_v is calculated utilizing the FMINCON minimization function within MATLAB 2020a. The constraints are obtained from the fact that compositional variables have to be non-negative and should not violate mass conservation (i.e. all species mole fractions must be less than one).

3.2.2 Route 2

Theory

In Route 2, simple oxide particles ($\mathrm{SiO_2}$) are assumed to form homogeneously in the melt, after which Mn reacts with these inclusions to form complex oxides ($\mathrm{MnO{-}SiO_2}$). The current model considers the formation of complex oxide inclusions by diffusion of elements into the initially-formed nucleus of a simple oxide. The mass transfer of species to the inclusion interface leads to inclusion growth until local equilibrium between the steel and the inclusion population is achieved.

To describe the evolution of Mn-silicates, the model considers mass transfer through a boundary layer (B.L.) to the surface of a pre-existing silica inclusion along with the diffusion through a product layer (P.L.). After the silica core has been consumed, the model considers only mass transfer through the BL. A schematic of these approaches is presented in Fig 3.2. The underlying assumptions of this model are as follows:

1. Pre-existing inclusions exist within the steel melt.
2. Inclusion particles are spherical; diameter changes with time are based solely on mass transfer.
3. Mass transport of Si, Mn, and O is only considered between the steel and the inclusion.
4. There is no change in the inclusion number density; the initially-chosen value is representative of the number density after larger particles float out to the top of the steel.
5. Chemical reactions are fast relative to mass transport processes, due to the high temperature, and are not considered to be rate controlling.
6. The bulk steel is well mixed; a uniform concentration of dissolved species exists throughout the steel at all instances.

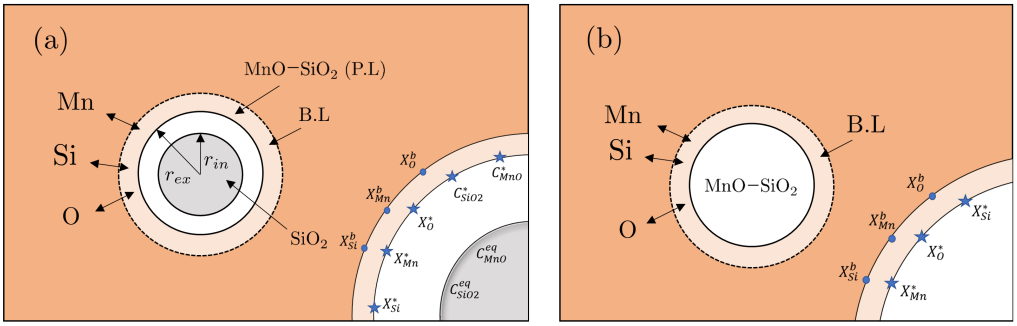

Figure 3.2: *Schematic of the two stages of inclusion evolution showing (a) diffusion through the PL and mass transfer through the B.L. during the transformation of the silica core; and (b) mass transfer through the B.L. after the silica core has been consumed. The relevant interfacial concentrations used in the model are also indicated.*

.

Model formulation

The reaction equilibria between Si, Mn and O at the steel/inclusion interface can be described as:

$$\begin{aligned} [\mathrm{Si}] + 2[\mathrm{O}] &= (\mathrm{SiO_2})_{\mathrm{inc}}, \\ \log K_{eq} &= \frac{30110}{T} - 11.40, \text{ and} \end{aligned} \tag{3.2.17}$$

$$X^*_{\mathrm{Si}} = \frac{a^*_{\mathrm{SiO_2}}}{\epsilon_{\mathrm{Si}} X^{*\,2}_{\mathrm{O}}} \quad \text{where} \quad \epsilon_{\mathrm{Si}} = \left(\frac{K_{\mathrm{SiO_2}} f_{\mathrm{Si}} MW_{\mathrm{Si}} f^2_{\mathrm{O}} MW^2_{\mathrm{O}} .100^3}{MW^3_{\mathrm{Fe}}} \right), \tag{3.2.18}$$

$$\begin{aligned} [\mathrm{Mn}] + [\mathrm{O}] &= (\mathrm{MnO})_{\mathrm{inc}}, \\ \log K_{eq} &= \frac{14880}{T} - 6.67, \text{ and} \end{aligned} \tag{3.2.19}$$

$$X^*_{Mn} = \frac{a^*_{\mathrm{MnO}}}{\epsilon_{\mathrm{Mn}} X^*_{\mathrm{O}}} \quad \text{where} \quad \epsilon_{\mathrm{Mn}} = \left(\frac{K_{\mathrm{MnO}} f_{\mathrm{Mn}} MW_{\mathrm{Mn}} f_{\mathrm{O}} MW_{\mathrm{O}} .100^2}{MW^2_{\mathrm{Fe}}} \right), \tag{3.2.20}$$

where f_i represents the Henrian activity coefficient of species i with respect to 1 wt % standard state, X_i and MW_i are the corresponding mole fraction and molar mass, K_{eq} is the equilibrium constant (which is evaluated at 1873 K [24]), ϵ_i is a fixed parameter based on the initial steel melt conditions at 1873 K, and $a^*_{SiO_2}$ and a^*_{MnO} are the interfacial activities of the species in the MnO−SiO_2 system. The activity coefficients of the steel species are calculated using the Unified Interaction Parameter Model (UIPF) [25] while the activities of the oxide components within the inclusions are calculated using the sub-regular solution model [26].

The mass transfer rate, N_i, (mol/s), of species i through the boundary layer from the bulk steel to the surface of a spherical particle can be described by

$$N_i = \pi d^2 k_{m,i} C_{v,m} (X_i^b - X_i^*), \tag{3.2.21}$$

where $k_{m,i}$ is the mass transfer coefficient of species i in the melt, $C_{v,m}$ is the molar density in the fluid phase, d is the particle diameter, X_i^b is the molar fraction in the bulk of the fluid phase, and X_i^* is the molar fraction at the interface between the particle and boundary layer. The mass transfer coefficient is calculated using

$$k_{m,i} = \frac{D_i \cdot Sh}{d}, \tag{3.2.22}$$

where D_i refers to the diffusivity of species i and Sh refers to the Sherwood number. A value of 2 was adopted for Sh as this is a typical value for inclusions that are less than 14 μm in diameter [27].

In the first stage, when the silica core reacts with the species in the melt, a shrinking core model (SCM) is used to calculate the transformation time needed to completely form a Mn-silicate type inclusion. The SCM was formulated based on a model by Tabatabaei et al. [12] which was initially developed for Ca-aluminates inclusions. Here, mass transfer within the $MnO-SiO_2$ inclusion is assumed to occur by quasi-steady state diffusion of MnO and SiO_2, through the liquid PL. A flux balance for the diffusing species through the PL and BL results in the following set of equations:

$$[N_{\mathrm{Si}}]_{B.L} = [N_{\mathrm{SiO_2}}]_{P.L}, \tag{3.2.23}$$

$$[N_{\mathrm{Mn}}]_{B.L} = [N_{\mathrm{MnO}}]_{P.L}, \text{and} \tag{3.2.24}$$

$$[N_{\mathrm{O}}]_{B.L} = 2[N_{\mathrm{SiO_2}}]_{P.L} + [N_{\mathrm{MnO}}]_{P.L}. \tag{3.2.25}$$

Using Eq. 3.2.21 and assuming steady state diffusion (Fick's 1st Law) through the liquid PL, the above equations can be rewritten as

$$4\pi r_{ex}^2 k_{m,\mathrm{Si}}^{st} C_v^{st} (X_{\mathrm{Si}}^b - X_{\mathrm{Si}}^*) = \left(\frac{4\pi r_{ex} r_{in}}{r_{ex} - r_{in}}\right) D_{\mathrm{SiO_2}}^{inc} (C_{\mathrm{SiO_2}}^{ex} - C_{\mathrm{SiO_2}}^{in}), \tag{3.2.26}$$

$$4\pi r_{ex}^2 k_{m,\mathrm{Mn}}^{st} C_v^{st} (X_{\mathrm{Mn}}^b - X_{\mathrm{Mn}}^*) = \left(\frac{4\pi r_{ex} r_{in}}{r_{ex} - r_{in}}\right) D_{\mathrm{MnO}}^{inc} (C_{\mathrm{MnO}}^{ex} - C_{\mathrm{MnO}}^{in}), \text{ and} \tag{3.2.27}$$

$$k_{m,\mathrm{O}}^{st} C_v^{st} (X_{\mathrm{O}}^b - X_{\mathrm{O}}^*) = 2(k_{m,\mathrm{Si}}^{st} C_v^{st} (X_{\mathrm{Si}}^b - X_{\mathrm{Si}}^*)) + k_{m,\mathrm{Mn}}^{st} C_v^{st} (X_{\mathrm{Mn}}^b - X_{\mathrm{Mn}}^*), \tag{3.2.28}$$

where r_{ex} and r_{in} are the outer and inner radius of the product layer, C_v^{st} is the molar density of steel, D_i is the diffusivity of species i, and C_i^{ex} and

C_i^{in} are corresponding concentrations at the external and internal radii. The C_i^{in} values are set to the equilibrium values, C_i^{eq} which are obtained from the $MnO-SiO_2$ phase diagram at 1873 K.

In the second stage, after the silica core has been consumed, mass transfer is assumed to occur only through the boundary layer. This simplifies the flux equations to

$$k_{m,\mathrm{O}}^{st} C_v^{st} (X_{\mathrm{O}}^b - X_{\mathrm{O}}^*) = 2(k_{m,\mathrm{Si}}^{st} C_v^{st} (X_{\mathrm{Si}}^b - X_{\mathrm{Si}}^*)) + k_{m,\mathrm{Mn}}^{st} C_v^{st} (X_{\mathrm{Mn}}^b - X_{\mathrm{Mn}}^*). \quad (3.2.29)$$

In this second stage, growth of a spherical inclusion particle is considered to take place by only mass transfer with the growth rate of the inclusions is given by

$$\frac{dr}{dt} = N_i \cdot \Omega, \quad (3.2.30)$$

where r is the radius of the inclusion. The transfer of elements to the inclusions results in a corresponding depletion of solutes in the bulk liquid steel. This change in composition can be taken into account by assuming that solute transfer to each inclusion takes places independently of each other, i.e. the mean distance between inclusions significantly exceeds the solute diffusion length in the liquid. This can be expressed as

$$\frac{dX_i}{dt} = -\frac{\pi d^2 k_{m,i}}{V_c} \cdot (X_i^b - X_i^*) \quad (3.2.31)$$

where dX_i/dt represents the change in concentration in the bulk steel, and $V_c = 1/Z$ is the catchment volume with Z being the inclusion density per m^3 of steel.

Numerical methodology

The solution of the interfacial concentrations was obtained numerically by solving the above non-linear equations using MATLAB 2020a. Using the equilibrium equations in Eqns. 3.2.18, and 3.2.20 along with the flux equations in Eqns. 3.2.26, 3.2.27, 3.2.28, and 3.2.29, one can solve for the interfacial concentrations for the two stages of the model. At any given timestep, after obtaining converged values for the interfacial concentrations, the compositional change within the bulk steel and inclusions, as well as the growth in inclusion radius were computed. The time step for all calculations was set to 0.001 s.

3.2.3 Calculation of activities of oxides in inclusion

In order to carry out the numerical calculations for the Route 1 and Route 2 models, the activities of oxides in the $MnO-SiO_2$ system are required. In this study, they are calculated by the sub regular solution model (SRSM) as described by Zhang et al. [26] for the $CaO-MnO-SiO_2-Al_2O_3$ system. Specifically, the activities can be expressed as

$$a_{\mathrm{M_xO_y}} = X_{\mathrm{M_xO_y}} \exp\left(\frac{G^{ex}_{\mathrm{M_xO_y}} - G^{o}_{\mathrm{M_xO_y}}}{RT}\right), \tag{3.2.32}$$

where $X_{\mathrm{M_xO_y}}$ is the mole fraction of an oxide $\mathrm{M_xO_y}$ in the oxide system, $G^{ex}_{\mathrm{M_xO_y}}$ is the excess partial mole free energy of the oxide in reference to the pure liquid state and $G^{o}_{\mathrm{M_xO_y}}$ is the mole free energy of phase transformation of the oxide from liquid to solid [28].

For the quarternary $CaO-MnO-SiO_2-Al_2O_3$ system, $G^{ex}_{M_xO_y}$ is expressed with a set of formulae in a multi component framework ($\mathrm{M_xO_y}$ = 1 to 4), for which 1 to 4 denote the four oxide components as

$$G^{\mathrm{ex}}_{\mathrm{M_xO_y}} = \sum_{0}^{j'} \sum_{0}^{k'} \sum_{0}^{l'} A_{jkl} \mathrm{Y}^j \mathrm{Z}^k \mathrm{U}^l = G^{\mathrm{ex}}_{\mathrm{M_xO_y}}(\mathrm{Y}, \mathrm{Z}, \mathrm{U}) \tag{3.2.33}$$

Here, j', k', l' refer to the order of the system, A_{jkl} are empirical parameters of the SRSM model, and Y, Z, and U are the reduced composition variables,

$$Y = 1 - X_1 \tag{3.2.34}$$
$$Z = 1 - (X_2/Y) \tag{3.2.35}$$
$$U = 1 - (X_3/YZ) \tag{3.2.36}$$

For the ($MnO-SiO_2$) binary system, the model reduces to one composition variable, Y.

3.3 Results

3.3.1 Activity model

Figure 3.3 compares the activity of MnO as a function of mole fraction of SiO_2 in the $MnO-SiO_2$ system as calculated by the model via the SRSM approach and data from the literature [29]. As can be seen, very good agreement is achieved, demonstrating the validity of our implementation of the SRSM model.

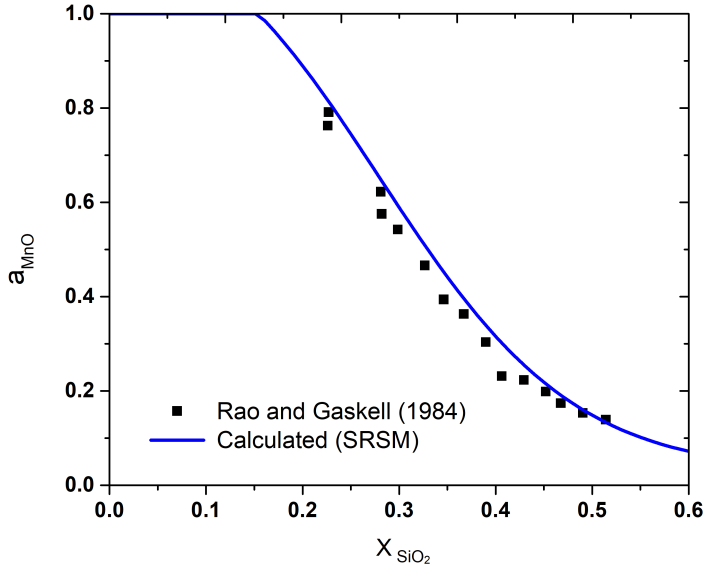

Figure 3.3: *Comparison of calculated and measured activities of MnO using SRSM in $MnO-SiO_2$ system at 1873 K.*

3.3.2 Route 1: Nucleation model

A base oxygen level of 500 ppm was chosen for the nucleation calculations since it is close to the value expected in steel coming from primary steelmaking process [30]. The Mn and Si levels have been chosen to be 1.05 and 0.21 wt % respectively, representing the composition of a typical long product. Other required properties are listed in Table 3.3.1.

Table 3.3.1: *Physico-chemical properties used in this study (St: Steel, Inc: Inclusion) [35, 41]*

Species	Parameter	Unit	Value
Steel	Density	kg/m^3	7000
	Temp.	K	1873
SiO_2	Density	kg/m^3	2650
	Molar volume	m^3/mol	22.06×10^{-6}
	Interfacial tension (St/Inc)	J/m^2	0.25
$MnO-SiO_2$	Density	kg/m^3	3650
	Molar volume	m^3/mol	20.16×10^{-6}
	Interfacial tension (St/Inc)	J/m^2	0.25

Figure 3.4a shows the variation in total Gibbs free energy, ΔG with inclusion radius, r for different X_{MnO} values and calculated at $\sigma = 0.75$ N/m. As can

be seen, the different nucleii compositions result in different ΔG^* values. There is also a corresponding change in nuclei radius. Figure 3.4b shows resulting variation in r_c with X_{MnO}. It can be seen that there is not a great change in r_c until large values of X_{MnO}, and the minimum critical radii is obtained around $X_{\mathrm{MnO}} = 0.3$. An accurate prediction of this value could also be obtained by minimizing ΔG_v as discussed in Section 3.2.1.

Figure 3.5 shows the variation in the chemical driving force, ΔG_v, needed for nucleation as well as the critical radius, r_c, of both $MnO-SiO_2$ complex inclusions and SiO_2 simple inclusions as a function of temperature in the range typically used for liquid metal processing. As can be seen, the stability of the $MnO-SiO_2$ inclusion is slightly higher than that of the SiO_2 inclusion. This is an indication that complex oxide inclusions can directly precipitate from the melt as the primary deoxidation product. Consequently, the critical radius of the $MnO-SiO_2$ inclusion is lower than the SiO_2 inclusion. Owing to the less significant differences between the critical radii of the two inclusions, it can be surmised that the both these inclusion phases can precipitate simultaneously in the steel melt.

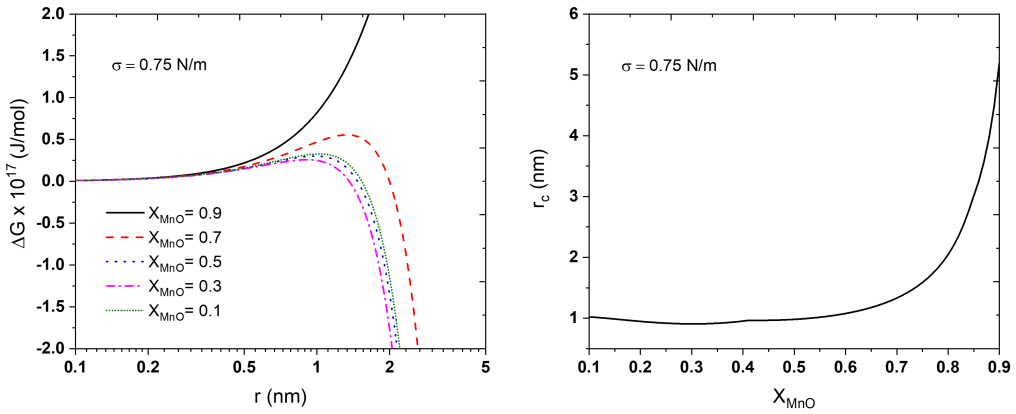

Figure 3.4: *(a)Variation of ΔG of an $MnO-SiO_2$ inclusion with radius, r for different X_{MnO} values, (b) variation of r_c with X_{MnO}.*

Effect of oxygen in steel

Figure 3.6a shows the variation of ΔG_v and r_c of SiO_2 and $MnO-SiO_2$ phases at 1873 K as a function of dissolved oxygen content within the steel melt. In keeping with established knowledge [1], it is evident from Figure 3.6a that the chemical driving force for the formation of $MnO-SiO_2$ type inclusions is more than that of SiO_2 inclusions. This again emphasizes that the nucleation

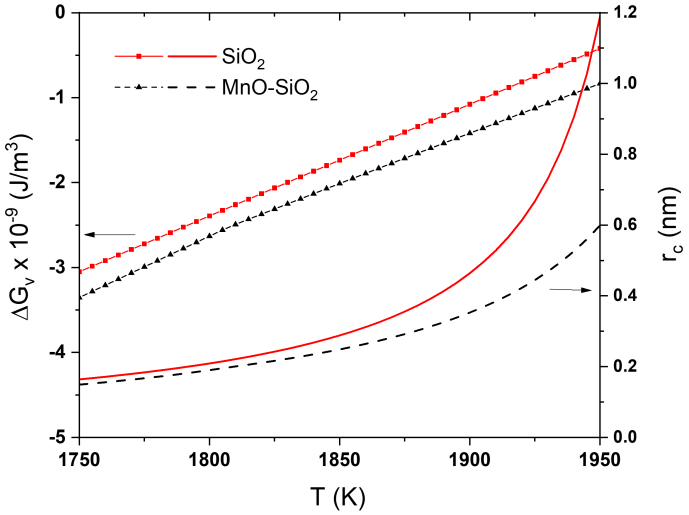

Figure 3.5: *Variation of ΔG_v and r_c of SiO_2 and $MnO-SiO_2$ phases with temperature at 500 ppm oxygen.*

of the complex oxide is more favourable than the simple oxide. Consequently, the critical radius of the complex oxide is smaller suggesting that it is likely to nucleate earlier from the melt. Finally, it can be seen that higher oxygen levels give rise to higher driving forces for precipitation.

In Figure 3.6b, the effect of dissolved oxygen levels in steel on X_{MnO} (mole fraction of MnO in oxide nucleus) is shown. As can be seen, there is a decrease in X_{MnO} within increasing oxygen content, i.e. the composition of the nucleus becomes enriched in SiO_2, especially for the typical oxygen levels encountered in an oxidized liquid steel (200 - 500 ppm O). This can be also shown from the analytical expression in Eq. 3.2.13, where higher oxygen levels leads to lower MnO content in the nucleus. An overall lower MnO (30-35 mol %) in the nucleus mixture can be explained by the stability of the SiO_2 component, which is rendered by the exponential term in Eq. 3.2.13.

Effect of deoxidizer concentration in steel

Figure 3.7a and 3.7b show the variation in Mn-silicate nuclei composition for different Mn and Si levels. An oxygen level of 500 ppm has been selected for these simulations. As can be seen, the MnO content in the inclusions gradually increases with increasing Mn within the steel. However, the MnO content decreases sharply when the Si increases within the steel, and reaches a value of $\approx$ 30 mol % MnO at Si levels $>$ 0.04 wt. % . At some critical concentrations of Si and Mn, the MnO content is seen to change abruptly. This is mainly due to differences in the way the reaction proceeds with the

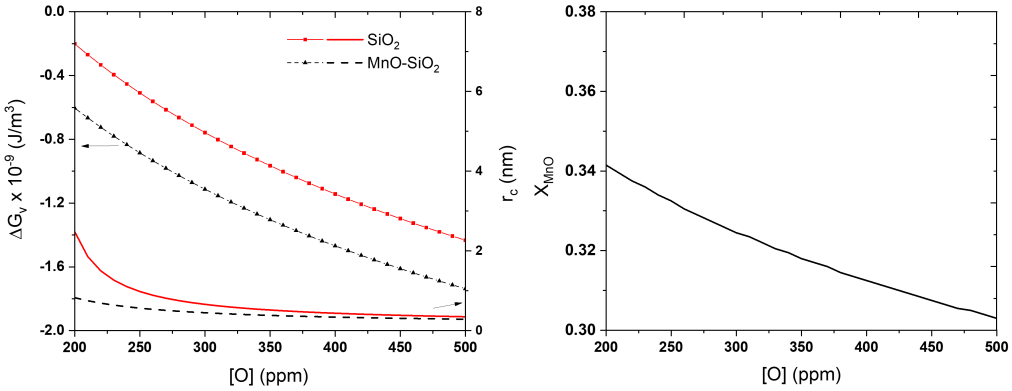

Figure 3.6: *(a) Variation of ΔG_v, r_c of SiO_2 and $MnO-SiO_2$ phases, and (b) variation of X_{MnO} as a function of dissolved oxygen content in steel at 1873 K.*

available dissolved oxygen and the activity relationships between the oxides in $MnO-SiO_2$ system. The higher content of SiO_2 is mainly due to the stronger deoxidation capability of Si compared to Mn. The results also show that different oxide nuclei compositions are obtained with different Si and Mn levels in the steel, which suggests that non-uniform mixing of ferroalloy additions caused by the kinetics of dissolution and bath mixing can have an impact on the nucleation process.

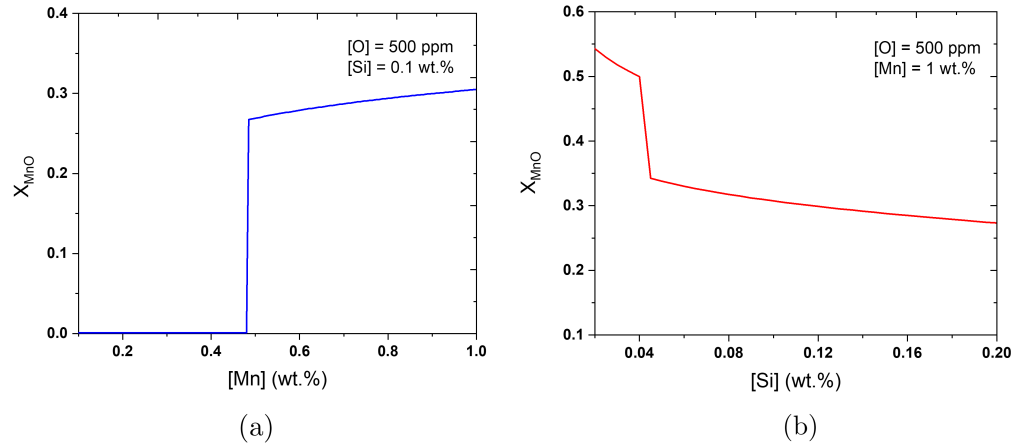

Figure 3.7: *Effect of (a) Mn, and (b) Si levels on the compositions of the oxide nuclei for O = 500 ppm.*

3.3.3 Route 2: Mass transfer model

As noted earlier, the bulk concentrations of dissolved Si, Mn, and O are the input boundary conditions for Route 2. A value of 1.05 wt% Mn, 0.21 wt%

Si and 100 ppm O is assumed for the base case, matching Route 1, but will be examined in the sensitivity analysis. The important model parameters are listed down in Table 3.3.2, and the diffusion coefficients used for the calculations are summarized in Table 3.3.3.

Table 3.3.2: *Model parameters*

Parameter	Unit	Value
Steel mass	kg	0.650
Inclusion density	$/m^3$	10^{13}
Inclusion diameter	μm	5
Initial inclusion mass	kg	6.39×10^{-5}

Table 3.3.3: *Diffusion coefficients of species in steel melts at 1873 K used in this study [12]*

	MnO	SiO_2	Mn	Si	O
D $\times 10^9$ (m^2/s)	0.1	0.1	5.45	3	3.1

Figure 3.8 shows the decrease in SiO_2 core diameter with time after reacting with Mn. As can be seen, after a short time, the SiO_2 core is completely consumed, ending up with liquid manganese silicate as the final phase. It should be noted that this modification process is quite fast, which is consistent with our understanding of high driving forces for mass transfer. In this calculation, it is assumed that the concentration of dissolved Si, and Mn is constant. However, due to the interplay of mixing and dissolution kinetics, there could be unequal deoxidation in different locations across the bath at the same instance. This might lead to non-equilibrium inclusions which subsequently modify to liquid manganese silicates. This is illustrated via Figure 3.9, which shows the change of driving force at the steel-inclusion interface with time. Here, the activity difference of species between the bulk steel and inclusion interface diminishes quickly with time, for a fixed number density of inclusions. As can be seen, the local equilibrium between steel and inclusion is established quickly ($\approx$ 7 sec), suggesting that diffusional growth of inclusions is not the rate determinant of deoxidation. In order to further investigate the rate controlling step for manganese silicate formation, a sensitivity analysis was conducted in which the diffusion coefficients of the species in the boundary and product layers were changed by one order of magnitude. In these calculations, a fixed inclusion number density of 10^{13} was considered based on previous literature values [27].

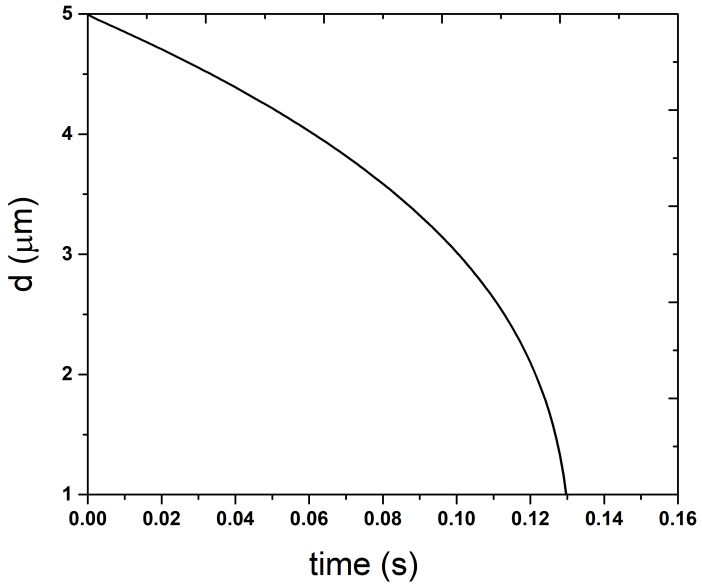

Figure 3.8: *Change of SiO_2 core diameter with time for [Mn] = 1.05 wt% , [Si] = 0.21 wt% , [O] = 100 ppm.*

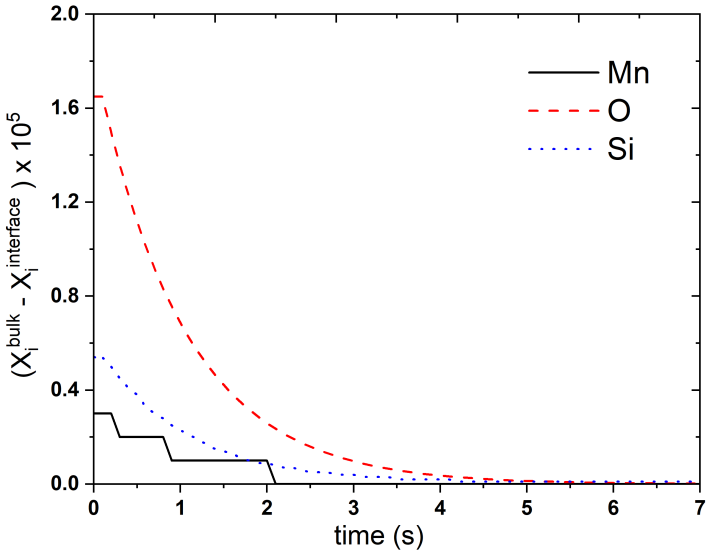

Figure 3.9: *Change of driving force at the steel-inclusion interface with time.*

Sensitivity analysis: Effect of diffusivities of MnO and SiO_2 in product layer

The effect of varying diffusivities in the liquid $MnO-SiO_2$ by one order of magnitude on the modification of silica to liquid manganese silicate is presented in Figure 3.10. As can be seen, increasing and decreasing the diffusivity by a factor of 10 does not show any notable impact on the transformation

time, indicating that the transformation process is independent of MnO and SiO_2 diffusivity in the product layer.

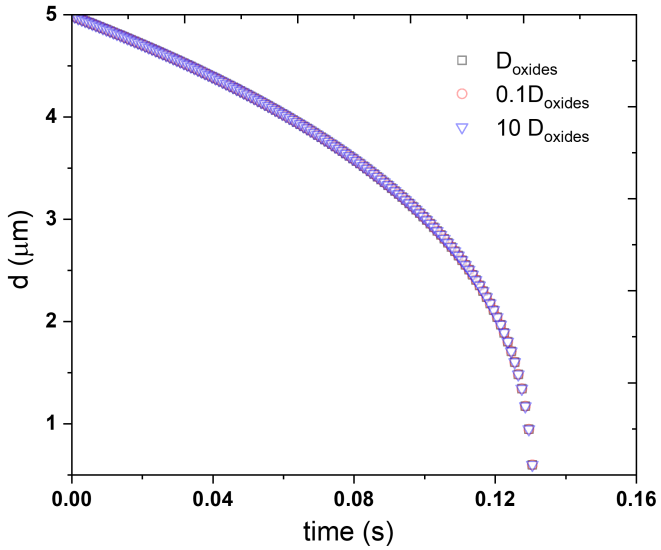

Figure 3.10: *Effect of changing diffusivities of MnO and SiO_2 on the transformation time of SiO_2 to $MnO-SiO_2$.*

Sensitivity analysis: Effect of diffusivities of solutes in boundary layer

Figure 3.11 shows the effect of changing the diffusivity of solutes in the melt by an order of magnitude. Decreasing the mass transfer coefficient from the melt increases the transformation time to 0.636 seconds, a 4.82-fold increase; conversely, increasing the mass transfer coefficient causes a decrease to 0.015 seconds, a 8.8-fold decrease. These changes indicate that mass transport to the inclusion surface might control the rate or in other words, control lies in the liquid boundary layer around the inclusion. In reality, the projected transformation periods are substantially shorter (< 1 s) than mixing time scales in the steel reactor (≈ 100 s), implying that the rate-determining step for the formation of liquid manganese silicates is most likely solute delivery to the melt. In this regard, adding a deoxidizer dissolution step and mixing kinetics to the model can give the time delay response for all inclusions to reach local equilibrium.

Sensitivity analysis: Effect of concentration of solutes in bulk steel

Figures 3.12, 3.13, and 3.14 depict the effects of Mn, Si and O content within the steel on the SiO_2 core to Mn-silicate transformation rate. It is seen that

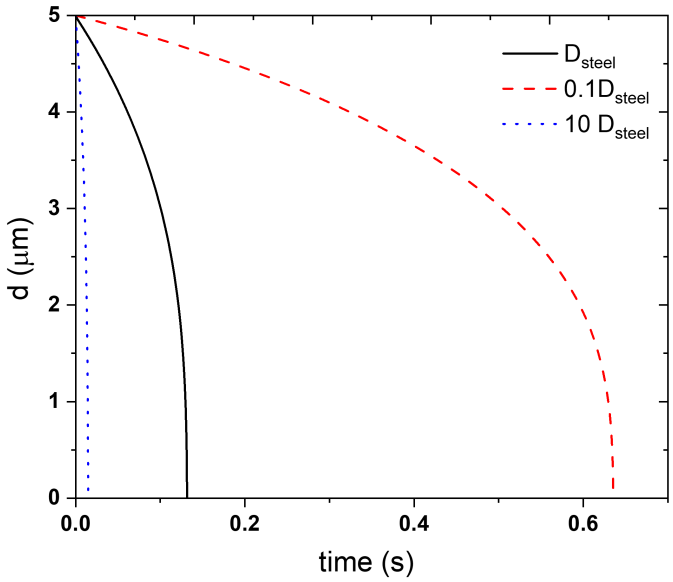

Figure 3.11: *Effect of changing diffusivities of solutes on the transformation time of SiO_2 to $MnO-SiO_2$.*

the rate of transformation increases by a factor of 7.6 upon increasing the Mn content from 0.6 to 1.0 wt%. On the other hand, increasing the dissolved silicon from 0.05 to 0.2 wt.% leads to an increase in the time of transformation by a factor of 2.8 (Figure 3.13). This shows that it is the Mn/Si ratio that is important in deciding the transformation rate rather than the individual Mn, and Si levels, indicating towards mixed rate control mechanics between Si and Mn. It is interesting to see that increasing oxygen content of the steel has negligible effect on the SiO_2 transformation rate (Figure 3.14). This is supported by the negligible oxygen fluxes between the inclusion and the steel during the duration of transformation. The change in inclusion composition may be considered as an exchange of Si and Mn between the metal and the inclusion, as Mn reacts with the existing SiO_2. More participation is expected to occur during the mass transfer growth process at the time of deoxidation when the oxygen flux to the inclusion is significant and is an important part of the process.

3.4 Discussion

3.4.1 Route 1: Nucleation model

The model results present interesting aspects of the nucleation process where the competition between SiO_2 and $MnO-SiO_2$ type inclusions is studied. The

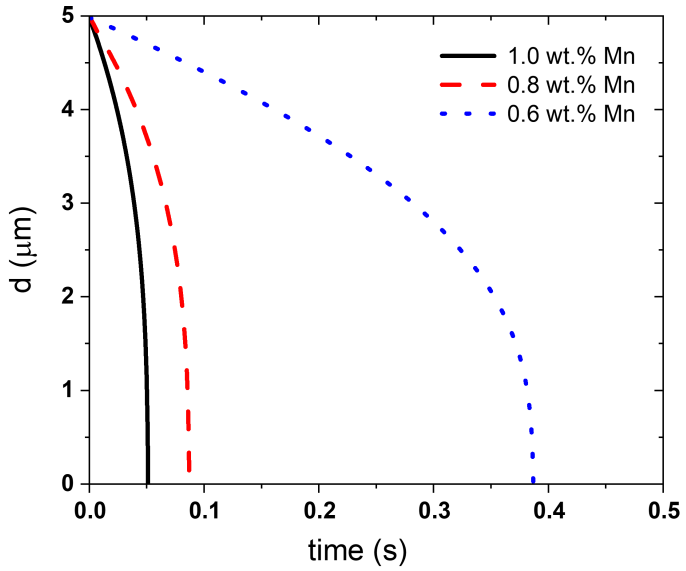

Figure 3.12: *Effect of [Mn] on transformation rate. [Si] = 0.1 wt.%, [O] = 100 ppm*

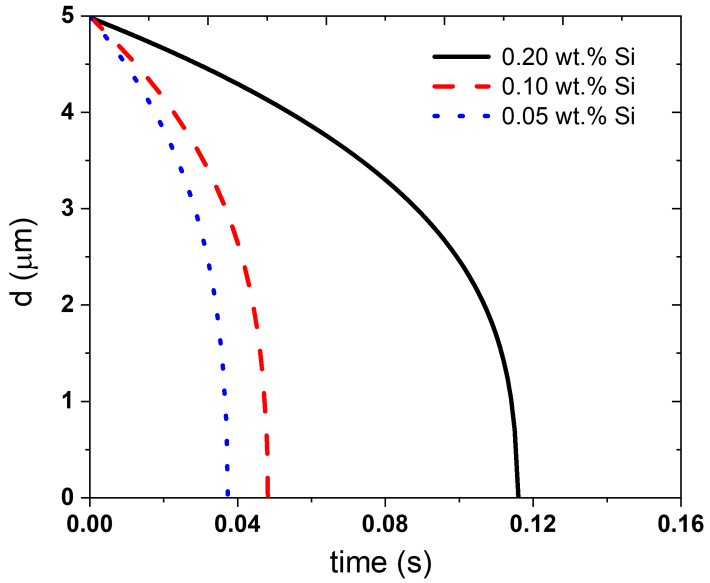

Figure 3.13: *Effect of [Si] on transformation rate. [Mn] = 1.0 wt.%, [O] = 100 ppm*

results show that the formation of complex oxide nuclei is highly possible and much more favorable than simple oxides in a multicomponent steel melt during the time of deoxidation. Such situations could arise when multiple deoxidizers are added at the same time. The study also establishes an expression for the calculation of ΔG_v, required to calculate the nucleation rates using

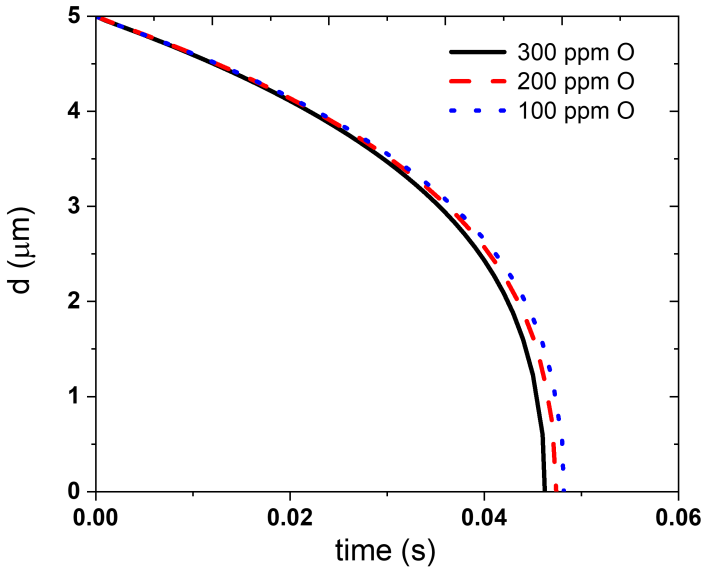

Figure 3.14: *Effect of [O] on transformation rate. [Si] = 0.1 wt.%, [Mn] = 1.0 wt.%*

Classical Nucleation Theory. The relations derived in this study should hold for the nucleation of complex oxides during deoxidation by Al. For example, such a model would be useful in modelling calcium aluminates in Al-killed steel where Ca-containing Fe-Si is added with Al during deoxidation.

From the expression for y_{min} in Eq. 3.2.13, the dependence on the initial composition (supersaturated state) of the steel and the thermodynamic properties of $MnO{-}SiO_2$ system (containing the effects of temperature) can be seen. This is of important consequence since it implies that different nuclei compositions of complex oxides are obtained in the melt with different steel compositions and temperatures. Both these scenarios are possible in actual steelmaking systems. The kinetics of dissolution of ferroalloys/deoxidizers can lead to concentration fields in the melt. Also, thermal stratification in the melt can lead to non-isothermal conditions. Interestingly, these results are also consistent with industrial findings where different Mn/Si ratios have been obtained in the inclusions. However, it needs to be noted that supersaturation must be attained to nucleate any oxide particle in the melt. The foregoing calculations allow the estimation of the critical composition of steel melt to nucleate a complex oxide particle. Supersaturation can be achieved in the melt by either additions of deoxidizers or high oxygen steel in a ladle or a combination thereof, both of which are effected by tapping additions during ladle filling.

Figure 3.15 shows the variation of nucleation rates with different oxygen levels

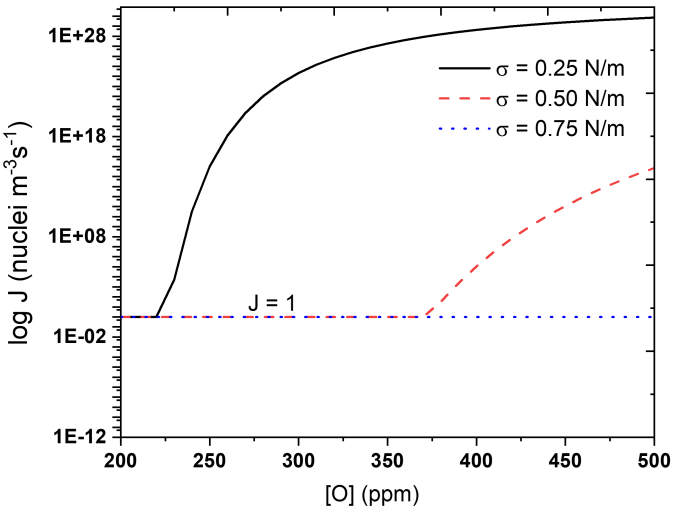

Figure 3.15: *Variation of nucleation rate with different oxygen levels considering different interfacial tension values between steel and inclusions.*

calculated with different interfacial tension values. From the nucleation rate calculations, it can be found that a high oxygen potential close to 225-375 ppm should create enough supersaturation to nucleate silica and manganese silicates during Si/Mn killed deoxidation of steels. Below this limit, homogeneous nucleation of these inclusions cannot occur, and the components in the steel melt will remain in the supersaturated state. A similar conclusion was obtained by Wasai and Mukai [32] while considering the nucleation process of alumina in liquid iron. However, it is important to point that in such a case, heterogeneous nucleation can predominate, provided there exists some oxide particles during the addition of deoxidizers. The effect of interfacial tension values on the nucleation characteristics is described further in Section 3.4.1.

Effect of excess free energy contribution

The calculation of ΔG_v without considering the activities of the components in the oxide mixture is expected to give an inaccurate estimation of the composition of the oxide nucleus in the steel melt. This approach has been commonly employed to study precipitation of carbides, nitrides, and carbonitrides in solid steels [33] where the ΔG^{XS} terms are not taken into account.

In order to understand the effect of ΔG^{XS} term, an analytical solution for Eq. 3.2.11 was obtained where the excess free energy term, ΔG^{XS} was neglected while calculating the composition of the oxide nucleus. Figure 3.16 shows the effect of ΔG^{XS} on ΔG_v and X_{MnO}. As can be seen, the effect of ΔG^{XS}

on ΔG_v (Figure 3.16a) is minimal up to a temperature of around 1800K. With increasing temperature above 1800 K, the deviation increases slightly as a result of neglecting the excess free energy term. The effect of ΔG^{XS} at temperatures above 1800 K on the MnO content is, however, significant, showing about a three-fold decrease in X_{MnO} as a result of neglecting the excess free energy term. This shows the importance of using the activities of the oxides in Eq. 3.2.16 which implicitly consider the contribution of ΔG^{XS} and the chemical characteristics of the oxide system.

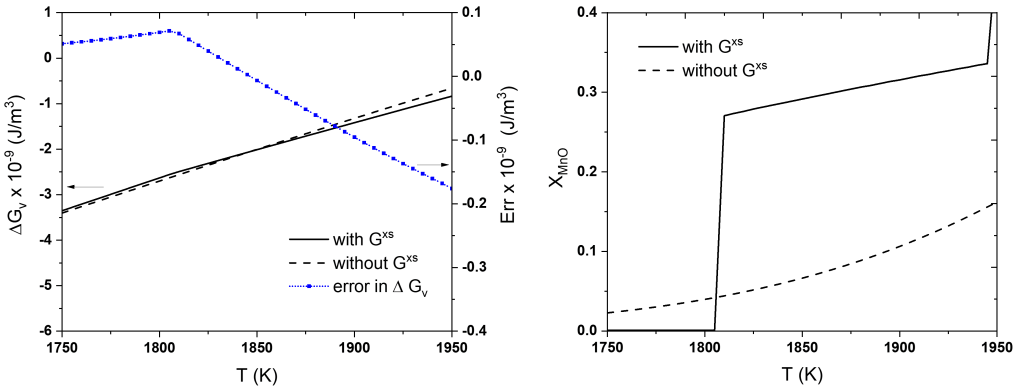

(a) (b)

Figure 3.16: *(a) Variation of ΔG_v and (b) X_{MnO} of the $MnO-SiO_2$ nuclei calculated with and without the contribution of G^{XS}.*

Effect of interfacial tension

In the aforementioned calculations, the values chosen for interfacial tension between the oxides and steel melt is assumed to be independent of temperature and melt composition. It can be agreed that interfacial tensions of different oxides in a steel melt are difficult to obtain as it is a complex function of the solutes in the steel. In order to model the effect of oxygen and sulphur on the surface tension of steel, previous researchers [23, 34] have used an expression of the form as:

$$\sigma = 0.50 + BT\ln(1 + K_S a_S + K_O a_O); \tag{3.4.1}$$

where B is a constant, T is the temperature (K), K_i are adsorption coefficients, a_i are solute activities.

The critical Gibbs free energy change for homogeneous nucleation can be

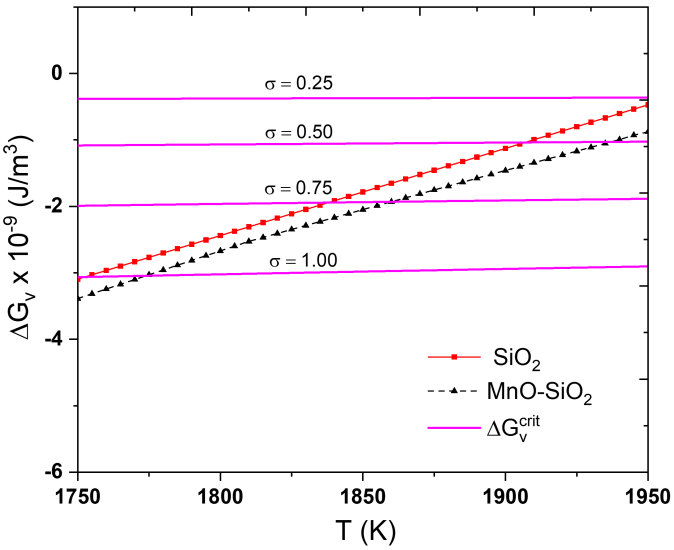

Figure 3.17: *Variation of ΔG_v of SiO_2 and $MnO-SiO_2$ phases with temperature superimposed on the variation of ΔG_v^{crit} calculated at different values of interfacial tension.*

calculated by setting $J = 1$ m^{-3}s^{-1} in Eq. 3.2.4, resulting in:

$$\Delta G_v^{crit} = -4.09\sqrt{\frac{\sigma^3}{k_B T \ln(A)}} \tag{3.4.2}$$

A strong dependence on the interfacial tension, σ can be noticed from the above expression. This can be further illustrated with Figure 3.17 where the effect of the interfacial tension on the oxide stability calculations is presented. It can be clearly observed that increasing interfacial tension values limit the nucleation process at higher temperatures since the ΔG_v^{crit} line lies above the ΔG_v lines of both SiO_2 and $MnO-SiO_2$ phases (calculated with $\sigma = 0.25$ N/m). Furthermore, it can also be shown that the choice of values influence the nucleation rates significantly.

Although the effect of a substrate in the nucleation process was not considered, the low value (0.25 N/m) used in this study can be justified in the case of heterogeneous nucleation. Moreover, it is difficult to agree whether the interfacial tensions of oxides measured on a large scale applies to a nano-scale event like nucleation. Such uncertainties prevail with the application of CNT to a real industrial process but certain approximations allow it to be valid and useful while estimating nucleation rates during deoxidation.

Effect of molar volume

In this study, the dependence of molar volume on the composition of the complex oxide nuclei has been neglected for the sake of simplicity. For certain cases, the molar volume of different complex oxides can exhibit a significant compositional dependence as shown in model studies carried out by Thibodeau et al. to correlate molar volume to oxide compositions [35]. To investigate the effect of molar volume on the foregoing calculations, a simple linear regression model has been fitted based on their study for the computation of molar volumes for different compositions in the $MnO-SiO_2$ system, which can be written as:

$$\Omega\,(\mathrm{cm}^3/\mathrm{mol}) = 11.9X_{\mathrm{SiO_2}} + 15.06 \tag{3.4.3}$$

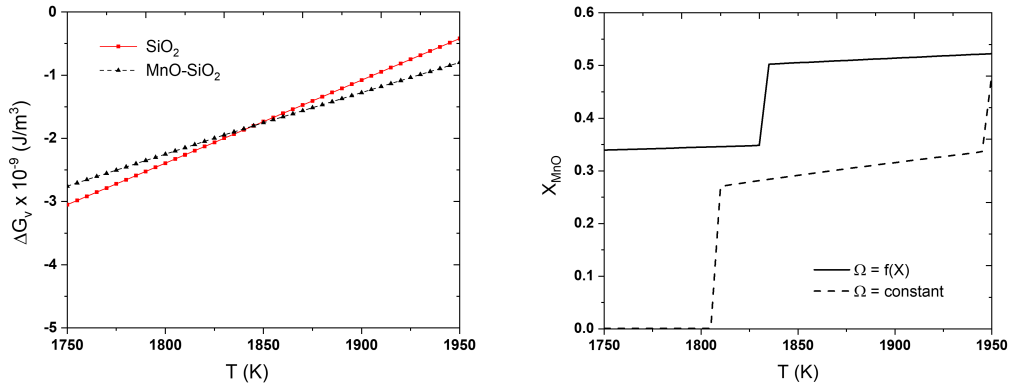

(a) (b)

Figure 3.18: *(a) Variation of ΔG_v, of SiO_2 and $MnO-SiO_2$ phases with temperature, considering molar volume (M.V) = f(X_{MnO}), and (b) variation of X_{MnO} with temperature showing the effect of molar volume dependence.*

Using the same values as in Section 3.3.2 and re-performing the minimization of Eq. 3.2.16, the variation of ΔG_v with different temperatures are calculated and shown in Figure 3.18a. Here, it can be seen that the stability order changes at 1845 K, below which a SiO_2 inclusion is more stable than a $MnO-SiO_2$ inclusion. This is in contrast with the results in Figure 3.5a, implying that the effect of molar volume on the oxide stability is significant. Also, the effect of the choice of molar volume function on X_{MnO} is shown in Figure 3.18b. Here, the composition of the nucleus mixture seems to be affected by the choice of molar volume values. At temperatures lower than 1823 K, MnO content close to 33 mol % can be found in the complex oxide nuclei, while selecting a fixed value of molar volume gives no MnO content at

those temperatures. Hence, this shows that the consideration of molar volume dependence on oxide composition is necessary for evaluating an accurate initial nuclei composition. However, the preceding calculations were chosen to be done using a fixed value of molar volume for the sake of simplicity.

3.4.2 Route 2: Mass transfer model

The results from the nucleation model showed that SiO_2 particles can nucleate in the melt, given that the supersaturations exist. In such situations, these inclusions quickly transform into Mn-silicate inclusions based on the kinetic model results presented in Section 3.3.3. This model seems to be more useful in predicting the modification of existing simple oxide particles, e.g. for reaction of inclusions with solutes reduced at the slag-steel interface or when deoxidizers are added at different intervals.

Kim et al. [37] conducted laboratory experiments where they studied the features of primary and secondary inclusions in Mn/Si and Mn/Si/Ti deoxidized steels in MgO crucibles. The final composition of the manganese silicate inclusions from the model calculations in this study were compared with some results from the Si/Mn deoxidation experiments which are presented in Figure 3.19. It can be seen that the calculated results are in good agreement with the observed compositions of the inclusions which are in equilibrium with the steel melt. This shows that the kinetic model converges to the thermodynamic equilibrium condition towards the end. Furthermore, this also points out the validity of the thermodynamic relationships used in this study.

The current kinetic model indicates that diffusion-controlled reactions in the inclusion are fast, as one would anticipate for a micron-sized particle at high temperature, taking only seconds to complete, especially since the elements involved in this reaction system (Fe-Mn-Si-O) are available in excess in the bulk steel. Previous researchers in the authors' laboratory [12, 14] came to the same conclusion while studying the formation of Mg-spinels, calcium aluminates in Al-killed steel. Although the transformation time is found to be small ($\sim$ 1 s) in all calculations, inclusions with partially transformed silica core can be encountered in some real situations [31]. The presence of such inclusions could be explained with the help of a non-homogeneous melt where the driving force for full transformation is not present. These situations could arise typically in crucible experiments where stirring is not present. The importance of mixing time is elucidated further by comparing the characteristic time scales of nucleation, mass transfer growth and mixing

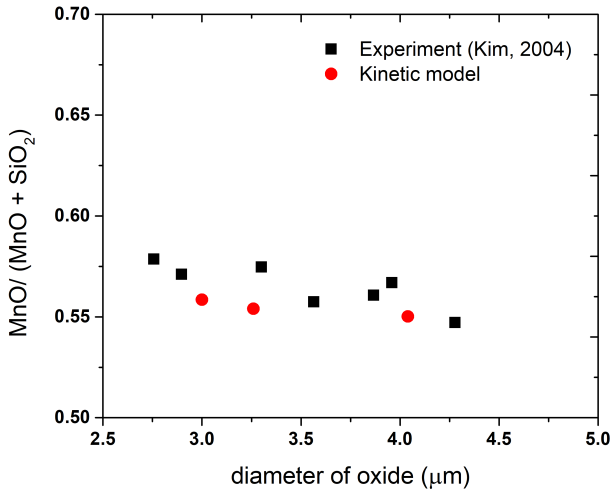

Figure 3.19: *Comparison of MnO content in the manganese silicate inclusions obtained through experiments and via the kinetic model as a function of inclusion size.*

as follows:

$$t_{nuc} = \frac{1}{4\pi r_c D_O N_{eq}} \tag{3.4.4}$$

$$t_{mass} = \frac{r^2}{D_O} \tag{3.4.5}$$

$$t_{mix} = 25.4 Q^{-0.33} L^{-1.0} R^{2.33} \tag{3.4.6}$$

where t_{nuc}, t_{mass}, and t_{mix} are the characteristic time scales for nucleation, mass transfer and mixing. In these equations, r_c is the critical nuclei size (= 0.5 nm), D_O is the diffusivity of oxygen in liquid steel(= 3.1×10^{-9} m^2/s), N_{eq} is the number of atoms of oxygen at equilibrium in the melt (here, 70 ppm O for Si-Mn deoxidation gives 1.845×10^{25} m^{-3}), r is the inclusion radius at local equilibrium with the melt (= 5 μm), Q is the gas flow rate (= 18.3×10^{-2} m^3/s), L and R are the bath depth (= 2.625 m) and radius (= 1.79 m) of the gas agitated vessel for which the mixing time is computed. The values obtained by substituting the values gives t_{nuc}, t_{mass}, and t_{mix} as 2.767×10^{-9} s, 8.064×10^{-3} s, 140.68 s. From these calculations, it can be concluded that mixing should strongly influence the overall rate of deoxidation and time to achieve global chemical equilibrium. The generation of numerous inclusions of the order of $10^{12} - 10^{14}\,\mathrm{m}^{-3}$ should allow oxygen levels to reach equilibrium values quickly. The mixing time influences the number of nuclei generated as shown by Sigworth and Elliot [36] and the rate of deoxidation.

Effect of diffusivities of solutes in the steel

Diffusion coefficients of the different solutes involved in this study, i.e., Si, Mn, O are of the order of $10^{-9}\, m^2/s$. It is difficult to measure their values to high precision and accuracy, for which molecular based models can be useful. In this regard, the Stokes-Einstein equation can yield reasonable approximate values. In Figure 3.20, it is shown how the transformation rates can change by varying the diffusion coefficients of the different species. As can be seen, the effect of diffusivities are important while considering mass transfer controlled growth but the time scale in which they affect transformation or formation rates is small ($<$ 1 s). Hence, the impact can be considered to be minimal on the overall determination of deoxidation rates owing to the high driving forces for mass transfer existing in the steel melt.

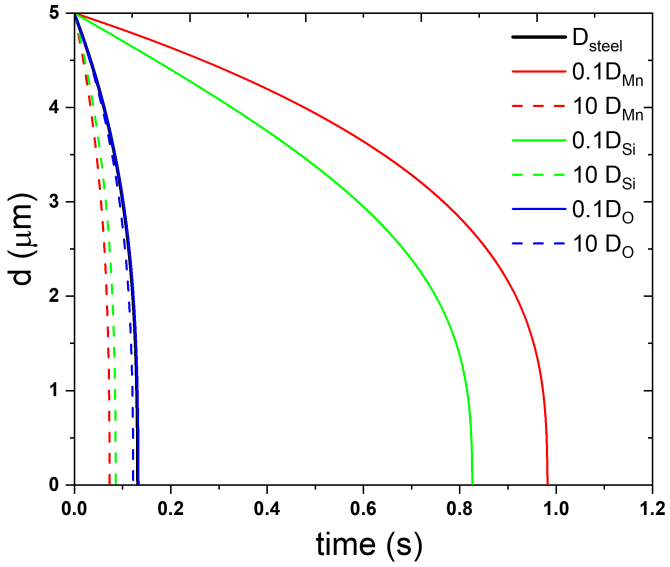

Figure 3.20: *Effect of change in diffusivities of Si, Mn, O in the steel on the transformation time of SiO_2 to $MnO-SiO_2$ inclusions.*

3.4.3 Practical implications

Previous modelling approaches that have taken into account fluid dynamics of the ladle have achieved better predictions of steel chemistry as summarised by Jonsson and Jonsson [38]. Owing to bath circulation, the driving force for nucleation and growth by mass transfer can be unequal, leading to the formation of inclusions with different chemistries in the steel melt. Such an effect cannot be accounted for in a local equilibrium based modelling approach where inclusions in equilibrium with the local steel bath are calculated. However, when nucleation rates are considered in a thermo-kinetic

model, these events can be reasonably modelled. The incorporation of nucleation kinetics along with the particle size distribution (PSD) to these models provides a greater picture to the overall inclusion landscape in the steel reactor. Most models [21, 22, 39, 40] of this type have focussed on simulating the dynamics of a simple oxide like alumina or titania. The incorporation of a sub model for the formation of complex oxides in liquid steel, such as the one developed in this study, with spatio-temporal mixing phenomena should allow a better prediction of the occurrence of different types of inclusions in the steel. However, there is a large computational overhead in capturing the compositional changes and population evolution of multiple inclusion types along with the fluid dynamics in a steel reactor. Rimbert et al. [41] have used innovative techniques like Quadrature Method of Moments (QMOM) to simplify population dynamics equations and achieved interesting results. In any case, the description of nucleation events and mixing seems to be necessary, which was illustrated in this study. The development and extension of the model developed in this work to a ternary or quaternary oxide system should also allow one to consider the effect of Al and Ca in Si/Mn killed steels. The current nucleation and growth model can be used by the steelmakers to model the formation of other unwanted complex oxide inclusions, supporting process improvements that reduce the occurrence of nozzle clogging incidents.

3.5 Conclusion

A mathematical model was developed for the steel-inclusion reactions during Si/Mn deoxidation of steel. Two modes of formation of complex oxides, i.e, manganese silicates, were considered. Firstly, a nucleation model was developed to compute the chemical free energy needed for formation of manganese silicates based on existing thermodynamic relationships. Secondly, a kinetic model for the transformation of SiO_2 to Mn-silicates was developed by considering multicomponent diffusion of Mn, Si, and O through the boundary layer and within the product layer constrained by thermodynamic equilibrium at the interfaces. From the results of these models, the following conclusions can be made:

1. Based on the nucleation calculations, the homogeneous nucleation of liquid manganese silicates can take place spontaneously in the liquid steel melt, along with the formation of SiO_2 when the necessary supersaturation ratios exist.
2. Based on the kinetic growth model results, any SiO_2 particle should quickly react with Mn and O, and form manganese silicates in a short

span of time.

3. The rate control for $MnO-SiO_2$ formation is determined by rate of supply of solutes to the bulk steel, indicating the importance of reagent dissolution kinetics in inclusion formation.
4. In the nucleation model, the effect of interfacial tension on the critical free energy change for nucleation and nucleation rate calculations is significant.
5. The molar volume dependence on oxide composition needs to be considered for accurately predicting the composition of oxides in the nuclei forming in the melt.
6. The effect of solute diffusivities on the transformation rates of SiO_2 was evident but not so critical compared to other rate-controlling steps since the reactions happen at a rapid rate.
7. The mixing time scale is important in predicting the number of nuclei forming as a result of homogeneous nucleation, as well as driving forces for mass transfer in the liquid steel melt.

References

[1] A. Ghosh: Secondary Steelmaking: *Principles and Applications*, 2001.

[2] R. Kiessling: *Non-Metallic Inclusions in Steel: Part III: The Origin and Behavior of Inclusions and Their Influence on the Properties of Steels, The Metals Society, London*, 1968.

[3] L. Zhang and Y. Ren: *AISTech - Iron Steel Technol. Conf. Proc.*, 2015, vol. 2, pp. 2250-9.

[4] P. Kaushik, J. Lehmann, and M. Nadif: *Metall. Mater. Trans. B Process Metall. Mater. Process. Sci.*, 2012, vol. 43, pp. 710-25.

[5] B.A. Webler and P.C. Pistorius: *Metall. Mater. Trans. B Process Metall. Mater. Process. Sci*, 2020.

[6] J.H. Park and L. Zhang: *Metall. Mater. Trans. B Process Metall. Mater. Process. Sci.*, 2020.

[7] M. L. Turpin and J. F. Elliott: *J. Iron Steel Inst.*, London, 1966, vol. 204, pp. 217-25.

[8] G. Forward and J. F. Elliott: *Met. Trans.*, 1970, vol. 1, pp. 2889-98.

[9] G.K. Sigworth and J.F. Elliott: *Metall. Trans.*, 1973, vol. 4, pp. 105-13.

[10] H. Fredriksson and O. Hammar: *Metall. Trans. B*, 1980, vol. 11, pp. 383-408.

[11] E. T. Turkdogan: *J. Iron Steel Inst.*, 1960, vol. 204, pp. 914-919.

[12] Y. Tabatabaei, K.S. Coley, G.A. Irons, and S. Sun: *Metall. Mater. Trans. B*, 2018, vol. 49B, pp. 375-87.

[13] G. Okuyama, K. Yamaguchi, S. Takeuchi, and K. Sorimachi: *ISIJ Int.*, 2000, vol. 40, pp. 121-28.

[14] A. Galindo, G.A. Irons, S. Sun, and K.S. Coley: *Proc. Challenges and Transformative Solutions to Sustainable Steelmaking and Casting for Environment-Friendly Metallurgical Innovation, Iron and Steel Institute of Japan, Tokyo*, 2015, pp. 22-31.

[15] O. Levenspiel: *Chemical Reaction Engineering*, 2nd ed., Wiley, New York, NY, 1999

[16] K.J. Graham and G.A. Irons: *Iron Steel Technol.*, 2009, vol. 6, pp. 164-73.

[17] I.H. Jung, S.A. Decterov, and A.D. Pelton: *ISIJ Int.*, 2004, vol. 44, pp. 527-36

[18] Y. Ren and L. Zhang: *Ironmak. Steelmak.*, 2018, vol. 45, pp. 585-91.
[19] S.P.T. Piva, D. Kumar, and P.C. Pistorius: *Metall. Mater. Trans. B*, 2017, vol. 48B, pp. 37-45.
[20] D. Kumar and P.C. Pistorius: *Metall. Mater. Trans. B*, 2019, vol. 50B, pp. 181-91.
[21] L. Zhang and W. Pluschkell: *Ironmak. Steelmak.*, 2003, vol. 30, pp. 106–10.
[22] J. Zhang and H.G. Lee: *ISIJ Int.*, 2004, vol. 44, pp. 1629–38.
[23] J. Lehmann, P. Rocabois, and H. Gaye: *J. Non. Cryst. Solids*, 2001, vol. 282, pp. 61-71.
[24] M. Hino and K. Ito: *Thermodynamic Data for Steelmaking, 1st ed.*, Tohoku University Press, Tokyo, 2010, pp. 16-17.
[25] C.W. Bale and A.D. Pelton: *Metall. Trans. A*, 1990, vol. 21, pp. 1997-2002.
[26] Z.X. Bing, J.G. Chang, and X.K. Di: *Calphad Comput. Coupling Phase Diagrams Thermochem.*, 1997, vol. 21, pp. 311-20.
[27] F. Oeters: *Metallurgy of Steelmaking*, 1st ed., Verlag Stahleisen, Dusseldorf, 1994, pp. 316-35.
[28] H. Gaye and J. Welfringer: *in Second Int. Symp. Metall. Slags Fluxes*, 1984, pp. 357-75.
[29] B.K.D.P. Rao and D.R. Gaskell: *Metall. Trans. B*, 1981, vol. 12B, pp. 311-17.
[30] C. Bernhard, P. Dorrer, S. Michelic, and R. Rössler: *BHM Berg- und Hüttenmännische Monatshefte*, 2019, vol. 164, pp. 475–8.
[31] K. Kirchheimer, R. Schnitzer, G. Klosch, J. Fasching, C. Bernhard, S. Michelic.: *AISTech 2020 Iron and Steel Tech. Conf. 2020*, pp. 1491-02.
[32] K. Wasai and K. Mukai: *Metall. Mater. Trans. B Process Metall. Mater. Process. Sci.*, 1999, vol. 30, pp. 1065-74.
[33] M. Perez, M. Dumont, and D. Acevedo-Reyes: *Acta Mater.*, 2008, vol. 56, pp. 2119-32.
[34] Y. Chung and A.W. Cramb: *Metall. Mater. Trans. B Process Metall. Mater. Process. Sci.*, 2000, vol. 31, pp. 957-71.
[35] E. Thibodeau, A.E. Gheribi, and I.H. Jung: *Metall. Mater. Trans. B Process Metall. Mater. Process. Sci.*, 2016, vol. 47, pp. 1147-64.
[36] G. K. Sigworth, and J. F. Elliott. : Can. Metall. Q., 1972, Vol 11, pp. 337-349.
[37] H.S. Kim, H.G. Lee, and K.S. Oh: *ISIJ Int.*, 2002, vol. 42, pp. 1404-11.
[38] P.G. Jonsson and L.T.I. Jonsson:*ISIJ Int.*, 2001, 41, vol. 41, pp. 1289-02.
[39] H. Lei, K. Nakajima, and J.C. He: *ISIJ Int.*, 2010, vol. 50, pp. 1735-45.
[40] Y.J. Kwon, J. Zhang, and H.G. Lee: *ISIJ Int.*, 2008, vol. 48, pp. 891-900.
[41] N. Rimbert, L. Claudotte, P. Gardin, and J. Lehmann: *Ind. Eng. Chem. Res.*, 2014, vol. 53, pp. 8630-39.

Chapter 4

Modeling study of steel–slag–inclusion reactions during the refining of Si–Mn killed steel

In Chapter 4, the model development consisting of average oxide inclusion composition tracking along with the analysis was entirely carried out by me. The data for validation was taken from Ref. [13]. Useful discussions on the results were provided by Dr. Kenneth S. Coley and Dr. André B. Philion.

The manuscript was initially drafted by me and edited to the final version by Dr. Kenneth S. Coley and Dr. André B. Philion. This work was presented in STEELSIM 2021, which was later selected to be published in Steel Research International, 2022, DOI: https://doi.org/10.1002/srin.202100831. The following Chapter is the pre-publication version of the article.

Modeling study of steel–slag–inclusion reactions during the refining of Si–Mn killed steel

Angshuman Podder[1], **Kenneth Coley**[1,2], **André Phillion**[1]

[1] *McMaster Steel Research Center*
Department of Materials Science and Engineering,
McMaster University, Hamilton, Ontario, Canada, ON L8S 4L7
[2] *Department of Mechanical and Materials Engineering,*
Western University, London, Ontario, Canada, ON N6A 3K7

Abstract

Complex deoxidation by Si and Mn is beneficial for certain steel long products since it leads to the formation of low temperature melting manganese silicates. However, the introduction of Al via steel-slag reactions can lead to unwanted inclusion formation which can cause nozzle clogging down the process line. To simulate steel-slag-inclusion reactions during refining of steel, a kinetic model based on the mass transfer of steel species has been developed for $MnO-SiO_2-Al_2O_3$ inclusions and integrated with a previously developed steel/slag coupled reaction model. Using the model, the rate determining step for inclusion transformation was clarified and the effect of slag-metal reactions on inclusions was investigated. The model calculations have been validated using experimental data reported in the literature. Subsequently, the influence of slag compositions on the chemistry of inclusions and the effect of mass transfer coefficient on deoxidation characteristics is examined through a parametric study. The results are helpful for understanding inclusion dynamics during ladle refining of Si-Mn killed steel.

4.1 Introduction

Non-metallic inclusions (NMIs) in steel can have deleterious effects on the final steel quality by affecting the mechanical strength, toughness, and processability [1]. In this regard, the understanding of the quantity, chemical composition, and morphology of NMIs is critical to improving the overall efficiency and performance of any steelmaking process. During deoxidation, oxide inclusions are generated from the reaction between added deoxidizers and dissolved oxygen in the steel, which are then removed mostly via stirring-induced mechanisms [2]. However, to prevent nozzle clogging, it is crucial to understand the nature of the residual micro-inclusions in the molten steel reactor.

Although aluminum is the most prevalent deoxidizer, in certain products like tire cord steel, spring steel, and strip steel, silicon and manganese are used instead in order to avoid the formation of harmful alumina inclusions. The addition of silicon and manganese results in the formation of highly

deformable manganese silicate inclusions which are favoured during casting and rolling of long products [3]. However, in Si/Mn killed steels, it has been found that an excess presence of aluminium in the steel can lead to alumina rich inclusions (that come from the added ferroalloys or steel-slag reactions). These inclusions are detrimental to steel castability since they have high melting points and poor deformation indices [4]. One of the major concerns of steelmakers is the reduction of alumina and related oxides within the slag since this results in an increase in the Al and O levels in the steel, which in turn causes the formation of undesirable inclusions [1]. Thus, a better knowledge of the governing steel-slag and steel-inclusion reactions is necessitated. Furthermore, it is beneficial for the steelmaking industry to have the capacity to predict the conditions facilitating the formation of harmful inclusions.

In Si-Mn killed steel, the typical non metallic inclusions encountered during ladle refining belong to the $MnO-SiO_2-Al_2O_3$ and $CaO-SiO_2-Al_2O_3$ system. Kang and Lee [5] studied the inclusion chemistry of Mn/Si deoxidized steel using both thermodynamic models and experimental methods. They showed that inclusions having (MnO/SiO_2 by mass) ratio near unity and Al_2O_3 in the range of 10-20 mass% give $MnSiO_3$ and $Mn_3Al_2Si_3O_{12}$ soft phases having low liquidus temperatures (1150-1200℃). Chen et al. [6] found that favorable inclusions could be achieved by controlling the Al_2O_3 content in top slag below 10 wt%. and the binary basicity of top slag (CaO/SiO_2 by mass) around 1.0. Park and Park [7] conducted equilibrium laboratory experiments between $CaO-Al_2O_3-SiO_2$-$CaF_2-MgO(-MnO)$ slag and Si-Mn killed steel melts and found that the (MnO/SiO_2 by moles) in the non metallic inclusions was almost equal to 0.8 with Al_2O_3 content increasing from about 10 to 40 mol % by changing the basicity of slag (CaO/SiO_2 ratio) from 0.7 to 2.1.

In the past two decades, the development of integrated kinetic models has allowed the prediction of inclusion composition changes over time under different conditions, as recently reviewed by Park and Zhang [8]. In these studies, steel-slag reaction kinetics have been modelled using mass transfer coefficients derived from plant trials, experimental studies or empirical relationships while steel-inclusion reaction kinetics have been assumed to be fast and modelled based on instantaneous local equilibrium with the steel [9, 10, 11]. Zhang et al. [12] developed a reaction model to investigate the transient evolution of inclusions during the ladle mixing process of Si-Mn killed steel, which was tested with varying sequences of ferroalloy addition and different concentrations of Si, Mn, and Al. However, the simulated inclusion compositions were not validated and the effect of slag was not included

in their study. Recently, Piva et al. [13] extended the Effective Equilibrium Reaction Zone model (EERZ) [14] methodology to develop a kinetic model for Si-Mn killed steels where the effect of slag on inclusion compositions was studied. In both these studies, inclusions are considered to be in equilibrium with the local steel melt.

Over the past fifteen years, researchers at McMaster University [15, 16, 17] have developed a kinetic process model for Al-killed steels that combines a calcium dissolution model with a shrinking core model for inclusion transformation ($CaO-MgO-Al_2O_3$), that is coupled with a slag-steel reaction model. The model can track the changes in steel and slag compositions, and evolution of inclusions under conditions matching those in industry. The results have been validated with heat data from a single North American steel plant and, so far, have shown good agreement. In the present study, this modelling approach is extended further to model predominant inclusions in Si/Mn killed steel. Specifically, a kinetic model is proposed that predicts the occurrence of microinclusions belonging to $MnO-SiO_2$ and $MnO-SiO_2-Al_2O_3$ systems. Subsequently, the inclusion kinetic model is integrated with the previously developed steel-slag coupled reaction model to predict the compositional change of inclusions after slag addition.

The proposed modelling approach is differentiated from previous approaches, such as the EERZ method, by including explicit descriptions of kinetic equations for the steel-inclusion reactions considering number density and inclusion size. To validate the approach, the calculated results are compared against experimental data reported in the literature [13]. Finally, the effect of slag composition on variations in inclusion composition is investigated and the effect of mass transfer coefficient on deoxidation characteristics is examined in order to put the model's results in the context of actual industrial conditions.

4.2 Mathematical model

The overall model consists of separate kinetic models considering different steel-inclusion, and steel-slag reactions while the influence of other variables including refractory interaction and air reoxidation is not included. At each time step, the compositions of metal, slag and inclusions are updated via a mass balance. This enables one to track the compositional variables in the multicomponent, multiphase system. A schematic of the relevant interactions can be seen in Figure 4.1.

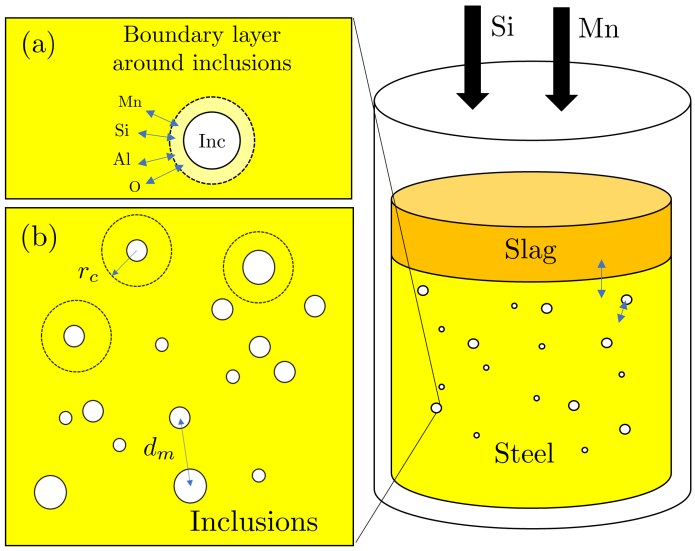

Figure 4.1: *Schematic of steel-slag-inclusion reactions showing (a) an enlarged view of the solutes diffusing through a boundary layer of an inclusion (b) catchment volume of inclusions.*

4.2.1 Steel-inclusion model

The steel-inclusion model considers a uniform distribution of SiO_2 inclusions with a high separation distance, d_m (Figure 4.1), ensuring the solute diffusion zones do not overlap between different inclusions. Diffusion of species (Mn, Si, O) to the inclusion interface leads to the transformation of these inclusions to $MnO{-}SiO_2$ until equilibrium between the steel and inclusions is established. A shrinking core model based on the model of Ca-aluminates by Tabatabaei et al. [15] was formulated to describe the evolution of Mn-silicates ($MnO{-}SiO_2$) in the steel melt by considering local equilibrium conditions that exist at the steel/inclusion interface. To study the Rate Determining Steps (RDS) for inclusion transformation, both diffusion in the boundary and product layers is investigated. The model was then extended to the $MnO{-}SiO_2{-}Al_2O_3$ system, which is commonly encountered in deoxidation inclusions in Si-Mn killed steel. The main assumptions of the model were:

1. SiO_2 inclusions form instantaneously and are present at $t = 0$. Additionally, a small layer of Mn-silicate exists at the surface of the SiO_2 inclusion. This layer can be considered to have a negligible impact on the mass balance.
2. The inclusions have spherical geometry.
3. There is no change in average inclusion number density within the melt.
4. Chemical reactions are not rate controlling.

5. The bulk steel is well mixed at all times.

Equilibrium equations

The reaction equilibrium between element, M, and dissolved oxygen, O, at the steel/inclusion interface can be described by:

$$\mathrm{x[M] + y[O] = (M_xO_y)_{inc}} \tag{4.2.1}$$

$$X_{\mathrm{M}}^{*x} = \frac{a^*_{\mathrm{M_xO_y}}}{e_{\mathrm{M}} X_{\mathrm{O}}^{*y}} \tag{4.2.2}$$

$$e_{\mathrm{M}} = \frac{K_{\mathrm{M_xO_y}} \left(f_{\mathrm{M}} \cdot MW_{\mathrm{M}}\right)^x \cdot \left(f_{\mathrm{O}} \cdot MW_{\mathrm{O}}\right)^y \cdot 100^{x+y}}{MW_{\mathrm{Fe}}^{x+y}} \tag{4.2.3}$$

where $K_{\mathrm{M_xO_y}}$ are the equilibrium constants for the respective deoxidation reactions evaluated at 1873 K shown in Table 4.2.1, X_i^* is the mole fraction of species i at the interface, a_i are the activities of the ith oxides in $\mathrm{MnO{-}SiO_2{-}Al_2O_3}$ system which are calculated at the interface by the Sub Regular Solution Model (SRSM) [18], MW_i is the molar mass of species i, and f_i represents the Henrian activity coefficient of ith species with respect to 1 wt. % standard state, calculated using Unified Interaction Parameter Formalism [19].

Table 4.2.1: *Equilibrium constants for different steel-inclusion reactions*

Reaction	log Keq	Ref.
2[Al] +3[O] = Al_2O_3 (s)	64000/T - 20.57	[17]
[Si] + 2[O] = SiO_2 (s)	30110/T - 11.40	[17]
[Mn] + [O] = MnO (s)	14880/T - 6.67	[17]

Mass transfer equations

The mass transfer rate, $\mathrm{N_i}$ (mol/s) of species i through the boundary layer from the bulk steel to the surface of a spherical particle, is given by:

$$\mathrm{N}_i = 4\pi r^2 k_{m,i} C_{v,m} \left(X_i^b - X_i^*\right) \tag{4.2.4}$$

where $k_{m,i}$ (m/s) is the mass transfer coefficient of species i across the boundary layer in the melt, $C_{v,b}$ (mol/m^3) is the molar density in the bulk steel phase, r is the particle radius, X_i^b is the molar fraction of the species i in the bulk of the fluid phase, and X_i^* is the molar fraction of the species i at the interface of the particle and boundary layer. Using the Sherwood number, Sh, the diameter of the particle, d and, diffusivity D_i , the mass transfer

coefficient between the steel and inclusion, $k_{m,i}$ can be defined as:

$$k_{m,i} = \frac{D_i \cdot Sh}{d} \tag{4.2.5}$$

A Sherwood number of 2 is adopted in the current study since the size of the inclusions is less than 14 μm [20]. Mass transfer through the liquid manganese silicate layer within the silica inclusion is treated on a phenomenological basis as, quasi-steady-state, counter molecular diffusion of MnO and SiO_2. The mass transfer rates of MnO and SiO_2 are driven by the concentration gradient existing across the product layer, which can be described by:

$$N_i = \left(\frac{4\pi r_{ex} r_{in}}{r_{ex} - r_{in}}\right) \cdot (C_v D_i) \cdot \left(X_i^{ex} - X_i^{in}\right) \tag{4.2.6}$$

where r_{ex}, r_{in} are exterior and interior radius of the product layer, respectively, $C_{v,l}$ is the molar density of the liquid layer, and X_i^{ex}, and X_i^{in} are the mole fractions of species i at exterior and interior radius, respectively. The flux balance between the diffusing species within the boundary layer of the inclusion results in an additional set of equations:

$$N_{\mathrm{M}} = x N_{\mathrm{M_xO_y}}, \text{and} \tag{4.2.7}$$

$$N_{\mathrm{O}} = \sum y N_{\mathrm{M_xO_y}}. \tag{4.2.8}$$

Following this, the change of concentration in the bulk steel and inclusions due to steel-inclusion reaction is calculated via:

$$\frac{dn_i^{inc}}{dt} = \pi d^2 k_{m,i}^{st} C_{v,m} \cdot \left(X_i^b - X_i^*\right), \tag{4.2.9}$$

$$X_i^{inc} = n_i^{\mathrm{inc}} \,/\, \sum n_i^{\mathrm{inc}}\,, \tag{4.2.10}$$

$$\frac{dX_i^{st}}{dt} = -\frac{\pi d^2 k_{m,i}^{st}}{V_c} \cdot \left(X_i^b - X_i^*\right), and \tag{4.2.11}$$

$$V_c = \frac{4}{3}\pi r_C^3 \text{ where } r_C = \left(\frac{3}{4\pi Z}\right)^{1/3} \tag{4.2.12}$$

where r_c is the catchment radius (Refer Figure 4.1) and Z is the average number density of the inclusions.

4.2.2 Steel-slag model

In the present work, the multicomponent kinetic model of Graham and Irons described in greater detail in Reference [17] was used to calculate the effect

of steel?slag reactions on the inclusion compositions. The model is based on the mixed coupled reaction model proposed by Robertson et al. [21] which have been successfully used to describe dephosphorization and desulphurisation of hot metal. The main governing equations, used in conjunction with Equations 4.2.2 and 4.2.3, are:

$$k^{st}_{m,i}C^{st}_{v}\left(X^{b}_{i}-X^{*}_{i}\right)=xk^{sl}_{m,M_xO_y}C^{sl}_{v}\left(X^{*}_{\mathrm{M_xO_y}}-X^{b}_{\mathrm{M_xO_y}}\right) \tag{4.2.13}$$

$$k^{st}_{m,\mathrm{O}}C^{st}_{v}\left(X^{b}_{O}-X^{*}_{O}\right)=\sum yk^{sl}_{m,\mathrm{M_xO_y}}C^{sl}_{v}\left(X^{*}_{\mathrm{M_xO_y}}-X^{b}_{\mathrm{M_xO_y}}\right) \tag{4.2.14}$$

All the equations are rearranged to compute the X^{*}_{O} at the slag/metal interface, after which the change of concentration in the bulk steel and slag due to steel?slag reaction can be calculated via:

$$\frac{dX^{b}_{i}}{dt}=\frac{k^{st}_{m,i}A_{st/sl}}{V_{st}}\cdot\left(X^{b}_{i}-X^{*}_{i}\right) \tag{4.2.15}$$

$$\frac{dX^{sl}_{i}}{dt}=\frac{k^{sl}_{m,i}A_{st/sl}}{V_{sl}}\cdot\left(X^{b}_{\mathrm{M_xO_y}}-X^{*}_{\mathrm{M_xO_y}}\right) \tag{4.2.16}$$

4.2.3 Numerical implementation

The system of the differential equations (Equations 4.2.9, 4.2.11, 4.2.15, 4.2.16) was converted into a set of non-linear equations, which were then solved using the Newton-Raphson method in MATLAB 2020b. A time step of 0.005 s was used for the steel-inclusion reactions, while the steel-slag reactions were considered in every 0.1 min, owing to their slow rates.

4.3 Results and Discussions

A sequential approach was carried out in order to validate the current model. First, the activities of the oxide species calculated with SRSM are compared with those existing in literature [22, 23]. Second, the rate determining steps for steel-inclusion reactions were analyzed with the help of sensitivity analyses as described in Section 4.3.2. Finally, the results of the combined steel-slag-inclusion model are presented in Section 4.3.3, were compared with experimental data of Piva et al. [13]. The model parameters and initial conditions used in this comparison, taken from Reference [13], are listed in Tables 4.3.1, 4.3.2, 4.3.3.

Having validated the model calculations, the effect of steel-slag reactions are further studied to understand its effect on inclusion compositions and

Table 4.3.1: *Model initizialization parameters*

Parameter	**Units**	**Value**
Steel Mass	kg	0.650
Slag Mass	kg	0.185
Crucible diameter	m	0.058
Effective reaction area	m^2	3.32 x 10^{-3}
$k_m^{st}A$	m^3/s	2.65 x 10^{-8}
k_m^{sl}/k_m^{st}	-	0.1
Inclusion number density	$/m^3$	10^{10}
Initial inclusion diameter	μm	5
Initial inclusion mass	kg	6.39 x 10^{-5}

dissolved oxygen changes in Si-Mn killed steel. The role of the mass transfer coefficients at the steel/slag interface have also been discussed in Section 4.3.6. Finally, some limitations of the current model are pointed out.

Table 4.3.2: *Base steel composition*

Case	C	Mn	Si	Al	O	S	Fe
ST1	0.2	1.05	0.2	0.001	0.01	-	Balance

Table 4.3.3: *Slag compositions*

Case	CaO	MgO	SiO_2	Al_2O_3
SL1	47	10	35	8
SL2	47	10	8	35

4.3.1 Oxide activity calculation

The endogenous oxide inclusions encountered within the modelled system as a result of deoxidation belong to the $CaO-MnO-SiO_2-Al_2O_3$ system. The oxide activities in this system can be represented by the sub regular solution model [18], using :

$$a_{M_xO_y} = X_{M_xO_y} \exp\left(\frac{G^{ex}_{M_xO_y} - G^{\circ}_{M_xO_y}}{RT}\right) \tag{4.3.1}$$

where $X_{M_xO_y}$ is the mole fraction of an oxide M_xO_y in the oxide system, $G^{ex}_{M_xO_y}$ is the excess partial molar free energy of the oxide in reference to the pure liquid state, $G^{o}_{M_xO_y}$ is the molar free energy associated with the oxide?s transformation from liquid to solid, and $G^{ex}_{M_xO_y}$ is expressed with a set of formulae in a multi-component system (M_xO_y = 1 to 4) in which 1 to 4

denote four oxide compounds in a quaternary oxide system. The activities calculated using a computerized version of this model in the $MnO-SiO_2$ and $MnO-SiO_2-Al_2O_3$ systems are shown in Figures 4.2a and 4.2b, respectively. As can be seen, an excellent match is achieved between the calculated values and those of the literature [22, 23].

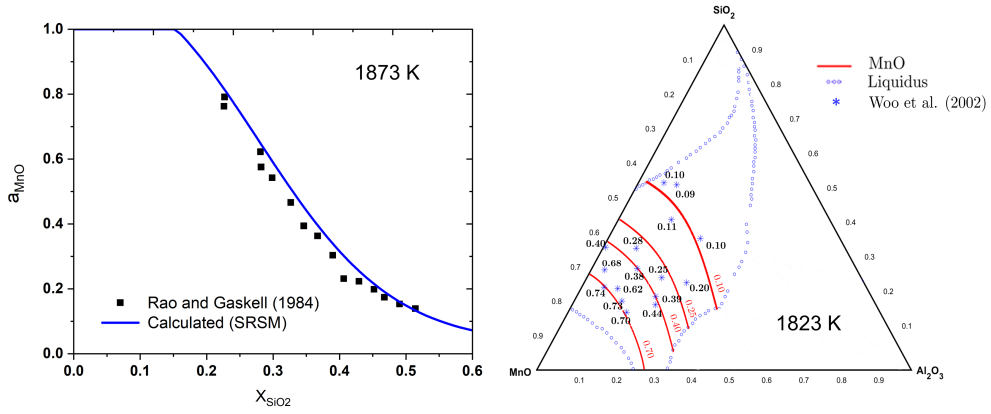

(a) (b)

Figure 4.2: *Comparison of (a) calculated activities of MnO in $MnO-SiO_2$ system at 1873 K ; (b) calculated iso-activities of MnO in $MnO-SiO_2-Al_2O_3$ system by sub-regular solution model (SRSM) at 1823 K with literature data [22, 23].*

4.3.2 Sensitivity Analysis and the Rate Determining Step

Figure 4.3 shows the results of a sensitivity analysis, in which the diffusion coefficients of the species in the boundary and product layers were changed by an order of magnitude to see the influence on transformation rates of SiO_2 to $MnO-SiO_2$. As can be seen, it is evident that the rate of manganese silicate formation is controlled by the mass transport of solutes (Mn, Si, O). Moreover, the transformation is complete within 1 s owing to the availability of Si and Mn in bulk steel, which as shown in Figure 4.3c, exerts a high driving force. From Figure 4.3a and 4.3b, it can also be seen that the rate controlling step is not likely mass transport through the product layer in this case but rather diffusion of solutes in the boundary layer. Figure 4.4 shows how the activity difference between species in the bulk steel and at the inclusion interface diminishes with time for a fixed number density of inclusions. It can be seen that a local equilibrium between steel and inclusion is established quickly ($\approx$ 5 s), suggesting that diffusional growth of inclusions is not rate determining for deoxidation since the acting time is much less. These findings allow the kinetic model to be simplified to only

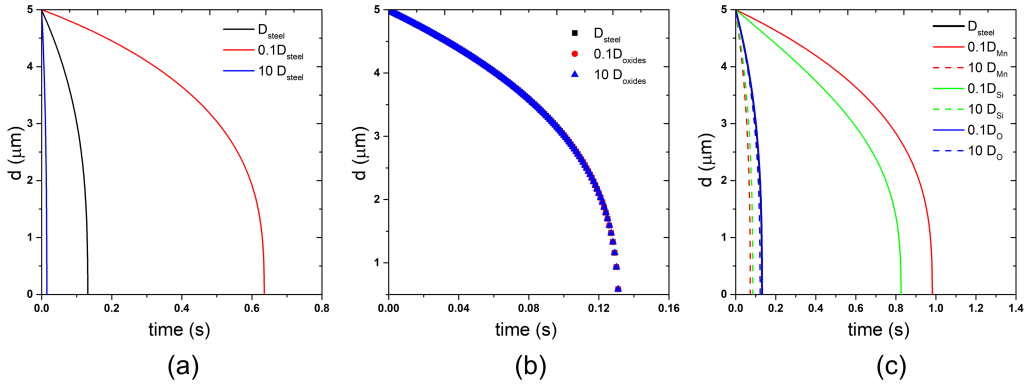

Figure 4.3: *Sensitivity analysis: Effect of (a) diffusivities of bulk steel species, (b) diffusivities of oxides in product layer (c) diffusivities of Si, Mn, O on rate of SiO_2 transformation.*

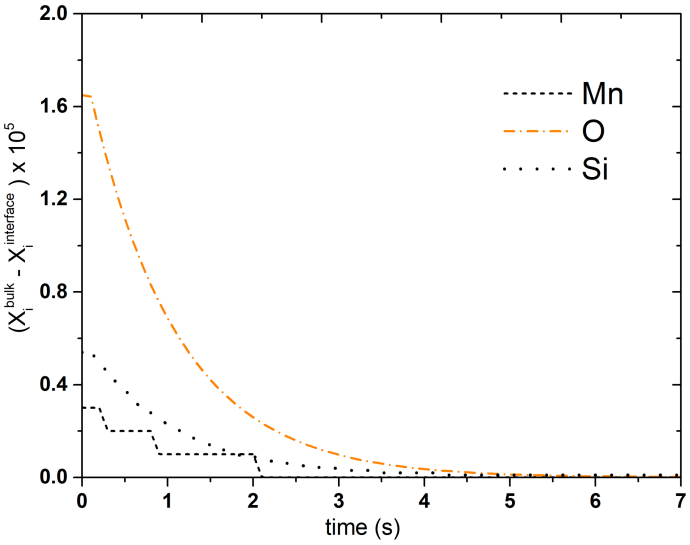

Figure 4.4: *Variation of bulk steel concentration difference at the steel-inclusion interface with time.*

consider mass transfer between steel and a homogeneous inclusion belonging to the $MnO-SiO_2-Al_2O_3$ system.

4.3.3 Comparison with literature data

Figure 4.5 compares the predicted variation of inclusion composition with time after the addition of slag, with experimental data reported by Piva et al. [13] along with their model predictions. The steel and slag compositions used for the simulations correspond to that of ST1, and SL2 (Refer to Table 4.3.2 and 4.3.3). As can be seen, both models predict reasonably well

the trends in average inclusion composition changes. The prediction of the MnO content in the inclusions seem to be better than SiO_2 content in their model versus the current model calculations, whereas the results of Al_2O_3 are comparable. The deviation of the model could be explained by compositional changes taking place during solidification. Due to the high residual oxygen, inclusion may form by reaction between the rejected solutes and oxygen. Consequently, 'secondary' manganese silicates can form along with SiO_2 precipitating internally owing to the low saturation limit. This can partly explain the higher SiO_2 in the inclusions in the reported experimental data. Please note that the greater agreement in predicting the alumina component within the inclusions is a result of the fact that the mass transfer coefficient employed in this work for all the components at the steel/slag interface were taken from the reference who based these values on the Al pickup rate. Additionally, the discrepancy around 1000s could be explained from the fact that the effect of reoxidation is excluded in the current model, which considers only the compositional changes of the $MnO-SiO_2-Al_2O_3$ inclusions occurring after deoxidation.

4.3.4 Study of Al pickup rate

The rate of change of Si/SiO_2, Al/Al_2O_3 in steel, slag phases is shown in Figure 4.6, where the Al pickup can be explained by the reduction of Al_2O_3 by Si. While using a high alumina slag for steel refining, a redistribution of silica and alumina can be observed between the inclusions and the slag (Refer to Figure 4.5c and 4.6b). If the alumina activity in the slag is sufficiently high and the silica activity sufficiently low, the silicon activity in the steel may be high enough to reduce the alumina via a reaction similar to Equation 4.3.2. The aluminum activity in the steel may then be high enough for Reaction 4.3.3 to proceed replacing silica in the inclusion with alumina. The overall reaction between the respective species is shown in Reaction 4.3.4.

$$3[Si] + 2\,(Al_2O_3)_{slag} = 4[Al] + 3\,(SiO_2)_{slag} \tag{4.3.2}$$

$$4[Al] + 3\,(SiO_2)_{inc} = 3[Si] + 2\,(Al_2O_3)_{inc} \tag{4.3.3}$$

$$(Al_2O_3)_{slag} + 1.5\,(SiO_2)_{inc} = 1.5\,(SiO_2)_{slag} + (Al_2O_3)_{inc} \tag{4.3.4}$$

The driving force for Al reduction at the steel-slag interface can be described quantitatively by Equation 4.3.5, and from Figure 4.7, it is shown that the driving force goes down with time as the overall reaction approaches equilibrium.

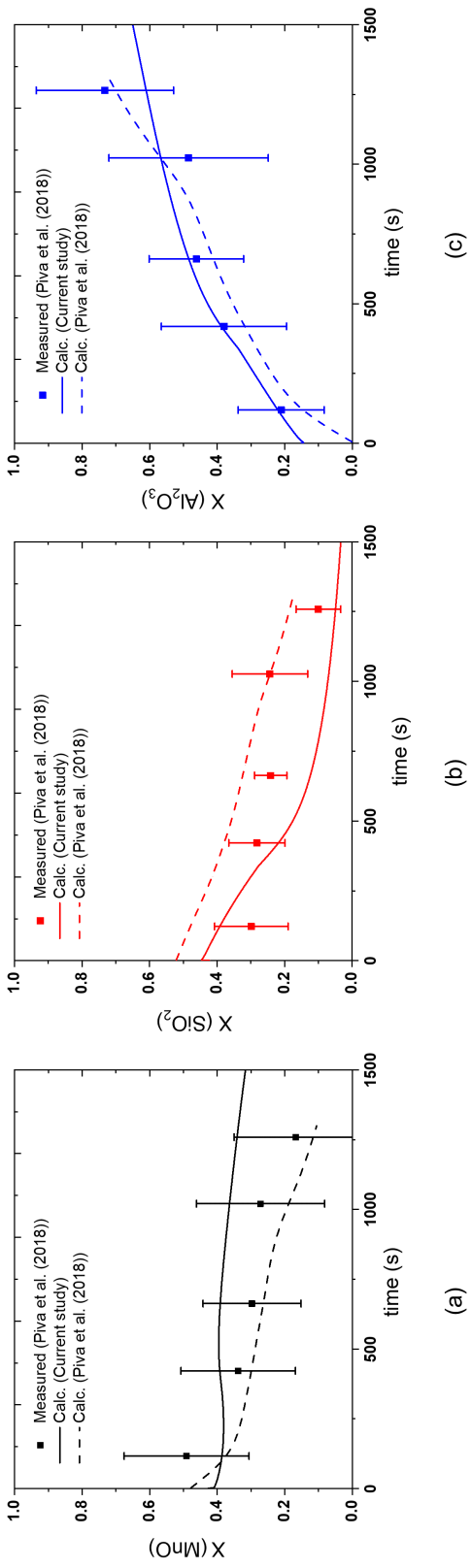

Figure 4.5: *Comparison of the transient changes in average inclusion composition after slag addition: (a) SiO_2, (b) MnO, and (c) Al_2O_3 with reported literature data [13] for slag S1.*

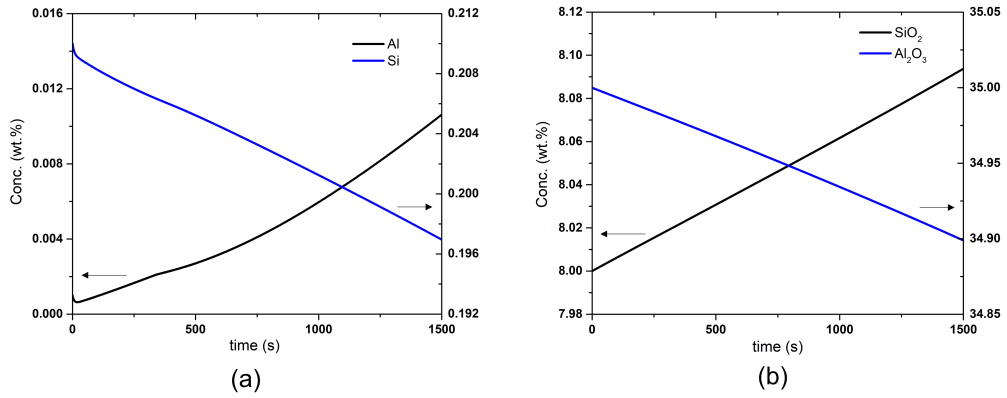

Figure 4.6: *(a). Variation of Al, Si in steel (wt.%); (b) Variation of SiO_2, Al_2O_3 in slag with time (wt.%).*

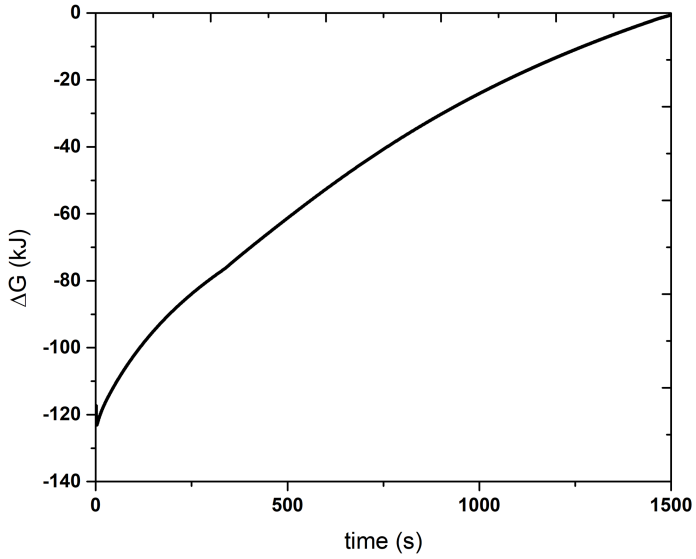

Figure 4.7: *Variation of driving force for alumina (Al_2O_3) reduction at the steel-slag interface with time.*

$$\Delta G = \Delta G^0 + RT \ln Q \quad \text{where, } \Delta G^0 = 0, \text{ and } Q = \frac{a_{Al_2O_3,\ inc} \cdot a^{1.5}_{SiO_2,\ slag}}{a_{Al_2O_3,\ slag} \cdot a^{1.5}_{SiO_2,\ inc}} \tag{4.3.5}$$

4.3.5 Effect of slag compositions

Having established the model, the effect of different slag compositions is studied with both silica-rich and alumina-rich slags as tabulated in Table 4.3.3. As can be seen in Figure 4.8a, there is a noticeable change in the way in which the inclusion composition changes based on the type of slag with little alumina pickup in the inclusions for a silica rich slag, and much more with an alumina rich slag. This can be attributed to less silicon-aluminum exchange because a lower activity difference between oxygen at the interface and oxygen in the bulk steel leads to less reduction of oxides from the slag. Furthermore, this observation is in line with previous studies where alumina in the slag was recommended to be maintained around 10-15 wt.% [5, 6] for avoiding harmful solid alumina inclusions. In such cases, some industries have resorted to Ca treatment to modify these inclusions, when the alumina in the inclusions was more than 20 wt.% [24]. This indicates the use of silica rich slags as top ladle slag in processing for Si-Mn killed steels [7] to obtain the desirable spessartite ($Mn_3Al_2Si_3O_{12}$) type inclusions. Figure 4.8b shows

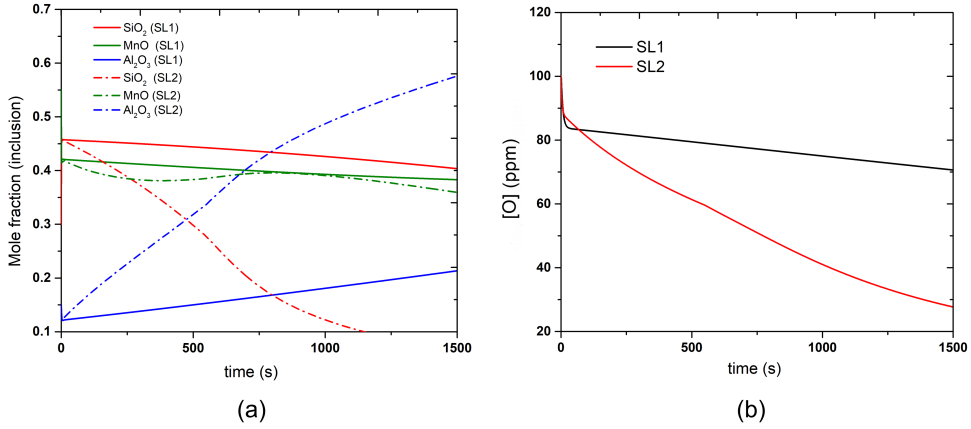

Figure 4.8: *(a) Variation of inclusion mole fraction; (b) dissolved oxygen in steel with time for different slag compositions (SL1 and SL2).*

the variation of dissolved oxygen in the steel where an alumina-rich slag produces less dissolved oxygen in the steel in comparison to a silica-rich slag.

The precipitation deoxidation reaction between oxygen and Al in the steel reduces the oxygen to low levels because the Al in equilibrium with Al_2O_3 at activity of one offers a much lower oxygen potential than Si in equilibrium with SiO_2 at activity of one. Although the total oxygen in steel is expected to be around 75 ppm for both slag types (SL1 and SL2) considering a crucible-based steel mass transfer coefficient, it is interesting to find that with SL2, the oxygen is 'trapped' in inclusions as excess alumina. However, this is not desirable practically since it would reduce the deformability index of the inclusions [4]. Alternatively, by Equation 4.3.6, one can show that a lower activity of SiO_2 in the slag can produce less oxygen in the steel.

$$a_o = \sqrt{\frac{a_{\mathrm{SiO_2,\ slag}}}{a_{\mathrm{Si}} \cdot K_{eq,\mathrm{SiO_2}}}} \tag{4.3.6}$$

Overall, these results show that with silica rich slags it is possible to obtain less oxygen in the steel by keeping CaO/Al_2O_3 ratio high, which ensures a low silica activity and low alumina. This is crucial since the 'diffusion deoxidation' or 'slag-aided deoxidation' mechanism is important for obtaining low oxygen levels in Si/Mn killed steels because the inherent deoxidation capability of Si/Mn is not so high [1]. Moreover, introducing long stirring times, which increases the mass transfer across the steel-slag interface, allows faster equilibration of steel with the slag. It is worth mentioning that in such as case, the inclusion type can change to being close to that of the slag composition, i.e., calcium silicates, provided sufficient equilibration time is provided.

4.3.6 Effect of steel mass transfer coefficient

Figure 4.9 shows the effect of the steel mass transfer coefficient, k_m^{st} on the slag deoxidation characteristics for silica-rich slags. As can be seen, a higher k_m^{st} leads to faster equilibration of the steel with slag. In this study, the steel-slag reactions are assumed to be under mixed mass transport control, with mass transport occurring in both the steel and slag. Hence, the overall reaction kinetics can be quantified through a term known as the overall mass transfer coefficient, k_o, defined as:

$$\frac{1}{k_o} = \frac{1}{k_m^{sl} L_o} + \frac{1}{k_m^{st}}, \tag{4.3.7}$$

Using $k_m^{sl} = 0.1 k_m^{st}$, Eq. 4.3.7 shows that increasing k_m^{st} increases the overall mass transfer coefficient, k_o. Consequently, this decreases the time constant of steel-slag reactions reaching equilibrium. This time constant, τ, can be

expressed as:

$$\tau = \left(\frac{k_o \rho_{st} A}{W_{st}} \left(1 + \frac{W_{st}}{W_{sl} L_o} \right) \right)^{-1}, \tag{4.3.8}$$

where L_o refers to the partition ratio of oxygen between slag and steel and is defined as $(\%O)_{eq}/[\%O]_{eq}$, $W_{st}$and W_{sl} refer to weight of the steel and slag, respectively, A is the steel-slag reaction area and ρ_{st} is the density of steel. From this expression, it can also be shown that slow mass transfer rates in crucible experiments does not allow oxygen levels in the bulk steel to go down significantly during the refining process as was seen in Figure 4.8b.

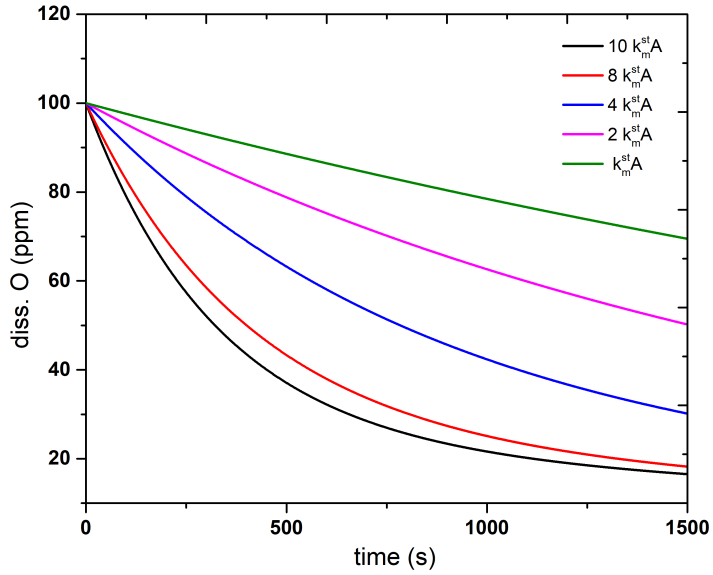

Figure 4.9: *Effect of steel mass transfer coefficient at the steel/slag interface on the variation of oxygen with time.*

4.3.7 Limitations of the model

In this work, *apriori* knowledge is needed of the inclusion phases present within the system, in order to track their compositional changes. Additionally, the model is currently unable to capture the variance in inclusion chemistry within a sample. Finally, the effect of fluid flow in the ladle reactor is not included in the present study which could also influence the final composition of the steel, slag, and inclusions. These limitations could potentially be overcome by using a Population Balance Model (PBM) coupled with a thermo-kinetic code, including the effects of nucleation. Using a PBM approach, different size classes of inclusions can be modelled considering the effect of nucleation, growth, aggregation and breakage processes simultaneously. Furthermore, this framework could be further incorporated in a fluid

flow description of the reacting vessel. Using a PBM approach, the evolution of different sized inclusions and competition between multiple inclusion types can be studied as shown in a study by Rimbert et al. [25]. While the incorporation of such complexity into the model increases its fidelity, it also adds considerable computational expense. In this regard, the developed mass transfer model is simpler and useful for predicting composition changes taking into account the important refining process variables which is more suited for process control.

4.4 Conclusion

In the current study, a kinetic model was developed for manganese silicate inclusions and combined with a prior steel-slag model to study the effect of slag on the inclusion compositional changes in the steel. Overall, the model was able to capture the inclusion changes with time and the 'slag aided deoxidation' mechanism at the steel/slag interface reasonably well. The salient findings of the study are as follows:

- It was shown that diffusion of solutes to the inclusions is the probable rate-determining step for inclusion transformation while diffusion through the liquid product layer was not. Also, the transformation rates are relatively high, indicating that the formation of manganese silicates is fast in molten steels.

- After combining the steel-slag and steel-inclusion models, the model calculations showed good agreement with previous literature data. This indicates the applicability of the coupled reaction modelling methodology to typical ladle refining reactions in Si-Mn killed steel.

- The simulations showed that steel-slag reactions with alumina rich slags could lead to excess Al pick up in Si/Mn killed steels which can further modify inclusions and cause the formation of undesired solid phases inside the steel.

- The dissolved oxygen goes down mainly by precipitation deoxidation when there is excess Al in the steel. On the other hand, silica-rich slags which is shown to cause less Al pickup, have a less detrimental effect on the inclusion compositions.

- Additionally, it was shown that in crucible experiments, unlike plant conditions, the time needed to reduce oxygen levels with slags is high

owing to sluggish mass transfer at the steel-slag interface.

One way to improve our predictions of inclusion composition is to couple a population balance model with the kinetic model of inclusions. This will be presented in our future work.

References

[1] A. Ghosh, *Secondary Steelmaking: Principles and Applications*, 2001.

[2] J. Aoki, L. Zhang, B.G. Thomas, *ICS 2005 - Proc. 3rd Int. Congr. Sci. Technol. Steelmak.* 2005319 .

[3] X. Zhang, H. Roelofs, S. Lemgen, U. Urlau, S. V Subramanian, *Steel Res. Int.* 2004, 75, 314 .

[4] L. Zhang, C. Guo, W. Yang, Y. Ren, H. Ling, *Metall. Mater. Trans. B Process Metall. Mater. Process. Sci.* 2018, 49, 803 .

[5] Y.B. Kang, H.G. Lee, *ISIJ Int.* 2004, 44, 1006 .

[6] S.H. Chen, M. Jiang, X.F. He, X.H. Wang, *Int. J. Miner. Metall. Mater.* 2012, 19, 490 .

[7] J.S. Park, J.H. Park, *Metall. Mater. Trans. B Process Metall. Mater. Process. Sci.* 2014, 45, 953 .

[8] J.H. Park, L. Zhang, *Metall. Mater. Trans. B Process Metall. Mater. Process. Sci.* 2020, 51, 2453.

[9] D. Kumar, K.C. Ahlborg, P.C. Pistorius, *Metall. Mater. Trans. B Process Metall. Mater. Process. Sci.* 2019, 50.

[10] A. Harada, N. Maruoka, H. Shibata, M. Zeze, N. Asahara, F. Huang, S. Kitamura, *ISIJ Int.* 2014, 54.

[11] J.H. Shin, Y. Chung, J.H. Park, *Metall. Mater. Trans. B Process Metall. Mater. Process. Sci.* 2017, 48.

[12] Y. Zhang, Y. Ren, L. Zhang, *Metall. Res. Technol.* 2017, 114, 1 .

[13] S.P.T. Piva, D. Kumar, P.C. Pistorius, *Metall. Mater. Trans. B Process Metall. Mater. Process. Sci.* 2017, 48, 37 .

[14] M.A. Van Ende, I.H. Jung, *Metall. Mater. Trans. B Process Metall. Mater. Process. Sci.* 2017, 48, 28.

[15] Y. Tabatabaei, K.S. Coley, G.A. Irons, S. Sun, *Metall. Mater. Trans. B Process Metall. Mater. Process. Sci.* 2018, 49, 375 .

[16] A. Galindo, *Kinetics of the Formation of Magnesium Aluminate Inclusions, Masters Thesis, McMaster University, 2015.*

[17] K. Graham, Integrated Ladle Metallurgy Control, PhD Thesis, McMaster University, 2008.

[18] Z.X. Bing, J.G. Chang, T. Kai, X.J. Lun, D.W. Zhong, X.K. Di, *Calphad* 1997, 21, 301.

[19] C.W. Bale, A.D. Pelton, *Metall. Trans. A* 1990, 21, 1997.

[20] F. Oeters, Metallurgy of Steelmaking, Verlag Stahleisen, 1994.

[21] D.G.. Robertson, B. Deo, S. Ohguchi, *Ironmak. Steelmak.* 1984, 11, 41.

[22] B.K.D.P. Rao, D.D.R. Gaskell, *Metall. Trans. B* 1981, 12, 311.

[23] D.H. Woo, Y.B. Kang, H.G. Lee, *Metall. Mater. Trans. B: Process Metall. and Mater. Process. Sci.* 2002, 33.

[24] W. Tiekink, R. Van Den Bogert, T. Breedijk, A. Ferguson, *Ironmak. Steelmak.* 2003, 30, 146 .

[25] N. Rimbert, L. Claudotte, P. Gardin, J. Lehmann, *Indus. and Eng. Chem. Res.* 2014, 53.

Chapter 5

Development of a multi-oxide kinetic model to study inclusion transient evolution in molten steel: Application to Si-Mn killed steel

In Chapter 5, the original concept of a multi-oxide kinetic model was proposed by me. The data for validation was taken from experimental and previous literature data. The model development and the analysis were entirely carried out by me. Useful discussions on the results were provided by Dr. Kenneth S. Coley and Dr. André B. Philion.

The manuscript was initially drafted by me and edited to the final version by Dr. Kenneth S. Coley and Dr. André B. Philion. This chapter has been published in Metallurgical and Materials Transactions B, 2023. The following Chapter is the accepted version of the article.

Development of a multi-oxide kinetic model to study inclusion transient evolution in molten steel: Application to Si-Mn killed steel

Angshuman Podder[1], **Kenneth Coley**[1,2], **André Phillion**[1]

[1] *McMaster Steel Research Center*
Department of Materials Science and Engineering,
McMaster University, Hamilton, Ontario, Canada, ON L8S 4L7
[2] *Department of Mechanical and Materials Engineering,*
Western University, London, Ontario, Canada, ON N6A 3K7

Abstract

A first principles-based multi-oxide inclusion kinetic model is proposed to predict the transient evolution of oxide inclusion composition in secondary steelmaking processes. The model provides information about different oxide particles as opposed to an average inclusion composition, by taking into account the thermodynamics ($\Delta G_{\text{ox}}^{tot}$) and kinetics of the formation of different stoichiometric oxide inclusions. When coupled with a previously-developed steel-slag model [1], the model is used to predict the type and amount of predominant inclusions encountered during the refining of Si-Mn killed steels. These predictions show good agreement with laboratory and industrial, experimental measurements. The model is able to demonstrate the linkages between the inclusion precipitation sequence and steel and slag compositional variables.

5.1 Introduction

In secondary steelmaking, deoxidation and reoxidation reactions lead to the formation of nonmetallic inclusions (NMIs), which need to be controlled to obtain good steel quality [2]. It is important to understand the formation and types of harmful inclusion phases that can deteriorate the performance of the steelmaking process. Automated inclusion analysis (AIA) of industrial samples provides useful information regarding the process dynamics and the formation reactions of the inclusions in high-temperature reactors. However, predictive models that can simulate the formation and evolution of inclusions throughout the refining process are also needed to optimize the process parameters, thus, increasing reactor efficiency. In this regard, kinetic models have been developed by many researchers over the past two decades to

simulate inclusion evolution during the refining process. The literature pertaining to such models has been recently reviewed by Park and Zhang [3]. In one approach, commercial thermodynamic packages like FactSage are used to compute the equilibrium mass fractions of the stable phases according to the chemical compositions of the steel. In most cases, this approach seems reasonable since the steel-inclusion reactions do not seem to be rate controlling owing to the high interfacial area [4] as well as a quick establishment of local equilibrium between steel and inclusions. However, Rimbert et al. [5] showed that this approach was not successful in simulating non-equilibrium inclusions. Their study demonstrated that incorporation of the kinetics of particulate events, including nucleation, growth, aggregation, and removal of inclusions, was needed to improve the accuracy of the simulations. A second approach that is used to model inclusion chemistry is the tracking of the average inclusion composition through mass transfer equations for the different reacting species [6, 7]. Although there seems to be an explicit description of particles, this approach does not track the different types of inclusions precipitating within the molten steel. Hence, there is a need to develop a modelling approach that is capable of simulating both equilibrium as well as non-equilibrium inclusions during the steelmaking process. Moreover, there has been a growing interest in coupling reactor mixing kinetics and inclusion transport with chemistry prediction models in order to study the transient behavior of inclusion evolution in molten steel.

In this study, a new approach, namely, the multi-oxide inclusion (MOI) kinetic model, is proposed to simulate the transient evolution of oxide inclusion chemistry in molten steel. First, the assumptions and equations used in this model are introduced. Second, the MOI kinetic model is coupled with a steel-slag model previously developed in our group [1] to simulate the effect of different slag compositions on inclusion evolution. Third, the model results are validated against experimental data from laboratory deoxidation experiments for the Fe-Si-Mn-O system. Fourth, the coupled model results are compared against previous literature data to show the applicability to ladle refining reactions. Finally, some discussions are made on the application and future possibilities of the model.

5.2 Model development

5.2.1 Multi-oxide inclusion kinetic model

When deoxidizers are added to molten steel, there are reactions between the solutes ([Si], [Mn], [Al], etc.) and [O], resulting in a large population of different oxide inclusions (simple or complex oxides). Each of these oxide

inclusions has its individual stability and growth dynamics that determine evolution characteristics and lifetime in liquid steel. The multi-oxide inclusion (MOI) kinetic model employs separate calculations for each inclusion type encountered in the process so that the evolution of each type can be tracked as a function of time. The thermodynamics and kinetics of inclusion formation are described by the equilibrium constant and species mass transfer equations, respectively, as described in the next section. The inclusions are assumed to be stoichiometric solid or liquid phases whose internal compositions do not change with time.

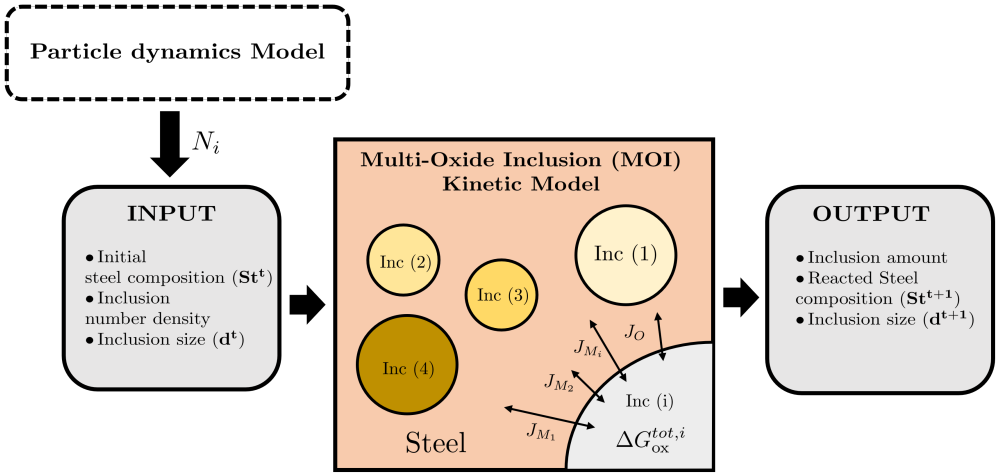

Figure 5.1: *Schematic showing an overview of the multi-oxide inclusion (MOI) kinetic model. Note: The particle dynamics model is not included in this current version.*

In addition to predicting the development of multiple oxide inclusions, the model has the potential to accommodate the inclusion number density and size changes that take place during the dynamic process, thereby facilitating the future development of a particle dynamics model coupled with chemical kinetics. For example, the total number density, N, could be provided from another sub-model pertaining to particle size distributions (Refer to Figure 5.1). By including the initial conditions of all relevant inclusion types, the model essentially introduces 'seeds' in the melts which do not alter the mass of the steel significantly. The model, then allows all inclusions to grow based on their mutual stabilities with changing melt conditions. In other words, the amount/mass of the multiple oxide inclusions can be tracked with time by allowing the mass transfer to dictate the formation and evolution of 'only' the stable inclusion types. Figure 5.1 shows a schematic of the modelling framework, i.e., the initial inputs required by the multi-oxide inclusion kinetic model and the resulting desired output. Please note that this study

does not include a particle dynamics model. Instead, the inclusion number density is treated as a constant that does not change with time (assuming it to be the steady state value).

Although the model could be easily adapted for oxide inclusions belonging to many deoxidation systems such as Fe-Al-O, Fe-Al-Ti-O, etc., this study is focused on inclusions pertaining to Si-Mn killed steels, whose properties are shown in Table 5.2.1. As can be seen in the table, each inclusion phase is characterized by the size (d_i) and the number density (N_i), which is initialized to the same value, irrespective of inclusion type, in this work.

Thermodynamic equations

All the steel-inclusion formation reactions considered in this study can be represented as follows:

$$x_1\underline{\mathrm{M_1}} + x_2\underline{\mathrm{M_2}} + x_3\underline{\mathrm{M_3}} + x_n\underline{\mathrm{M_n}} + y\underline{\mathrm{O}} = \mathrm{M_{1,x_1}M_{2,x_2}...M_nO_y}, \tag{5.2.1}$$

where x_i and y represent the stoichiometric values, $\mathrm{M_n}$ represents a cation (Si, Mn, Al, etc.), and O is the oxygen anion. Now, at the interface between the steel and the inclusion, local equilibrium is assumed:

$$K_{eq,\mathrm{M_{1,x_1}M_{2,x_2}...M_nO_y}} = \frac{a_{\mathrm{M_{1,x_1}M_{2,x_2}..M_nO_y}}}{\prod_i h_{\underline{\mathrm{M_i}}}^{x_i} h_{\underline{\mathrm{O}}}^{y}}, \tag{5.2.2}$$

where h_i represents the Henrian activity of ith species with respect to 1 wt. % standard state, calculated using Unified Interaction Parameter Formalism [8] and the activity of the complex oxide, $a_{\mathrm{M_{1,x_1}M_{2,x_2}..O_y}}$ is taken as one. For simple oxides, the values of equilibrium constants, $K_{eq,i}$, can be found in Refs. [1, 9]. For complex oxides, the corresponding equilibrium constants are calculated using the following:

$$K_{eq,i} = \exp\left(-\frac{\Delta G_{\mathrm{ox},i}^{tot}}{RT}\right). \tag{5.2.3}$$

Here, the Gibbs free energy change associated with complex oxide inclusion formation, $\Delta G_{\mathrm{ox},i}^{tot}$ can be calculated using the following:

$$\Delta G_{\mathrm{ox},i}^{tot} = -\sum_j x_j RT \log K_j + \Delta G_i^{mix} + \Delta G_i^{L\rightarrow S}\,(\text{if solid}), \tag{5.2.4}$$

where j refers to the jth oxide constituting the complex oxide. Now, the first term on the RHS refers to the sum of the formation energies of 'j' oxides, the second term refers to the mixing free energy of the formation of

Table 5.2.1: *Information regarding the inclusions considered in the model for Si-Mn killed steel*

Inc type	Units	Silica	Alumina	Rhodonite	Tephroite	Spessartite	Galaxite
Si	-	1	0	1	1	3	0
Mn	-	0	0	1	2	3	1
Al	-	0	2	0	0	2	2
O	-	2	3	3	4	12	4
Number density, N_i	m^{-3}	N_1	N_2	N_3	N_4	N_5	N_6
Mean size, d_i	μm	d_1	d_2	d_3	d_4	d_5	d_6
$\log(K_i)$, **(1873 K)**	-	4.676	12.500	6.425	7.741	35.351	13.876
Molar volume	cm^3mol^{-1}	25.74	25.57	35.32	48.62	118.16	42.40

Silica: SiO_2; Alumina: Al_2O_3; Rhodonite: $MnO \cdot SiO_2$; Tephroite: $2MnO \cdot SiO_2$; Spessartite: $3MnO \cdot 3SiO_2 \cdot Al_2O_3$; Galaxite: $MnO \cdot Al_2O_3$

the liquid oxide system, and the third term refers to the free energy change required to form a solid inclusion from the liquid solution. The computation of ΔG^{mix} requires the activities of the constituting oxide components in the inclusion, a_{M_xOy}. In this study, these have been calculated using a Sub Regular Solution Model (SRSM) [7, 10] based on the solid reference state at 1873 K. It is worthwhile pointing out that the value of $\Delta G^{tot}_{\text{ox}}$ essentially dictates the formation tendency of an inclusion. This allows the model to be generic and be able to simulate a wide variety of oxide inclusions arising in steel.

Kinetic equations

The mass flux rate, J_i of species i through the boundary layer from the bulk steel to the surface of a spherical particle is given by:

$$J_i = k_{m,i}\pi d^2(C_i^b - C_i^*), \tag{5.2.5}$$

where C_i^b and C_i^* are the concentrations of solute i at the bulk and interface, respectively, and $k_{m,i}$ is the mass transfer coefficient between the steel and inclusion. This last term can be defined using the Sherwood number, Sh, and diffusion coefficients, D_i as:

$$k_{m,i} = \frac{D_i \cdot Sh}{d}. \tag{5.2.6}$$

A Sherwood number of 2 has been utilized since the size of the inclusions is less than 14 μm [11].

Finally, in the multi-component system, the flux equations must satisfy mass balance as follows:

$$\frac{J_{\text{M}_1}}{x_1} = \frac{J_{\text{M}_2}}{x_2} = \frac{J_{\text{M}_3}}{x_3} ... = \frac{J_{\text{M}_n}}{x_n} = \frac{J_{\text{O}}}{y} \tag{5.2.7}$$

Please note that the concept of fixed particle composition is introduced as an artificial constraint to simplify the calculations. In reality, in a molten system, the solubility of oxides within each other is rather high, thus rendering the oxide composition a non-stoichiometric variable.

Based on Eq. 5.2.7, $(n-1)$ equations can be constructed from the flux balance equations. The final equation is obtained from consideration of local thermodynamic equilibrium at the steel/inclusion interface (Eq. 5.2.2). For example, 2 flux balance relations and 1 thermodynamic equation are needed

to compute the interfacial species concentrations to model $MnO{-}SiO_2$ type inclusions within the Mn-Si-O system. Numerically, the values of interfacial concentration of the involved species are obtained by solving a set of non-linear kinetic equations using the Newton-Raphson method. Following this, the amounts of each inclusion are calculated using mass balance relations. The depletion of solutes in the bulk steel is calculated via the following:

$$\frac{dX_i}{dt} = -N_t \cdot \pi d^2 k_{m,i} \cdot (X_i^b - X_i^*), \tag{5.2.8}$$

where dX_i/dt represents the change in concentration in the bulk steel, and N_t is the inclusion number density in the molten steel.

Inclusion growth

Although in principle, the size and morphology of inclusions can change through different physical aggregation mechanisms [12], in this work, the inclusion sizes are constrained to change through mass transfer and chemical reactions only. Specifically, the growth rate of inclusions resulting from the chemical transformation is computed via [13]:

$$\frac{\mathrm{d}r}{\mathrm{d}t} = \frac{D_O}{r} \cdot \frac{X_O - X_O^*}{\alpha X_O^{\mathrm{inc}} - X_O^*}, \tag{5.2.9}$$

where $r = (d/2)$ is the radius of the inclusion, $\alpha = v_{\mathrm{at}}^{\mathrm{Fe}}/v_{\mathrm{at}}^{\mathrm{inc}}$ is the ratio of steel (Fe) to inclusion molar volumes (mean volume per atom), D_O is the diffusivity of oxygen in liquid steel at 1873 K, X_O is the bulk mole fraction of oxygen in the liquid steel, X_O^* is the mole fraction of oxygen at the slag/steel interface, and X_O^{inc} is the mole fraction of oxygen in the oxide inclusion.

5.2.2 Steel-slag model

Steel-slag reactions can be adequately described by the multicomponent kinetic model originally proposed by Robertson et al. [14], where the species mass transfer equations are coupled and solved at the reaction interface. In the present work, this model is used to investigate the effect of steel-slag reactions on the inclusion compositions. More details about the calculation procedure can be found in Ref. [1]. In principle, X_O^* is calculated by the respective thermodynamic and flux balance equations. Using this, the interfacial concentrations of other elements are calculated, which is followed by the update of the bulk compositions of steel and slag using the following:

$$\frac{dX_M^{st}}{dt} = \frac{k_{m,M}^{st} A_{st/sl}}{V_{st}} \cdot \left(X_M^b - X_M^*\right) \tag{5.2.10}$$

$$\frac{dX^{sl}_{M_xO_y}}{dt} = \frac{k^{sl}_{m,M_xO_y} A_{st/sl}}{V_{sl}} \cdot \left(X^{b}_{M_xO_y} - X^{*}_{M_xO_y} \right) \tag{5.2.11}$$

where X^{st}_{M}, $X^{sl}_{M_xO_y}$ are the mole fractions of the metal and oxide in the bulk steel and slag, respectively, $A_{st/sl}$ is the area of the steel/slag interface, and V_{st} and V_{sl} are the total steel and slag volume, respectively.

5.2.3 Calculation methodology

A schematic of the calculation methodology is shown in Figure 5.2. First, the initial steel and slag compositions are input into the model along with their corresponding masses, as well as the inclusion number density and size. The inputs are used to obtain the thermodynamic properties, and the calculation of the mass transfer coefficient is done based on the stirring rate information or supplied data. After these pre-calculations, the steel-slag model is run with a time step of 1 second (Δt) since the steel-slag reactions ought to be slower. Finally, the multi-oxide inclusion kinetic model is applied with a time step of 0.01 seconds (dt) to determine the type, amount, and size of inclusions, as well as the new steel chemistry. All numerical computations were carried out using MATLAB 2022a.

Please note that it is assumed that (a) the temperature of the molten steel is kept constant (1873 K) and uniform throughout the bulk, (b) the dissolution of alloying additions occurs rapidly, and (c) the composition of the bulk steel is taken to be homogeneous at all times.

5.3 Data used for validation

In order to verify the model results, data pertaining to Si-Mn killed steels was collected from different crucible experiments both performed in the authors' laboratory and found in the literature [4, 15]. A brief background of these experiments and trials is provided below. The steel and slag compositions used in this study are tabulated in Table 5.3.1 while the values used for model initialization are listed in Table **??**.

5.3.1 C1 : Deoxidation experiment

Deoxidation experiments with industrial grade FeSi (wt.%Si $\approx$ 79%) and FeMn (wt.%Si $\approx$ 80%) were carried out in a vertical resistance-heated tube furnace. A pre-weighted mixture of electrolytic iron (Fe) and Fe_2O_3 (source of oxygen) were placed in a MgO crucible (58 mm ID; 62 mm OD; 104 mm H) to yield a 300 g melt containing about 400 ppm [O]. This was then heated to

Table 5.3.1: *Steel and slag compositions used in the model*

	Steel (wt. %)						Slag (wt. %)			
Case	C	Si	Mn	Al	Ca	O	SiO_2	Al_2O_3	MgO	CaO
C1a (after FeSi)	0.010	0.140	0.045	0.0015	<0.001	0.032	-	-	-	-
C1b (after FeMn)	0.022	0.140	1.395	0.0015	<0.001	-	-	-	-	-
C2	0.310	0.210	1.080	0.001	-	0.030	7.5	35	10	47
C3	0.060	0.270	1.000	0.001	-	0.050	28	7	10	44

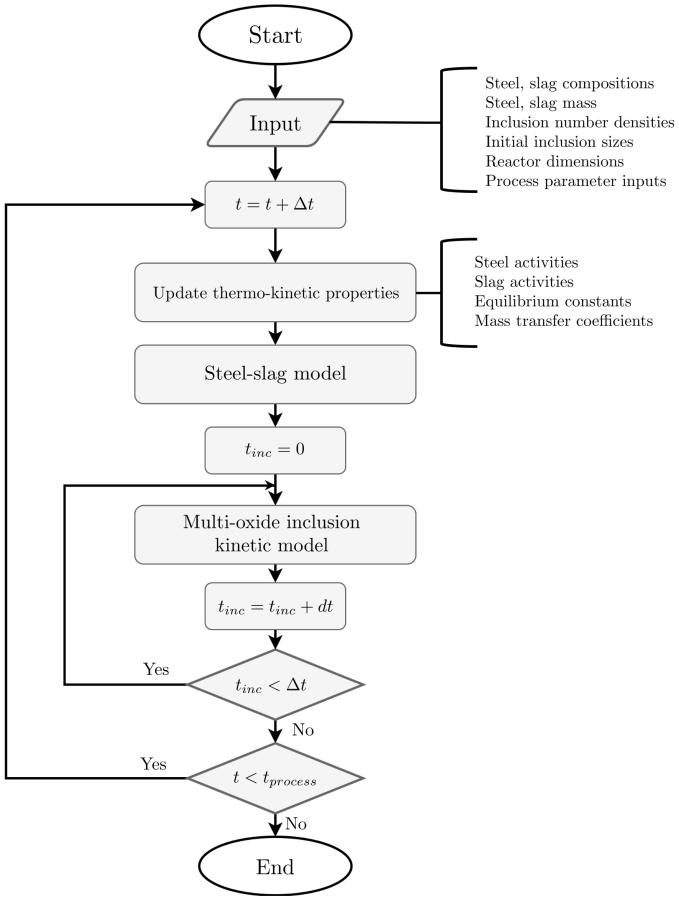

Figure 5.2: *Flow chart of steel-slag-inclusion reaction model.*

1873 K (1600°C) in an inert argon atmosphere which was ensured by passing 5N pure argon gas through titanium turnings at around 700°C. After melting, homogenization was done for about 30 minutes, after which alloy additions were made from the top of the furnace through a hollow alumina pipe. First, FeSi was added (t = 0), followed by FeMn after an interval of 600 s in an argon atmosphere. After the addition of the alloys, melt samples (S1- S4) were taken at different holding times (30, 300, 630, 900 s) using a quartz tube. A schematic showing the timing of samples is presented in Figure 5.3. The experimental setup used for the experiments is the same as used by Nabeel et al. [16].

Chemical analyses of the steel samples were then carried out by induction coupled plasma optical emission spectrometry (ICP-OES). SEM-EDS inclusion analysis (AIA) was conducted using the AZTEC software. The inclusions were classified based on the following nomenclature: M = MnO; S =

Table 5.3.2: *Model initialization parameters*

Parameter	Units	C1	C2	C3
Steel Mass	kg	0.296	0.650	170000
Slag Mass	kg	-	0.185	3000
Crucible/Ladle diameter	m	0.058	0.058	2.612
Effective reaction area	m^2	-	3.32×10^{-3}	7.11
$k_m^{st} A_{st/sl}$	m^3/s	-	6.80×10^{-8}	$6 \times 10^{-6} \dot{\epsilon}^{1.4} V_{st}$
k_m^{sl}/k_m^{st}	-	-	0.1	0.1
Inclusion number density	$/m^3$	1×10^{13}	1×10^{13}	1×10^{13}
Initial inclusion diameter	μm	1	1	1

Note: $\dot{\epsilon}$ is the effective stirring power (W/t)

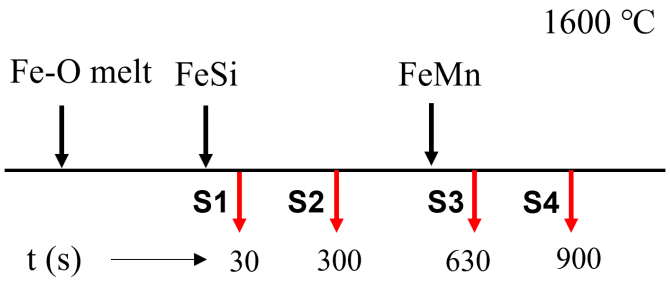

Figure 5.3: *Schematic of sampling used in the experiments.*

SiO_2, A = Al_2O_3 ; MS = MnO−SiO_2 ; MS-low Al = MnO−SiO_2 with low Al ; AS = Al_2O_3–SiO_2 ; MS-Ca = MnO−SiO_2 with Ca ; MS-high Al = MnO−SiO_2 with high Al.

The corresponding simulation was carried out using the steel composition (C1a) shown in Table 5.3.1. First, the steel was allowed to reach equilibrium with the inclusions after FeSi was added to the oxygen-rich iron melt. After 600 s, the steel composition was changed to that of C1b to represent the addition of FeMn, following which the same was repeated.

5.3.2 C2: Steel-slag crucible experiments (Piva et al., 2018)

Piva et al. [4] performed laboratory experiments to study steel-slag reactions in Si-Mn killed steels in an induction furnace. Electrolytic iron (Fe) was melted in a MgO crucible and deoxidized using controlled compositions of ferroalloys, FeMn and SiMn, to yield a [Mn]/[Si] mass ratio of 5 in the steel.

A prepared slag mixture was then added to the crucible 360 seconds after deoxidation. Samples were taken at time intervals of 300 s. Steel composition was analyzed using ICP-OES, while the inclusion data was obtained via ASPEX analysis.

The corresponding simulation was carried out using the steel and slag composition (C2) shown in Table 5.3.1. For this simulation, the steel-slag mass transfer coefficient was selected to match the Al pickup rate in the steel and reported observations of the inclusion population.

5.3.3 C3: Industrial trials (Bhansali et al., 2021)

Bhansali et al. [15] reported data for Si-Mn killed steels produced through the electric arc furnace (EAF) and ladle metallurgical furnace (LMF) route. Deoxidation was done in the LMF after tapping the steel from the EAF (open tap), which was followed by the addition of the pre-weighed mixture of SiMn, dolomite, silica sand, and lime.

The corresponding simulations were carried out using the steel and slag composition listed as C3 in Table 5.3.1. However, as the details regarding stirring rate information (flow rate variation, number of plugs, gas flow rate) were not provided, they had to be assumed based on another study from a similar industrial plant [17]. A constant flow rate of 7 SCFM (Standard cubic feet per minute) with one plug was selected for computing the mass transfer coefficient at the steel/slag interface in the model calculations. The stirring energy, $\dot{\epsilon}$ was calculated from the flow rate as:

$$\dot{\epsilon} = \frac{\dot{n}RT}{W_{\text{st}}} \ln\left(\frac{P_{\text{t}}}{P_0}\right), \tag{5.3.1}$$

where $\dot{n}, R, W_{\text{st}}, P_{\text{t}}$, and P_0 denote the molar gas flow rate (Nm^3/hr), ideal gas constant (J/mol/K), steel weight (kg), the gas pressure at the base of the ladle, and at the melt surface (Pa), respectively. Please note that although Ca injection was also performed experimentally, the authors reported a low recovery, and thus in these simulations, the presence of Ca was ignored.

5.4 Results

5.4.1 Model validation

C1: Deoxidation experiments

Figure 5.4 compares the inclusion analysis data from experiments with those obtained from the model calculations. It is seen that a good agreement is obtained for the type of oxide inclusions that are precipitating in the liquid steel. After FeSi addition, mostly the inclusion population consists of silica inclusions, while after FeMn addition, they are mostly manganese silicates with some aluminium. Although alumina inclusions were predicted after FeSi addition, they were not observed experimentally. This might be because sufficient supersaturation for alumina nucleation was not present in the melt. However, this was not considered in the present model. The predicted average compositions of inclusions are plotted in Figure 5.5, which shows very good agreement with the experimental data. The corresponding changes in the [O], [Si], [Mn], and [Al] in the bulk steel are shown in Figure 5.6. As can be seen, the addition of FeMn further decreases the dissolved oxygen by forming manganese silicates owing to the stronger deoxidation capability of the combined action of [Si] and [Mn] in the steel [2].

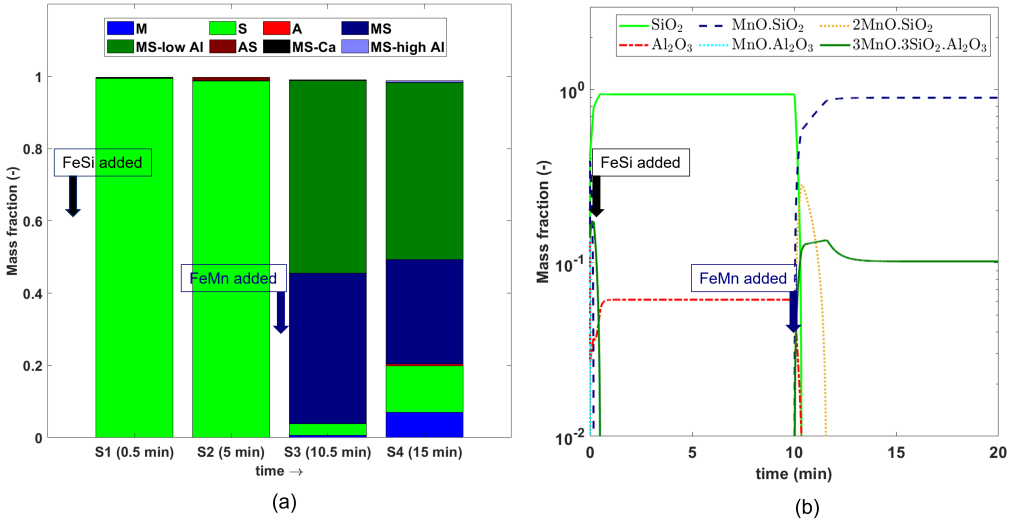

Figure 5.4: *(a) Variation in inclusion chemistry with time (a) during deoxidation experiments and (b) calculated from MOI model (C1).*

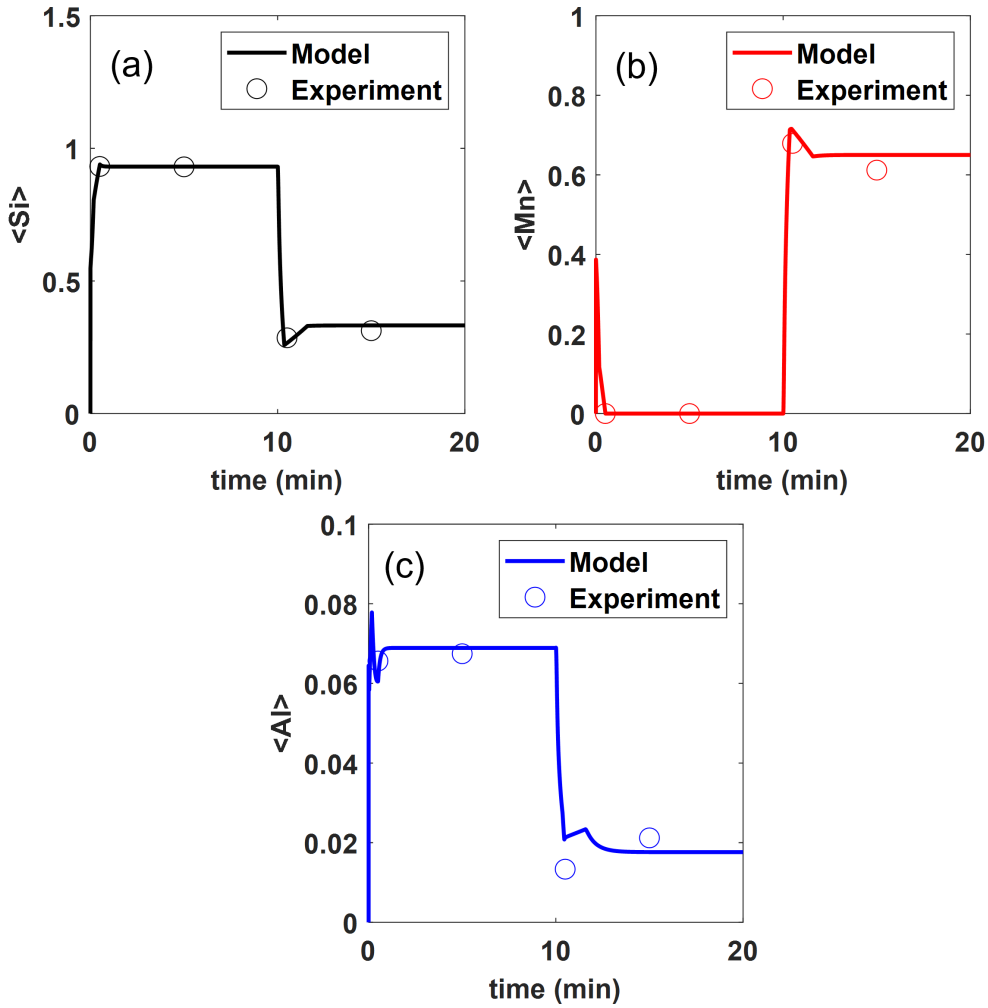

Figure 5.5: *Variation of average species concentration (a) Si, (b) Mn, (c) Al in the inclusion phase as a function of time (C1). Note: <> refers to the element concentration in the inclusion phase.*

C2: Steel-slag crucible experiments (Piva et al., 2018)

Figure 5.7 shows a comparison between the average inclusion composition (mole fraction of oxides) obtained from the experiments with that calculated from the MOI model. It can be seen that a reasonable agreement is obtained between the simulated results and experimental data. Figure 5.8 shows the precipitation sequence of the different oxides in the liquid steel because of the dynamic reactions. Due to the presence of high alumina slag (Al_2O_3=35%), there is considerable Al pickup which reacts with the inclusions and ultimately leads to a high concentration of alumina inclusions. This is in line

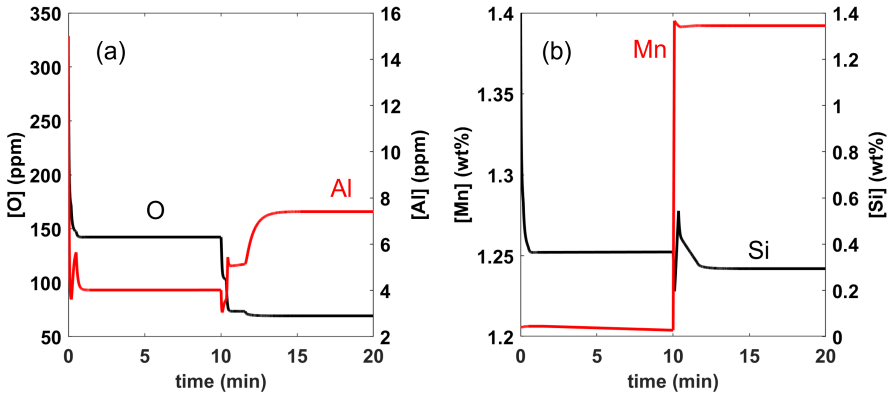

Figure 5.6: *Evolution of steel composition with time calculated from MOI model (C1).*

with the physical observations from the experiment [4]. However, the under-prediction of the model in predicting the average oxide inclusion composition till $\approx$ 660 s is possibly from the fact that the spessartite type inclusions considered in the model have a fixed stoichiometry. In reality, the solubility of Al in $MnO-SiO_2$ can be much higher, leading to different $MnO-SiO_2-Al_2O_3$ inclusions. It is expected that the deviations in the model results presented in Figure 5.7 could be circumvented by including other possible inclusions and an accurate description of the number density variation with time.

C3: Industrial trials (Bhansali et al., 2021)

Figure 5.9 shows a comparison between the average inclusion composition (atomic fraction of elements in oxides) obtained from the industrial trials with the values calculated from the MOI model. As can be seen, excellent agreement between the industrial and model results is achieved. It is worthwhile pointing out that the model parameters were not selected to fit this data but instead assumed to be the best available. The precipitation sequence in Figure 5.10 illustrates that the majority of the inclusions are of the $MnO-SiO_2$ and $MnO-SiO_2-Al_2O_3$ type, which also matches with the inclusion data of the various samples reported in the literature. Furthermore, it can be seen that no alumina inclusions form based on the conditions that are input in the model. This is because the Al pickup is less from the steel-slag reactions [7] in the presence of a silica-rich slag.

5.5 Discussion

Having validated the model, a parametric analysis is now carried out to demonstrate the applicability of the model in predicting the effect of steel

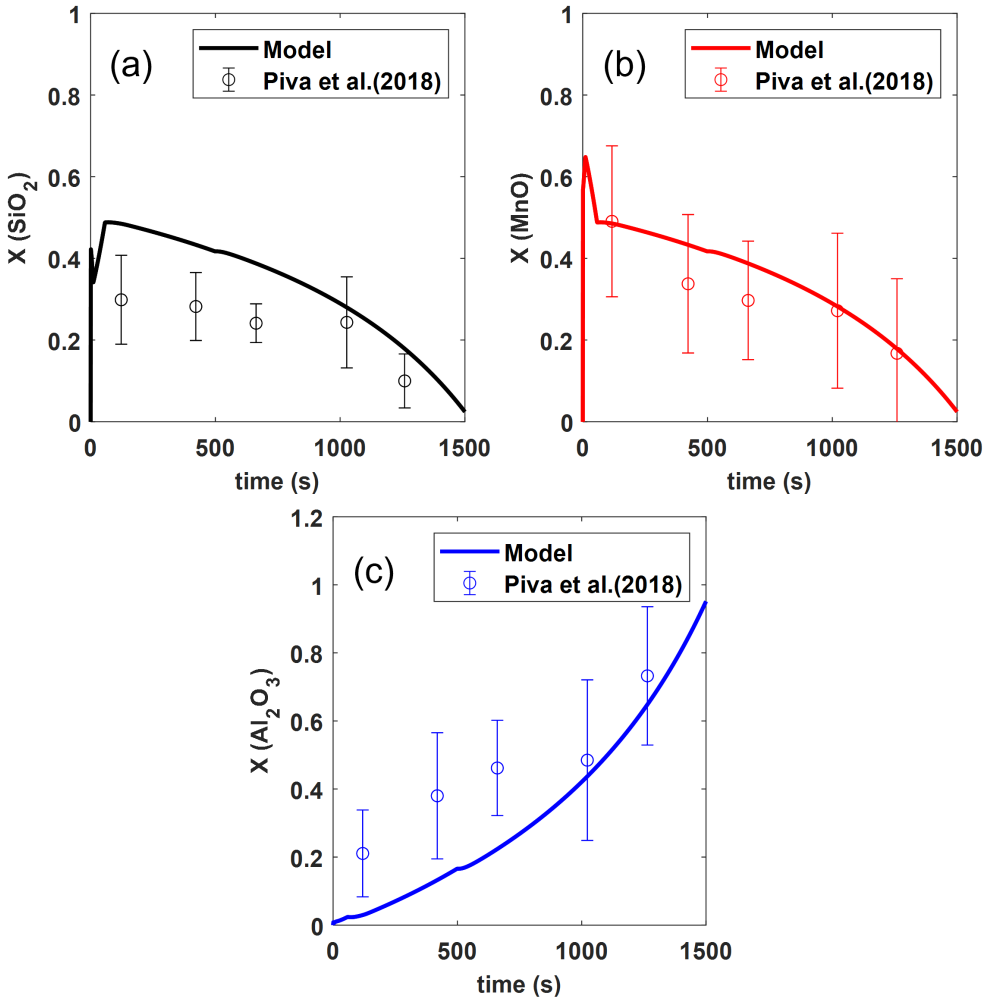

Figure 5.7: *Comparison of experimental and model results for inclusion evolution with time (C2).*

composition on inclusion evolution. Figures 5.11, 5.12, and 5.13 depict the variation of inclusion precipitation sequence with time for different initial [Al], [Mn]/[Si] ratio, and [O] levels, respectively. It can be seen in Figure 5.11 that with an increase in [Al] concentration, the amount of Al_2O_3 type inclusions increases. This observation is in line with previous findings [18, 19] where a critical permissible [Al] was identified to avoid solid alumina inclusions in the steel. In Figure 5.12, it can be observed that with a decrease in [Mn]/[Si] ratio, silica inclusions are mostly stable with the fraction of $MnO-SiO_2$ inclusions diminishing owing to lower Mn content. Turkdogan [23] came to a similar conclusion based on his thermodynamic and experimental investigations. However, with higher ratios, $MnO-SiO_2$ and $MnO-SiO_2-Al_2O_3$ type inclusions precipitate in the steel as the [Mn]

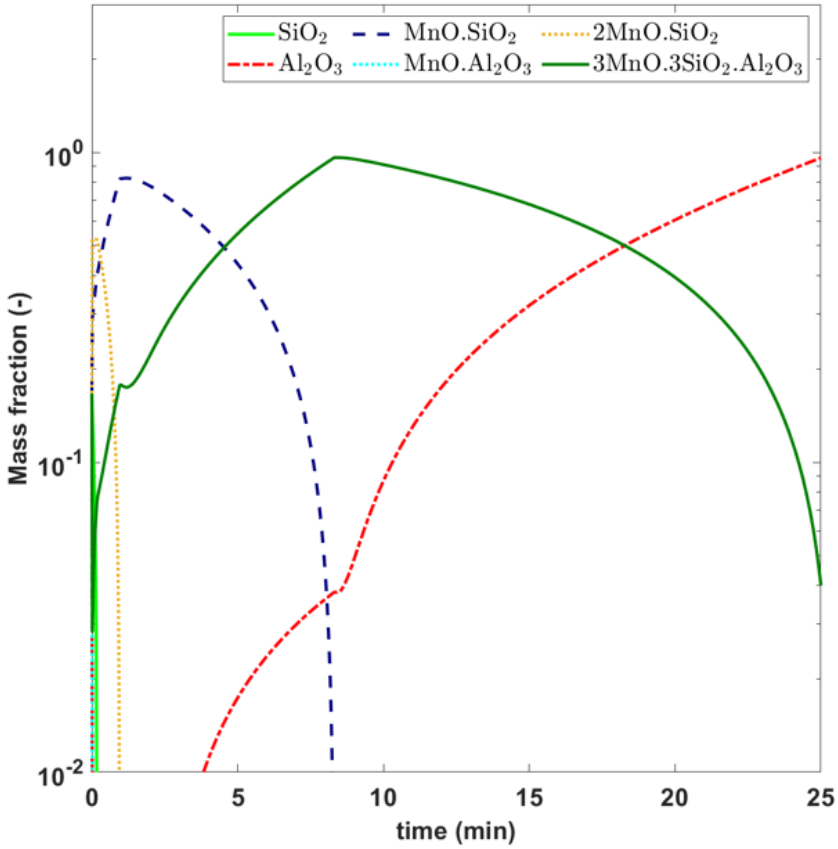

Figure 5.8: *Predicted precipitation sequence of oxide inclusions with time presented as mass fraction relative to the total inclusion population (C2).*

levels in the steel increase (Refer to Figures 5.12a and 5.12b). In Figure 5.13, it is seen that $MnO{-}SiO_2$ inclusions are not stable when the initial [O] in the steel was lowered from 300 to 100 ppm while leading to mostly $MnO{-}SiO_2{-}Al_2O_3$ inclusions. This is mainly due to the higher affinity of [Al] towards [O], but $MnO{-}SiO_2$ inclusions can be found to exist at higher [O] levels because of higher oxygen availability for [Si], [Mn] to react and form oxide inclusions. Based on these results, it can be shown that the model is applicable to different steel grades and conditions.

It is important to point out that the inclusion population changes with time in actual refining conditions. In the past, various particle size distribution (PSD) models have been formulated to simulate the different events that govern the dynamics of inclusion population [5, 12, 20, 21, 22]. However, few studies have considered the simultaneous evolution of multiple oxides since the added complexity poses a computational challenge. Interestingly, some of the results from these models can be used in conjunction with chemistry

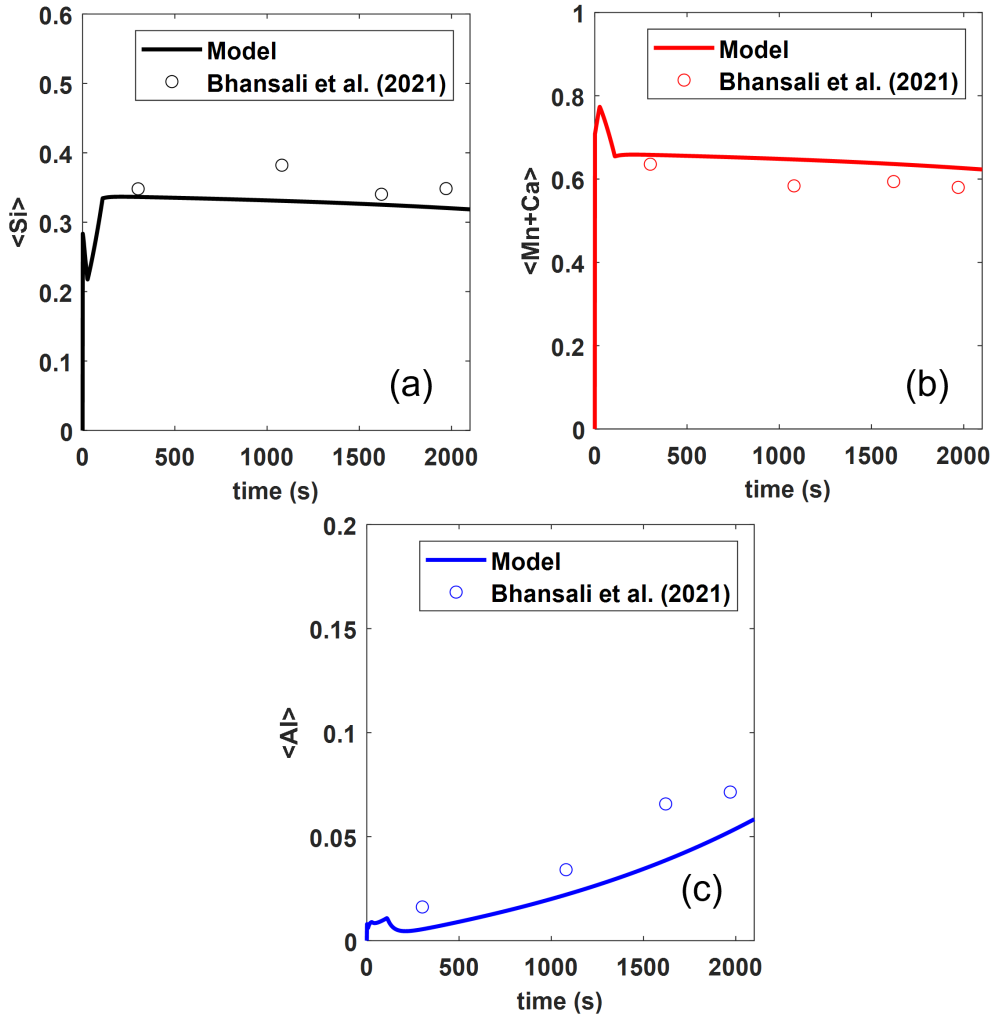

Figure 5.9: *Comparison of industrial and model results for inclusion evolution with time (C3). Note: The cation fractions have been normalized.*

prediction models, such as that developed in this work, to model coupled behavior of multiple inclusions.

In this study, to illustrate the model application with chemical reactions, no physical steps such as aggregation and removal were considered. Moreover, all calculations were carried out using a fixed particle number density for all types of oxide inclusions (Refer to Table 5.3.2) since no reliable information was available to determine physical constants for the removal and aggregation of complex oxide inclusions.

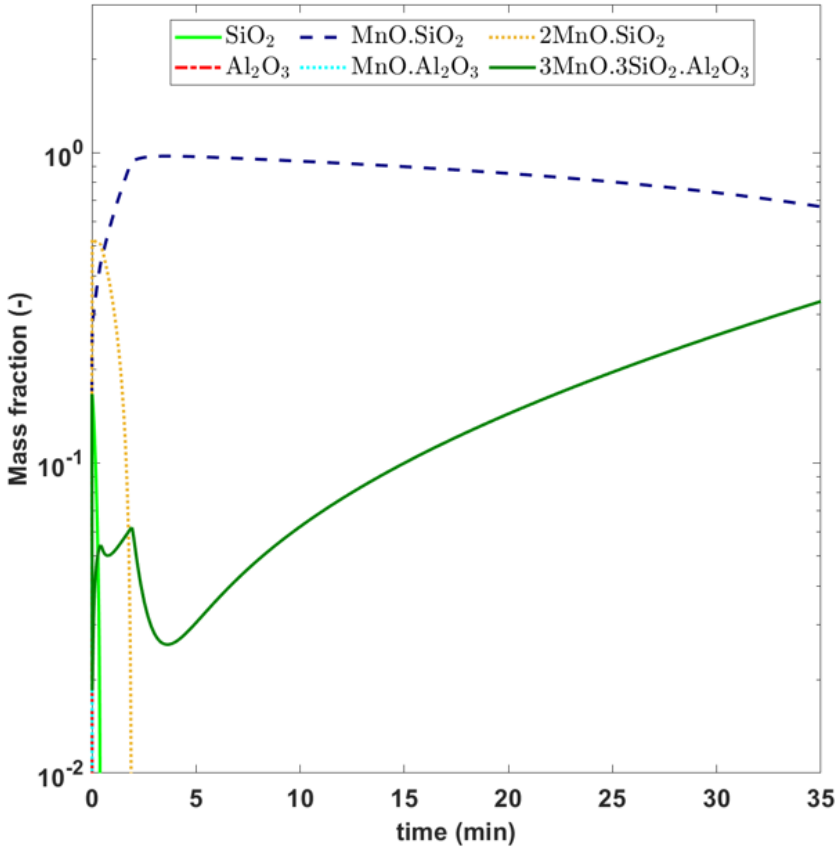

Figure 5.10: *Predicted precipitation sequence of oxide inclusions with time presented as mass fraction relative to the total inclusion population (C3).*

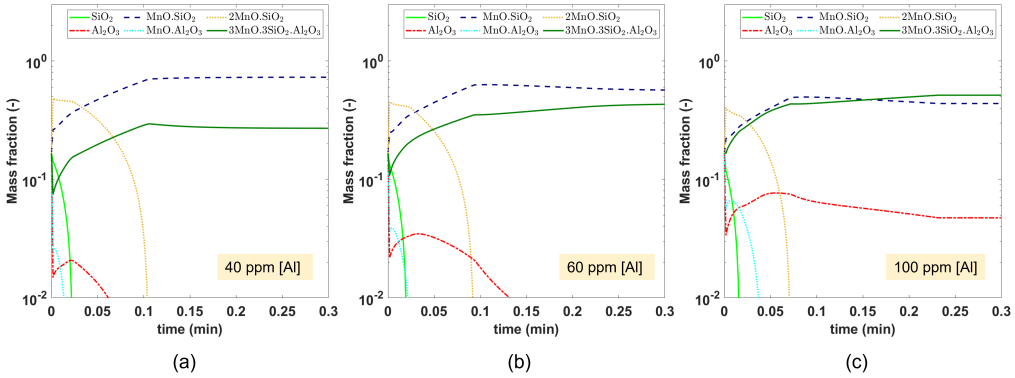

Figure 5.11: *Effect of [Al] on the precipitation sequence of oxide inclusions ([Mn] + [Si] = 1 wt%; [Mn]/[Si] = 5 ; [O] = 500 ppm; $N_t = 10^{14}$).*

5.6 Conclusions

A multi-oxide inclusion kinetic model is proposed to predict the transient evolution of oxide inclusion composition during the steel refining process.

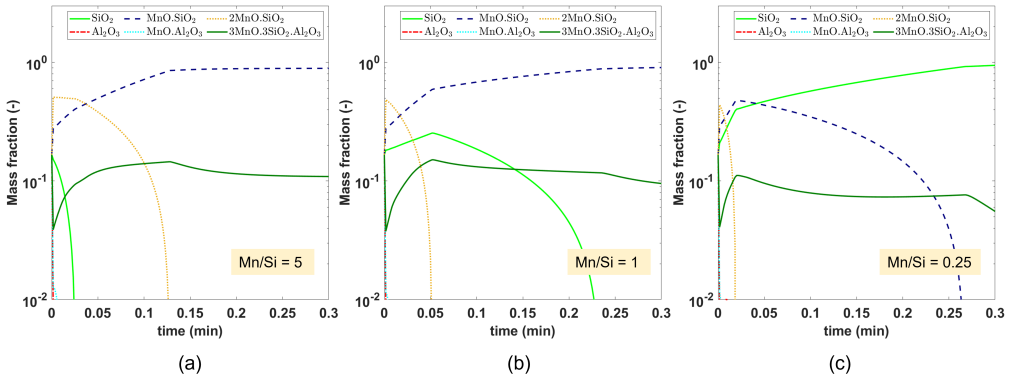

Figure 5.12: *Effect of [Mn]/[Si] on the precipitation sequence of oxide inclusions ([Mn] + [Si] = 1 wt%; [Al] = 20 ppm; [O] = 500 ppm; $N_t = 10^{14}$).*

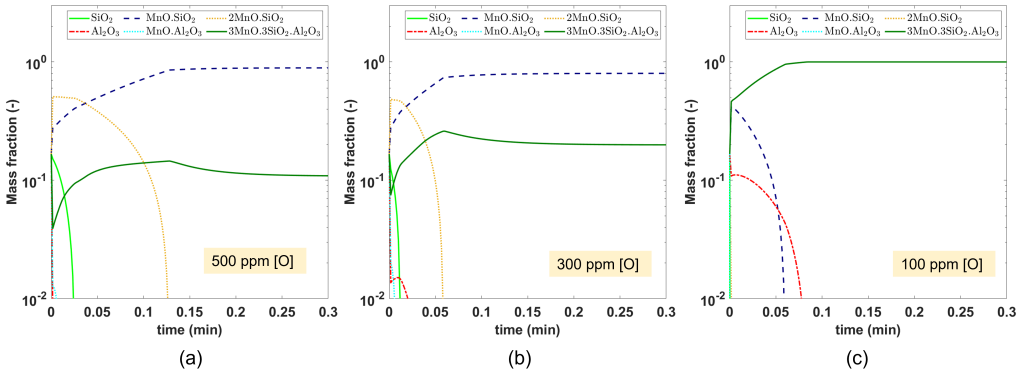

Figure 5.13: *Effect of [O] on the precipitation sequence of oxide inclusions ([Mn] + [Si] = 1 wt%; [Mn]/[Si] = 5 ; [Al] = 20 ppm; $N_t = 10^{14}$).*

Compared to previous models, the model was structured to include seed particles across a range of possible inclusion compositions and allowed the competition for growth or shrinkage among the different inclusions to be dictated by their thermodynamic stability and kinetics of mass transfer between steel and inclusions. Based on a parametric study of the model performance, one may draw the following conclusions:

1. The method of assuming seed particles representing each inclusion type allows the model to accurately predict the competition between different oxide particles and the way in which the population evolves with changing melt chemistry. This is supported by experimental observation at the laboratory and industrial scale.
2. By combining the steel-slag kinetic model with the aforementioned methodology, it is possible to faithfully reproduce the way in which slag composition affects the evolution of the inclusion population.

3. The agreement between parametric analyses and experimental observations suggests that the proposed model offers a powerful approach to evaluating different ladle metallurgy practices.

Efforts are underway in the authors' laboratory to extend this chemical reaction model to include information from high-fidelity particle size distribution models or mean field models, thus giving a more detailed picture of the evolving inclusion population during the refining process.

References

[1] K.J. Graham and G.A. Irons: *Iron Steel Technol.*, 2009, vol. 6, pp. 164-73.
[2] A. Ghosh: Secondary Steelmaking: *Principles and Applications*, 2001.
[3] J.H. Park and L. Zhang: Metall. Mater. Trans. B, 2020, vol. 51, pp. 2453-82.
[4] S.P.T. Piva, D. Kumar, and P.C. Pistorius: *Metall. Mater. Trans. B*, 2017, vol. 48B, pp. 37-45.
[5] N. Rimbert, L. Claudotte, P. Gardin, and J. Lehmann: *Ind. Eng. Chem. Res.*, 2014, vol. 53, pp. 8630-39.
[6] Y. Tabatabaei, K.S. Coley, G.A. Irons, and S. Sun: *Metall. Mater. Trans. B*, 2018, vol. 49B, pp. 375-87.
[7] A. Podder, K.S. Coley, and A.B. Phillion: Steel Res. Int., 2022, vol. 93, pp. 2100831.
[8] C.W. Bale and A.D. Pelton: *Metall. Trans. A*, 1990, vol. 21, pp. 1997-2002.
[9] M. Hino and K. Ito: *Thermodynamic Data for Steelmaking, 1st ed.*, Tohoku University Press, Tokyo, 2010, pp. 16-17.
[10] Z.X. Bing, J.G. Chang, and X.K. Di: *Calphad Comput. Coupling Phase Diagrams Thermochem.*, 1997, vol. 21, pp. 311-20.
[11] F. Oeters: Metallurgy of Steelmaking, Verlag Stahleisen, 1994.
[12] L. Zhang and W. Pluschkell: *Ironmak. Steelmak.*, 2003, vol. 30, pp. 106-10.
[13] C. Zener: J. Appl. Phys., 1949, vol. 20, pp. 950-3.
[14] D.G. Robertson, B. Deo, and S. Ohguchi: Ironmak. Steelmak., 1984, vol. 11, pp. 41-55.
[15] A. Bhansali, H. Oltmann, and E. Pretorius: in AIST proceedings: AISTech 2021, 2021, pp. 1-13.
[16] M. Nabeel, M. Alba, A. Karasev, P. G. Jönsson, and N. Dogan: Metall. Mater. Trans. B Process Metall. Mater. Process. Sci., 2019, vol. 50, pp. 1674-85.
[17] J. Peter, K.D. Peaslee, D.G.C. Robertson, and B.G. Thomas: AISTech - Iron Steel Technol. Conf. Proc., 2005, vol. 1, pp. 959-73.
[18] Y. Zhang, Y. Ren, and L. Zhang: Metall. Res. Technol., 2017, vol. 114, pp. 1-8.
[19] J.S. Park and J.H. Park: Metall. Mater. Trans. B Process Metall. Mater. Process. Sci., 2014, vol. 45, pp. 953-60.
[20] H. Lei and J. He: *J. Mater. Sci. Technol.*, 2012, vol. 28, pp. 642-6.
[21] H. Lei, K. Nakajima, and J.C. He: *ISIJ Int.*, 2010, vol. 50, pp. 1735-45.
[22] I.L.A. Daoud, N. Rimbert, A. Jardy, B. Oesterlé, S. Hans, and J.P. Bellot: Adv. Eng. Mater., 2011, vol. 13, pp. 543-9.
[23] E. T. Turkdogan: *J. Iron Steel Inst.*, 1960, vol. 204, pp. 914-919.

Chapter 6

Simulation of ladle refining reactions of Si–Mn killed steel

In Chapter 6, all of the modelling work and data analysis was carried out by me. Useful discussions on the results were provided by Dr. Kenneth S. Coley and Dr. André B. Philion.

The manuscript was initially drafted by me and edited to the final version by Dr. Kenneth S. Coley and Dr. André B. Philion. This chapter has been submitted to Steel Research International. The following Chapter is the draft version of the manuscript.

Simulation of ladle refining reactions of Si–Mn killed steel

Angshuman Podder[1], **Kenneth Coley**[1,2], **André Phillion**[1]

[1] *McMaster Steel Research Center*
Department of Materials Science and Engineering,
McMaster University, Hamilton, Ontario, Canada, ON L8S 4L7
[2] *Department of Mechanical and Materials Engineering,*
Western University, London, Ontario, Canada, ON N6A 3K7

Abstract

Steel quality, to a large extent, is controlled by ladle refining reactions. The understanding of such reactions can help to prevent the formation of unwanted phases and improve the overall high temperature process control. A new approach, namely the Multi-Oxide Inclusion (MOI) kinetic model has been been recently developed [25] to simulate steel-inclusion reactions in liquid steel. The coupling of this kinetic model with a multicomponent, multiphase steel-slag reaction interface model leads to an overall model framework to predict the evolution of steel, slag, and inclusion composition. The current work shows the application of the model to simultaneous deoxidation and desulphurisation during ladle refining of Si-Mn killed steel. The model shows good performance with industrial data. It is demonstrated that for ladle refining practices, silica-rich slags should be strictly used with basicity (CaO/SiO_2) between 1-1.2, and with Al_2O_3 content less than 5 wt.%. Additional simulations were also carried out to reveal the capability of the model to aid in online process control. Finally, certain limitations of the current model are discussed.

6.1 Introduction

Ladle refining is commonly used industrially to make steel more amenable to processes like deoxidation, desulphurisation, temperature management, and composition control [1]. Complex deoxidation by Si and Mn is beneficial for certain steel products including tire cords, springs, saw wire, and other thin strip cast steels [2]. This is because the use of such deoxidants leads to the formation of low melting inclusions in place of high melting aluminates. The latter is encountered predominantly when Al is used for deoxidation and has been seen to cause nozzle clogging [3], as well as impair the steel deformability [4].

In Si-Mn killed steels, oxide inclusions resulting from deoxidation typically belong to $MnO{-}SiO_2{-}Al_2O_3$ system [5]. In order to control the Al_2O_3 content in the inclusions without calcium treatment, slags with low basicity and low Al_2O_3 content [5, 6] are used to help generate favourable inclusions.

However, such low basicity slags have been reported to have poor desulphurisation characteristics [8] owing to their poor sulfide capacity. In principle, in order to realize low sulphur limits, a slag with high basicity and low oxygen activity in the bulk steel is desired [1]. Bhansali et al. [9] recently showed that although the amount of dissolved oxygen in the steel is controlled by the amount of deoxidizers added to the steel, slag compositions can also exert control on the [O] content [10]. To track such multifarious physico-chemical reactions together with the effect of dynamic changes taking place in the ladle, the development of an integrated model, linked to processing variables, can be helpful. This will allow steelmakers to not only anticipate process uncertainties but help them optimize process parameters to have better casting schedules.

Over the years, a number of kinetic models have been proposed for refining of Al-killed steel utilizing the reaction interface model [11, 12, 13, 14, 15, 16, 17] and the reaction zone model [18, 19, 20, 21, 22, 23, 24]. However, only a few kinetic models have so-far been developed for industrial refining of Si/Si-Mn killed steels [22, 23]. From an industrial point of view, the prediction of change in total and dissolved oxygen along with the composition of steel and inclusions is of prime importance. While total oxygen change is a complex function of process and hydrodynamic variables, other compositional changes can be tracked with the help of a first-principles-based kinetic model.

The current work aims to simulate the steel-slag and steel-inclusion reactions taking place during the ladle refining process of Si-Mn killed steels. For this, a mathematical model recently developed by the current authors [25] based on the reaction interface model is used to study the steel-slag-inclusion reaction kinetics along with behaviour of [Al], [S] and [O] in steel. While our previous study focused on model formulation and validation, this study investigates in detail the industrial refining practices of Si-Mn killed steels. The model results are then compared with two different industrial heat data sets to ascertain the reliability of the model. Following this, the effect of different steel, slag, process, and inclusion variables is demonstrated through extensive simulations. Finally, the further extension of the model to other industrial scenarios and grades is presented.

6.2 Mathematical model

6.2.1 Overview

The model adopted in this work consists of two parts (Refer to Figure 6.1) that take into consideration: a) steel-slag reactions (i.e. the steel-slag model),

and b) steel-inclusion reactions (i.e. the Multi-Oxide Inclusion (MOI) Kinetic Model). The major equations used in the overall model are summarised in Table 6.2.1.

For the first part, the multicomponent steel-slag kinetic model developed by Graham and Irons [15] was used, based on the mixed coupled reaction interface model proposed by Robertson et al. [31]. This model assumes that

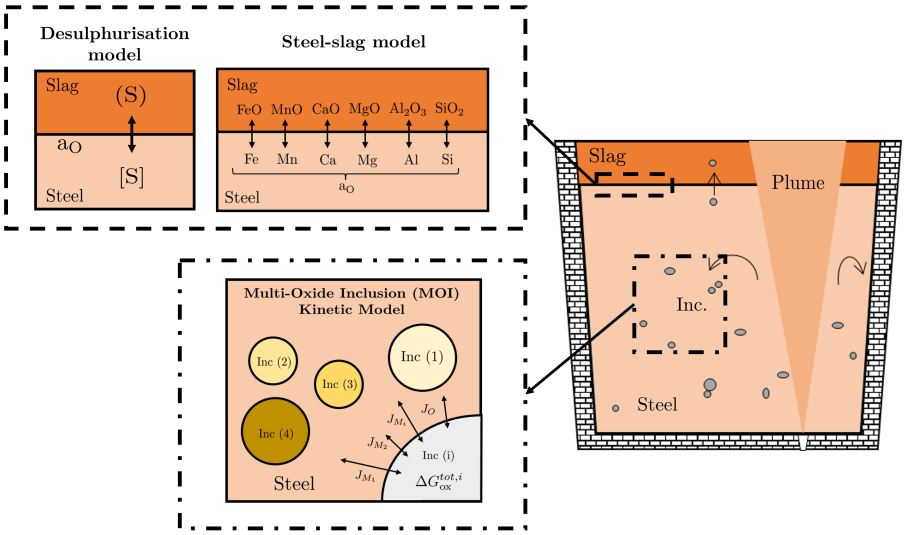

Figure 6.1: *Schematic of steel-slag-inclusion kinetic model.*

the rates of reaction are controlled by multicomponent transport in both metal and slag. Additionally, the chemical reactions are considered to be fast at the slag-metal interface, thus maintaining local equilibrium. This steel-slag kinetic model is linked with a desulphurisation model to model the [S] behavior in steel, utilizing the interfacial oxygen concentration. The desulphurisation model is further described in Section 6.2.2.

For the second part, the steel-inclusion reactions are described by a thermo-kinetic model recently published by the authors [25], which predicts the amount and size changes of multiple oxide inclusions within the molten steel. This model is based on equilibrium thermodynamics and mass transfer theories and can handle the mutual competition between different inclusions. For the system under consideration, the inclusions are a) silica, b) alumina, c) rhodonite, d) tephroite, e) spessartite, and f) galaxite. Please note that the equilibrium constants for the different reactions ([M]-[O]) have been sourced from Ref. [15].

Table 6.2.1: *Summary of equations for steel-slag-inclusion reaction model*

Phase interaction	Equations	
Steel-inclusion	**Thermodynamics :**	
	$x_1\underline{\mathrm{M_1}} + x_2\underline{\mathrm{M_2}} + x_3\underline{\mathrm{M_3}} + x_n\underline{\mathrm{M_n}} + y\underline{\mathrm{O}} = \mathrm{M_{1,x_1}M_{2,x_2}...O_y}$	(6.2.1.1)
	$K_{eq,\mathrm{M_{1,x_1}M_{2,x_2}...O_y}} = \dfrac{a_{\mathrm{M_{1,x_1}M_{2,x_2}..O_y}}}{\prod_i h_{\underline{\mathrm{M_i}}}^{x_i} h_{\underline{\mathrm{O}}}^{y}},$	(6.2.1.2)
	$K_{\mathrm{eq},i} = \exp\left(-\dfrac{\Delta G_{\mathrm{ox}}^{tot}}{RT}\right)$	(6.2.1.3)
	$\Delta G_{\mathrm{ox},i}^{tot} = -\sum_j x_j RT \log K_j + \Delta G_i^{mix} + \Delta G_i^{L\to S}$ (if solid)	(6.2.1.4)
	Kinetics :	
	$J_i = k_{m,i}\pi d^2(C_i^b - C_i^*).$	(6.2.1.5)
	$\dfrac{J_{\mathrm{M_1}}}{x_1} = \dfrac{J_{\mathrm{M_2}}}{x_2} = \dfrac{J_{\mathrm{M_3}}}{x_3}... = \dfrac{J_{\mathrm{M_n}}}{x_n} = \dfrac{J_{\mathrm{O}}}{y}$	(6.2.1.6)
	Inclusion chemical growth :	
	$\dfrac{\mathrm{d}r}{\mathrm{d}t} = \dfrac{D_O}{r}\cdot\dfrac{X_O - X_O^*}{\alpha X_O^{\mathrm{inc}} - X_O^*}$	(6.2.1.7)
Steel-slag	**Thermodynamics :**	
	$x[\mathrm{M}] + y[\mathrm{O}] = (\mathrm{M}_x\mathrm{O}_y)$	(6.2.1.8)
	$K_{\mathrm{M}_x\mathrm{O}_y} = \dfrac{a_{\mathrm{M}_x\mathrm{O}_y}}{a_M^x \cdot a_O^y},$	(6.2.1.9)
	$a_i = 100\dfrac{f_{\mathrm{i}} X_{\mathrm{i}}^* \mathrm{MW_i}}{\mathrm{MW_{Fe}}}$	(6.2.1.10)
	Kinetics :	
	$\dfrac{dX_M^{st}}{dt} = \dfrac{k_{m,M}^{st} A}{V_{st}}\cdot\left(X_M^b - X_M^*\right)$	(6.2.1.11)
	$\dfrac{dX_{M_xO_y}^{sl}}{dt} = \dfrac{k_{m,M_xO_y}^{sl} A}{V_{sl}}\cdot\left(X_{M_xO_y}^b - X_{M_xO_y}^*\right)$	(6.2.1.12)

6.2.2 Desulphurisation model

The desulphurisation reaction occurring between the steel and the slag in Si-Mn killed steels is assumed to take place according to:

$$\frac{1}{2}[\mathrm{Si}] + [\mathrm{S}] + (\mathrm{CaO}) = (\mathrm{CaS}) + \frac{1}{2}(\mathrm{SiO_2})\,. \tag{6.2.1}$$

The thermodynamic extent of the desulphurisation process is measured using the sulfur partition ratio (L_S), which is a function of the sulfide capacity (C_S), oxygen activity, a^*_O at the interface as well as temperature, T, and is calculated as:

$$\log L_\mathrm{S} = \log \frac{(\%\mathrm{S})}{[\%\mathrm{S}]} = -\frac{935}{T} + 1.375 + \log(C_\mathrm{S}) + \log f_\mathrm{S} - \log a^*_\mathrm{O}, \tag{6.2.2}$$

C_s represents the desulphurization 'power' of the liquid slag and is a function of temperature and slag composition. In this work, Young's model [32] is utilized to compute this term, which is expressed as a function of optical basicity, Λ.

For Λ <0.8 :

$$\begin{aligned}\log(C_S) = &-13.913 + 42.84\Lambda - 23.82\Lambda^2 - (11710/T)\\ &- 0.02223\,(\%\,\mathrm{SiO_2}) - 0.02275\,(\%\,\mathrm{Al_2O_3})\end{aligned} \tag{6.2.3}$$

For $\Lambda \geq 0.8$:

$$\begin{aligned}C_S = &-0.6261 + 0.4808\Lambda + 0.7197\Lambda^2 + (1697/T)\\ &- (2587/T) + 0.000514\,(\%\,\mathrm{FeO})\end{aligned} \tag{6.2.4}$$

The optical basicity of the slag is calculated as [33]:

$$\Lambda = \frac{\sum(x_i n_i \Lambda_i)}{\sum(x_i n_i)} \tag{6.2.5}$$

where the optical basicities of the pure oxides i are listed in Table 6.2.2.

Table 6.2.2: *Optical Basicity values of Pure Oxides [32]*

	CaO	SiO_2	FeO	MgO	MnO	Al_2O_3
Λ_i	1.0	0.48	0.51	0.78	0.59	0.61

Finally, the kinetics of desulfurisation are described by combining the rate equations in Eqns. 6.2.1.11 and 6.2.1.12, the sulphur partition ratio (Eq. 6.2.2), and the mass balance of sulphur between steel and slag:

$$\frac{dn_S}{dt} = k^{\circ}_{m,S} A \left(C_{V,st} X^{b}_{[S]} - C_{V,sl} \frac{X^{b}_{(S)}}{L'_S} \right). \tag{6.2.6}$$

Here, k°_m is defined as:

$$\frac{1}{k^{\circ}_m} = \frac{1}{k^{st}_m} + \frac{1}{k^{sl}_m L_S} \tag{6.2.7}$$

and L'_S is defined as:

$$L'_S = \frac{W_{st}}{W_{sl}} L_S \tag{6.2.8}$$

6.2.3 Determination of activities of species

For the thermodynamics of the chemical reactions, activities of each species within different phases are required. The activities in the liquid steel were calculated using a subroutine utilizing the unified interaction parameter formalism (UIPF) by Pelton and Bale [35]. The activities of the slag components were calculated using a subroutine involving the Gaye and co-workers' cell model [36, 37] for slags. Please note that the contribution of S^{2-} and F^{-} towards oxide activity calculation was not considered in the cell model since oxides constituted more than 90 wt% of the slag. Finally, the inclusion oxide activities were calculated using the sub-regular solution model (SRSM) developed by Xiaobing et al. [38], instead of the cell model, owing to its better accuracy for the $CaO{-}MnO{-}SiO_2{-}Al_2O_3$ system.

6.2.4 Determination of mass transfer coefficients

The mass transfer capacity for steel-slag reactions is described as follows:

$$K = \frac{k^{st}_m A}{V_{st}} = B\dot{\epsilon}^{n} \tag{6.2.9}$$

where the effective stirring energy from gas flow rates [13] is computed via:

$$\dot{\epsilon} = \left(\frac{101330}{273} \right) \cdot \left(\frac{N \cdot Q \cdot T}{W_{\mathrm{st}}} \right) \ln \left(1 + \frac{P_{\mathrm{t}}}{101330} \right) \tag{6.2.10}$$

Finally, for steel-inclusion reactions, the mass transfer problem can be treated as that between a fluid medium and a dispersion of spherical particles where the Sherwood number is taken as 2 [29]. As a result, the mass transfer coefficient for the steel-inclusion reactions is given by:

$$k_{m,i} = \frac{D_i \cdot Sh}{d} \tag{6.2.11}$$

6.3 Description of Simulation Studies

In order to validate the model, data from two industrial trials pertaining to the ladle refining process of Si-Mn killed steel have been used. A brief description of each process, denoted as C1 and C2, is provided in Table 6.3.1. After validating the model against literature data, parametric studies were carried out to understand the role of different steel, slag, process, and inclusion variables on the model results, specifically, inclusion composition, as well as [Al], [S], and [O] variations with time. The base steel and slag compositions for this simulation are denoted as P1. Tables 6.3.2 and 6.3.3 show the chemical compositions of the steel and slag for C1, C2, and P1, while the corresponding model initialization parameters are provided in Tables 6.3.4 and 6.3.5. Wherever not mentioned, the model parameters for P1 are the same as C2. Finally, the composition and recovery rates of the additions for C2 are listed in Table 6.3.6. The details of the sampling and analysis procedures can be found in [9, 23]. Please note that since some information was not made available in the original research articles, they had to be assumed. These are denoted with a * in the tables.

To complete the model, additional assumptions and considerations are required. First, the alloy addition rate is tuned to match the dissolution and mixing rate determined from the measured steel composition data. Second, the alloy and slag additions are made to the steel and slag bulk phases, respectively, which are input to the model as an auxiliary file. Third, although industrial practice includes Ca injection, calcium dissolution kinetics are not included. This is because Ca recovery, and Ca pickup within inclusions are both assumed to be small [34]. Fourth, the refractory-steel reactions have not been included since in the current situations, Mg pickup is seen to [24] only negligibly affect inclusion composition.

Table 6.3.1: *Summary of case studies used in this work*

Case	Authors	Ref.	Route	Steel Grade	Comments
C1	Peter et al.	[23]	EAF-LF-CC	Low C steel	FeSi (120 kg) and SiMn (2126 kg) were used for deoxidation; Other additions include spar (340 kg), lime (1281 kg), MgO (54 kg), FeV (45 kg); CaSi (9 kg), Oxidized skull/Fe_2O_3 (104 kg); steel and slag composition data were reported; METSIM model was used for dynamic simulation.
C2	Bhansali et al.	[9]	EAF-LF-CC	Low C steel	Pre-weighed mixture of SiMn, dolomite, silica sand, and Lime was added in the ladle after tap; steel compositions, initial slag composition and inclusion analysis were reported; FactSage thermodynamic calculations performed.

Table 6.3.2: *Chemical composition of the steel used as inputs in this study*

Case	**C**	**Mn**	**Si**	**Al**	**Ca**	**S**	**O**	**Fe**
C1	0.06	0.11	0.005	0.003	0.00	0.047	0.050*	Bal.
C2	0.06	1.05	0.27	0.001	0.0005	0.021	0.052	Bal.
P1	0.06	1.00	0.25	0.001	0.0005	0.020	0.030	Bal.

Note: * indicates that the parameter is assumed.

Table 6.3.3: *Chemical composition of the slag used as input in the model*

Case	**CaO**	**SiO_2**	**Al_2O_3**	**MgO**	**FeO**	**MnO**	**CaS**	**CaF_2**	**Basicity**
C1	40	25	3.5	14	8	4	0.1	1	1.60
C2	44	28	7	10	0.7	0.4	0.001	-	1.57
P1	44	28	8	10	0.7	0.4	0.001	-	1.57

Table 6.3.4: *Model initialization parameters*

Parameter	**Units**	**C1**	**C2**
Steel Mass	ton	120	170
Slag Mass	ton	2.5	3
Crucible/Ladle diameter	m	2.612	2.612*
Effective reaction area	m^2	7.11	7.11
K	s^{-1}	$6 \times 10^{-6}\dot{\epsilon}^{1.5}$	$6 \times 10^{-6}\dot{\epsilon}^{1.4}$
Inclusion number density	m^{-3}	1×10^{13}	1×10^{13}
Initial inclusion diameter	μm	1	1
Gas flow rate	Nm^3/hr	11.24	11.24*
Plugs	–	1	2*
$\Delta t_{st/inc}$	s	0.05	0.05
$\Delta t_{st/sl}$	s	1	1

Note: * indicates that the parameter is assumed.

Table 6.3.5: *Ratio of mass transfer coefficient in slag and metal phases*

k_m^{sl}/k_m^{st}	**CaO**	**SiO_2**	**Al_2O_3**	**MgO**	**FeO**	**MnO**	**CaS**
C1	0.1	0.2	0.3	0.1	0.1	0.25	0.1
C2	0.1	0.2	0.3	0.1	0.1	0.1	0.1

Table 6.3.6: *Chemical composition of raw materials used for C2.*

	C	Mn	Si	Al	Ca	S	Fe	Recovery (%)
FeSi	0.05	0.212	79.96	1.12	0.08	-	Bal.	75
SiMn	1.00	71.80	16.3	-	0.001	0.007	Bal.	85
CaSi	1.00	-	65.00	-	33.00	0.040	Bal.	30

6.4 Results

6.4.1 Comparison of Model Predictions to Industrial Data

In this section, the model results have been compared with steel, slag, and inclusion data that were available from the reported literature, Table 6.2.1. Figure 6.2 shows the comparison of steel composition measurements ([Si], [Mn], [C], [Al], [S]) with that obtained from the model. As can be seen, excellent agreement is achieved for both C1 and C2. From the model predictions, it was found that the variation of species with high concentrations ([Si], [Mn], [C]) is dictated essentially by the amount of additions and the rate at which they dissolve and mix, whereas the variation of species with lower concentrations ([Al], [S]) is dictated by the steel-slag reactions and the mutual interaction with the inclusions.

Figure 6.3 shows the comparison of average inclusion composition data with model predictions, while Figure 6.4 shows the formation of different inclusion phases with time. It can be seen the model predictions show great agreement with that obtained from industrial trial C2. Figure 6.4 also illustrates that the types of inclusions in these steel and slag conditions lie primarily between Mn silicates and Mn aluminosilicates. This coincides with what is observed in actual inclusion analysis data reported for C2. Unfortunately, since no inclusion information was reported for C1, it is difficult to compare the model predictions in that case. However, the authors strongly believe similar observations are likely to persist.

6.4.2 Parametric study

Following the validation of the model in Section 6.4.1, the following sections will employ the model to explore the effects of various composition and process parameters. Figures 6.5-6.11 show the results of a series of simulations carried out with different steel and slag composition variables. The base steel and slag composition is shown as P1 in Tables 6.3.1 and 6.3.2. For one set of

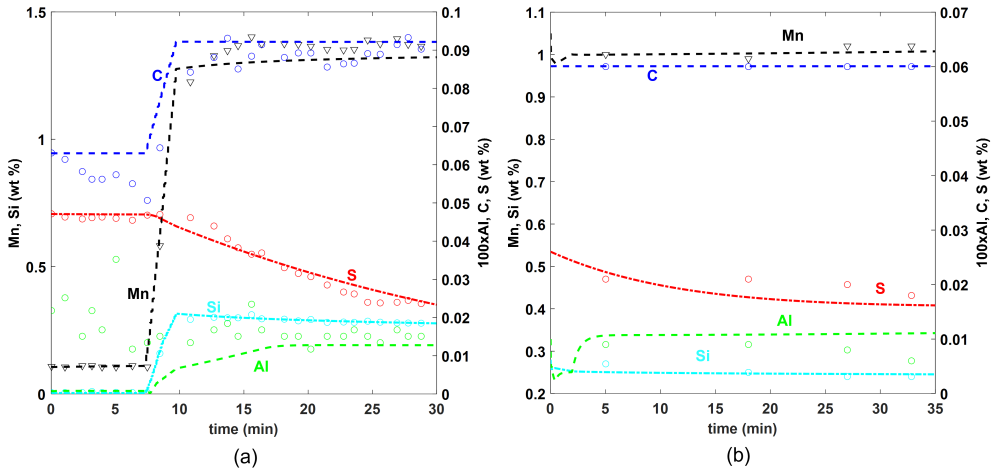

Figure 6.2: *Comparison of steel composition evolution predicted by the model, and that obtained from measurements for cases (a) C1 and (b) C2.*

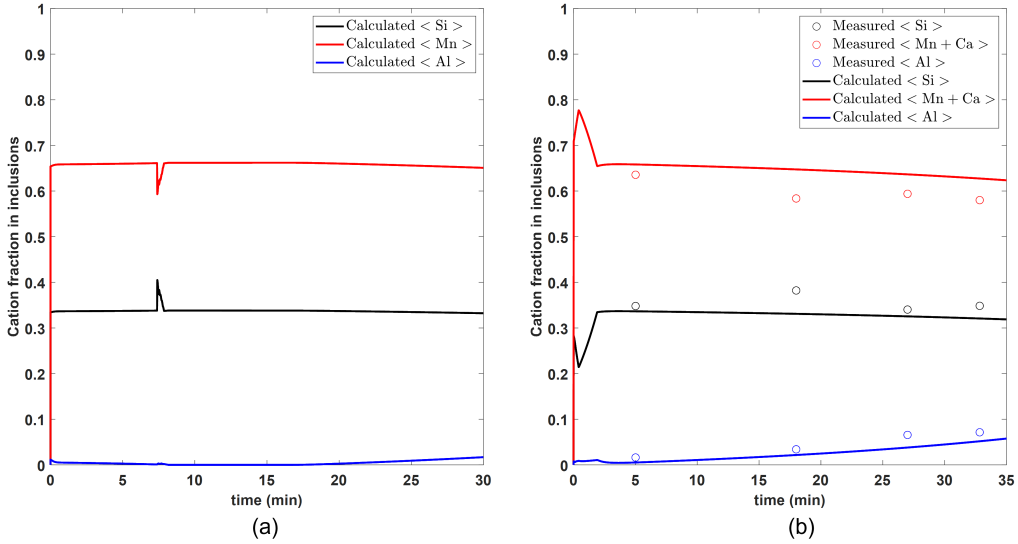

Figure 6.3: *Inclusion composition (cation fraction) evolution predicted by the model for cases (a) C1 and (b) C2, and that obtained from measurements for C2*

simulations, the [A] and [O] content within the steel were varied. For a second set of simulations, the basicity (R = CaO/SiO_2), (C/A = CaO/Al_2O_3), and (FeO + MnO) were changed. For a third set of simulations, the process variables specifically the stirring rate and local reoxidation have been changed. Finally, the effect of different inclusion number densities was studied.

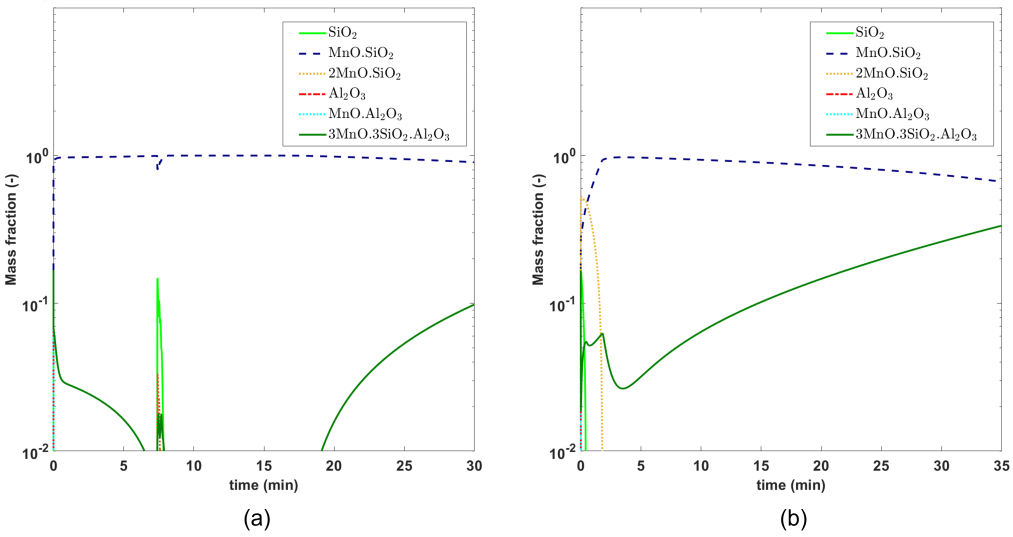

Figure 6.4: *Inclusion precipitation sequence for cases (a) C1 and (b) C2 as predicted by the model.*

Effect of steel composition

Figure 6.5 shows the effect of initial [Al] content on the average Al_2O_3 inclusion content as well as the type of inclusions forming within the steel with time. As can be seen in Figure 6.5a, at low levels of [Al] the fraction of pure Al_2O_3 remains low with complex Mn aluminosilicate mostly precipitating. However, above a certain limit (here, around 200 ppm), a significant fraction of the precipitates are pure Al_2O_3, with only a small amount of the Al forming complex inclusions. This point is further indicated in Figure 6.5b, whereby for low [Al] the fraction of pure Al_2O_3 decreases with time, but for high [Al] (i.e. 200 ppm), the fraction of pure Al_2O_3 increases with time, along with Mn silicates (not shown in the figure). Please note that the identified 200 ppm limit is a strong function of the oxygen content in the steel. Also, it can be expected that in such a case, Mn aluminosilicates will be rich in Al.

Figure 6.6 shows the effect of initial [O] content on the average Al_2O_3 content of inclusions, as well as the [O] variation with time and the [S] variation with time. From Figure 6.6a, it can be seen that lowering the initial oxygen levels leads to more Al-rich inclusions as well as pure alumina. This is because the driving force for forming other inclusion phases is not high in these conditions. From Figure 6.6b, it can be seen that [O] is predicted to drop suddenly at the beginning of refining owing to the high driving force for oxide formation. Additionally, a decrease in initial [O] content is also shown to lead to lower final [O] contents, as dictated by the Al-O deoxidation equilibriium. It can also be seen that the [S] level drops with time, albeit at a much slower rate

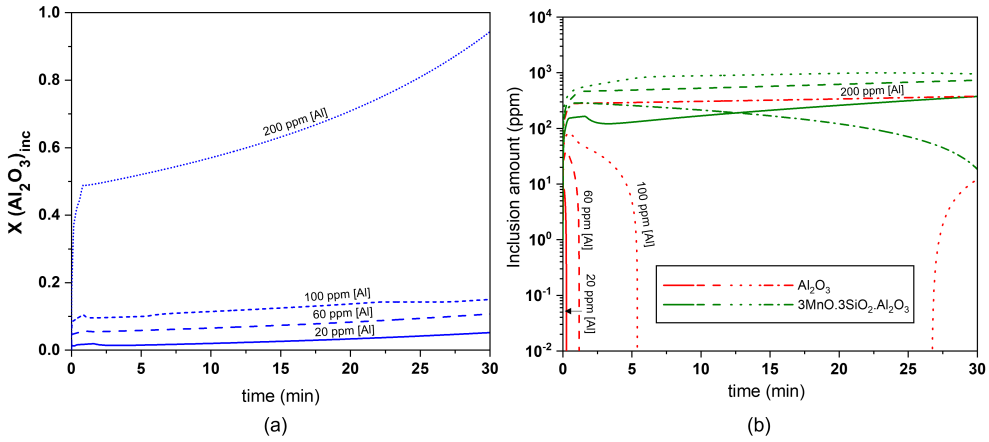

Figure 6.5: *Effect of initial [Al] content on the evolution of (a) the average Al_2O_3 content within all inclusions in the melt and (b) Al_2O_3 and Mn aluminosilicate precipitation sequence.*

than [O]. However, de-sulphurization is minimally affected by different initial oxygen levels.

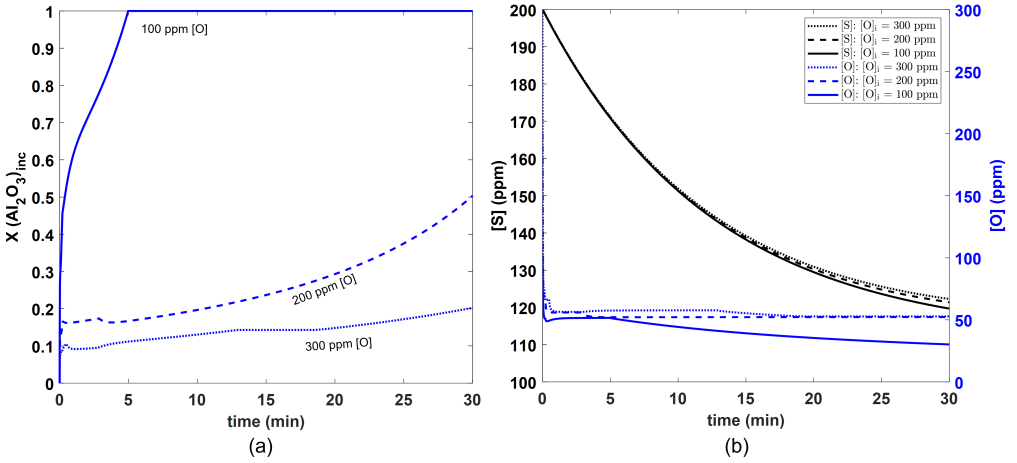

Figure 6.6: *Effect of initial [O] content on the evolution of (a) the average Al_2O_3 content within all inclusions, and (b) the de-oxidation as well as the de-sulphurization of the steel.*

Effect of slag composition

Figures 6.7, 6.8, and 6.9 show the effect of basicity (R = CaO/SiO_2), (C/A = CaO/Al_2O_3), and (FeO + MnO) on the evolution of (a) the [Al] content and the average Al_2O_3 content within all inclusions, as well as (b) de-oxidation as well as de-sulphurization of the steel.

It can be seen in Figure 6.7a that a slag with higher basicity (($R = CaO/SiO_2$) will promote more Al pick-up owing to the lower silica in the slag (higher Al_2O_3 in slag), which in turn promotes more Mn-aluminosilicates and alumina inclusions within the steel. Please refer to Ref. [10, 24], for a discussion on the Al pickup from slags. Figure 6.7b shows that lower final [O] levels are reached owing to precipitation deoxidation with an increase in basicity, while lower [S] levels can be realized with higher basicity slags especially with R≈ 2-2.5 since such slags exhibit higher sulfide capacities [39].

Figure 6.8a show that a decrease in the ($C/A = CaO/Al_2O_3$) ratio (obtained by changing the Al_2O_3/SiO_2 ratio in the slag) leads to more Al pick up in steel and greater Al_2O_3 within all inclusions. This again suggests that alumina-rich slags cannot be utilized for such steels. However, with lower C/A ratios, lower final [O] levels are obtained since more [Al] is available to react with [O]. Furthermore, it is seen that a greater extent of de-sulphurization is obtained with lower (C/A) ratios. This is because of higher Al_2O_3 and lower SiO_2 within slag (i.e. a higher basicity).

Figure 6.9 a shows that there is a fade of [Al] with an increase in (FeO + MnO), as well as a slight fade in [Si] and [Mn] (but not shown). Although the Al_2O_3 within all inclusions is one order of magnitude lower than seen in Figures 6.7 and 6.8, different inclusions can precipitate depending on how [O] reacts with other species within the steel [24]. Figure 6.9b shows further that an increase in (FeO + MnO) affects significantly de-sulphurization, but not de-oxidation. This is because higher (FeO + MnO) content in slag increases the interfacial activity of oxygen at the steel/slag interface.

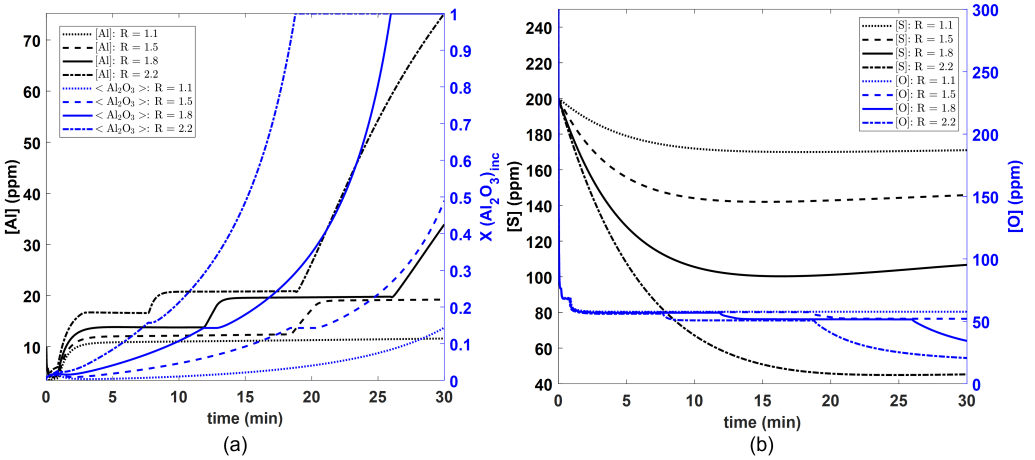

Figure 6.7: *Effect of basicity ($R = CaO/SiO_2$) on the evolution of (a) the [Al] content and the average Al_2O_3 content within all inclusions, and (b) the de-oxidation as well as the de-sulphurization of the steel.*

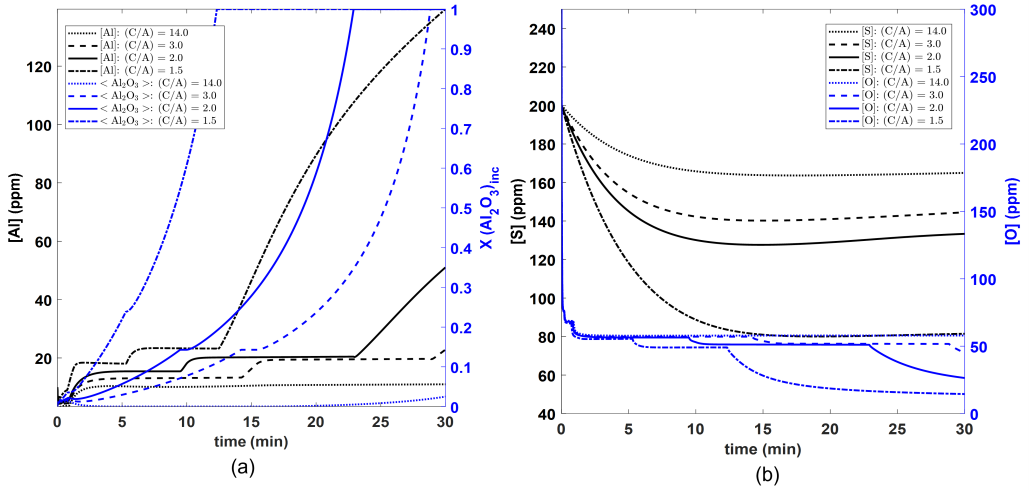

Figure 6.8: *Effect of ($C/A = CaO/Al_2O_3$) on the evolution of (a) the [Al] content and the average Al_2O_3 content within all inclusions, and (b) the de-oxidation as well as the de-sulphurization of the steel.*

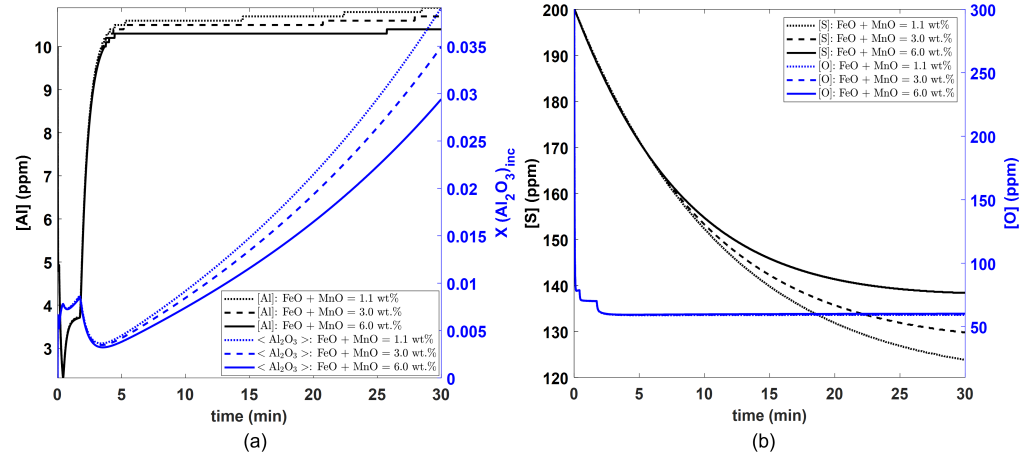

Figure 6.9: *Effect of (FeO + MnO) on the evolution of (a) the [Al] content and the average Al_2O_3 content within inclusions, and (b) the de-oxidation as well as the de-sulphurization of the steel.*

Effect of process variables

Figure 6.10 shows the effect of different gas stirring rates on the evolution of the [Al] content and the average Al_2O_3 content within all inclusions, as well as the de-odixation and the de-sulphurization of the steel. As shown in Figure 6.10a, more mass transfer (Al pickup) is promoted at the steel/slag interface at higher gas flow rates thus increasing the average Al_2O_3 content within

all inclusions. Figure 6.10b shows that de-oxidation is minimally affected by higher gas stirring rates (until longer times), while de-sulphurization is significantly affected. However, after about 15 min, Figure 6.10a shows a significant increase in the [Al] within the steel at both 300 NL/min and 400 NL/min. This is a result of more inclusion precipitation reactions within the steel, leading to further de-oxidation of the steel. With these higher gas flow rates, the [S] reaches a minimum value at which point it begins to revert back into the steel owing to sulphur in the slag exceeding the slag sulphide capacity. Please note that the contribution of air reoxidation (through an open 'slag eye') can be significant with higher stirring rates, affecting the [O] and [S] and inclusion population dynamics [41]. However, this phenomenon is not currently included in the model.

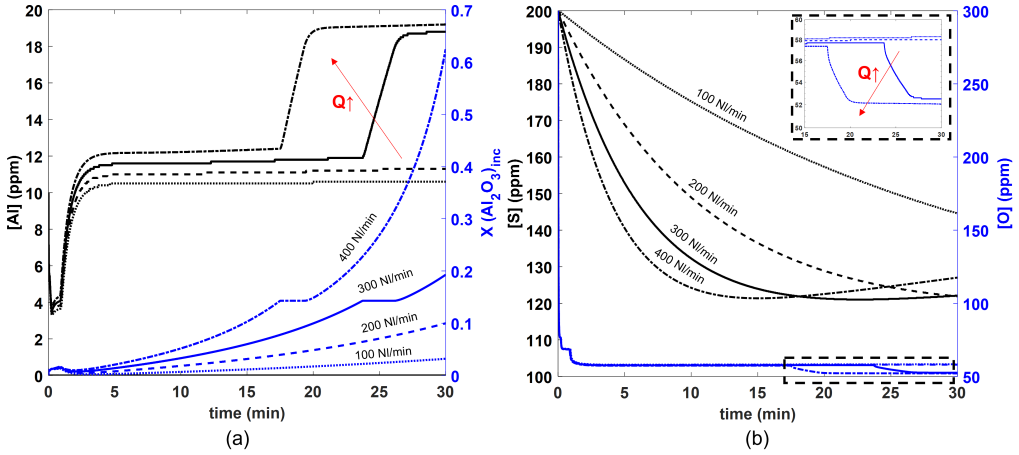

Figure 6.10: *Effect of stirring rates on the evolution of (a) the average Al_2O_3 content within all inclusions, and (b) the de-oxidation as well as the de-sulphurization of the steel.*

Figure 6.11 shows the effect of local reoxidation on the precipitation sequence of all inclusions included within the model. As can be seen, a sudden increase in oxygen ($\approx$ 100 ppm [O]) at 15 min leads to the destabilization of Mn-silicates. This results in the formation of additional Mn aluminosilicates owing to a reaction between the excess [O] with the [Al] and existing inclusions.

Effect of inclusion number density within steel

The simulations conducted above assumed a constant number density for the inclusion population [11], with all inclusions having the same size. Figure 6.12 shows how the average composition of inclusions evolves for three different average number densities, $N_t = 10^{11}, 10^{12}$, and 10^{13} $/m^3$. As can be seen,

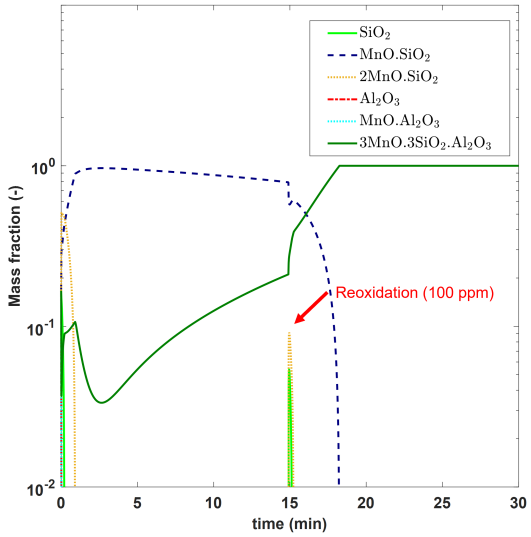

Figure 6.11: *Effect of local reoxidation, i.e. the addition of ≈ 100 ppm [O] at 15 min, on the inclusion precipitation sequence.*

a lower value for N_t leads to an increase in the time that it takes for the compositional equilibrium between inclusion and melt to be reached. This indicates that an instantaneous, local equilibrium assumption between steel and inclusions might not always hold throughout the entire refining time. Furthermore, the inclusion concentration is known to decrease with time as inclusions get removed from the steel by the slag and/or by the refractory walls [1]. This combined with the results shown in Figure 6.12 demonstrates the importance of considering an evolving inclusion number density. Such phenomena will be included in a future model.

6.5 Industrial applications

Having conducted a wide number of parametric analyses, the model is now applied to three other industrial situations: a slag-changing operation and two additional steel grades, to demonstrate its capabilities.

In an effort to improve desulphurisation [42, 43, 44, 45], certain steel producers have opted to change the slag basicity during refining. Similar to a previous study [46], in this study, the slag basicity was increased from 1.5 to 2.0 by adding 250 kg CaO to the slag (denoted as P1) after about 6 min of refining. The modelling results are presented in Figure 6.13. As can be seen, the effect of the slag change is to increase the [Al] in the melt (and correspondingly increase the alumina and Al-rich inclusions), but concurrently

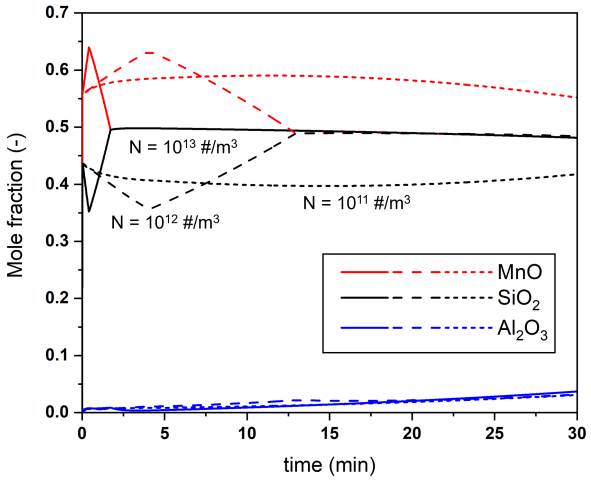

Figure 6.12: *Effect of inclusion number density on the evolution of inclusion composition.*

decreasing the [S]. Thus, one of the uses of this model is in process optimization, in order to determine the ideal window for minimizing both [Al] and [S].

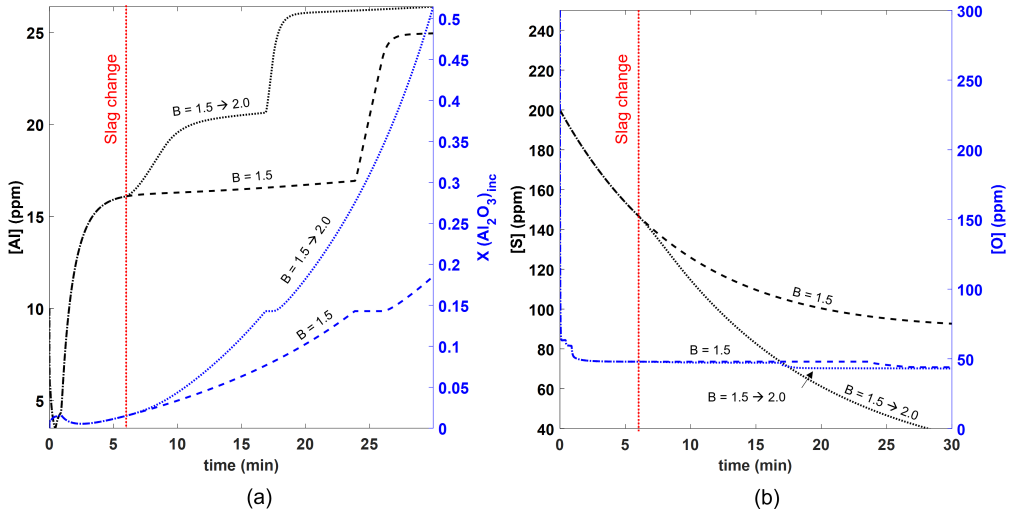

Figure 6.13: *Effect of slag change (R = 1.5 to 2.0) on the evolution of (a) the [Al] content and the average Al_2O_3 content within inclusions, and (b) the de-oxidation as well as the de-sulphurization of the steel*

As was seen in the parametric analysis, the steel compositional variables play an important role in controlling the inclusion composition. Figure 6.14 shows how the current model can be used to predict inclusion composition

for two different steel chemistries, a typical Si-killed spring steel and a tire cord (high-carbon grade) steel (S1 and S2 in Table 6.5.1).

Figure 6.14a shows the inclusion precipitation sequence for S1, and also identifies that silica inclusions constitute the major fraction. This prediction is consistent with experimental observations [47] where the majority of inclusions encountered in grades where the [Mn]/[Si]< 1 are mostly silica or silicates (e.g. mullite). Figure 6.14b shows in contrast that the inclusion precipitation sequence for S2 includes not only Mn silicates but also Mn aluminosilicates. This prediction is consistent with the fact that in such steels, the inclusions are reported to belong to mostly Al-rich Mn aluminosilicates [46].

Table 6.5.1: *Chemical composition of the spring steel and tire cord steel used as model inputs*

Case	C	Mn	Si	Cr	Al	Ca	S	O	Fe
S1	0.55	1.00	0.70	0.67	0.001	0.0005	0.020	0.030	Bal.
S2	0.81	0.76	0.25	-	0.001	0.0005	0.020	0.030	Bal.

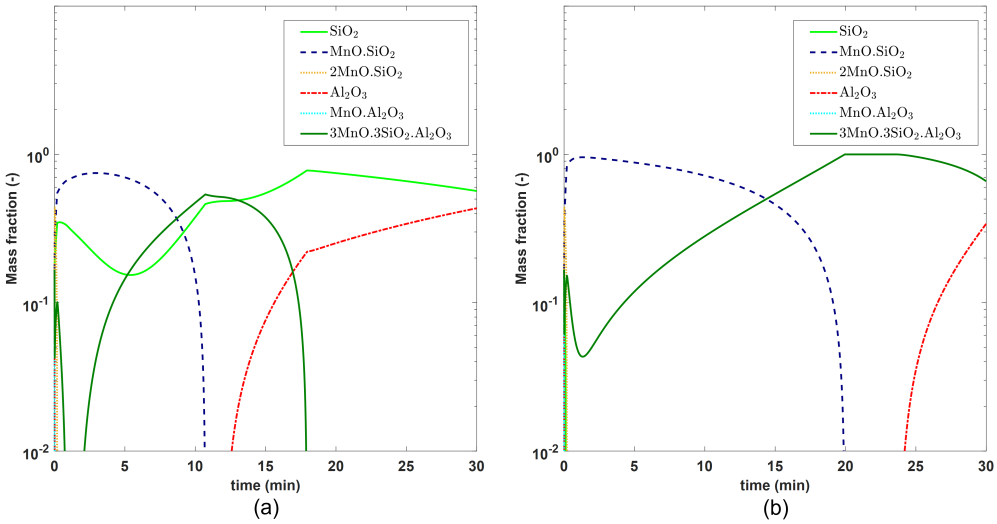

Figure 6.14: *Inclusion precipitation sequence for (a) spring steel (S1); (b) tire cord steel (S2)*

.

6.6 Discussion

The current study provides a comprehensive basis for many aspects of ladle metallurgy in Si-Mn killed steels by conducting a wide range of simulations with the proposed steel-slag-inclusion model. From the simulations conducted with different slag compositions, a top slag with a basicity of 1.0-1.2 with an Al_2O_3 content of less than 5 wt.% is suggested to be used for optimum inclusion composition control. However, higher initial [S] in steel cannot be reduced to a considerable extent in the ladle furnace with such slags at moderate stirring. Resorting to slag adjusting or longer refining times in vacuum degassing stations can be useful in such cases. Furthermore, the (FeO+MnO) should be minimized to avoid affecting [S] removal rates although it helps in decreasing [Al] pick-up rates in the steel.

6.6.1 Comparison with Al-killed steel

In the context of this study, it is worthwhile pointing out certain differences between killing practices that are typically used for other high Mn, high Al steel grades. First, higher [Al] contents in Al-killed steel lead to lower [O], and [S] levels in steel than Si-Mn killed steels [1]. However, this comes at the cost of producing alumina inclusions. These often turn into Mg spinels, and calcium aluminates [11] (post-Ca treatment), most of which are responsible for nozzle clogging. In Si-Mn killed steel, as seen above, Mn-silicates and Mn aluminosilicates are the inclusions most likely to be encountered, with the former being preferred for smooth casting operations. Moreover, as seen in Sec. 6.4.2, a high initial [Al] in steel can be detrimental to Si-Mn killed steel production. The current findings indicate that FeSi ferroalloy with a high Al fraction can seldom be used for deoxidation and that the permissible level of Al impurity within the ferroalloy should be fairly small. Second, the type of slags employed in Si-Mn killed steels should be silica-rich, in contrast to alumina-rich slags in Al-killed steels. The result of this is that very low [S] levels cannot be reached owing to the Si-rich slag's lower sulfide capacities. Additionally, the contribution of slag towards additional deoxidation in Si-Mn killed steel seems to be more pronounced since [O] levels in Al-killed steels are already very low ($\approx$ 2-5 ppm) post-deoxidation.

6.6.2 Inclusion formation at low oxygen concentrations

This study also showed that a high initial [O] in steel could lead to a lowering of alumina content within the inclusions. This was also recently observed in practice [48]. It is interesting to note that high-carbon steels have lower initial oxygen levels based on [C]-[O] equilibrium [48]. As a result, the total

mass of inclusions produced from the deoxidation process should be small owing to low supersaturation for inclusion nucleation and growth. However, in practice, inclusions are seen to be present in abundance in such steels which suggests the participation of impurity elements in ferroalloys like Al during the deoxidation process. The conditions in which certain unstable oxide inclusions form and prevail at low oxygen potentials need further investigation.

6.6.3 CaO based inclusions in Si-Mn killed steel

Studies [47, 51, 52, 53] have found CaO in the inclusions, whose source was believed to be from slag droplets rather than from Ca pickup resulting from the chemical reactions between the steel and slag. This mechanism was proposed because the concentration of [Al] in steel was deemed insufficient to reduce CaO from the slag and the initial solubility of Ca in steel was low [7]. Although not shown in this article, this was also seen in our simulations where Ca pickup in steel from slag was negligible. These observations have led researchers to seek another mechanism for formation on CaO containing inclusions. The most viable appears to be emulsification during high stirring periods in producing exogenous inclusions, as shown by Valentin et al. [55]. Furthermore, these inclusions generated from slag droplets can further interact with existing endogenous deoxidation inclusions, resulting in Ca-containing complex oxide inclusions.

6.6.4 Ca treatment in Si-Mn killed steel

A few steelmakers have resorted to Ca treatment [9, 23, 46, 49, 50] to reduce the melting point of the primary oxide inclusions in Si-Mn killed steels. However, the conditions when it is needed have not been entirely well rationalized since liquid inclusions seem to form in ideal conditions, and Ca recovery is considered to be small [53]. Furthermore, the presence of high [S] can interfere with the Ca treatment process. Tienkink et al. [49] indicated that Ca helps reduce incidents of irregular flow through metering nozzles and suggested that Ca helps control the inclusion composition when theAl_2O_3 content within the inclusions is higher than 20%. In this regard, the current model is capable of providing a prognosis for such unwanted casting problems. Specifically, it is able to predict the Al_2O_3 content in the inclusions along with the conditions in which alumina inclusions precipitate. However, to capture the efficiency and frequency of the Ca treatment process, including Ca-inclusion interactions seems an important addition to the model. This will be left as a topic of future study.

6.6.5 Evaluation of steel/slag mass transfer

From the simulation results presented in Section 6.4.2, it was clearly noticed that mass transfer between steel and slag plays an important role in refining kinetics of [S], [O], and [Al], among others, which essentially is described by the mass transfer coefficients of different species. Since the ladle is dominated by inertial forces, different correlations have been proposed based on the effective stirring power or gas flow rate in some instances [54]. However, it has been seen that there is a clear lack of unification among the expressions, as has been shown in Figure 6.15, which displays the relationship between mass transfer capacity (mtc) and stirring power. The exact source of these

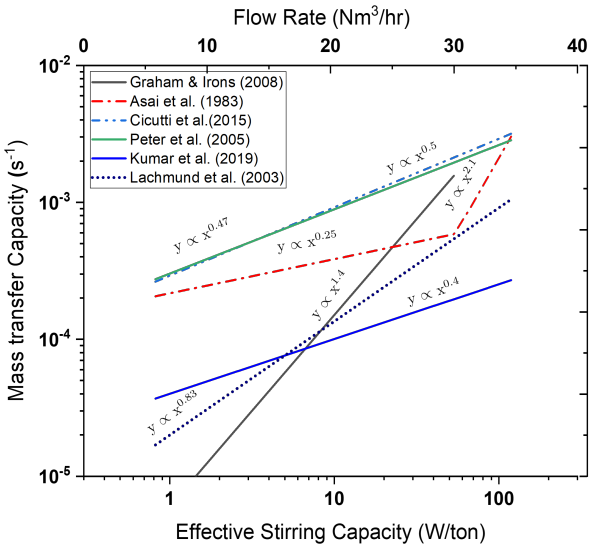

Figure 6.15: *Relationship between mass transfer capacity and stirring power [15, 17, 20, 23, 56, 57].*

differences has been somewhat puzzling and warrants further attention from a fundamental standpoint. As can be observed, many authors have not used two-regime mtc relationships as Asai et al. [56] have suggested, and what is found to exist in many other cold experiment studies [54]. This has been primarily attributed to mass transfer acceleration caused by emulsification. The possible reasons for this noticeable disagreement could be differences in reactor configurations, plug geometries, operation parameters, slag liquidus temperatures, in addition to temperature fluctuations, and gas flow inconsistencies. In most situations, the mass transfer coefficients are tuned to match the composition trajectories of species in the bulk steel and are often well justified. The current study used the relationship chosen in Graham and Irons' work which seems to work below the onset of emulsification ($\dot{\epsilon} < 60$ W/ton [56]). It is worth pointing out that most authors in the past have reported an

incorrect value of B in Eq. 6.2.9 (0.006 instead of 6×10^{-6}) to estimate the mass transfer capacity derived by Graham and Irons' work which can often be misleading.

6.7 Conclusions

In this work, a first principles-based kinetic model has been developed to predict ladle refining reactions for Si-Mn killed steels. Particularly, the model was able to simulate the compositional changes of steel, slag, and inclusions in the steel subject to various simultaneous chemical reactions. The industrial measurements taken from previous literature were well reproduced through the calculated results from the model, which shows the adequacy of the model features to simulate situations of practical interest to steelmakers. Different parametric analyses revealed the effect of important steel, slag, inclusion, and process variables on the refining reactions quantitatively. The following conclusions can be drawn from the model results:

1. The model showed that the amount of alloy additions and the rate at which they dissolve and mix decide the temporal evolution of species with higher concentrations ([Si], [Mn], [C]). On the other hand, the reactions at the steel-slag interface along with the mutual interaction of the solutes with the existing inclusions decide the temporal evolution of species with lower concentrations ([Al], [S], [O]).
2. The model is able to identify limiting concentrations of initial [Al] and [O] in the steel that leads to a low alumina content within the oxide inclusions, which vary with different steel grades.
3. Based on multiple model calculations, slag basicity of around 1 with an Al_2O_3 content of less than 5 wt.% is proposed to realize optimum control of inclusion composition.
4. The extent of refining time and the timing of slag basicity change could be informed from the model so as to obtain a better extent of desulphurisation.
5. The model showed that reoxidation of steel can lead to a new population of inclusions while destabilizing existing inclusions, through the reaction of the excess oxygen with the existing solutes and inclusions in the steel.
6. It was seen that the inclusion number concentration in steel exerts a role in the time needed for steel-inclusion reactions to reach equilibrium, affecting the compositional trajectory of inclusions.

Overall, it has been demonstrated that the current model can be used to

predict reaction kinetics for a wide range of operating conditions in Si-Mn killed steel. This should be able to assist practitioners in improving the refining process for that particular steel grade, although the nature of refining practices differs across steel plants. This work has also pointed out the need for more fundamental studies to clarify certain aspects of the refining process such as the accurate determination of steel mass transfer coefficients.

References

[1] A. Ghosh: Secondary Steelmaking: *Principles and Applications*, 2001.

[2] H. Suito and R. Inoue: ISIJ Int., 1996, vol. 36, pp. 528-36.

[3] R. Kiessling: *Non-Metallic Inclusions in Steel: Part III: The Origin and Behavior of Inclusions and Their Influence on the Properties of Steels*, The Metals Society, London, 1968.

[4] P. Kaushik, J. Lehmann, and M. Nadif: *Metall. Mater. Trans. B Process Metall. Mater. Process. Sci.*, 2012, vol. 43, pp. 710-25.

[5] Y.B. Kang and H.G. Lee: *ISIJ Int.*, 2004, vol. 44, pp. 1006-15.

[6] S.H. Chen, M. Jiang, X.F. He, and X.H. Wang: *Int. J. Miner. Metall. Mater.*, 2012, vol. 19, pp. 490-8.

[7] C. Liu, X. Gao, S. Ueda, S.-Y. Kitamura. *ISIJ Int.* 2019, 59, pp. 268

[8] H.L. Yang, X.L. Wu, J.S. Ye, Y. Fang, and X.B. Zhao: *Ironmak. Steelmak.*, 2018, vol. 45, pp. 386-92.

[9] A. Bhansali, H. Oltmann, and E. Pretorius: in *AIST proceedings: AISTech 2021*, 2021, pp. 1-13.

[10] A. Podder, K.S. Coley, and A.B. Phillion: *Steel Res. Int.*, 2022, vol. 2100831, p. 2100831.

[11] Y. Tabatabaei, K.S. Coley, G.A. Irons, and S. Sun: *Metall. Mater. Trans. B*, 2018, vol. 49B, pp. 375-87.

[12] G. Okuyama, K. Yamaguchi, S. Takeuchi, and K. Sorimachi: *ISIJ Int.*, 2000, vol. 40, pp. 121-28.

[13] A.N. Conejo, F.R. Lara, M. Macias-Hernandez, and R.D. Morales: *Steel Res. Int.*, 2007, vol. 78, pp. 141-50.

[14] A. Galindo, G.A. Irons, S. Sun, and K.S. Coley: *Proc. Challenges and Transformative Solutions to Sustainable Steelmaking and Casting for Environment-Friendly Metallurgical Innovation, Iron and Steel Institute of Japan, Tokyo*, 2015, pp. 22-31.

[15] K.J. Graham and G.A. Irons: *Iron Steel Technol., 2009, vol. 6*, pp. 164-73.

[16] A. Harada, N. Maruoka, H. Shibata, and S.Y. Kitamura: *ISIJ Int.*, 2013, vol. 53, pp. 2118-25.

[17] Y. Zhang, Y. Ren, and L. Zhang: Metall. Res. Technol., 2018, vol. 115, pp. 1-14. C. Cicutti, C. Capurro, and C. Cerrutti: 9th International Conference on Exhibition on Clean Steel, Simulation and Model Calculations, Hungarian Mining and Metallurgical Society (OMBKE), Budapest, 2015.

[18] M.A. Van Ende and I.H. Jung: *Metall. Mater. Trans. B Process Metall. Mater. Process. Sci.*, 2017, vol. 48, pp. 28-36.

[19] P.R. Scheller and Q. Shu: *Steel Res. Int.*, 2014, vol. 85, pp. 1310-6.

[20] D. Kumar, K.C. Ahlborg, and P.C. Pistorius: *Metall. Mater. Trans. B Process Metall. Mater. Process. Sci.*, 2019, vol. 50, pp. 2163-74.

[21] D. You, S.K. Michelic, and C. Bernhard: *Steel Res. Int.*, 2020, vol. 91, pp. 1-9.

[22] Y. Zhang, Y. Ren, and L. Zhang: Metall. Res. Technol., 2017, vol. 114, pp. 1-8.

[23] J. Peter, K.D. Peaslee, D.G.C. Robertson, and B.G. Thomas: *AISTech - Iron Steel Technol. Conf. Proc.*, 2005, vol. 1, pp. 959-73.

[24] S.P.T. Piva, D. Kumar, and P.C. Pistorius: *Metall. Mater. Trans. B*, 2017, vol. 48B, pp. 37-45.

[25] Podder et al.

[26] M. Hino and K. Ito: *Thermodynamic Data for Steelmaking*, 1st ed., Tohoku University Press, Tokyo, 2010, pp. 16-17.

[27] C.W. Bale and A.D. Pelton: *Metall. Trans. A*, 1990, vol. 21, pp. 1997-2002.

[28] Z.X. Bing, J.G. Chang, and X.K. Di: *Calphad Comput. Coupling Phase Diagrams Thermochem.*, 1997, vol. 21, pp. 311-20.
[29] F. Oeters: *Metallurgy of Steelmaking*, 1st ed., Verlag Stahleisen, Dusseldorf, 1994, pp. 316-35.
[30] H. Gaye and J. Welfringer: *in Second Int. Symp. Metall. Slags Fluxes*, 1984, pp. 357-75.
[31] D.G.C. Robertson, B. Deo, and S. Ohguchi: *Ironmak. Steelmak.*, 1984, vol. 11, pp. 41-55.
[32] R.W. Young, J.A. Duffy, G.J. Hassall, and Z. Xu: *Ironmak. Steelmak.*, 1992, vol. 29, p. 201.
[33] J.A. Duffy and M.D. Ingram: *J. Am. Chem. Soc.*, 1971, vol. 93, pp. 6448-55.
[34] C.B. Guo, H.T. Ling, L.F. Zhang, C. Liu, G.S. Wang, and Y.B.Gao: 6*th Int. Congress Sci. Technol. Steelmaking*, Beijing. 2015. pp. 817-20.
[35] C.W. Bale and A.D. Pelton: *Metall. Trans. A*, 1990, vol. 21, pp. 1997-2002.
[36] H. Gaye, J. Lehmann, T. Matsumiya, and W. Yamada: *in 4th International Conference on Molten Slags and Fluxes*, 1992, pp. 103-8.
[37] H. Gaye and J. Welfringer: *in Second Int. Symp. Metall. Slags Fluxes*, 1984, pp. 357-75.
[38] K. Xu, G. Jiang, X. Zhang, K. Tang, J. Xu, and W. Ding: *Jinshu Xue- bao/Acta Metall. Sin.*, 1998, 34, vol. 34.
[39] M.A.T. Andersson, P.G. Jönsson, and M. Hallberg: *Ironmak. Steelmak.*, 2000, vol. 27, pp. 286-93.
[40] Z.X. Bing, J.G. Chang, and X.K. Di: *in Molten Slags, Fluxes And Salts '97 Conference*, 1997, pp. 259-62.
[41] W. Lou and M. Zhu: Metall. Mater. Trans. B Process Metall. Mater. Process. Sci., 2014, vol. 45, pp. 1706-22.
[42] C. Wang, Y.S. Han, J.S. Zhang, D. Xiao, J. Yang, J. Chen, and Q. Liu: *Ironmak. Steelmak.*, 2021, vol. 48, pp. 466-76.
[43] C. Guo, H. Ling, L. Zhang, W. Yang, Y. Ren, and H. Zhou: *Metall. Res. Technol.*, 2017, vol. 114, pp. 1-7.
[44] T. Yuan, L. Zhang, Y. Ren, Q. Zhao, and C. Liu: *Steel Res. Int.*, 2021, vol. 92, pp. 1-8.
[45] Z. Liu, G. Song, Z. Deng, and M. Zhu: *Ironmak. Steelmak.*, 2021, vol. 48, pp. 893-900.
[46] Y. Dai, J. Li, C. Shi, and W. Yan: *Metall. Res. Technol.*, 2019, vol. 116, p. 411.
[47] S. Lyu, X. Ma, Z. Huang, Z. Yao, H.G. Lee, Z. Jiang, G. Wang, J. Zou, and B. Zhao: *Metall. Mater. Trans. B Process Metall. Mater. Process. Sci.*, 2019, vol. 50, pp. 732-47.
[48] N. Liu, W. Yang, L. Zhang, and S. Wu: *Steel Res. Int.*, 2022, vol. 93, pp. 1-8.
[49] W. Tiekink, R. Van Den Bogert, T. Breedijk, and A. Ferguson: *Ironmak. Steelmak.*, 2003, vol. 30, pp. 146-50.
[50] W.Y. Kim, K.S. Kim, and S.Y. Kim: *Metall. Mater. Trans. B Process Metall. Mater. Process. Sci.*, 2021, vol. 52, pp. 652-64.
[51] M. Jiang, J.C. Liu, K.L. Li, R.G. Wang, and X.H. Wang: *Metall. Mater. Trans. B Process Metall. Mater. Process. Sci.*, 2021, vol. 52, pp. 1950-4.
[52] K.P. Wang, M. Jiang, X.H. Wang, Y. Wang, H.Q. Zhao, and Z.M. Cao: *Metall. Mater. Trans. B Process Metall. Mater. Process. Sci.*, 2017, vol. 48, pp. 2961-9.
[53] K. Wang, M. Jiang, X. Wang, Y. Wang, H. Zhao, and Z. Cao: *Metall. Mater. Trans. B Process Metall. Mater. Process. Sci.*, 2016, vol. 47, pp. 282-90.
[54] A.N. Conejo: *Processes*, 2020, vol. 8, pp. 1-23.
[55] P. Valentin, C. Bruch, and J. Gaule: *Steel Res. Int.*, 2009, vol. 80, pp. 746-52.
[56] S. Asai, M. Kawachi, and I. Muchi: *SCANINJECT III, Refin. Iron Steel by Powder*

Inject., 1983, p. 12.

[57] H. Lachmund, Y. Xie, T. Buhles, and W. Pluschkell: *Steel Res. Int.*, 2003, vol. 74, pp. 77-85.

Chapter 7

Experimental study of inclusion behaviour after Si-Mn deoxidation

The idea behind the experiments was developed by me. All of the experiments were carried out by Dr. Kezhuan Gu and me. Dr. Muhammad Nabeel also provided assistance with the furnace setup. Xiaogang Li and Doug Culley provided support and training for instruments. Dr. Kezhuan Gu and Mr. Suwam Kumar help with the inclusion analysis. Post-processing of the results and further analysis were conducted by me. Useful discussions on the results were provided by Dr. Kenneth S. Coley and Dr. André B. Philion.

This short chapter summarises the motivation, background, and experimental methodology obtained so far. Premilinary analysis and discussion have also been presented in this chapter. This chapter is planned to be submitted to ISIJ International.

Experimental study of inclusion behaviour after Si-Mn deoxidation

Angshuman Podder[1], **Kezhuan Gu**[3], **Suwam Kumar**[1], **Kenneth Coley**[1,2], **André Phillion**[1]

[1] *McMaster Steel Research Center*
Department of Materials Science and Engineering,
McMaster University, Hamilton, Ontario, Canada, ON L8S 4L7
[2] *Department of Mechanical and Materials Engineering,*
Western University, London, Ontario, Canada, ON N6A 3K7
[3] *ArcelorMittal Dofasco,*
Hamilton, Ontario, Canada, ON L8N 3J5.

Abstract

Herein, the effect of oxygen content and alloying practice on the evolution of inclusions in Si-Mn deoxidised steels is investigated. Four deoxidation experiments were carried out using commercial grade FeSi and FeMn, where alloy addition times were changed and the initial oxygen content of the melt was varied using Fe_2O_3 additions. The samples extracted from the melts were polished and SEM-based 2D inclusion characterization was performed to quantify the type, size, and number density of inclusions. The predominant inclusions obtained in the experiments were silicates post FeSi additions and manganese silicates with varying Al_2O_3 content. The inclusion composition results agree with thermodynamic calculations carried out using FactSage. Furthermore, the results showed that the initial oxygen content influences the inclusion composition in terms of SiO_2 and Al_2O_3 content and also the inclusion removal rates. However, it was seen that the final inclusion composition was not affected much when concurrent addition of (FeSi + FeMn) was made compared to when FeSi and FeMn additions are made sequentially. On the other hand, the rate of inclusion removal seemed to be higher in the former case than the latter, which needs to be probed a bit further.

7.1 Introduction

Deoxidation inclusions typically belong to the $MnO{-}SiO_2{-}Al_2O_3$ category [1] in Si-Mn killed steels. However, the type of treatments and final product chemistry can largely influence the types of inclusions forming in steel. Turkdogan [2] showed that based on the Mn/Si ratio and temperature, either silica or manganese silicates would precipitate. Fedriksson and Hammar [3] conducted extensive deoxidation experiments and found that the majority of inclusions were either iron silicates (post Si deoxidation) or manganese silicates (post Si-Mn deoxidation). However, impurities are inherently present in most ferroalloys, which can impact steel cleanliness. Wijk and Brabie [4] assessed the effect of Al and Ca in laboratory deoxidation experiments, where they showed that the increased content of Al results in the formation of

alumina inclusions, which corroborated studies by Li et al. [5] and Mizuno et al. [6]. Wang et al. [7] conducted deoxidation experiments with and without slag in order to understand Ca pick-up from ferroalloys (FeSi and FeMn) and slag. They found the effect of Ca from ferroalloys on inclusion composition to be negligible for both cases, with and without slag. However, the studies so far have not investigated the conditions in which impurities in deoxidants participate in the steel-inclusion reactions. The formation of primary inclusions after deoxidation requires sufficient supersaturation for nucleation [8]. The presence of impurities such as Al and Ca in commercial ferroalloys can influence the supersaturation ratios owing to their strong affinity towards oxygen. In such cases, one can expect equilibrium oxygen levels lower than defined by Fe-Mn-Si-O equilibria as well as different inclusion compositions during the deoxidation process. Additionally, since the nucleation and growth kinetics are affected by the initial oxygen levels or increase in dissolved oxygen levels (in case of reoxidation), the inclusion population can change significantly. Thus, it is important to consider the effect of dissolved oxygen on inclusion characteristics since it affects the supersaturation limits in a multi-component liquid steel system. Recently, Liu et al. [9] found that increasing the dissolved oxygen at the endpoint of BOF can lead to a lowering of alumina content in the oxide inclusions in Si-Mn killed steel. Thus, while many experimental studies have been carried out on the topic of Si/Mn deoxidation, the effects of different oxygen levels on inclusion composition in such steels has not yet been undertaken. Furthermore, the role of ferroalloy impurities in the deoxidation process needs consideration.

The current study aims to investigate the compositional evolution and size distribution of inclusions after Si-Mn deoxidation for different alloying practices and initial oxygen levels. For this, a set of laboratory deoxidation experiments has been carried out. Subsequently, the samples were analyzed using scanning electron microscopy as well as automated micro-analysis. Thermodynamic calculations were carried out with the Fe-Mn-Si-Al-O system to understand the effects of [Al] and [O] on the inclusion composition.

7.2 Experimental methodology

Deoxidation experiments were carried out in a resistance-heated vertical tube furnace under Ar atmosphere, as shown in Figure 7.1. The raw materials consisted of pure electrolytic iron (E.I.), ferrosilicon (FeSi), ferromanganese (FeMn), whose compositions are listed in Table 7.2.1. Fe_2O_3 powder, compacted as pellets, was used as the source of oxygen. The temperature readings were taken using a B-type thermocouple.

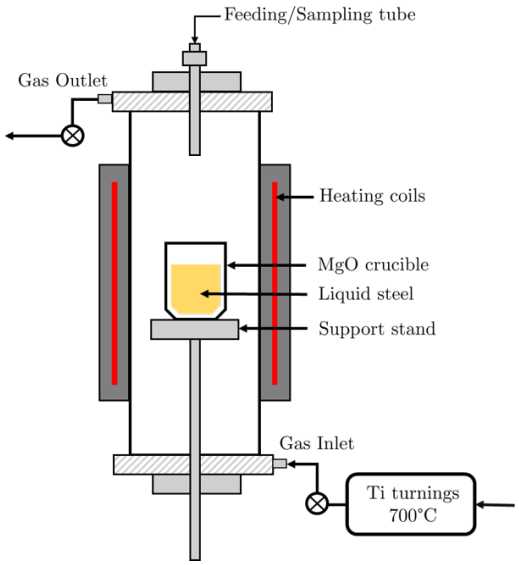

Figure 7.1: *Experimental setup*

Table 7.2.1: *Chemical composition of raw materials used in the study.*

	C	Mn	Si	Al	Ca	S	O	Fe
Electrolytic iron	0.008	0.001	0.003	-	-	0.002	0.010	99.9662
Graphite rods	99.995	-	-	-	-	0.001	-	-
FeSi	0.051	0.212	79.962	1.123	0.075	-	-	Balance
FeMn	0.407	79.603	0.187	0.007	0.001	0.002	-	Balance

Four sets of de-oxidation experiments (E1, E2, E3, E4) were conducted, as described in Table 7.2.2. In the first experiment (E1), about 295 g of electrolytic iron along with 0.25 g of Fe_2O_3 was put in the crucible and placed in the furnace. The furnace was sealed and evacuated using a vacuum pump to reach a partial pressure of 10^{-12} atm, followed by flushing using high-purity Ar (99.999%) gas. In order to absorb any residual oxygen present in the high-purity Ar, the gas was passed through Ti turnings at 923 K prior to entering the furnace. This was followed by raising the furnace temperature up to 1873 K. To ensure the melt was homogenized, the crucible was held at that temperature for 60 minutes. This was followed by the addition of FeSi and FeMn together from the top using a hollow alumina tube. This yielded a $\approx$ 300 g low C-steel melt with an Mn/Si ratio of 5. Subsequently, samples were extracted after different holding times using a quartz tube. The remaining experiments (E2 - E4) generally followed the same procedure however, (a) using different amounts of Fe_2O_3 (0.25, 1.01, and 0 g) and (b) the additions of FeSi and FeMn were made consecutively, 600 s apart, instead of concurrently. Each of the melt samples was then cut into small sections for

further analysis. The schematic of the experiments, containing the timings of alloy additions and sampling are shown in Figure 7.2. After the experiment, the crucibles were furnace-cooled at a rate of 0.166 K/s to room temperature.

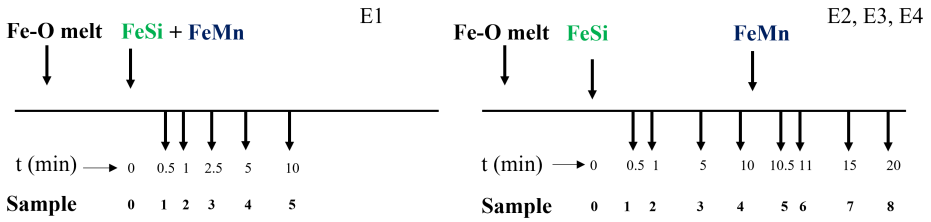

Figure 7.2: *Schematic of alloy additions and sampling times in experiments. The image on the left corresponds to E1, while the image on the right corresponds to E2, E3, and E4. Note that $t = 0$ refers to the time post-melt homogenization.*

Table 7.2.2: *Summary of deoxidation experiments used in the study. Note that $t = 0$ corresponds to the time post melt homogenization.*

Experiment	Addition 1 (t = 0 s)	Addition 2 (t = 10 min)	Initial oxygen (ppm)	Samples taken	Sampling times (min)
1	FeSi + FeMn	-	354	6	$0^{\dagger}$, 0.5*, $1^{*\dagger}$, $2.5^{*\dagger}$, $5^{*\dagger}$, $10^{\ddagger}$
2	FeSi	FeMn	321	9	$0^{\dagger}$, 0.5*, $1^{\dagger}$, 5*, $10^{\dagger\ddagger}$ **(A2)**, 10.5*, $11^{\dagger}$, 15*, $20^{\ddagger\dagger}$
3	FeSi	FeMn	550	9	$0^{\dagger}$, 0.5*, $1^{\dagger}$, 5*, $10^{\dagger\ddagger}$ **(A2)**, 10.5*, $11^{\dagger}$, 15*, $20^{\ddagger\dagger}$
4	FeSi	FeMn	136	9	$0^{\dagger}$, 0.5*, $1^{\dagger}$, 5*, $10^{\dagger\ddagger}$ **(A2)**, 10.5*, $11^{\dagger}$, 15*, $20^{\ddagger\dagger}$

Note: * Inclusion analysis; † LECO O/N analysis; ‡ ICP analysis; **A2** refers to Addition 2.

Chemical analyses of FeMn and the experimentally-extracted steel samples in terms of Si, Mn, Al, and Ca composition was carried out using induction coupled plasma optical emission spectrometry (ICP-OES), while the chemical analysis of the FeSi was carried out using X-ray fluorescence spectroscopy (XRF). To measure the carbon/sulphur of the steel samples, the combustion analysis technique was used in a LECO C/S analyzer (CS744). Finally, the total oxygen and nitrogen contents were measured using the inert gas fusion

method in a LECO O/N analyzer (ON736). The chemical composition of the steel samples at the end of the experiment and/or just prior to the FeMn addition is provided in Table 7.2.3 for all four experiments.

Table 7.2.3: *Chemical composition of selected steel samples from the experiments*

Experiment	C	Mn	Si	Al	Ca	S	Fe
E1-**S**5	0.018	1.170	0.119	0.004	<0.001	0.0017	Bal.
E2-**S**4	0.008	0.045	0.140	0.004	<0.001	0.0015	Bal.
E2-**S**8	0.017	1.395	0.140	0.006	<0.001	0.0014	Bal.
E3-**S**4	0.009	0.039	0.121	0.004	<0.001	0.0018	Bal.
E3-**S**8	0.013	1.391	0.116	0.004	<0.001	0.0016	Bal.
E4-**S**4	0.009	0.043	0.155	0.005	<0.001	0.0017	Bal.
E4-**S**8	0.016	1.331	0.146	0.005	<0.001	0.0016	Bal.

Note: In **EXSY**, X refers to the experiment (1, 2, 3, 4), and Y refers to sample (0, 1, 2, etc.)

7.2.1 Quantitative Inclusion Analysis

To obtain quantitative information about the inclusions within the steel, both manual and automated inclusion analyses have been carried out using a Scanning Electron Microscope (SEM: JEOL 6610LV) with an Energy-Dispersive Spectroscopy (EDS) detector (Oxford Instruments: 20 mm^2 detector area). An accelerating voltage of 15 kV, at a working distance of 10 mm was used to ensure proper steel matrix stimulation to reveal the features' composition. The area of inclusion analysis was varied between 4 and 8 mm^2 to optimize the number of features analyzed through SEM-EDS. Different magnifications, 400x and 800x, were tried to achieve a balance between analysis speed and prediction reliability. Inclusion size, morphology, and chemical composition were all characterized using AZTEC v6.0. Only inclusions having an average diameter (d_{avg}) larger than 1 μm were considered for analysis to prevent inclusion composition errors caused due to matrix interaction.

Inclusion Classification

Based on the chemical composition, inclusions were classified using the following criteria:

1. **Oxides:** (Si + Mn + Al + Ca - 2S) > 80% ; S < 10%
2. **Sulfides:** (Ca + Mn + S) > 80% ; Si < 10%
3. **Oxy-sulfides:** S > 10% ; (Si + Mn + Al + Ca - 2S) > 10%

The oxides were further classified into different inclusion types as shown in Table 7.2.4. This oxide classification table was reassessed and updated a few

Table 7.2.4: *Classification scheme for oxide inclusions*

Index	Abbrv.	Inclusion type	Si	Mn	Al	Ca
1	M	MnO	-	> 90	-	-
2	S	SiO_2	> 90	-	-	-
3	MA	Mn-aluminate	-	> 30	> 50	-
4	MS	Mn-silicate	> 20	> 50	-	-
5	MS-lA	Mn-silicate with low Al	> 20	> 50	< 10	-
6	MS-hA	Mn-silicate with high Al	> 20	> 50	> 10	-
7	AS	Al-silicate	> 20	-	> 40	-
8	MSAC	Mn-aluminosilicate with Ca	> 20	> 50	< 10	> 20
9	S-lA	Silica with low Al	> 70	-	< 20	-
10	S-hA	Silica with high Al	> 70	-	> 20	-

times to minimize unclassified inclusions.

Size distribution analysis

The resulting two-dimensional (2D) inclusion size distribution was then converted to three-dimensional (3D) using the Schwartz-Saltykov (SS) stereological technique in order to obtain the number density distribution of inclusions per unit volume [13, 14]. This technique was chosen because of its reliability with spherical and non-spherical particles. The following equation summarizes the operation:

$$N_V(j) = \frac{1}{\Delta} \sum_{i=j}^{k} \alpha(i,j) N_A(i) \tag{7.2.1}$$

where N_V is the number of inclusions per unit volume (mm^{-3}), N_A is the number of inclusions per unit area (mm^{-2}), Δ is the size range of the histogram, i, j are the class numbers in the histogram for particle and histogram, respectively, k is the maximum class number, and $\alpha(i,j)$ is the translation coefficient that uses the 2D morphological information. This last term can be calculated based on a series of operations as shown in Ref. [15]. A script employing the above routine was written in MATLAB 2022, which was used to post-process the information obtained from the SEM-EDS automated analysis.

7.3 Results and Discussion

In this work, total oxygen analysis and inclusion analysis via SEM-EDS of selected samples were conducted to investigate the effects of different alloying

practices (E1 and E2) and different initial oxygen levels (E1, E2 and E3). The following section summarises the observations and inferences obtained so far from these analyses. Additional work needs to be carried out in the future to understand these results further.

7.3.1 Total oxygen analysis

Figure 7.3 shows the variation of total oxygen (T.O.) in steel with time in E1, E2, E3, and E4.

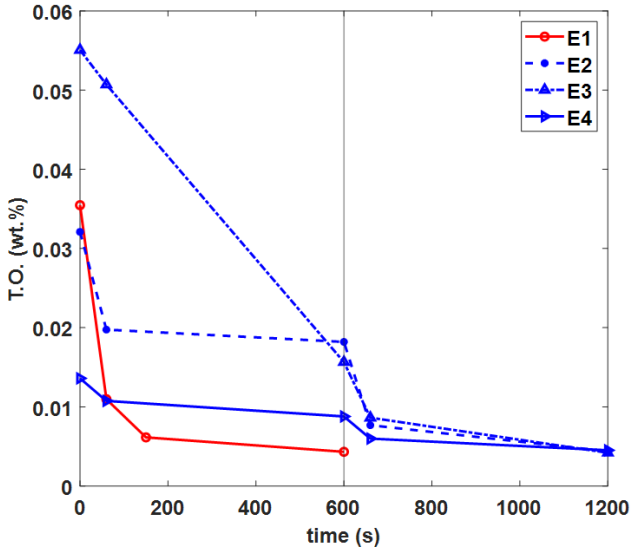

Figure 7.3: *Variation in total oxygen (T.O.) in steel with time for E1, E2, E3, and E4. Note: the red line indicates where FeSi and FeMn were added together.*

A few different observations can be made. First, it is seen that when FeSi and FeMn are added together (E1), the T.O. drops to lower values than when FeMn is added after 10 min following the addition of FeSi (E2, E3, E4). This agrees with the fact that the formation of Mn-silicates reduce the dissolved oxygen to lower levels than the formation of silica [18]. However, the final T.O. after 20 min in E2, E3, E4 post FeMn addition, is similar to that in E1($\approx$ 45 ppm). This is probably because the steel-inclusion system has reached the same equilibrium in all cases, and since the target composition of the steel was selected to be the same in all the experiments. Second, the T.O. after 1 min in E1 (110 ppm) is lower than E2 (198 ppm), which suggests that there could be faster coagulation and removal kinetics with manganese-silicate formation in E1 than with silica formation in E2. This is assuming that the equilibrium dissolved oxygen is reached after 60 seconds post-FeSi addition in E2. Third, in E2- E4, post deoxidation with FeSi, the T.O. are

not similar, with the T.O. in E2 (180 ppm) being almost two times higher than that in E4 (88 ppm) although the [Si] content was similar (0.12-0.16 wt.%). This suggests a lower efficiency of inclusion removal with only FeSi addition. Finally, in E3, it can be seen that a higher initial oxygen level after the addition of FeSi leads to a higher rate of decrease in T.O. compared to E3 and E4, which could be due to higher removal kinetics caused by larger inclusion generation, leading to more collision probabilities.

It is interesting to note that the final T.O. obtained in all the experiments are substantially lower than even the dissolved oxygen predicted by simple Fe-Si-Mn-O equilibrium thermodynamics (85-90 ppm) [18]. This is believed to be caused by ferroalloy impurities in FeSi and FeMn, which participate in the deoxidation process thus leading to lower dissolved oxygen levels after Si-Mn deoxidation even without the presence of slag. Although the removal kinetics is predominantly determined by the MnO and SiO_2 in the inclusions, the composition of the inclusions and the dissolved oxygen is governed by the reaction with Al. As will be discussed below, this was confirmed by SEM-EDS analysis, where oxide inclusions were seen to contain Al_2O_3 in them.

7.3.2 Inclusion Analysis

Figure 7.4 shows the fraction of oxide, sulfide, and oxysufide inclusions in the samples for all experiments based on the classification shown in Section 7.2.1. As can be seen, the majority of the inclusion population (more than 95 %) belonged to the oxides class. This is owing to the low [S] content in the melt ($<$ 20 ppm), as well as the fact that samples (taken at different holding times) were quenched to avoid secondary inclusions.

Figures 7.5-7.8 show the evolution of inclusion composition with holding times (refer to Table 7.2.2) for the four different experiments. The data is plotted on the $MnO{-}SiO_2{-}Al_2O_3$ ternary.

Figure 7.5 shows that when the FeSi and FeMn are added simultaneously, i.e. E1, the oxide inclusions belong to the manganese-silicate family but with some containing Al_2O_3 (6-8 wt.%). Most of these oxides lie within the liquidus region. Although some manganese-aluminates can be seen to exist in S1, these disappear with further holding times. This suggests that such inclusions form upon deoxidation but later evolve towards the equilibrium compositions. Moreover, this points to the fact that different complex oxides nucleate concurrently, interact with each other in the melt, and evolve with time i.e. showing the transient nature of the composition evolution of inclusions in steel melts. On the other hand, Figures 7.6-7.8 show that when the

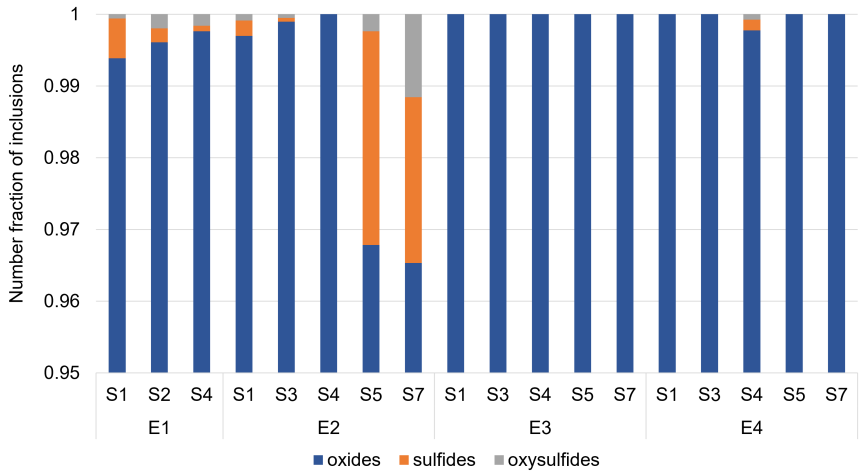

Figure 7.4: *Classification of inclusions into oxides, sulfides, oxysufides for all samples after inclusion analysis.*

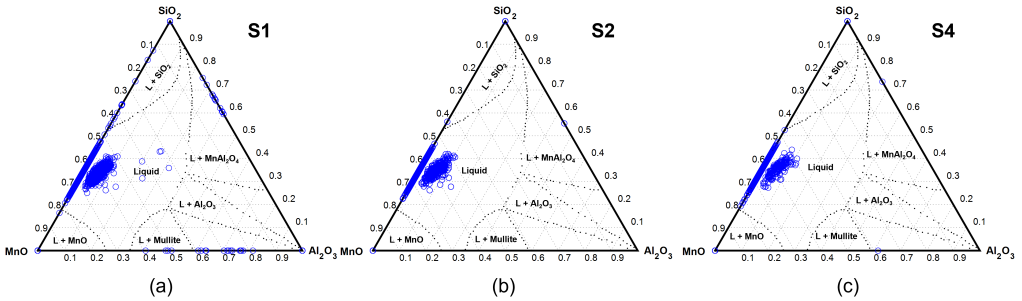

Figure 7.5: *Evolution of inclusion composition in E1: (a) 0.5 min after (FeSi + FeMn) addition, (b) 1 min after (FeSi + FeMn) addition, (c) 5 min after (FeSi + FeMn) addition. (Note: $MnO{-}SiO_2{-}Al_2O_3$ phase boundaries are plotted at 1873 K.)*

FeSi and FeMn and added 10 min apart, the initial oxide inclusions mostly belong to the $Al_2O_3{-}SiO_2$ region. These, in turn, become $MnO{-}SiO_2{-}Al_2O_3$ after the addition of FeMn. This could be either due to the modification of existing silica-based inclusions or a new nucleation event for manganese silicates post FeMn addition. In E4, with low initial oxygen [O] (T.O. = 136 ppm), the inclusions have slightly more Al_2O_3 (20-25 wt.%) in them, after both the FeSi addition and the FeMn addition (Figure 7.8). This suggests that low T.O. strongly affects the inclusion nucleation and growth characteristics of the oxide inclusions, allowing other [Al]-[O] reactions to occur in the melt.

Figure 7.9 shows the SEM-EDS ($K\alpha 1$ peaks) maps of some selected oxide

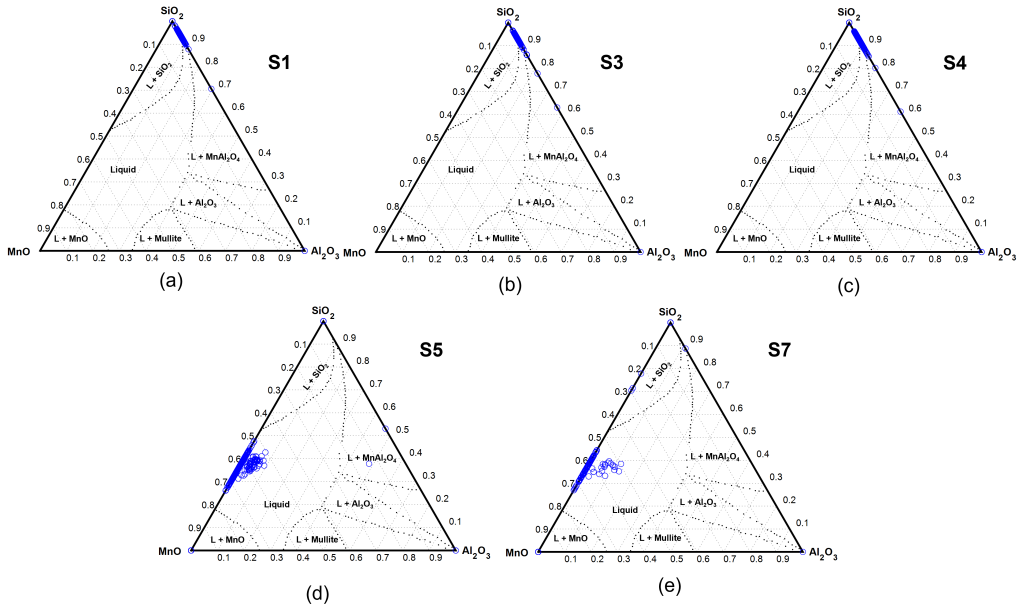

Figure 7.6: *Evolution of inclusion composition in E2: (a) 0.5 min after FeSi addition, (b) 5 min after FeSi addition, (c) 10 min after FeSi addition (d) 10.5 min after (FeSi + FeMn) addition, (d) 15 min after (FeSi + FeMn) addition. (Note: $MnO-SiO_2-Al_2O_3$ phase boundaries are plotted at 1873 K.)*

inclusions from the four experiments obtained to get some insight about the shape, morphology and distribution of elements within the inclusions. It is noticed that the inclusions are all nearly spherical, which made the assumption of spherical particles in the SS method valid. The EDS maps also revealed that there could be significant Al in the oxide inclusions post-deoxidation depending on the local availability of [Al] and [O] in the steel. Based on the concentration of Al_2O_3 in the inclusions, the Al-containing oxides were classified into three categories as shown in Table 7.2.2. Also, there seems to be hardly any Ca present in the inclusions which was due to the low Ca in all the prepared steel compositions.

Figure 7.10 shows the evolution of the inclusion number density and the types of inclusions using the oxide classification system introduced in Section 7.2.1. In all four experiments, the number density of the oxide inclusions steadily decreases with time. Additionally, as discussed before, Figures 7.10a-7.10d show that the inclusion composition consisted of silica-based inclusions post FeSi addition and manganese silicates post FeMn addition. Overall, the proposed classification system seems to capture the important changes in the inclusion composition satisfactorily which were verified with manual SEM-EDS maps of inclusions (shown in Figure 7.9). Again, a few specific

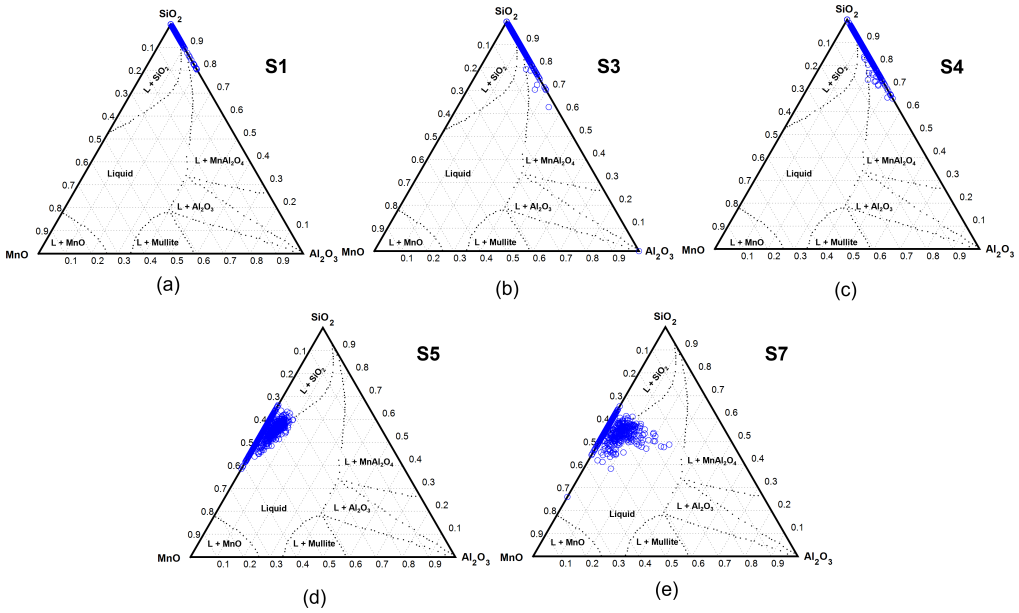

Figure 7.7: *Evolution of inclusion composition in E3: (a) 0.5 min after FeSi addition, (b) 5 min after FeSi addition, (c) 10 min after FeSi addition (d) 10.5 min after (FeSi + FeMn) addition, (d) 15 min after (FeSi + FeMn) addition. (Note: $MnO-SiO_2-Al_2O_3$ phase boundaries are plotted at 1873 K.)*

observations can be made.

First, the data shown in Figure 7.10a indicates that for E1, the fraction of manganese silicates having low Al_2O_3 decreases with longer holding times (S1, S2, S4). This might be because of the higher removal efficiency of the $MnO-SiO_2-Al_2O_3$ inclusions. Second, in E2-S1 (Figure 7.10b), the number density of inclusions (567) is less than that in E3-S1 (760) after the same holding time, which is interesting and could be due to low inclusion generation at that oxygen level (T.O. = 321 ppm). However, the inclusion number density for E4-S1 (747) is comparable to that in E2-S1, which suggests more oxide inclusion generation with lower T.O. but with greater participation of Al. Owing to the lower initial T.O., these inclusions are a mix of different Al-rich oxides. Third, in E3, the fraction of Al-based inclusions are small owing to higher initial [O] in the steel that allows for the precipitation of more manganese silicates. In E4, on the other hand, a significant population of Al-containing silicates forms along with Al-containing Mn-silicates after FeMn addition. This last finding is interesting especially since the Al in the ferroalloys was less than 1 wt.%. Finally, comparing Figure 7.10a and 7.10b, it can be seen that the number density of inclusions in E1-S1 is lower in E2-S1, which is in accordance with the T.O. analysis and can be attributed

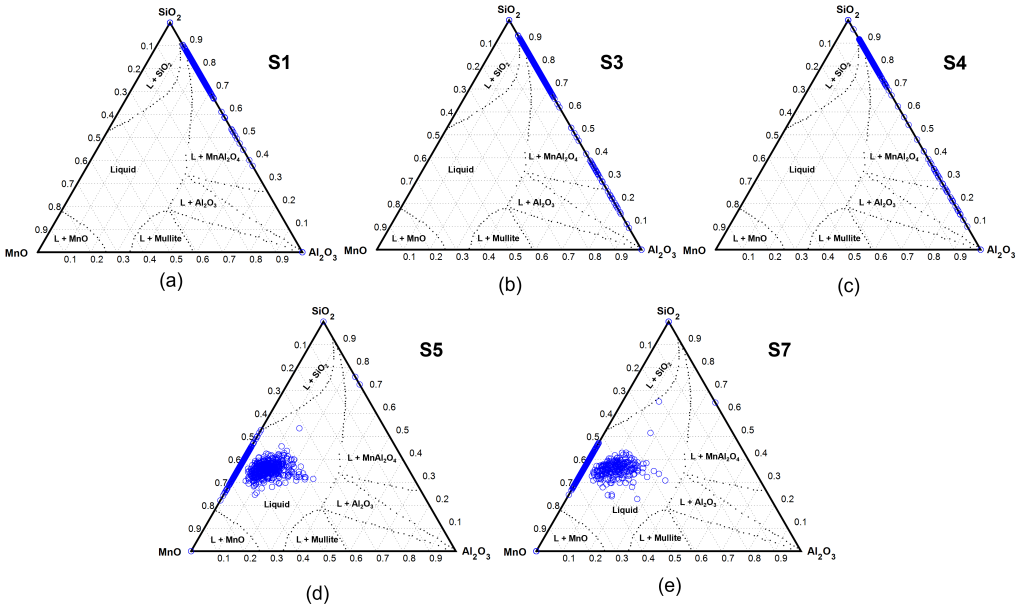

Figure 7.8: *Evolution of inclusion composition in E4: (a) 0.5 min after FeSi addition, (b) 5 min after FeSi addition, (c) 10 min after FeSi addition (d) 10.5 min after (FeSi + FeMn) addition, (d) 15 min after (FeSi + FeMn) addition. (Note: $MnO-SiO_2-Al_2O_3$ phase boundaries are plotted at 1873 K.)*

to faster removal kinetics with manganese silicates.

In order to ascertain the formation behaviour of inclusions, thermodynamic calculations were carried out using FactSage at 1873 K. The steel compositions were selected to be the same as what was obtained in the experiments with varying oxygen and aluminium levels in the steel. Figure 7.11 shows the variation of inclusion composition as predicted by Factsage for the steel composition listed in the figures for different [O] and [Al] within the steel. From Figure 7.11a, it can be seen that inclusions become enriched in Al, resulting in pure alumina inclusions as the [O] in steel is lowered. This explains the higher Al in the oxide inclusions observed experimentally in E4. On the other hand, from Figure 7.11b, it is seen that an increase in [Al] leads to a lowering of MnO and SiO_2 content while increasing the Al_2O_3 content within the inclusions, which ultimately could lead to the precipitation of pure alumina inclusions at around 275 ppm [Al]. This limit is a function of the [O] content in the steel (which was set as 500 ppm in the calculations). Interestingly, although [Al] was just around 50 ppm in all the experiments, significant Al_2O_3 content within the inclusions could be noticed, indicating the sensitivity of the melt to low concentrations of [Al] and fast steel-inclusion reaction kinetics.

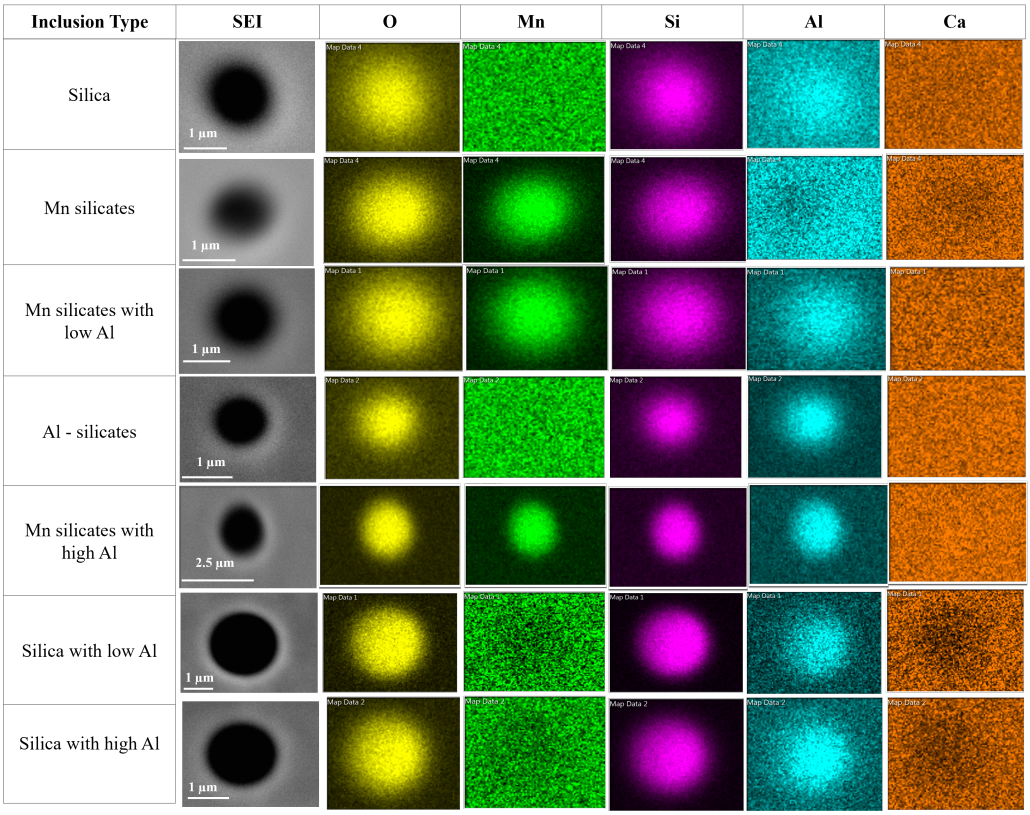

Figure 7.9: *Elemental mappings of typical oxide inclusions predominantly observed in the steel samples using the manual SEM method.*

Figure 7.12 shows the inclusion size distributions obtained in the different samples for E1-E4 after converting the 2D automated SEM-EDS data to 3D using the SS method. As can be seen, most of the inclusions are concentrated within 1-2.3 μm size range. Also, the number concentration of inclusions decreases with increasing holding times in nearly all the experiments.

7.4 Summary

In this study, the effect of oxygen and alloy addition sequence on inclusion formation in Mn-Si killed steels has been studied through a series of four experiments having different additions of FeMn, FeSi, and Fe_2O_3. The inclusion composition evolution and its characteristics were then quantified via scanning electron microscopy with EDS analysis and automated inclusion inspection via the AZtec software. The findings can be summarized as follows:

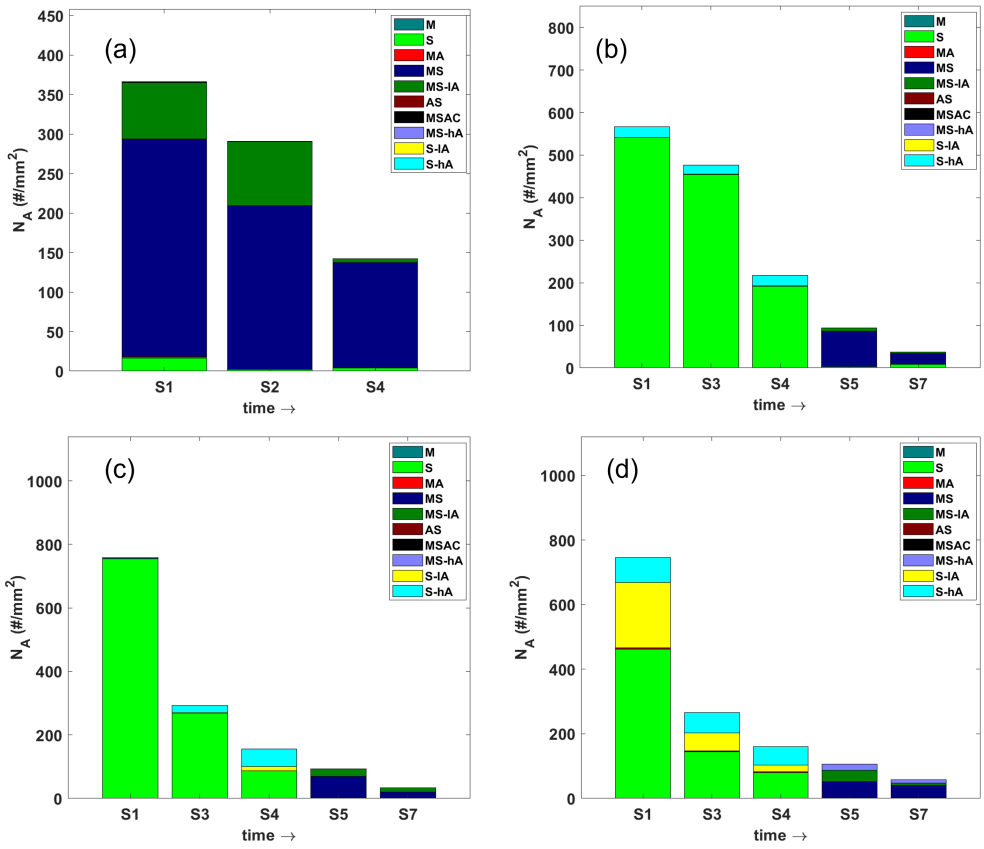

Figure 7.10: *Evolution of inclusion number density (along with their classifications) with different holding times for:(a) E1, (b) E2, (c) E3, and (d) E4.*

1. The total oxygen analysis revealed that a higher rate of inclusion removal is obtained with the addition of (FeSi + FeMn) than just with FeSi. Furthermore, higher removal rates are obtained with an increase in initial total oxygen levels from ≈ 100 to 550 ppm.
2. The proposed classification system for the inclusions post-automated SEM-EDS analysis is able to capture the different oxide inclusion populations in the steel.
3. Automated SEM-EDS analysis of the inclusions showed that oxide inclusions are nearly spherical in nature, and after FeSi additions, are essentially silica while after (FeSi + FeMn) additions, are manganese silicates. Some inclusions contain Al in them, whose content increases with the lower initial T.O. in steel.
4. Inclusions number concentration decreases uniformly with an increase in holding times in all the experiments.

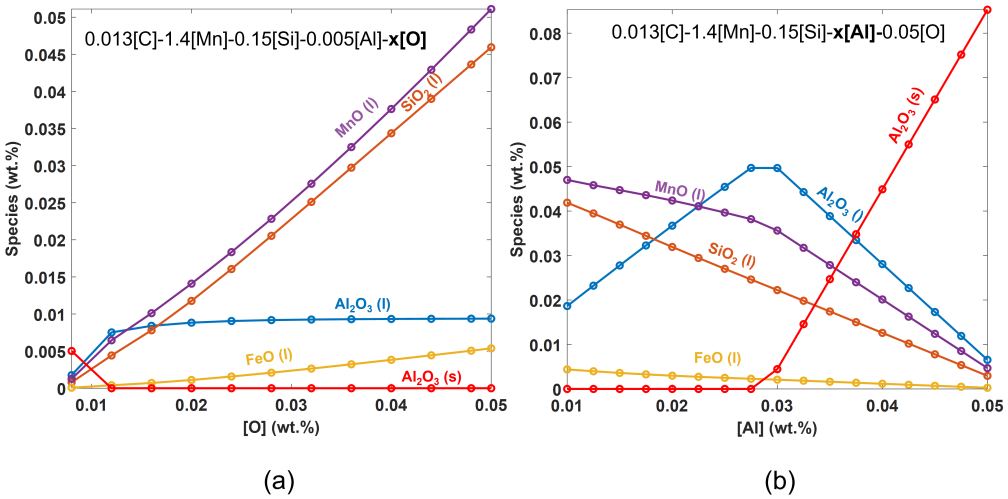

Figure 7.11: *Variation in inclusion composition for different (a) [O], and [Al] levels in steel as calculated using FactSage at 1873 K. Note: (l) stands for the liquid inclusion phase, $FeO-MnO-SiO_2-Al_2O_3$ (SLAG) while (s) stands for solid inclusion phase, corundum.*

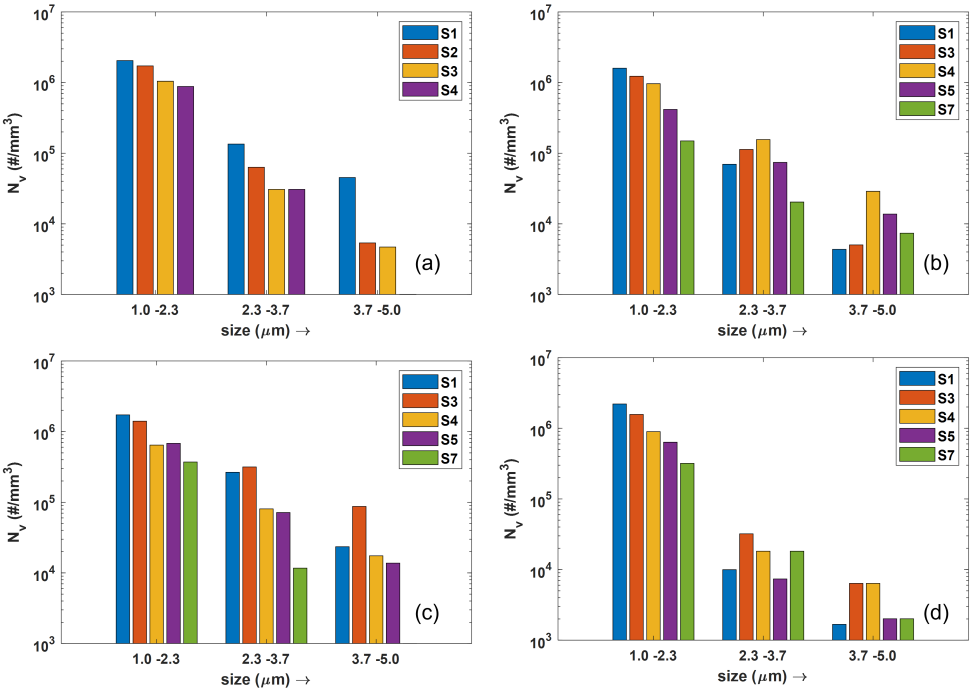

Figure 7.12: *Size distribution of inclusions in samples for (a) E1, (b) E2, (c) E3, and (d) E4 (Note: 3 uniform size bins have been used.)*

References

[1] Y.B. Kang and H.G. Lee: *ISIJ Int.*, 2004, vol. 44, pp. 1006-15
[2] E.T.Turkdogan: *Ironmak. Steelmak.*, 1988, vol. 15, pp. 311-7.
[3] H. Fredriksson and O. Hammar: *Metall. Trans. B*, 1980, vol. 11, pp. 383-408.
[4] O. Wijk and V. Brabie: *ISIJ Int.*, 1996, vol. 36, pp. S132-5.
[5] W. Li, Y. Ren, and L. Zhang: *Ironmak. Steelmak.*, 2019, vol. 9233, pp. 1-7.
[6] K. Mizuno, H. Todoroki, M. Noda, and T. Tohge: *Iron Steelmak.*, 2001, vol. 28, pp. 93-101.
[7] K.P. Wang, M. Jiang, X.H. Wang, Y. Wang, H.Q. Zhao, and Z.M. Cao: *Metall. Mater. Trans. B Process Metall. Mater. Process. Sci.*, 2017, vol. 48, pp. 2961-9.
[8] E.T. Turkdogan: *J. Iron Steel Inst.*, 1966, pp. 914-9.
[9] N. Liu, W. Yang, L. Zhang, and S. Wu: *Steel Res. Int.*, 2022, vol. 93, pp. 1-8.
[10] V. Thapliyal, A. Kumar, D.G.C. Robertson, and J.D. Smith: *Ironmak. Steelmak.*, 2015, vol. 42, pp. 382-94.
[12] Podder
[12] M.D. Higgins: *Am. Mineral.*, 2000, vol. 85, pp. 1105-16.
[13] H. A. Schwartz: *Met. Alloys*, 1934, vol.5, pp. 139.
[14] S. A. Saltykov: *Stereometric Metallography*, 2nd ed., Metallurgizdat, Moscow, (1958), pp. 81.
[15] J. Takahashi and H. Suito: *Metall. Mater. Trans. A Phys. Metall. Mater. Sci.*, 2003, vol. 34, pp. 171-81.
[16] M.A. Van Ende, M. Guo, E. Zinngrebe, B. Blanpain, and I.H. Jung: *ISIJ Int.*, 2013, vol. 53, pp. 1974-82.
[17] E. Zinngrebe, C. Van Hoek, H. Visser, A. Westendorp, and I.H. Jung: *ISIJ Int.*, 2012, vol. 52, pp. 52-61.
[18] A. Ghosh: Secondary Steelmaking: *Principles and Applications*, 2001.
[19] A. Bhansali, H. Oltmann, and E. Pretorius: in *AIST proceedings: AISTech 2021*, 2021, pp. 1-13.

Chapter 8

Concluding remarks

Non-metallic inclusion behaviour in molten steel has been the attention of many researchers in order to produce 'clean' steels. In this regard, different experimental and modelling work have been carried out to study the effect of different compositional and process variables on inclusion formation. Specifically, they have focused on the formation of harmful inclusions and how other phases such as slag and refractory, as well as Ca additions interact with them. The use of Al as a deoxidant leads to solid alumina inclusions that cause processability issues and product failures in certain long product steels. On the other hand, deoxidation with Si and Mn have shown that liquid inclusions form, making process of steelmaking less prone to clogging and lead to better mechanical properties. However, in such cases, it has been seen oxygen and sulphur levels cannot be decreased to very low levels, making slag selection a crucial task along with better process control. Moreover, the presence of Al in steel and other phase interactions can lead to changes in the composition of inclusions originating from deoxidation in Si/Si-Mn killed steels. This causes unwanted inclusions to form, which exhibit poor deformation characteristics, ultimately impairing steel performance and interfering with smooth casting operations. Another important aspect to note from the compositional analysis of inclusions in such steels is that although the deoxidation inclusions lie within the $MnO-SiO_2-Al_2O_3$ ternary system, the chemistry seems to show a variance even from samples taken from the same location. This non-equilibrium state seems to disagree with the local equilibrium theory proposed by numerous authors. Furthermore, inclusions such as Ca silicates are proposed to form from slag droplets that can further interact with existing inclusions and lead to various complex oxide inclusions. Thus, it is necessary to investigate the conditions which facilitate the formation

of such inclusions. Moreover, developing a tool to predict these conditions considering the important interactions will be invaluable for process control in steelmaking.

This thesis focused on mainly developing kinetic models to understand the compositional evolution of inclusions in a ladle furnace for Si-Mn-killed steel. Coupled with a steel-slag reaction model, the model was used to predict the chemical compositional evolution of steel, slag, and inclusion phases simultaneously. Furthermore, deoxidation experiments using FeSi and FeMn were conducted to understand inclusion behaviour under different conditions. The kinetic model was validated using data from experiments conducted in the author's laboratory and also previous steel plant data from the literature relevant to refining reactions for Si-Mn killed steel. A thorough analysis was conducted to understand the influence of parameters on the model. Potential limitations and improvements of the model were also discussed.

8.1 Key Findings and contributions

8.1.1 General overview

Chapter 1 introduced the background and motivation behind the current work of simulating ladle refining reactions. Chapter 2 summarised the state of the art in the control of oxide inclusions in Si-Mn killed steel and outlines the important topics in ladle metallurgy. The gaps in the existing literature and key aspects in modelling secondary steelmaking processes with regard to steel-slag reactions and steel-inclusion reactions were also discussed.

In Chapter 3, a systematic study on the formation of complex oxide formation was investigated mathematically at the nano and micron scales. Specifically, the rate-determining steps were identified through a nucleation model and a kinetic growth model for oxide modification. Chapter 4 then, uses the inclusion kinetic model developed in Chapter 3 with a previously developed steel-slag model. Using this model, the role of different slag compositions on Al pick-up in steel, the inclusion average composition ($MnO-SiO_2-Al_2O_3$) were investigated. Furthermore, the effect of steel mass transfer coefficient on slag-aided deoxidation was discussed.

In Chapter 5, an alternative technique to the model developed in chapter 4 was proposed, namely, the multi-oxide inclusion (MOI) kinetic model which is able to track the precipitation sequence of different oxide inclusions along with the average inclusion composition. Chapter 6 presented the application of the developed MOI model coupled with the steel-slag model to industrial

ladle refining reactions of Si Mn killed steel with special emphasis on Al pick up, inclusion composition, [S], and [O] variation in steel. The types of inclusions precipitating in Si-Mn-killed steel were shown as a function of time for different refining and processing variables in a ladle furnace.

Chapter 7 described the deoxidation experiments performed in the author's laboratory along with summary of the steel inclusion analysis carried out using automated SEM-EDS. This was done to understand the effect of oxygen and alloying addition practice on inclusion characteristics. Preliminary results and discussions were presented in this chapter.

8.1.2 Specific Findings

The research objectives presented in chapter 1 have now been achieved. The specific findings of the current study are as follows:

1. From Chapter 3, the mathematical analysis of nucleation of complex oxides following deoxidation revealed that the driving force for spontaneous nucleation of complex oxides can be as much as three times greater than for simple oxides. Different compositions of nuclei form based on the local availability of oxygen and solutes. Furthermore, the modification of simple oxides to complex oxides is fast (< 1 s) in Si-Mn-killed steel, which is in line with previous research conducted in Al-killed steels, indicating that both routes are possible given the sufficient supersaturation and driving force for mass transfer exists. This result further helped simplify the model for steel-inclusion reactions in molten steel.

2. In Chapter 3, sensitivity analysis on the nucleation model indicated that there is a role of interfacial tension and molar volume dependence on the composition of complex oxide nuclei in steel melts. On the other hand, the mass transfer model revealed that inclusion formation in Si-Mn killed steel is sensitive to solute concentrations, especially those in smaller amounts such as dissolved aluminum. This, in addition to the amount of dissolved oxygen and Mn/Si ratio, determines the overall inclusion formation behaviour in Si-Mn-killed steels. This effect is partly responsible for the persistence of non-equilibrium phases.

3. In Chapter 3, it was shown that the mixing time scales are higher than the nucleation and mass transfer time scales. This has important consequences on the inclusion composition variation with space and time.

Since circulating flow fields in the ladle transport inclusions to different regions with different solute concentrations, it will probably result in steel-inclusion reactions with different driving forces for inclusion transformation, leading to differences in inclusion chemistry. It would be interesting to model the coupled effect of the steel flow on the overall variation of inclusion compositions in the future.

4. The multi-oxide inclusion (MOI) kinetic model developed in Chapter 5 for steel-inclusion reactions when coupled with steel-slag reaction kinetics can adequately reproduce the observations from experimental data. This shows the success of the approach both at laboratory and industrial scales. This approach enables one to track the competition between different inclusion types by considering the thermodynamics and kinetics of inclusion formation. This offers more information than just the average inclusion composition trajectory that the model in Chapter 4 was able to only provide. Furthermore, this approach is an alternative to commercial thermodynamic software and is somewhat better owing to its ability to handle the effect of number density variation of inclusions in steel directly in its formulation.

5. In Chapter 6, while simulating steel-slag-inclusion reaction kinetics for industrial situations in Si-Mn killed steels, it was observed that the amount of alloy additions and the rate at which they dissolve and mix decide the temporal evolution of species with higher concentrations ([Si], [Mn], [C]). On the other hand, the species with lower concentrations ([Al], [S]) are influenced by the reactions at the steel-slag interface along with the mutual interaction of the solutes with the existing inclusions.

6. In Chapters 4 and 6, the developed steel-slag-inclusion kinetic model was successfully used to simulate the effect of slag composition on inclusion control, desulphurization and deoxidation. Specifically, it was demonstrated that:

    - Silica-rich slags impose a lower equilibrium oxygen potential at the steel/slag interface, leading to oxygen transfer through slags if the oxygen potential obtained from only Si-Mn deoxidation is higher than this value. This can be further increased with a higher mass transfer coefficient (caused by stirring).
    - Alumina in slags > 10 wt.% significantly affects the inclusion composition owing to a higher driving force for Al pick up in the steel, which can in turn lead to reactions with existing inclusions or

precipitation of new inclusions. However, optimizing its amount seems necessary since an increase in alumina in slags leads to higher sulfide capacities, thus promoting more desulphurisation.

- An increase in the slag basicity (CaO/SiO_2) with higher Al_2O_3 content will lead to an increase in higher aluminum activity at the steel-slag interface. This will lead to more Al reduction at the steel-slag interface which will increase the Al_2O_3 in the inclusions but simultaneously, lead to lower sulphur levels in the steel.
- Slag changing operations conducted to increase the slag binary basicity will lead to an increase of Al_2O_3 in the inclusion composition and a decrease in the sulfur levels in the steel. Delaying this operation with moderate stirring towards the end of the refining should be able to help suppress excess Al pickup in steel.
- The composition of inclusions in steel alters by reoxidation, which occurs due to a change in amount of available dissolved oxygen in the steel. This can either lead to a higher alumina content in the inclusions or a new population of inclusions depending on the [Al] and Mn/Si ratio. On the other hand, the desulphurisation process can be hindered by an increase in (FeO+MnO) in slags, which also slows the rate of Al pickup in steel.

7. From the laboratory deoxidation experiments described in Chapter 7, it was seen that after FeSi addition, inclusions were SiO_2 with trace amounts of Al_2O_3 whereas after subsequent addition of FeMn, these transformed into $MnO-SiO_2$ with some containing Al_2O_3 in them. The inclusions were found to be spherical in morphology. At lower initial oxygen levels, the inclusions contained more Al while the alloying addition practice did not affect the inclusion composition to a significant extent. This shows that the oxygen levels in steel prior to deoxidation influence the alumina content of the inclusions in Si-Mn killed steel even at low initial aluminium levels. Furthermore, the rate of inclusion removal seemed to be higher when FeSi and FeMn are added concurrently than when they are added sequentially, which needs to be probed a bit further.

8.2 Suggestions for future work

- In this work, the multi-oxide inclusion model has been made to consider the formation of inclusions relevant to Si-Mn killed steel but its generic framework enables its application to other deoxidation systems such as Al, Al-Ca, Al-Ti, etc. In the future, this could be explored further.

- For steel grades where there are higher alloying elements such as stainless steel, high carbon steels, high Mn steels, certain compositional variables lie within the Raoultian regime. The current version of the model utilizes the Unified Interaction Parameter formalism (UIPF) model. This sub-model seems to be somewhat unsuccessful in predicting activities of steel species in these cases reliably. In that regard, evaluation of interaction parameters in UIPF might be needed to predict the steel species activities.
- Since the bulk steel does not remain entirely homogenized throughout the refining time, it might influence the supply of solutes to the steel/inclusion interface and thus constitute as an important rate determining step. Effects of mixing can be considered using models proposed in Ref. [4].
- The current steel-slag-inclusion model does not take into account the calcium dissolution kinetics that might be important for situations where Ca treatment is practiced in Si-Mn killed steels. This could be done similarly to the method proposed by Tabatabaei et al. [3], where Ca interaction with inclusions was simulated for Al-killed steels.
- Since most particle size distribution (PSD) models have focussed on simple oxides, the current nucleation model developed in this work for complex oxides could be utilized in calculating the particle size distribution of complex oxide inclusions in the steel, following nucleation.
- The effect of inclusion number density variation on the compositional changes of inclusions has been ignored in this study. This could be incorporated into the MOI model developed in this work through mean-field models, Quadrature Method of Moments models (zeroth moment) or PSD models.
- Further analysis of the oxide inclusion characteristics obtained from the deoxidation experiments performed in our laboratory need to be carried out to understand the removal rate of inclusions following deoxidation which could shed some light on the coagulation behaviour of liquid inclusions.
- As discussed in Section 2.2.4, there seems to be dearth of fundamental studies regarding the effect of slag in silicon rich steels and high alloy steels killed using FeSi and FeMn. Experimental studies concerning the same will help understand the behaviour of inclusions, [O], [Al] and [S] with time.
- As discussed in Section 2.3.1, the mass transport steps with regard to sulphur reaction between steel and slag at low aluminium levels need to be probed, conditions which are relevant to Si-Mn killed steel. These studies need to be carried out at different oxygen, and sulphur levels in steel.

References

[1] H. Gaye and J. Lehmann: Molten Slags, Fluxes Salts '97 Conf., 1997, pp. 27–32.
[2] J. Lehmann and L. Zhang: Steel Res. Int., 2010, vol. 81, pp. 875–9.
[3] Y. Tabatabaei, K.S. Coley, G.A. Irons, and S. Sun: Metall. Mater. Trans. B Process Metall. Mater. Process. Sci., 2018, vol. 49, pp. 2744–56.
[4] J. Mietz and F. Oeters: Steel Res., 1989, vol. 60, pp. 387–94.

Appendices

Appendix A

Sub-regular solution model for liquid oxides

The Sub-Regular Solution Model (SRSM) belongs to the subset of 'thermodynamics parameter models' and can be used to define the activities for liquid oxide slag systems, such as those relevant for secondary steelmaking systems, $CaO-MgO-SiO_2-Al_2O_3$ and $CaO-MnO-SiO_2-Al_2O_3$ by Xiao Bing et al. [1].

This model contains many empirical parameters that are estimated based on the fitting of the existing physical and chemical behavior of slags. Owing to the simplicity of the model implementation and accuracy in the above oxide systems, this model seems very 'reliable' for predicting the activities of the inclusion components. For a detailed thermodynamic derivation, the reader is left to the original publication [1].

The activity of M_xO_y in a multicomponent oxide system can be calculated as:

$$a_i = X_i \exp\left(\frac{G_i^{ex} - G_i^o}{RT}\right), \tag{A.0.1}$$

where X_i is the mole fraction of an oxide M_xO_y in the oxide system, G_i^{ex} is the excess partial mole free energy of the oxide in reference to the pure liquid state and G_i^o is the mole free energy of phase transformation of the oxide from liquid to solid [2].

For any quaternary oxide system, G_i^{ex} is expressed with a set of formulae in a multi-component framework (M_xO_y = 1 to 4), for which 1 to 4 denote the

four oxide components as

$$G_1^{ex} = \sum_{2}^{j'} \sum_{0}^{k'} \sum_{0}^{l'} A_{jkl} Y^j Z^k U' \tag{A.0.2}$$

$$G_2^{ex} = -\sum_{2}^{j'} A_{j00}/(1-j) + \sum_{2}^{j'} \sum_{0}^{k'} \sum_{0}^{l'} \left\{ A_{jkl} Y^j Z^k U^l \{1 + (j-k)/[Y(1-j)]\} \right\} \tag{A.0.3}$$

$$G_3^{ex} = -\sum_{2} \sum_{0} A_{jk0}/(1-j) + \sum_{2} \sum_{0} \sum_{0} \{A_{jkl} Y^j Z^k U^l \{1 + (j-k)/[Y(1-j)] + (k-l)/[YZ(1-j)]\}\} \tag{A.0.4}$$

$$G_4^{ex} = -\sum_{2}^{j'} \sum_{0}^{k'} \sum_{0}^{l'} A_{\mathrm{jkl}} Y/(1-\mathrm{j}) - \sum_{2}^{j'} \sum_{0}^{k'} \sum_{0}^{l} A_{\mathrm{jkl}} Y^{\mathrm{j}} Z \mathrm{T}^{\mathrm{j}} \{1 + [(\mathrm{j}-\mathrm{k})/\mathrm{Y}(1-\mathrm{j})] + [(\mathrm{k}-1)/YZ(1-\mathrm{j})] + [1/YZT(1-\mathrm{j})]\} \tag{A.0.5}$$

Here, j', k', l' refer to the order of the system, A_{jkl} are empirical parameters of the SRSM model, and Y, Z, and U are the reduced composition variables,

$$Y = 1 - X_1 \tag{A.0.6}$$

$$Z = 1 - (X_2/Y) \tag{A.0.7}$$

$$U = 1 - (X_3/YZ) \tag{A.0.8}$$

A.1 Model parameters

The A_{jkl} for CaO−MgO−SiO_2−Al_2O_3 and CaO−MnO−SiO_2−Al_2O_3 are given in Table A.1.1 and A.1.2 which are taken from Ref. [3].

Table A.1.1: *Parameters A_{jkl} of $CaO-MgO-SiO_2-Al_2O_3$*

j	l	k = 0	k = 1	k =2	k = 3	k = 4
2	0	-345.5	235.8	1333.8	-1066.6	-34
	1	0	-6659.1	11874.9	-4916.2	-248.7
	2	0	24403.5	-40282.9	15807.8	0
	3	0	-27882.9	37039	-9265.3	0
	4	0	10762.6	-10708.9	0	0
3	0	572.5	3036.7	-12479.7	9858.9	-1043.3
	1	0	11345.6	-17184.3	4466.5	1043.3
	2	0	-48575.5	79574.2	-30430.5	0
	3	0	55765.3	-73810.4	18044.6	0
	4	0	-21525.3	21525.3	0	0
4	0	-120.7	-4541	13574.6	-10263.7	889.2
	1	0	3013.3	-9285.8	7503.2	-889.2
	2	0	-347.3	0	0	0
	3	0	0	0	0	0
	4	0	0	0	0	0

Please note: 1 - SiO_2, 2 - Al_2O_3, 3 - CaO, 4 - MgO

Table A.1.2: *Parameters A_{jkl} of $CaO-MnO-SiO_2-Al_2O_3$*

j	l	k = 0	k = 1	k =2	k = 3	k = 4
2	0	61.7	159.7	-1093.3	1810.0	-847.4
	1	0.0	-11725.7	25802.0	-26600.9	11924.6
	2	0.0	20811.3	-13751.7	-686.2	-3866.5
	3	0.0	-15710.8	-5970.7	22455.1	-5128.6
	4	0.0	6286.1	-3461.6	-521.7	296.4
3	0	-589.8	8.9	3887.7	-7263.6	3288.1
	1	0.0	58391.4	-136302.9	153339.5	-69784.6
	2	0.0	-105915.2	116631.0	-98501.7	66974.0
	3	0.0	75352.3	2986.0	-35051.3	-9961.6
	4	0.0	-25806.0	6855.2	0.0	0.0
4	0	583.1	-205.3	-3588.1	6324.1	-2510.5
	1	0.0	-52463.6	127755.8	-145651.5	64362.2
	2	0.0	96439.0	-129690.0	131091.7	-75286.9
	3	0.0	-65895.9	10232.0	0.0	20064.4
	4	0.0	19850.8	0.0	0.0	0.0

Please note: 1 - MnO, 2 -SiO_2, 3 - Al_2O_3, 4 - CaO

References

[1] Z.X. Bing, J.G. Chang, and X.K. Di: *Calphad Comput. Coupling Phase Diagrams Thermochem.*, 1997, vol. 21, pp. 311-20.

[2] H. Gaye and J. Welfringer: *in Second Int. Symp. Metall. Slags Fluxes*, 1984, pp. 357-75.

[3] X. Zhang: *Acta Metallurgica Sinica*, 2004, vol. 40 (5) pp. 509-14.

Appendix B

Comparison between reaction zone and reaction interface model

B.1 Similarity of kinetic equations

In the reaction zone model, a complex process is divided into a finite number of reaction zones in which equilibrium state is calculated. Here, a finite volume of each phase is allowed to react near the interface (See Figure B.1).

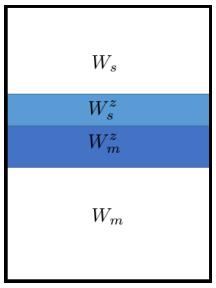

Figure B.1: *Schematic illustrating the concept of reaction zone model.*

The reaction zone mass per unit step is considered for describing the mass transfer in each phase instead of the general flux density equations. That is, a constant volume of metal (V_m^z) from the bulk metal and a constant volume of slag (V_s^z) from the bulk slag enter the metal-slag reaction zone at a fixed time interval (Δt). The superscripts t and $(t + \Delta t)$ are at previous and current time steps, respectively. The reaction zone mass per unit time step

for metal phase and slag phase (W_m^z and W_s^z) can be described as follows:

$$W_m^{z,t} = \rho_m k_m A\ \Delta t \tag{B.1.1}$$

$$W_s^{z,t} = \rho_s k_s A \Delta t \tag{B.1.2}$$

where the subscripts m and s represent metal phase and slag phase, respectively, W^t represents reaction zone mass at time t, ρ represents density of each phase, k represents the mass transfer coefficients[1], and A represents the interface area between the metal and slag phase.

After the reaction, the mass of metal phase changes at the interfacial volume, which can be written as:

$$W_m^{z,t+\Delta t} = \rho_m k_m\ A\Delta t - \Delta W_m = \rho_m k'_m A \Delta t \tag{B.1.3}$$

where ΔW_m is the change in mass of the reaction zone after reaction and k'_m is a constant coefficient (significance discussed later).

Utilizing the reaction zone model concept, the amount of metal phase present at new time $t+\Delta t$, $[\%M]_b^{t+\Delta t}$ is thus given as follows:

$$[\%M]_b^{t+\Delta t} = \frac{[\%M]_b^t \cdot W_m + [\%M]_e \cdot W_m^{z,t+\Delta t}}{(W_m + W_m^{z,t+\Delta t})} \tag{B.1.4}$$

where W_m and $[\%M]_e$ represent total weight of unreacted metal phase and the equilibrium concentration of metal in the reaction zone.

Using Eq. B.1.1 in Eq. B.1.4, we have the following :

$$[\%M]_b^{t+\Delta t} \cdot (W_m + \rho_m k'_m A\Delta t) = [\%M]_b^t \cdot W_m + [\%M]_e \cdot \rho_m k'_m A \Delta t \tag{B.1.5}$$

Rearranging Eq.(B.1.5) gives:

$$([\%M]_b^{t+\Delta t} - [\%M]_b^t) \cdot W_m = ([\%M]_e - [\%M]_b^{t+\Delta t}) \cdot \rho_m k'_m A \Delta t \tag{B.1.6}$$

$$\frac{([\%M]_b^{t+\Delta t} - [\%M]_b^t)}{\Delta t} = \frac{\rho_m k'_m A}{W_m}([\%M]_e - [\%M]_b^{t+\Delta t}) \tag{B.1.7}$$

[1] this is based on the *mtc* from reaction interface model

For small time step (Δ t $\rightarrow$ 0), the differential form can be written as:

$$\lim_{\Delta t \to 0} \frac{([\%M]_b^{t+\Delta t} - [\%M]_b^t)}{\Delta t} = \frac{\rho_m k'_m A}{W_m}([\%M]_e - [\%M]_b^{t+\Delta t}) \tag{B.1.8}$$

$$\text{or,} \quad \frac{d[\%M]_b}{dt} = \frac{\rho_m k'_m A}{W_m}([\%M]_e - [\%M]_b) \tag{B.1.9}$$

$$\text{or,} \quad -\frac{d[\%M]_b}{dt} = \frac{k'_m A}{V_m}([\%M]_b - [\%M]_e) \tag{B.1.10}$$

Thus, we see that when the equations are cast in the form given by reaction interface model, the coefficient introduced is not strictly equal to the *mtc* derived for RIM. However, they can show the same order, based on the change in reaction mass at the interface, ΔW_m as shown in Eq. B.1.3. If the change is small or equal to zero, the terms would be numerically equal. The above derivation answers an interesting question of whether the *mtc* used in both the models are identical or not. Furthermore, the interface value is defined at local equilibrium between the phases, assuming it exists.

B.2 Similarity of thermodynamic equations

For the following reaction:

$$[\mathrm{M}] + x[\mathrm{O}] = (\mathrm{MO_x}) \tag{B.2.1}$$

the amount of equilibrium phases is often determined by the equilibrium constant method:

$$K_{\mathrm{M/MO_x}} = \frac{a_{\mathrm{MO_x}}}{a_{\mathrm{M}} \cdot a_{\mathrm{O}}^x} \tag{B.2.2}$$

Together with the knowledge of the activities of elemental species, temperature and by performing the necessary mass balances, one can obtain the equilibrium state. However, the situation gets complicated when multiple species and phases are involved. Alternatively, the formation of any species in a multicomponent system at a particular temperature is accompanied by a change in the Gibbs free energy of the system. As a result, the equilibrium state can be computed by the Gibbs free energy minimization (GFEM) method as shown:

$$\frac{\partial G}{\partial n_{i,p}} = 0 \tag{B.2.3}$$

where G is the Gibbs free energy of the entire system given by Eq. B.2.4, $n_{i,p}$ is the number of moles of the i-th component in the phase p.

$$G = \sum n_t G_i^o + \sum n_i^{ox} \Delta G_i^{ox} + \sum n_i^{ox} RT \ln(a_i^{ox}) + \sum n_t^{dis} RT \ln(a_i^{dis}) \tag{B.2.4}$$

where n_t, n_i^{ox}, n_i^{dis} refer to the total moles, moles of species in oxide and dissolved phase, respectively. G_i^o is the standard Gibbs free energy of species, while ΔG_i^{ox} is the formation Gibbs free energy change for oxides.

It needs to be noted that Eq. B.2.2 and Eq. B.2.3 yield similar equilibrium compositions, with the reaction interface model requiring the form of equations belonging to Eq. B.2.2 while the reaction zone model utilizing the GFEM concept. Depending on the formulation of the thermodynamic problem, we then choose an adequate method of solution. However, from a physical point of view, a question arises of whether local equilibrium persists in an interface or in a zone near the interface.

Appendix C

Analytical formulation of diffusion through product layer in MnO-SiO_2 inclusions

From the reaction of [Si], [Mn], and [O] at the interface of a SiO_2 inclusion, a finite product layer consisting of $MnO{-}SiO_2$ is created on preexisting inclusions, which is allowed to grow based on subsequent reaction with the SiO_2. To model the diffusion of MnO and SiO_2 through the resulting liquid product layer, an inclusion with spherical geometry is considered. Chemical reactions are fast relative to mass transport processes due to the high temperature, so equilibrium is attained at all interfaces. The thickness of $MnO{-}SiO_2$ formed depends on the equimolar counter diffusion of MnO and SiO_2, with growth only occurring inside the inclusion, R_{in}, with a shrinking core of SiO_2. The interfacial concentration at the external radii, R_{ex}, are solved from equations resulting from the reactions at the steel-inclusion interface by mass transfer through the boundary layer. A schematic of the reactions and important variables is shown in Figure C.1.

If J is the diffusion rate of MnO through the product layer (Fig. 4.3), then according to Fick's law:

$$J = -D_{\mathrm{MnO}} A \frac{\partial C_{\mathrm{MnO}}}{\partial r} = -D_{\mathrm{MnO}} \cdot 4\pi r^2 \frac{\partial C_{\mathrm{MnO}}}{\partial r} \tag{C.0.1}$$

To solve the above, pseudo steady state approximation can be used i.e., the concentration gradient remains fixed with the radius change of the particle. In other words, the concentration profile is only a function of time at different

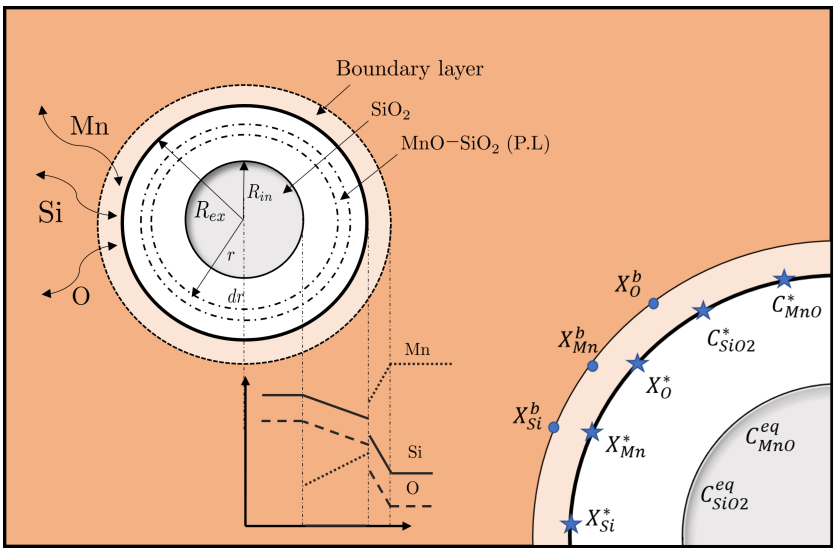

Figure C.1: *Schematic of steel-inclusion interactions*

radii. Consequently, $\partial C_{\mathrm{MnO}}/\partial r$ is constant and can be replaced as dC_{MnO}/dr.

$$4\pi D_{\mathrm{MnO}} dC_{\mathrm{MnO}} = -J\frac{dr}{r^2} \tag{C.0.2}$$

Assuming D_{MnO} remains constant through the process, integrating between the limits at the inner and external radii results in:

$$4\pi D_{\mathrm{MnO}} \int_{in}^{ex} dC_{\mathrm{MnO}} = -J\int_{in}^{ex} \frac{dr}{r^2} \tag{C.0.3}$$

$$4\pi D(C^*_{\mathrm{MnO}} - C^{eq}_{\mathrm{MnO}}) = J\left(\frac{1}{R_{ex}} - \frac{1}{R_{in}}\right) \tag{C.0.4}$$

$$J = -\frac{4\pi R_{ex}R_{in}D}{(R_{ex}-R_{in})}(C^*_{\mathrm{MnO}} - C^{eq}_{\mathrm{MnO}}) \tag{C.0.5}$$

$$J = \frac{-dn_{\mathrm{MnO}(r)}}{dt} = -\frac{4\pi D(C^*_{\mathrm{MnO}} - C^{eq}_{\mathrm{MnO}})}{\left(\frac{1}{R_{in}} - \frac{1}{R_{ex}}\right)} \tag{C.0.6}$$

$$\frac{-4\pi\rho R_{in}^2}{M_w}\cdot\frac{dr}{dt} = -\frac{4\pi D(C^*_{\mathrm{MnO}} - C^{eq}_{\mathrm{MnO}})}{\left(\frac{1}{R_{in}} - \frac{1}{R_{ex}}\right)} \tag{C.0.7}$$

$$\left(R_{in} - \frac{R_{in}^2}{R_{ex}}\right)dr = -\frac{DM_w}{\rho}\cdot(C^*_{\mathrm{MnO}} - C^{eq}_{\mathrm{MnO}})dt \tag{C.0.8}$$

Integrating between limits and considering C^*_{MnO} constant between the time

step, t, we have:

$$\int_{R_{ex}}^{R_{in}} \left(R_{in} - \frac{R_{in}^2}{R_{ex}} \right) dr = -\int_0^t \frac{DM_w}{\rho} \cdot (C^*_{\mathrm{MnO}} - C^{eq}_{\mathrm{MnO}}) dt \tag{C.0.9}$$

$$\left(\frac{R_{in}^2}{2} - \frac{R_{in}^3}{3R_{ex}} \right) \Bigg]_{Rex}^{Rin} = -\frac{DM_w}{\rho} \cdot (C^*_{\mathrm{MnO}} - C^{eq}_{\mathrm{MnO}}) t \tag{C.0.10}$$

$$\frac{1}{2} R_{in}^2 - \frac{1}{6} R_{ex}^2 - \frac{1}{3} \frac{R_{in}^3}{R_{ex}} = -\frac{DM_w \Delta C}{\rho} t \tag{C.0.11}$$

where $\Delta C = (C^*_{\mathrm{MnO}} - C^{eq}_{\mathrm{MnO}})$

Defining the fractional reduction in mass/volume of the core (SiO_2) in terms of a parameter, β, we have:

$$\beta = \frac{\frac{4}{3}\pi R_{ex}^3 - \frac{4}{3}\pi R_{in}^3}{\frac{4}{3}\pi R_{ex}^3} = 1 - \left(\frac{R_{in}}{R_{ex}} \right)^3 \tag{C.0.12}$$

Using C.0.12 in Eq. C.0.11, after simplification, we can write the following:

$$1 - \frac{2}{3}\beta - (1-\beta)^{2/3} = \frac{2M_w D \Delta C}{\rho R_{ex}^2} t \tag{C.0.13}$$

It can be seen from Eq. C.0.13 that a characteristic time, t^* can be used to estimate the time needed for inclusion modification or transformation,

$$t^* = \frac{\rho R_{ex}^2}{2M_w D \Delta C} \tag{C.0.14}$$

END